

**STRUCTURE, DYNAMICS, AND REACTIVITY OF MOLECULAR ASSEMBLIES
AT INTERFACES**

by

Tao Ye

BS, Peking University, 1997

Submitted to the Graduate Faculty of
Arts and Sciences in partial fulfillment
of the requirements for the degree of
Doctor of Philosophy

University of Pittsburgh

2003

UNIVERSITY OF PITTSBURGH
FACULTY OF ARTS AND SCIENCES

This dissertation was presented

by

Tao Ye

It was defended on

Dec. 9, 2003

and approved by

Prof. Shigeru Amemiya, Department of Chemistry, University of Pittsburgh

Prof. Andrew Gellman, Department of Chemical Engineering, Carnegie Mellon University

Prof. David Waldeck, Department of Chemistry, University of Pittsburgh

Prof. Eric Borguet, Department of Chemistry, University of Pittsburgh
Dissertation Director

Structure, Dynamics, and Reactivity of Molecular Assemblies at Interfaces

Tao Ye

University of Pittsburgh, 2003

The central theme of my research is to understand self-assembly of molecules at interfaces and to develop strategies that control the arrangement of atoms and molecules at the nanometer length scale.

We have sought molecular level insight into the mechanism of photoreactivity of octadecylsiloxane (ODS) self-assembled monolayers (SAMs), which has implications in high resolution nanolithography. We have improved the reproducibility of preparation of ODS SAMs by controlling the water content in the reaction solution and in the ambient environment. We have demonstrated that atomic oxygen is the primary agent for the UV photoreactivity of ODS SAMs. UV degradation proceeds via oxidation of carbon chains instead of the siloxane headgroups. We found that degradation introduces microscopic roughness in SAMs. Using a novel technique, Fluorescence Labeling of Surface Species, we identified low-concentration surface functional groups produced as intermediates in UV degradation. We proposed a reaction mechanism based on hydrogen abstraction.

To understand the rules governing self-assembly at electrochemical interfaces and how they can be exploited to control the arrangement of molecules, we performed in-situ STM investigations. To probe the effect of hydrophobic interactions, we investigated how the electrode potential transforms the microscopic structure of a completely hydrophobic molecule, hexadecane. Molecular level evidence suggests that the competition between

hexadecane and the electrolyte plays a pivotal role in the self-assembled structures at the charged interface. We studied how the electrode potential can affect the dynamics of self-assembly of 5,10,15,20-Tetra(4-Pyridyl)-21H,23H-Porphine (TPyP), which can not be displaced by the electrolyte due to much stronger adsorption. Our results suggest that while TPyP can be kinetically trapped in a disordered structure, its ordering process can be facilitated at electrode potentials where molecule substrate interaction is strong enough to confine molecules in ordered arrays but also weak enough to allow facile lateral reorganization, a key requirement for self-assembly. Our investigation also suggests that electrode potential can direct the formation of multilayers due to the π stacking interaction of TPyP. We observed distinct electrochemical reactivity of adsorbed TPyP, due to the interaction between TPyP and the Au substrate.

Finally, we have demonstrated that the intrinsic length scales of molecular assemblies may be exploited to grow metal nanostructures of controlled spacing. Our study of metal electrodeposition on surface micelles affords insight into the interaction between metal nanostructures. In particular, how the interaction can be controlled to grow metal nanoscale structures, are relevant to electrocatalysis and nanoscale electronics.

TABLE OF CONTENTS

1.	Preparation of alkylsiloxane self-assembled monolayers: the issue of reproducibility.	1
1.1.	Introduction.....	1
1.1.1.	Importance of SAMs.....	1
1.1.2.	Growth of SAMs.....	3
1.1.3.	Motivation.....	8
1.2.	Experimental section.....	9
1.2.1.	Substrate treatment.....	9
1.2.2.	Self-assembly.....	9
1.2.3.	Characterization.....	11
1.3.	Results and discussion.....	12
1.3.1.	Criteria for a high quality ODS SAM.....	12
1.3.2.	Effect of freshness of OTS.....	18
1.3.3.	Effect of water content.....	20
1.3.4.	Roles of ambient humidity.....	21
1.3.5.	Conclusions and future work.....	25
	BIBLIOGRAPHY.....	28
2.	Mechanism of UV photoreactivity of alkylsiloxane self-assembled monolayers. ...	32
2.1.	Introduction.....	32
2.1.1.	Possible mechanisms of photoreactivity of SAMs.....	34
2.1.2.	Objectives of this study.....	36
2.2.	Experimental Section.....	37
2.2.1.	SAM preparation.....	37
2.2.2.	UV photoreactivity.....	37
2.2.3.	Sample characterization.....	38
2.3.	Results.....	40
2.3.1.	Contact angle results.....	40
2.3.2.	FT-IR results.....	42
2.3.3.	AFM results.....	50
2.3.4.	XPS results.....	54
2.3.5.	Fluorescence labeling of surface species (FLOSS).....	57
2.4.	Discussion.....	63
2.4.1.	Summary of results.....	63
2.4.2.	Active agents.....	63
2.4.3.	Probable reaction pathways.....	66
2.4.4.	Reactive sites.....	68
2.4.5.	Implications on photopatterning.....	78
2.4.6.	Conclusions.....	80
2.4.7.	Future work.....	80
	BIBLIOGRAPHY.....	82
3.	Introduction to electrochemical interfaces.....	87

3.1.	Electrochemical interfaces: structure of the double layer.....	87
3.1.1.	The electrochemical interface and the electric double layer.....	87
3.1.2.	Electrode surfaces.....	90
3.2.	Adsorption and self-assembly of molecular adsorbates at electrochemical interfaces.....	93
3.2.1.	Molecular adsorbates at vacuum-solid and gas-solid interfaces.....	94
3.2.2.	Molecular adsorbates at electrochemical interfaces.....	95
3.3.	SPM study of molecular self-assembly.....	98
3.3.1.	Principles of electrochemical SPM.....	99
3.3.2.	EC-SPM study of molecular self-assembly.....	101
3.4.	Overview of the EC-STM section of this dissertation.....	102
	BIBLIOGRAPHY	104
4.	The role of hydrophobic chains in self-assembly at electrified interfaces: Observation of potential induced transformation of two dimensional crystals of hexadecane by in-situ scanning tunneling microscopy.....	107
4.1.	Introduction.....	107
4.1.1.	Role of hydrophobic tails in the structure of amphiphilic monolayers...	107
4.1.2.	Studies of alkanes at electrified interfaces.....	108
4.1.3.	Summary of previous investigations of the structure of alkanes on Au surfaces.	109
4.1.4.	Summary of this work.....	110
4.2.	Experimental.....	111
4.2.1.	Sample preparation.....	111
4.2.2.	STM experiments.....	112
4.3.	Results and discussion.....	113
4.3.1.	Structure of Hexadecane monolayers on reconstructed Au(111) surface.	113
4.3.2.	Potential-induced transformation of 2D hexadecane crystals on Au(111).	116
4.3.3.	Spontaneous molecular domain flipping.....	123
4.3.4.	Stabilization of substrate by molecular overlayers.....	127
4.3.5.	Discussion.....	128
4.4.	Summary.....	131
	BIBLIOGRAPHY	132
5.	Porphyrin self-assembly at electrochemical interfaces: Role of potential modulated surface mobility.....	135
5.1.	Introduction.....	135
5.1.1.	Molecular self-assembly on surfaces.....	135
5.1.2.	Motivation.....	136
5.2.	Experimental.....	139
5.3.	Results and discussions:.....	140
5.3.1.	Potential dependant mobility of TPyP.....	140
5.3.2.	Dynamics of the preadsorbed TPyP adlayer.....	145
5.3.3.	Summary.....	148
	BIBLIOGRAPHY	152

6.	In-situ STM study of electrode reactions and potential induced adsorption-desorption of porphyrin adsorbates.....	154
6.1.	Introduction.....	154
6.2.	Experimental section.....	157
6.3.	Results and discussion.	157
6.3.1.	Cyclic voltammetry results.	157
6.3.2.	STM results.....	165
6.3.3.	Surface interactions.....	175
6.3.4.	The reactivity of adsorbed species.....	177
6.4.	Conclusions and future work.	179
7.	Electrodeposition onto molecular scale templates.....	185
7.1.	Introduction.....	185
7.1.1.	Electrodeposition.	185
7.1.2.	Organic molecules as resists.	186
7.1.3.	Metal-organic interfaces.	187
7.1.4.	Self-assembled 2D structures of surfactants.....	188
7.1.5.	Motivation.....	190
7.2.	Experimental.....	191
7.3.	Results.....	193
7.3.1.	Potential dependant structures of SDS at electrochemical interfaces.....	193
7.3.2.	Electrodeposition on molecular-scale templates.....	198
7.4.	Discussion and conclusions.	210
7.4.1.	Discussion.....	210
7.4.2.	Future work.....	214
	BIBLIOGRAPHY.....	216
	Appendix A: Frictional cross-talk in atomic force microscopy.....	219
	Appendix B: Measuring ozone concentration.....	223
	Appendix C: EC-STM tip preparation.....	226
	Appendix D: Reference electrode for EC-STM.....	230
	Appendix E: List of publications.....	234
	Acknowledgements:.....	235

LIST OF TABLES

Table 2-1 Proposed mechanism of electron beam degradation of SAMs.....	36
Table 2-2 Reactions to generate atmospheric oxidants [34].....	65
Table 2-3 Formation of alkoxy radical	67
Table 2-4 Further oxidation.	67

LIST OF FIGURES

Figure 1–1 Proposed mechanism of ODS SAM formation.	3
Figure 1–2 Water contact angle of ODS on glass as a function of reaction time.	13
Figure 1–3 FT-IR spectra of ODS on glass for different reaction time spent in OTS solution (5 min, 15 min and 30 min) using Procedure 1.....	14
Figure 1–4 An example of deconvolution of the FTIR spectra of ODS SAMs.....	15
Figure 1–5 Integrated absorbance of SAMs at CH ₂ antisymmetric mode as a function of reaction time.....	16
Figure 1–6 AFM images of ODS SAMs with A: 3.3 mOD and B: 5 mOD peak absorbance at ~2918 cm ⁻¹ . Image size: 2 μm× 2 μm. Height scale (5nm)	17
Figure 1–7 AFM images of ODS images of submonolayer coverage ODS monolayer on Si substrate prepared with method 1 at reduced reaction time (30 sec) and temperature (10 °C).....	18
Figure 1–8 Typical AFM images of ODS SAMs on SiO ₂ /Si prepared with A: fresh OTS and B: old OTS. Reaction time 1 hour. (Image size: 2 μm ×2 μm, height scale 2 nm)	19
Figure 1–9 Effect of water content in the ODS SAM preparation on glass. 20°C, 60% relative humidity 60 minute reaction time.	20
Figure 1–10 FTIR spectra of ODS SAMs on glass after 60 min of reaction . Spectra are offset for clarity. From bottom to the top: A substrate equilibrated at 40% RH. Sealed container. B substrate equilibrated 5% and sealed container. C container opened to 40% RH. Reaction conditions: 12 mM water 2.1mM OTS in toluene. ..	21
Figure 1–11 ν _{as} CH ₂ peak absorbance as a function of reaction time when exposed to 40 and 50% relative humidity(12 mM water 2.1mM OTS in toluene).....	23
Figure 1–12 The role of humidity in ODS SAM formation.	26
Figure 2-1 Probable mechanisms of SAM photoreactivity.....	34
Figure 2-2 UV chamber a: Irradiation configuration 1, where both sides of the sample are exposed to the chamber. b: Irradiation configuration 2, where only a single side is exposed to the reactive species produced in the chamber.....	38
Figure 2-3 Contact angles of irradiated ODS SAMs on glass as a function of time under different ambient environments.	42
Figure 2-4 UV-vis spectrum of a 1mm thick microscope cover glass slide (VWR).	42
Figure 2-5 FT-IR spectra of double sided ODS sample and single sided ODS sample on glass.....	43
Figure 2-6 FT-IR spectra of ODS SAMs on glass irradiated for different amount of time, 0, 5 min, 20 min, 30 min, 45 min to 60 min in descending order. Spectra are offset for clarity.....	45
Figure 2-7 Integrated absorbance of ν _{as} CH ₂ and ν _s CH ₂ vs UV irradiation time (min). 46	46
Figure 2-8 ν _{as} CH ₂ and ν _s CH ₂ peak frequencies of ODS SAMs as a function of UV irradiation time.....	46
Figure 2-9 ν _{as} CH ₂ and ν _s CH ₂ peak width (full width at half maximum) of ODS SAMs as a function of UV irradiation time.....	47
Figure 2-10 Effect of acetone rinsing on a SAM exposed to 15 min of UV irradiation... 48	48

Figure 2-11 FT-IR spectra of ODS monolayers on glass irradiated with UV for 15 min under 35% and 5% relative humidity.....	48
Figure 2-12 FTIR spectrum of ODS SAM irradiated for 30 minutes in the carbonyl stretch region. Substrate SiO ₂ /Si.....	50
Figure 2-13 Contact mode AFM image of ODS on SiO ₂ /Si irradiated (from left to right) for a: 0 min, b: 15 min and c: 30 min. Height scale 2 nm.....	51
Figure 2-14 Tapping mode AFM images of a submonolayer ODS SAM on SiO ₂ /Si.....	52
Figure 2-15 Tapping mode AFM images and cross sections of ODS SAM on SiO ₂ /Si surface. (A) No UV irradiation. SAM height=1.7 nm (B) 15 min UV irradiation. SAM height=0.8 nm	53
Figure 2-16 Tapping mode AFM images of ODS on SiO ₂ /Si at an identical location (A) without UV irradiation (B) 60 min UV.....	54
Figure 2-17 XPS spectra of ODS SAMs with no irradiation and after 15 min of UV irradiation. Substrate: SiO ₂ /Si.....	57
Figure 2-18 Schematic of fluorescence labeling of CHO, COOH, and OH surface functional groups.	58
Figure 2-19 Detection of surface alcohol groups by covalent surface attachment of triphenylmethylchloride to a SAM surface irradiated for 30 minutes in UV/ O ₃ as well as SiO ₂ and unirradiated monolayer controls. Inset: calibration plot.	59
Figure 2-20 Detection of surface aldehyde groups by covalent surface attachment of 1-pyrenemethylamine to a SAM surface irradiated for 30 minutes in UV/ O ₃ and controls. Inset: calibration plot.	60
Figure 2-21 Detection of surface carboxylic acid groups by covalent surface attachment of 2-naphthaleneethanol to a SAM surface irradiated for 30 minutes in UV/ O ₃ and controls. Inset: calibration plot.	60
Figure 2-22 Surface concentration of oxygen containing functionality (▼OH, ■CO ₂ H, ✕CHO) at the SAM surface as a function of UV irradiation time.....	61
Figure 2-23 Estimated fractional coverage of hydrophilic groups as determined by contact angle results.....	72
Figure 2-24 Possible microscopic mechanisms of alkylsiloxane degradation.....	73
Figure 2-25 Simulated evolution (top to bottom) of a cross section of ODS SAM. Each bar represents an individual ODS chain. Height is in the unit of the height of a CH ₂ group (~0.14 nm). Horizontal distance is in unit of the lateral spacing between chains (~0.5 nm).	74
Figure 2-26 Evolution of simulated morphology assuming that chain scission is restricted to the top of chains. Each time increment represents the time it takes to react 1 ML of surface sites.....	75
Figure 3-1 Structure of double layer and the potential drop across double layer.	89
Figure 3-2 Model for the Au(111) reconstruction. The solid dots denote the positions of atoms in the second layer, whereas open circles denote the positions of atoms in the reconstructed top layer. C and A mark the regions of ABC (fcc) and ABA (hcp) stacking. The displacement of atoms from the straight line along the [1 $\bar{1}$ 0] direction of about 0.8Å is apparent [4].	91
Figure 3-3 STM images of Au(111) surface under 0.1M H ₂ SO ₄ at different electrode potentials, image size: 160 nm × 160 nm. A: reconstructed surface is observed at 0.05V. The double reconstruction stripes are rotated by 120, reflecting the	

symmetry of the (111) surface. Inset: atomic resolution image of the reconstructed surface (4.5 nm × 4.5 nm). The lattice constant is about 3 Å, which is in good agreement of the lattice constant of gold 2.88 Å. B: The reconstruction is lifted at 0.36V. The 4-5% extra gold atoms are released to form the monolayer islands.	92
Figure 3-4 Models for the unreconstructed Au(100) and the reconstructed Au(100) surfaces [6]......	93
Figure 3-5 Schematic of EC-STM. A bipotentiostat is used to control electrode potential in four electrode setup, including CE: counter electrode, RE: reference electrode.	100
Figure 3-6 Schematic of AFM. The force between the tip and the surface is sensed by the deflection of a cantilever. Reflection of a laser beam from the cantilever, measured by a split photodiode, monitors the deflection of the cantilever.....	101
Figure 4-1 Hexadecane on reconstructed Au(111)/ 0.1 M HClO ₄ interface at 0.25 V _{SCE} . Molecules adopt extended conformation as 2.2 nm long, and 0.45 nm wide rods parallel to the surface. The molecular axes cross the rows at about 60°. The domain boundaries of the molecular rows are pinned by the domain structure of the reconstruction stripes of the gold surface, as indicated by a black arrow. Scan area (A) 42×42 nm ² ; (B) 10×10 nm ²	114
Figure 4-2 Schematic model of the reconstructed gold surface and the relative arrangement of alkanes: (a) NN(30) and (b) NN(90).	115
Figure 4-3 Hexadecane on Au(111) in 0.1 M HClO ₄ solution at 0.65 V _{SCE} . The reconstruction is lifted and Au islands appear. At the same time, ordered hexadecane rows have disappeared, and dots, about 1 nm in diameter appeared on the surface and grew in number with time. (A) after 0-95 seconds after potential step to 0.65 V _{SCE} , (B) after 96-190 seconds after potential step. Scan area: 32×32 nm ² . Scan direction is indicated by black arrows at the top left side of each image.	117
Figure 4-4 Hexadecane on Au(111) in 0.1 M HClO ₄ solution, at 0.25 V _{SCE} after potential was stepped back from 0.65 V _{SCE} . The dots begin to disappear and the ordered molecular row structures recover on the unreconstructed Au(111) surface. (A) after 0-95 seconds after potential step to 0.25 V _{SCE} , (B) after 96-190 seconds after potential step. Scan area: 32 × 32 nm ²	120
Figure 4-5 Hexadecane on Au(111) in 0.1 M HClO ₄ solution. When potential was stepped from 0.15 V _{SCE} (A) to 0.05 V _{SCE} (B), the ordered molecular rows disappeared. Scan area: 32 × 32 nm ²	122
Figure 4-6 Hexadecane on Au(111) in 0.1 M HClO ₄ solution (A) obtained at 0.05 V _{SCE} . (B) after potential step to 0.25 V _{SCE} , the ordered molecular rows reappear immediately; (C) 96-190 seconds after potential step, ordered molecular layers domain continue to grow. Scan area: 65 × 65 nm ²	123
Figure 4-7 Spontaneous molecular domain flipping; Hexadecane on Au(111) in 0.1 M HClO ₄ solution at 0.25 V _{SCE} . Two different molecular orientations in a single row are indicated by arrows. (A) Sudden change of molecular orientation during scanning results in a single orientation. (B) The likely cause is the merging of domains, indicated by arrows in D. Scan area (A-B) 34.5 × 34.5 nm ² , (C) obtained before (A), 65 × 65 nm ² , (D) Zoom in of Figure 6 C, 20 × 20 nm ²	125

Figure 4-8 The effect of surface charge on molecular adsorption. At low surface charge density, hexadecane lies flat, forming an ordered domain. At high surface charge density, positive or negative, the solvent is attracted to the substrate, displacing hexadecane molecules.....	129
Figure 4-9 Alkane adsorbates confined at water/ Au interface and alkane/Au interface.	130
Figure 5-1 In-situ STM images ($50 \times 50 \text{ nm}^2$) of TPyP on Au(111) in $0.1 \text{ M H}_2\text{SO}_4 + 10^{-5} \text{ M TPyP}$ solution. Scan directions are indicated by black arrows. Tip locations when potential step occurred are indicated by white arrows. (A) Electrode potential 0.5 V . (B) Electrode potential 0.5 V (upper part), -0.3 V (lower part). (C) -0.3 V (upper part) 0.5 V (lower part).....	142
Figure 5-2 Cyclic voltammogram of Au(111) with pre-adsorbed TPyP in a blank $0.1 \text{ M H}_2\text{SO}_4$ solution, initially held at -0.25 V , scan rate 2 V/s	143
Figure 5-3 STM images of TPyP adlayers on reconstructed Au(111) in $0.1 \text{ M H}_2\text{SO}_4$ solution. ($40 \times 40 \text{ nm}^2$) (A) electrode potential -0.05 V . (B) The electrode potential was stepped progressively to 0.5 V after the ordered monolayer was formed at 0 V	145
Figure 5-4 Sequential STM images ($62 \times 62 \text{ nm}^2$) of TPyP on reconstructed Au(111) in $0.1 \text{ M H}_2\text{SO}_4$ solution at -0.05 V . A circle highlights a domain that recrystallized between images.	146
Figure 5-5 In-situ STM images ($62 \times 62 \text{ nm}^2$) sequence of TPyP on reconstructed Au(111) in neat $0.1 \text{ M H}_2\text{SO}_4$ solution. Scanning directions are indicated by the black arrows. (A) electrode potential -0.05 V . (B) obtained after electrode potential was stepped to -0.25 V . (C) was obtained after electrode potential was stepped back to -0.05 V	147
Figure 5-6 Influence of adsorbate binding energy E_{desorb} on surface diffusion.	149
Figure 6-1 Possible electrochemical reaction mechanism of TMPyP under acidic medium [5, 6].	155
Figure 6-2 Cyclic voltammograms of Au(111) in $0.1 \text{ M H}_2\text{SO}_4$ solution with $2 \times 10^{-4} \text{ M TPyP}$. The electrode potential scan rates were $0.02, 0.05, 0.1, 0.2, 0.6, 1, 2 \text{ V/s}$...	159
Figure 6-3 Cyclic voltammograms of Au(111) with pre-adsorbed TPyP in a blank $0.1 \text{ M H}_2\text{SO}_4$ solution, initially held at -0.25 V , scan rate 2 V/s (first cycle —, second cycle).....	160
Figure 6-4 Cyclic voltammograms of Au(111) with pre-adsorbed TPyP in a blank $0.1 \text{ M H}_2\text{SO}_4$ solution, initially held at 0.8 V , scan rate 2 V/s (first cycle —, second cycle)	161
Figure 6-5 Waveform for the cyclic voltammetric experiment of TPyP preadsorbed at a positive electrode potential.	162
Figure 6-6 Cyclic voltammograms of preadsorbed TPyP on Au(111). The electrode surface was equilibrated at -0.05 V for different durations. Scan rate 1 V/s	163
Figure 6-7 Integrated charge of preadsorbed TPyP as a function of duration at -0.05 V extracted from the CVs in Figure 6-6.	163
Figure 6-8 Proposed surface species of TPyP.....	165
Figure 6-9 In situ STM images of preadsorbed TPyP on reconstructed Au(111) in $0.1 \text{ M H}_2\text{SO}_4$ solution. (A) obtained at electrode potential -0.05 V , setpoint $I = 0.2 \text{ nA}$. (B-D) obtained after electrode potential was stepped to 0.15 V from -0.05 V , setpoint I	

= 0.2nA. E obtained at electrode potential 0.25 V. F obtained at electrode potential 0.35 V. Image size: 62 nm× 62 nm. Scan direction: upward.....	167
Figure 6-10 Time dependant STM images of TPyP adsorption onto Au(111). Solution: 1×10 ⁻⁵ M TPyP in 0.1 M H ₂ SO ₄ . A 0-109 sec after potential step from 0.5 V to 0.1 V. B 109-218 sec after potential step from 0.5 V to 0.1 V. Image size: 62× 62 nm ² . Scan direction: downward.....	170
Figure 6-11 A: STM image (20×20 nm ²) of a TPyP domain boundary under 1× 10 ⁻⁵ M/0.1 M H ₂ SO ₄ solution Molecular layer 2.5-3.1 Å high coexists with molecular layer 1.2-1.5 Å high. The molecules in the layer which has higher apparent height are fully resolved while only partial molecules in the lower layer are resolved at the boundary highlighted by the red line. B: A model for the proposed multilayer structure.	170
Figure 6-12 Time dependant STM images of TPyP adsorption onto Au(111) after potential step from 0.5 V to 0.1 V. Solution: 1×10 ⁻⁵ M TPyP in 0.1 M H ₂ SO ₄ . A. 109-218 sec. B. 218-327 sec. C. 327-436 sec. The red arrows point to the same domain which grew after potential step. Image size: 40×40 nm ² . Scan direction: downward.....	171
Figure 6-13 Fractional coverage of TPyP bilayer as a function of time after potential step from 0.5 V to 0.1 V.....	172
Figure 6-14 In situ STM images of TPyP on reconstructed Au(111) under 1× 10 ⁻⁵ M/0.1 M H ₂ SO ₄ solution. (A) obtained at electrode potential 0.1 V. (B-C) obtained after potential step to 0.15 V 0-109 sec and 109-218 sec respectively. (D) after potential step to 0.2 V., 0-109 sec. Image size: 62nm× 62 nm ² . Scan direction: downward.....	174
Figure 7-1 Proposed model of hemicylindrical structure of CTAB surface aggregates on hydrophobic surfaces [24].....	188
Figure 7-2 Hypothetical formation of silver nanowires on the hemicylindrical surface micelles. Parallel silver wires may be preferentially formed at the trench site, the surface site between the hemicylinders.....	190
Figure 7-3 Deflection mode AFM image of surface aggregates on Au(111) under 10 mM SDS. Image size 150×150 nm ² . Electrode potential: 0.3 V _{SCE}	193
Figure 7-4 Approach force-distant curve of Au(111) under 10 mM SDS at open circuit potential. The force is calculated using the nominal spring constant of the cantilever, 0.06 N/m.....	195
Figure 7-5 Surface charge dependant structure of SDS on Au(111). 10 mM SDS. Image size: 100×100 nm ²	196
Figure 7-6 Hypothetical structures of adsorbed SDS at positively charged Au(111). A: SDS forms a compact monolayer with sulfate groups attached to the positively charged surface. B. A bilayer structure. C. Micelle like structure on top of a monolayer	198
Figure 7-7 Anisotropic electrodeposition on Au(111) under 1 μM AgClO ₄ and 10 mM SDS. Electrode potential 0.3 V. Elongated islands were observed to grow along the surface micelles.....	199
Figure 7-8 Time dependant electrodeposition on Au(111) under 1μM AgClO ₄ and 10 mM SDS. Image size 225×225 nm ² . The electrode potential was stepped from 0.3 V to 0.2 V at the lower half of the image A. (Scan direction: downward.) B and C	

are sequential frames of A. Image acquisition speed 80sec/frame. Solid, dashed and dotted arrows identify the same spots in different images.....	199
Figure 7-9 AFM image of anisotropic electrodeposition on Au(111) under 1 μM AgClO_4 10 mM SDS. Electrode potential 0.3 V. Image size: $300 \times 300 \text{ nm}^2$	201
Figure 7-10 Proposed models for Ag-surface micelle adduct. A: silver grows in the trench sites and on top of surface micelles. B. Silver forms monolayer islands on the Au substrate. Surface micelles grow on the silver monolayer.....	202
Figure 7-11 AFM images of electrodeposited islands on Au(111) under 1 μM AgClO_4 10 mM SDS. Image size: $200 \times 200 \text{ nm}^2$. A: isolated stripes, as indicated by arrows, are observed at 0.1 V. B: the stripes collapse to form more circular islands at 0 V.	203
Figure 7-12 Proposed mechanism for the formation of circular islands at 0V. Without the support of surface micelles, the silver nanostructures collapse into islands.....	204
Figure 7-13 STM image of surface micelles on Au(111) under 10 mM SDS. Image size: $125 \times 125 \text{ nm}^2$. Electrode potential 0.2 V. Sample bias: 0.3 V. Tunneling current: 0.5nA. Some bright islands are resolved. The black arrows indicate elongated islands. Three cylinders overlaid with the surface micelles suggest that the islands grow in the trench sites.	207
Figure 7-14 STM image of hexadecane adlayer on Au(111) in 0.1M HClO_4 solution at $0.25V_{\text{SCE}}$. Image size: $34.5 \times 34.5 \text{ nm}^2$	208
Figure 7-15 Silver deposited onto a surface covered with a hexadecane adlayer at 0.1V under 0.1M H_2SO_4 . 1.5 \AA parallel lines connect 2 \AA high islands. A: image size $150 \times 150 \text{ nm}^2$. A majority of these lines are $4.8 \pm 0.2 \text{ nm}$ apart. B: image size: $30 \times 30 \text{ nm}^2$	210
Figure 7-16 A model for preferential electrodeposition on a self-assembled hexadecane template. Silver nanowires are selectively deposited in the space between molecular rows.....	210
Figure 7-17 Time dependant surface coverage of diffusion limited electrodeposition of Ag at different concentration of Ag^+	213
Figure A-1 AFM images of ODS monolayer at identical region acquired during a: Left to right scan and b: Right to left scan. Height scale 5nm.....	220
Figure A-2 Left to right and right to left scans when the friction is zero across the surface.	220
Figure A-3 Left to right scan when the island has higher friction.	221
Figure A-4 Right to left scan when island has higher friction.	221
Figure A-5 Tapping mode AFM images. Left to right and right to left scans now display nearly identical topography.....	222
Figure A-6 Sampling ozone in the UV chamber.....	224
Figure A-7 Absorption spectra of ozone trapped in a quartz cell as a function of time after sampling.....	225
Figure A-8 Tungsten Tip etching: a simple illustration of wire etching. The blue fluid represents a lamella of 3 M KOH. The small cone below is used to receive the fallen tip. Closer examination shows neck is formed as the wire is etched.....	226
Figure A-9 Schematic of copper hot plate for polymer coating.....	228
Figure A-10 Schematic of coating STM tips with melted polyethylene.....	229

- Figure A–11 STM images of Au(111) under 0.1 M HClO₄, 0.1 V_{SCE} with different reference electrodes. A: Acquired with a Pt reference electrode. Herringbone Au reconstruction is observed, suggesting that the surface is free of metal impurities. Image size: 150 nm × 150 nm. B: Acquired with a silver wire reference electrode. Image size: 150 nm × 150 nm. Many islands appear on the surface. Suggesting that metal impurity from the solution is deposited. Inset: An atomic resolution image(6 nm × 6 nm). The lattice constant, 3 Å and corrugation 0.4 Å is consistent with Ag(111) surface [5]. 231
- Figure A–12 Schematic of the preparation of a sealed Ag quasi reference electrode. A and B: A short glass tube is melt to form a glass bead on a short Pt wire. C,D: The glass bead is welded to one end of a glass tube. E: The glass tube is filled with supporting electrolyte. And a silver wire is inserted. F: The other end of the glass tube is sealed with parafilm. 232

1. Preparation of alkylsiloxane self-assembled monolayers: the issue of reproducibility.

1.1. Introduction.

In the 1940's, Zisman et al. discovered that an alkanolic acid could self-organized into a monolayer on a clean platinum surface driven by chemisorption from a solution phase [1]. Monolayers prepared by this method are called Self-Assembled Monolayers (SAMs). SAMs typically are more stable than organic thin film prepared by the Langmuir-Blodgett method [2] because the molecules in a SAM are attached to the solid surfaces via chemical bonds. The applications of organic thin films were further extended by the preparation of trifunctional alkylsiloxane monolayers on SiO₂ surfaces by Sagiv [3] and alkanethiol monolayers on gold surfaces by Nuzzo et al. [4] in the 1980's. Both types of monolayers are very robust due to the strong bonding between head groups and substrates.

1.1.1. Importance of SAMs.

SAMs may possess different physical, chemical and electronic properties depending on their structure and composition. Not mentioning their importance as a model system to study self-organization, intermolecular interactions and molecular-substrate interactions [5, 6], SAMs have found applications in a wide range of fields. Different applications utilize different properties of the SAMs. The numerous existing and potential applications of SAMs are summarized in the following three categories.

1.1.1.1. Applications that utilize the physical properties of SAMs.

SAMs can completely change wetting and frictional properties of the substrate. Moreover, the terminal groups of the organic molecules are not limited to methyl. By attaching functional groups such as OH, NH₂ and COOH, one can tailor the surface energy to different requirements [7]. Silanized surfaces have already found applications in gas and liquid chromatography [[7].

1.1.1.2. Applications that utilize the chemical properties of SAMs.

SAMs that consist of long chain alkanes can be compact and chemically inert. This makes it difficult for chemical reagents to penetrate and react with the substrate surface. The SAMs can serve as corrosion protection layers of metal and semiconductor surfaces. Siloxane films were demonstrated to be high resolution etching masks for microelectronics fabrication [8-10]. The area covered with siloxane remained inert while the bare silicon substrate was etched selectively during etching. Similarly, SAMs can serve as templates for area-selective deposition of metals and other materials [11-14]. One can tailor the interaction between the SAMs and other molecules or particles, by modifying the terminal groups on SAMs. Existing applications include solid-state synthesis of proteins, in which the peptide chains are attached to functionalized SAMs, eliminating tedious processes of separation [11-14]. Functionalized SAMs are also used as model system of biological surfaces [15]. Inspired by the capability of biological membranes to recognize specific chemical and biological stimuli and to convert them to measurable signals, researchers are trying to build chemical and biological sensor devices based on SAMs [16].

1.1.1.3. *Applications that utilize the electrical properties of SAMs.*

SAMs have different electrical characteristics such as conductivity, dielectric constant and capacitance. The flexibility of the electrical characteristics lies in the degree of conjugation, polarizability and dipole moment of the molecules and structure of the monolayers [17]. SAMs on semiconductor surfaces show promising potential as ultrathin gate insulating layers in microelectronics [17-19]. In addition, SAMs are widely anticipated to be the building blocks of molecular electronics [20].

1.1.2. **Growth of SAMs.**

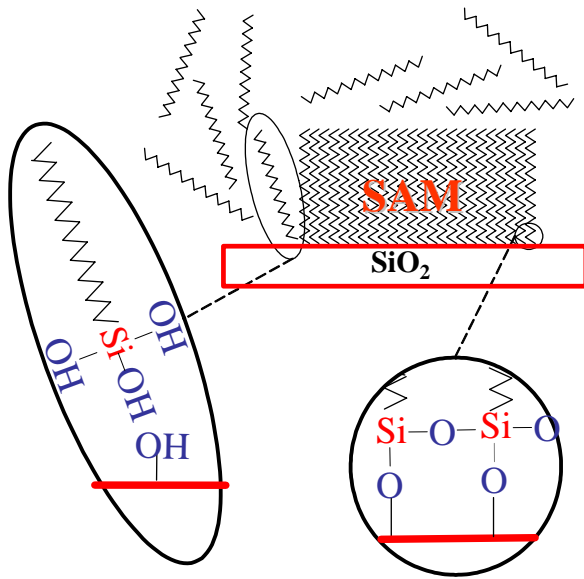


Figure 1–1 Proposed mechanism of ODS SAM formation.

Much attention has been paid to the preparation and structure of SAMs [5, 6]. At a first glance, the preparation of alkylsiloxane monolayers appears quite simple [3]. A sample is dipped into an organic solvent (typically nonpolar) containing chlorosilane (concentration is on the order of mM) for a certain period of time ranging from seconds

to hours. It is assumed that the chlorosilane molecules undergo hydrolysis to form siloxane and cross-link (R 1-1, R 1-2, and Figure 1–1) [21].



Eventually, the cross-linked siloxane headgroups become covalently attached to silanol groups on the substrate (Figure 1–1) [21].

As simple as the preceding scheme may appear, reproducibly producing a compact monolayer of alkylsiloxane remains challenging. Different laboratories report strikingly different results. ODS SAMs have been reported to require reaction times ranging from a few minutes [22] to 24 hours [23, 24] or even days [25]. Equally troubling is that often the reaction is not self-limited to monolayers. Often multilayers with ill-defined morphology are formed [26]. The irreproducibility of siloxane SAM preparation severely hampers their surface modification applications where well-defined and compact monolayers are required [27]. The underlying details of the SAM formation mechanism remain controversial. Central to the irreproducibility issue is silanol's tendency to polymerize. Horizontal polymerization (cross-linking along the surface plane) is desirable since the cross-linking of the siloxane network enhances the stability of siloxane SAMs. However, the bulk polymerization is undesirable since the polymerization creates macroscopic islands with ill-defined morphology [26]. The bulk polymerization is induced by the hydrolysis of trichlorosilane, and is catalyzed by HCl [21], a product of the hydrolysis. The reaction kinetics therefore is complex and sensitive to reaction conditions. It is believed that subtle variations of some experimental

conditions, such as trace amount of water, may alter the growth behavior of monolayer significantly [6]. Key factors that affect the growth of silane SAMs are summarized below.

1. Concentration of silane and reaction time. It was confirmed by a number of FT-IR experiments that the growth of silane monolayer roughly follows pseudo Langmuir kinetics [28, 29].

$$\theta = 1 - e^{(-kct)} \quad \text{Equation 1-1}$$

θ is the adsorbate coverage, k represents the reaction rate constant, c is the concentration of the silane solution and t is the reaction time. However, Langmuir kinetics is solely determined by the competition between desorption, which is assumed to be proportional to the adsorbate surface coverage θ , and adsorption, which is assumed to be proportional to area unoccupied by adsorbate $1-\theta$. The experimental evidence, however, suggests that the self-assembly of siloxane is clearly not a simple Langmuir kinetics. The adsorption and desorption depend not only on adsorbate surface coverage but also diffusion, nucleation, lateral organization [22], as well hydrolysis and polymerization [21, 22]. Hence, a pseudo-Langmuir model accounts for these effects in an ad hoc manner.

2. Substrate. The substrate can play an important role because the affinity between the surface and the quality of monolayers may vary with the surface density of OH groups [24, 30, 31]. The affinity influences the adsorption rate of the silane molecules and the structure of the monolayer. For substrates lacking OH groups,

such as mica, steam treatment before silanization appears important for SAM formation [24]. Thermal or electric field treatment may significantly reduce the OH concentration on SiO₂, therefore suppressing the adsorption rate [30, 31]. The precise role of the OH groups on the surface remains controversial. In some reports OH groups are assumed to be the source of the affinity since at least some of the silane molecules are attached to the surface via reaction with the OH groups [28, 31]. Others suggest that the OH groups can adsorb a thin layer of water, which is believed to be important for silanization reactions [32-34]. Regardless of the precise mechanism in which surface silanol groups promote the self-assembly of alkylsiloxanes, it is generally accepted that to facilitate the self-assembly process, surface pretreatments that make the substrate clean and hydrophilic are necessary.

3. Water content. However, even for siloxane monolayer growth experiments carried out in a dry nitrogen glove box, trace amount of water is considered to be crucial for the covalent attachment of siloxane molecules to the substrate [21]. In the absence of significant amount of water, siloxane SAM growth is extremely slow (it may require days of reaction) [21]. Water content, which is difficult to control, may be the major source of discrepancy among different laboratories. Experiments showed that water promotes the reaction rate [29, 35]. Water is also observed to promote the island growth at the initial stage [36]. It is now well established that the presence of water in the range of a few monolayers on the substrate promotes the ordering. Evidence include:

- a. On high surface area silica gel, three monolayers of water is necessary for high quality surface film formation[37].
 - b. Infrared spectroscopy [21, 32, 38] and sum frequency generation spectroscopy [39] provided direction evidence for a thin water film of molecular thickness. At the initial stage of SAM growth, silane or silanol molecules are physisorbed on the water film and subsequently cross-link to form 2D network. Normally few molecules are directly attached to the substrate [37]. The molecules are stabilized by lateral attraction with neighboring molecules and hydrogen bonding with the substrate.
 - c. In addition, the ordering process of alkylsiloxanes was found to depend on the temperature in a manner similar to LB films, suggesting the presence of water on which the siloxanes float. This will be discussed in the following paragraph.
4. Temperature. It was found that silane molecules can reorganize laterally on the surface to undergo 2D phase transition [40, 41]. At temperatures higher than the critical temperature T_c , the monolayer was completely disordered [40, 41]. T_c decreases with decreasing length of the alkyl chains. This behavior is analogous to LB films prepared at air water interfaces. It is then hypothesized that the silane or silanol molecules physisorb on the water thin film with minimal amount of bonding to the surface [41, 42]. This hypothesis is supported by an AFM study [41], which directly observed the temperature dependant structures indicative of the coexistence of Liquid condensed(LC), liquid extended(LE), and Gas(G) -like phases of the SAM on the solid substrate. These structures and their behavior are indeed analogous to

LB films at the air water interface, supporting the notion of liquid water on the solid substrate. Therefore, to achieve high quality SAMs, it is important to keep the reaction temperature below T_c , such as 27°C for octadecyl siloxane SAM [40, 41].

5. Rinsing. A frequently neglected factor in the quality of prepared monolayers is rinsing. Rinsing may remove molecules that have not yet covalently bonded to the substrate. Studies showed that monolayers that were ordered before rinsing became disordered after rinsing [43]. However, if the reaction time is long enough (> 1 hr), almost all the molecules attached to the surface can endure the rinsing because the molecules are chemisorbed onto the surface [43].

1.1.3. Motivation.

To date, the knowledge of the influence of different factors in SAM preparation is highly fragmented. It is not yet clear what conditions lead to the reaction kinetics that varied by orders of magnitude [22-25]. Due to the large number of parameters, few groups have addressed the reproducibility issues in a systematic way. Many authors can only draw conclusions from their specific conditions. Since our immediate goal is to understand the photoreactivity of alkylsiloxane SAMs [44], reproducible preparation of SAMs with well defined structure at the molecular level is essential. There is no guarantee that an optimum parameter in one lab is applicable to our conditions. Therefore there is a need to undertake a more systematic study, to explore a wide range of different parameters and gain insight into how each parameter affects the self-assembly process and how we can optimize these parameters. A more long term goal in this study is to develop strategies to

prepare high quality SAMs, that are easy to reproduce in other research laboratories or industrial environments. Since water appears to play such an important role in the reaction, and because its precise roles remain controversial, our study is mainly focused on how water affects the reproducibility of ODS SAM formation.

1.2. Experimental section.

1.2.1. Substrate treatment.

Microscope glass slides (VWR Scientific, cat. # 48300-025) and native SiO₂ grown on Si wafers were used as the substrates. The substrates were sonicated in acetone, methanol and then water. The substrates were then subjected to cleaning in a UV/ozone chamber 1 hour or to RCA SC1 H₂O:NH₄OH:30%H₂O₂ (4:1:1) treatment at 80-90 °C for 30 min-1 hour. After final treatment, the substrates have a water contact angle close to 0°, suggesting that both UV/ozone and RCA SC1 treatment are effective in producing clean and hydrophilic surfaces.

1.2.2. Self-assembly.

To achieve good control over the water content in the solvents, all the solvents used for the self-assembly of ODS were dehydrated with baked molecular sieves (4A, Davison). Water concentration in toluene is controlled by mixing dehydrated toluene with water saturated toluene (25 mM H₂O) [36, 45] or adding controlled amount of water to dehydrated toluene [36, 45]. We found that the exposure of octadecyltrichlorosilane (95%, Acros) OTS to ambient was a major source of irreproducibility. To minimize moisture exposure, the OTS bottle was capped with a rubber septum and stored in a

desiccator. OTS was withdrawn with a dry syringe through the rubber septum under a positive pressure of argon or nitrogen.

Two types of procedures were adopted for SAM formation. Both were carried out at room temperature ($23\pm 2^\circ\text{C}$). Procedure 1 was employed to prepare submonolayer coverage ODS SAM at reduced temperature as described in Ref. 40. Procedure 2 is mainly used to study the effect of water content since the concentration of water in toluene can be varied significantly and controllably.

Procedure 1: The cleaned substrates were then immersed in mM OTS solutions prepared in mixture of hexadecane (99%, Acros), HCCl_3 (GR grade, EM Science) and CCl_4 (GR grade EM Science) [3, 40, 41]. After reaction, the samples were rinsed in CCl_4 at least three times.

Procedure 2: The cleaned substrate was immersed under toluene (GR grade, EM Science) containing mM OTS for a desired period of time [34]. After reaction, the samples were immediately rinsed with HCCl_3 for at least three times.

A glove bag was used as the environmental chamber when control of ambient humidity was necessary. An Omega CTH 89 humidity recorder was used to monitor the relative humidity in the chamber. The glove bag was purged with a mixture of dry compressed air and wet compressed air. The humidity can be controlled by adjusting the relative flow rates of the dry and wet compressed air.

1.2.3. Characterization.

1.2.3.1. Water contact angle.

Unirradiated SAMs were cleaned with acetone or chloroform prior to characterization. Unless otherwise mentioned, irradiated SAMs were characterized without any treatment because perturbation induced by rinsing is a concern for the irradiated samples. Water contact angle measurements were performed using the sessile drop method with VCA-2000 Laboratory Surface Analysis System (AST Productions Inc.). Static contact angles were measured. 4-5 measurements were averaged for each sample.

1.2.3.2. FT-IR measurement.

Transmission FT-IR spectra were collected with Nicolet Avatar 360 IR or a Brüker Tensor 27 FTIR spectrometer at normal incidence. Spectral resolution was either 4 cm^{-1} or 8 cm^{-1} . Corresponding uncoated substrates were used as the background. 256 to 512 scans were averaged.

1.2.3.3. Atomic force microscopy (AFM).

Contact mode AFM images were acquired with a Molecular Imaging PicoSPM system. Silicon Nitride tips were used. Cantilevers with spring constant of 0.06-0.12 N/m were selected for imaging. The tips have curvature of radius about 10-20 nm. A Dimension 3100 AFM system (Digital Instrument) was used to acquire tapping mode AFM images. The integrated sample stage and optical microscope allowed us to reposition the sample to a precision within 2-5 microns. Coupled with marks such as scratches on the surface, we were able to image the identical areas on a surface before and after irradiation. Noncontact mode Si tips were purchased from Silicon MDT. The radius of curvature is

typically less than 10 nm. The cantilever with spring constant about 0.3 N/m and resonance frequency around 30 kHz was chosen for imaging. Typical line scan frequency was about 1 Hz. All images are shown as raw data that undergo no filtering other than flattening.

1.3. Results and discussion.

1.3.1. Criteria for a high quality ODS SAM.

Evidently to address the reproducibility issue one needs to have reliable criteria for the quality of ODS SAMs. On a microscopic level, a high quality ODS film should consist of highly ordered closely packed alkyl chains. It should have uniform monomolecular thickness and it must be terminated with methyl groups on the top. Common SAM characterization techniques include Atomic Force Microscopy (AFM), Fourier Transform Infrared spectroscopy (FT-IR), ellipsometry, X-ray photo-electron spectroscopy (XPS), and contact angle [46]. Ellipsometry and XPS can reveal the amount of molecules deposited on the surface but are less informative than FT-IR and AFM in terms of microscopic structural information.

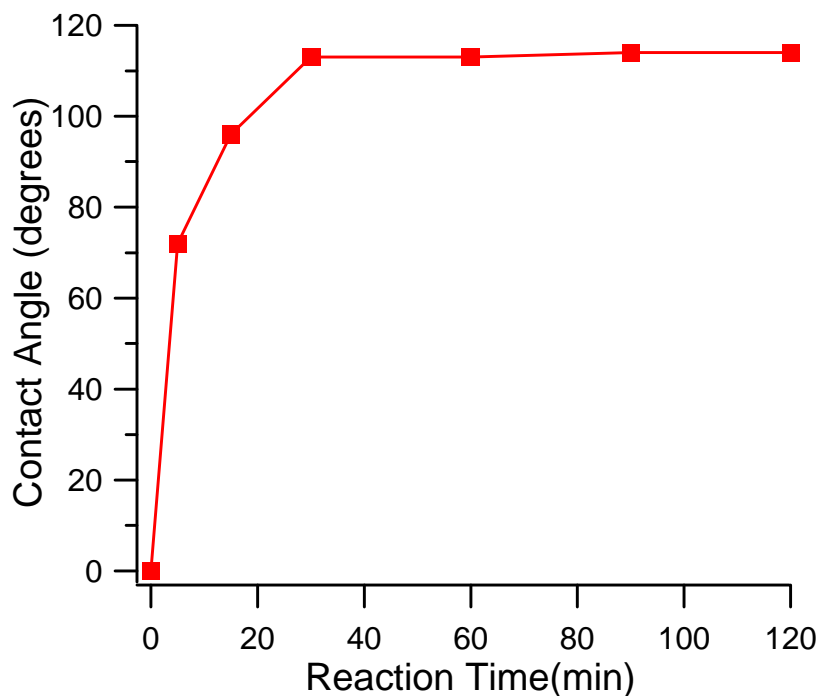


Figure 1–2 Water contact angle of ODS on glass as a function of reaction time.

Glass slides were immersed in 2.5mM OTS solution from 5 to 120 min with method 1. The results of the contact angle measurements are shown in Figure 1–2. The increase of the contact angle suggests the increasing amount of hydrophobic hydrocarbon chains attached to the surface. There was a sharp increase of contact angle in the first half hour. The contact angle reached a plateau after 30min of reaction. The plateau value of 112 degrees is in agreement with values from ordered and compact alkanethiol SAMs terminated with methyl groups [5].

1.3.1.1. FT-IR results.

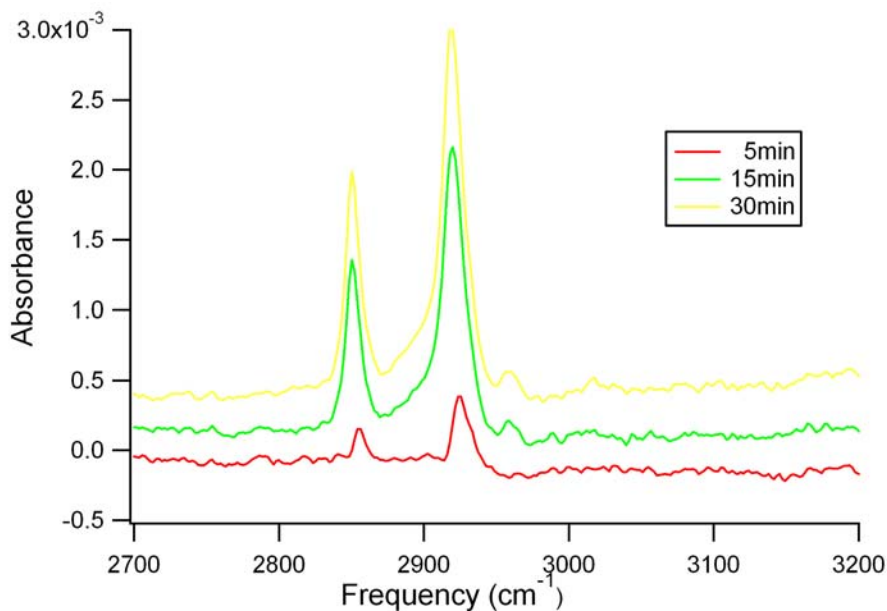


Figure 1–3 FT-IR spectra of ODS on glass for different reaction time spent in OTS solution (5 min, 15 min and 30 min) using Procedure 1.

The ODS monolayers on glass were also characterized with transmission FT-IR. Figure 1–3 shows FT-IR spectra of ODS samples prepared with different reaction times. As the time spent in OTS solution increases, the CH stretch peaks grow, suggesting increase of ODS coverage on the surface (Figure 1–3).

The spectra were fitted using sums of lorentzian functions. The analytical expression of the fitting is shown in Equation 1-2. I is the intensity in absorbance units. x represents the frequency in wave numbers. K_0 is the offset. K_1 , K_2 and K_3 are the parameters of the lorentzian functions.

$$I = K_0 + \sum_{i=1,4} \frac{K_{1,i}}{(K_{2,i} - x)^2 + K_{3,i}} \quad \text{Equation 1-2}$$

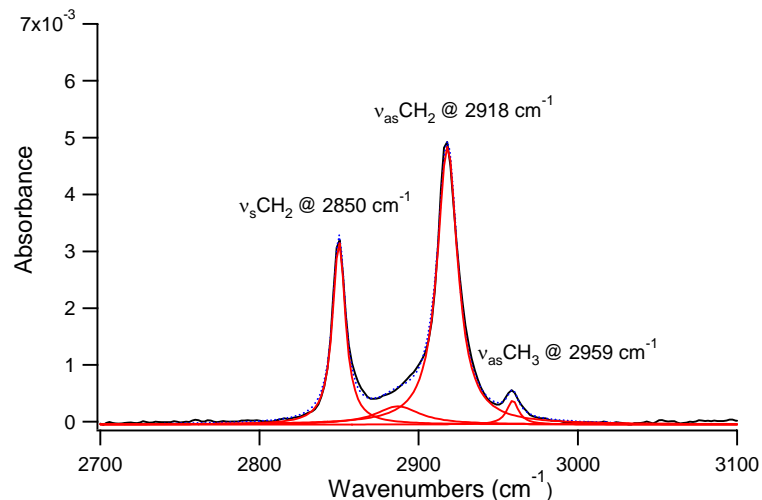


Figure 1–4 An example of deconvolution of the FTIR spectra of ODS SAMs.

The CH₃ symmetric stretch mode at 2950 cm⁻¹, CH₂ antisymmetric stretch mode at 2918 cm⁻¹, and CH₂ symmetric stretch mode at 2850 cm⁻¹ are easily discernable Figure 1–4 [47]. There is also a shoulder peak near 2880 cm⁻¹ attributed to the CH₃ symmetric mode.

Figure 1–5 shows the integrated absorbance of the CH₂ antisymmetric mode. The absorbance increases then begins to level after 30 minutes of reaction. As more surface sites are occupied by silane adsorbates, there are less open sites for adsorption. Therefore growth should be limited at monolayer coverage, when all the surface sites are saturated. This behavior is similar to the growth kinetics of alkanethiol SAMs. However, unlike alkanethiol SAMs, which display a limiting coverage [5], the coverage of ODS will eventually exceed monolayer coverage. This indicates the formation of multilayers on the surface. After an extended period of time, the OTS molecules in the reaction mixture may start to polymerize, resulting in multilayers attached to the surface. The onset of the multilayer growth is dependant on a number of factors such as freshness of OTS, water

content, and ambient humidity. The relative importance of these factors will be detailed in the next sections. What should be noted here is that while FT-IR suggests multilayer formation at 120 min, there is no significant change in water contact angle on the same sample. This suggests that compared to FT-IR, water contact angle is less sensitive to multilayer formation¹, a central concern in preparing well defined SAMs. Since peak height and integrated absorbance are correlated, when the peak width is constant. The peak absorbance at the CH₂ antisymmetric mode, is used as a convenient rough indicator for the quality of films.

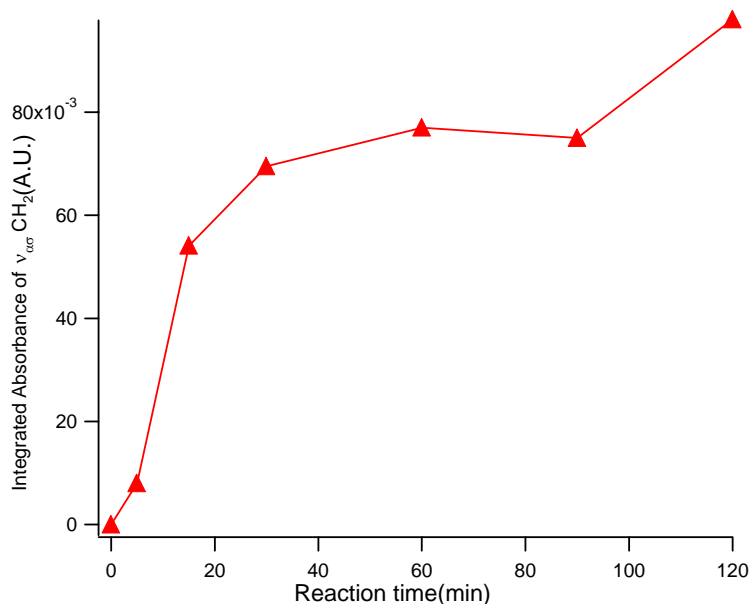


Figure 1–5 Integrated absorbance of SAMs at CH₂ antisymmetric mode as a function of reaction time.

1.3.1.2. AFM results.

AFM is capable of accessing nanometer scale morphological information on surfaces. A typical AFM image of an ODS SAM, with IR absorbance at 3.3 mOD at 2918 cm⁻¹, displays only small degree of polymerization, as evidenced by the small number of islands 3-5 nm high (Figure 1–6). Most of the surface appears to be covered with a single

¹ We refer to the static contact angle we use. However, dynamic contact angle may be more sensitive to the ordering the SAMs as suggested by Reference 40.

monolayer since the surface is smooth. By contrast B, with absorbance of 5 mOD, displays many more islands that can be as high as 10 nm.

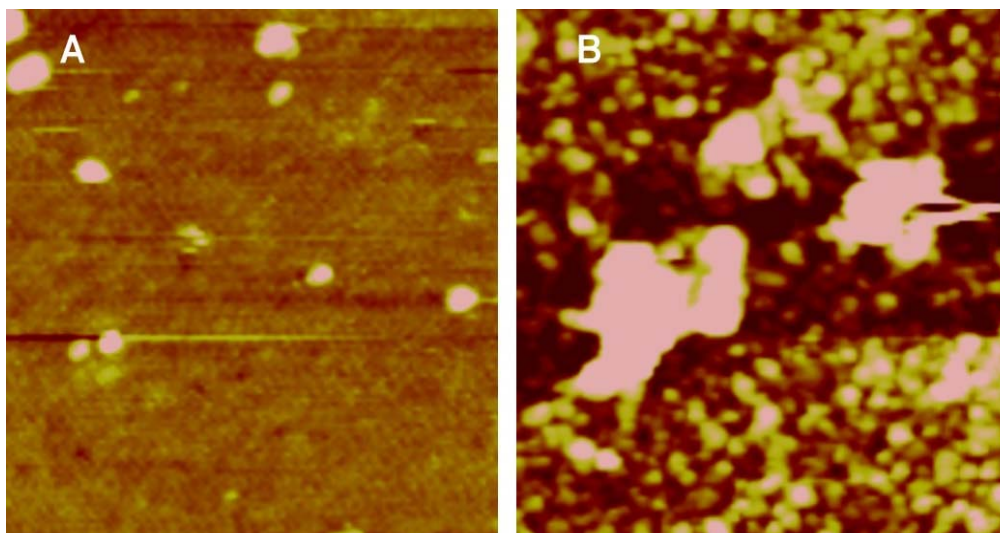


Figure 1–6 AFM images of ODS SAMs with A: 3.3 mOD and B: 5 mOD peak absorbance at $\sim 2918\text{ cm}^{-1}$. Image size: $2\text{ }\mu\text{m} \times 2\text{ }\mu\text{m}$. Height scale (5nm)

In addition, AFM can access the structural information of SAM formation at the initial stage. For reasons that will be discussed in chapter 2, surfaces covered with ODS monolayers with well defined monolayer islands needed to be prepared. The latter type of sample was successfully prepared using Procedure 1 in the Experimental section by reducing the immersion time to about 30 sec and lowering the reaction temperature to 10 °C. Images of a sub-monolayer coverage ODS sample are shown in Figure 1–7. The ODS molecules aggregated into flower-shaped islands that were 1.5-2 nm high. The fractal shape is characteristic of diffusion limited 2D growth [22]. A higher resolution image showed that the islands were porous.

It had been proposed that under certain conditions OTS molecules cross-link to form small patches in the bulk solution [22]. Subsequently, the patches aggregate to form

islands. There is space between the patches. If the reaction time is short, the ODS molecules do not have time to fill the defects. Therefore many holes appeared on the surface.

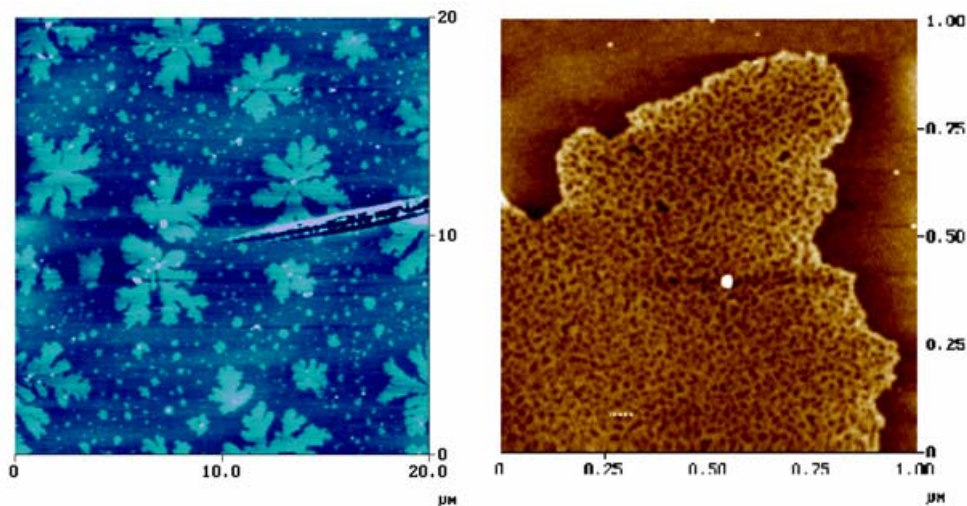


Figure 1–7 AFM images of ODS images of submonolayer coverage ODS monolayer on Si substrate prepared with method 1 at reduced reaction time (30 sec) and temperature (10 °C)

By combining AFM and FT-IR data, one can obtain a fairly complete picture of the quality of the ODS SAMs. Langmuir-Blodgett films are compact and structurally ordered. A high quality ODS SAM should have a similar IR spectrum to that of a LB film with the same number of hydrocarbon groups [46]. The IR spectrum should have absorbance about 3.5 mOD at the peak of $\nu_{\text{as}}\text{CH}_2$ [5, 42, 46]. In an AFM image, a well defined compact monolayer should be very smooth, (RMS roughness < 0.5 nm on Si substrate) and have few islands.

1.3.2. Effect of freshness of OTS.

OTS is very moisture sensitive, which has been recognized as a major source of discrepancy among the reactions performed in different laboratories [6]. Once exposed

to ambient, OTS can absorb trace amount of moisture and become hydrolyzed to silanol. White flakes appear in the otherwise transparent OTS liquid or at the surface of the liquid. We found that if aged OTS was used, within 5min, the coverage exceeded 1 monolayer. Islands tens of nm height covered the entire surface when aged OTS is used (Figure 1–8 B). Often white flakes became visible in the reaction solution within 1 hr if aged solution is used.

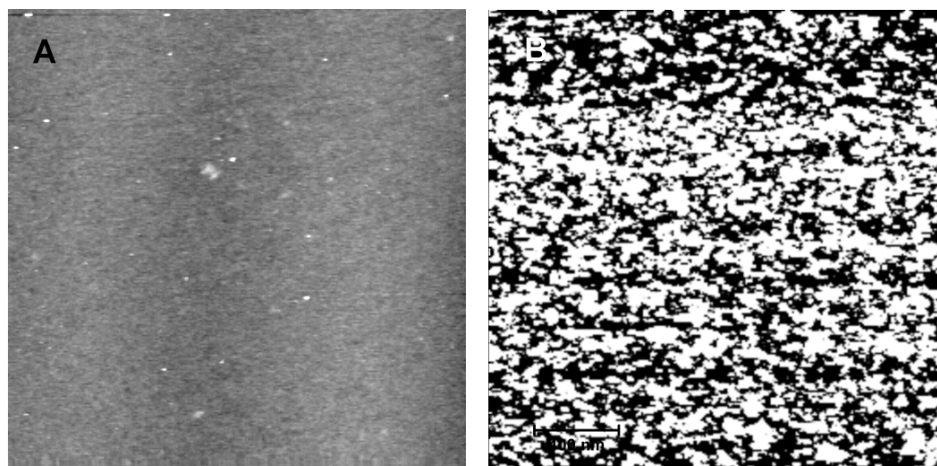


Figure 1–8 Typical AFM images of ODS SAMs on SiO₂/Si prepared with A: fresh OTS and B: old OTS. Reaction time 1 hour. (Image size: 2 μm × 2 μm, height scale 2 nm)

It appears that the contact with moisture creates oligomers that act as nucleation centers for bulk polymerization processes. If the oligomer aggregates are too large, they can form multilayer on surfaces. The dramatic difference in growth kinetics for solution prepared from fresh OTS, which contains few aggregates and aged OTS with many more aggregates, suggest that patches of oligomers have better chance to adsorb onto the surface than monomers. The degree of polymerization may be the major reason for irreproducibility. Therefore, to improve the reproducibility, exposure of the stock OTS to moisture must be minimized. We later employed the sealing procedure described in the experimental section to protect OTS from ambient moisture.

1.3.3. Effect of water content.

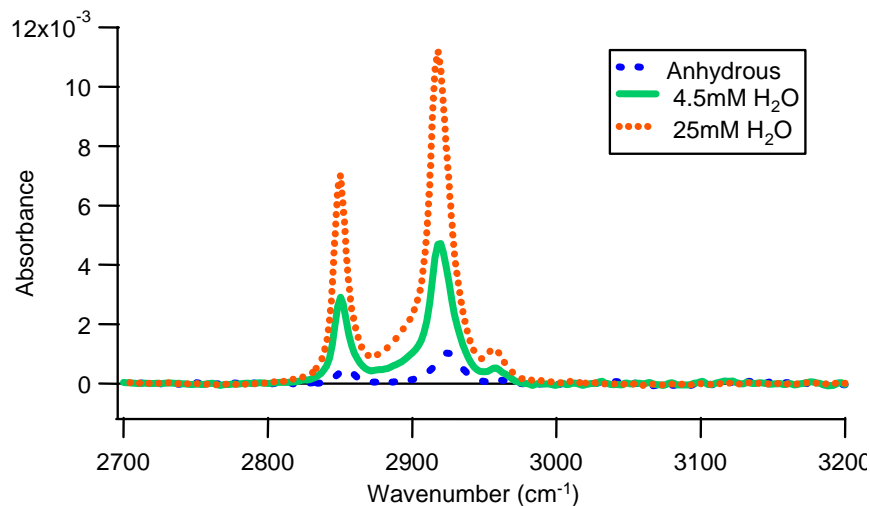


Figure 1-9 Effect of water content in the ODS SAM preparation on glass. 20°C, 60% relative humidity 60 minute reaction time.

The effect of water concentration is dramatic on the growth of ODS SAMs as illustrated in Figure 1-9. Evidently, water promotes the attachment of ODS to the surface. Bulk water may play several possible roles in ODS SAM formation. First, water hydrolyzes trichlorosilane into silanol. The silanol molecules should have higher affinity with the surface than do OTS molecules because in contrast with trichlorosilane groups, the silanol head groups can interact with surface water much more strongly through hydrogen bonding. Another reason for the enhanced reaction rate is that the silanol molecules may cross-link to form oligomers (R1-2), having better affinity with the surface because they have more groups to interact with the surface than monomers. The third reason is that the bulk water is in equilibrium with the surface water, which is believed to be important for high quality monolayer formation. If the bulk water concentration is high, the water thin

film may grow. If the toluene is anhydrous, it may extract water from the substrate surface and consequently inhibit the silanization reaction.

1.3.4. Roles of ambient humidity.

In our laboratory, we found that typically the silanization was significantly faster in summer than in winter, when the humidity is much lower. This prompted us to perform more systematic studies in which the relative humidity (RH) is controllably varied. Humidity may form a surface water film on hydrophilic surfaces [32]. To understand whether the presence of a surface water film on the substrate prior to immersion into reaction solutions is important in our experiment, we equilibrated glass substrates at 40% RH and the substrates were immersed in reaction vessels under the same RH. After immersion, the vessels were sealed with parafilm and the humidity of the surrounding was reduced to 5%.

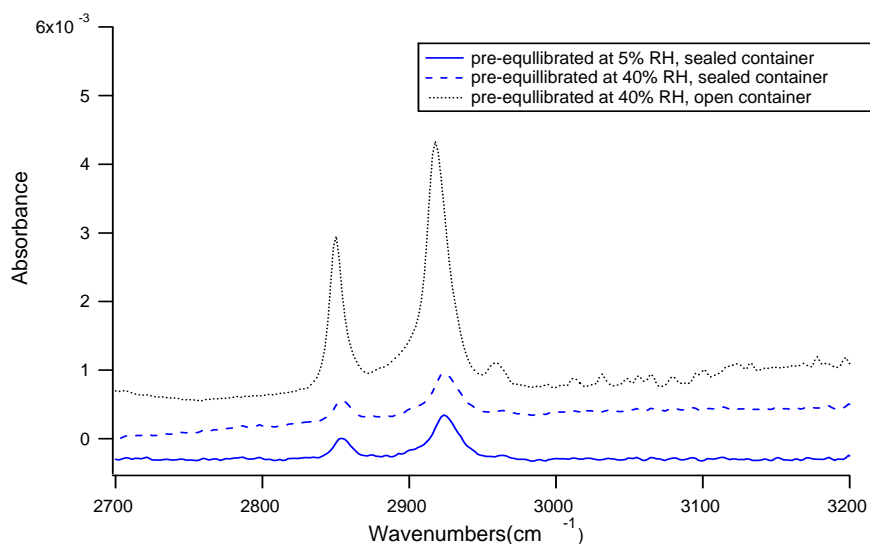


Figure 1–10 FTIR spectra of ODS SAMs on glass after 60 min of reaction . Spectra are offset for clarity. From bottom to the top: A substrate equilibrated at 40% RH. Sealed

container. B substrate equilibrated 5% and sealed container. C container opened to 40% RH. Reaction conditions: 12 mM water 2.1mM OTS in toluene.

We found that the equilibration of substrate at a given humidity before reactions has no significant effect (Figure 1–10). Even when the substrate had been equilibrated for 30 min at 40% prior to immersion, $\nu_{\text{as}}\text{CH}_2$ peak absorbance only reached 0.65 mOD after 60 min and 1.7 mOD after 5 hours of reaction if the reaction container was sealed immediately after immersing the substrate into the solution. When the substrate was equilibrated with dry air (RH less than 5%) for 30 min before the silanization reaction, the absorbance reached 0.6 mOD. The difference is rather small. However, if the reaction solution is exposed to ambient environment at 40% RH during the silanization reaction, we found that the $\nu_{\text{as}}\text{CH}_2$ peak absorbance reached 3.3 mOD within 30 min, suggesting a compact monolayer (Figure 1–11). We found that exposing the solution to RH over 50% often led to rapid polymerization as indicated by the IR absorbance exceeding that of a monolayer. Within one hour, the reaction solution became visually cloudy, suggesting large amount of polymerization. Therefore, we decided that the optimum humidity is 40%.

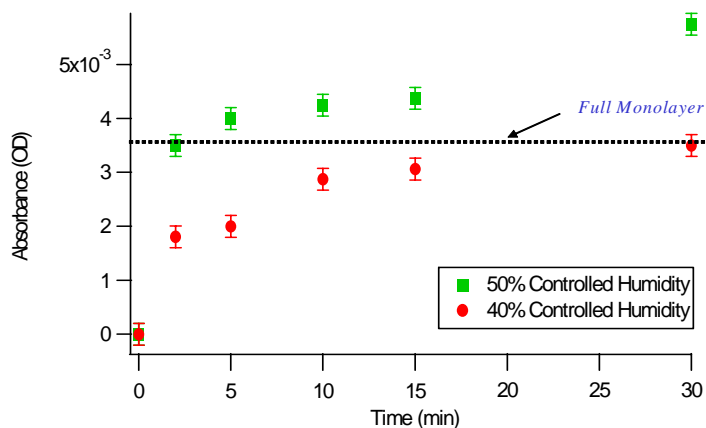


Figure 1–11 $\nu_{\text{as}}\text{CH}_2$ peak absorbance as a function of reaction time when exposed to 40 and 50% relative humidity (12 mM water 2.1 mM OTS in toluene).

Clearly, exposing the reaction solution to humidity has a much more dramatic effect on kinetics of the self-assembly of ODS than simply exposing the substrate to humidity. Therefore, in contrast to a number of existing studies, the surface film of water prior to reaction does not appear to play a significant role under our conditions. Fairbank et al. found that it was important to equilibrate the substrate with 50% humidity to achieve dense ODS films on high surface area silica gel [37]. At 50% humidity approximately 3 ML of water is adsorbed [37]. At higher humidity, bulk polymerization started to occur as suggested by NMR [37]. On 1g high surface area silica gel (350 g/m^2), the amount of adsorbed water is 0.7 g if equilibrated at 50% RH [37]. Because the amount of adsorbed water far exceeds the extraction capacity of the solvent, 20 ml heptane, the amount of surface water should not change significantly when the silica gel was added to the heptane.

However, the arguments relevant to high area materials are not necessarily applicable to the SAM formation on planar surfaces. On a planar substrate, even if the substrate is equilibrated at a set RH and several monolayers of water are formed on the surface, the amount of water present on the surface is insignificant compared to the water extraction capacity of the solvent. Therefore, after immersion into the reaction solution, equilibrium between the surface water and water present in the solvent may change the amount of surface water significantly. Depending on the tendency for the solvent to extract water, the water film may grow [21] or dissolve into the solvent [45]. Therefore, we believe the

applicability of conclusions from the silica gel to planar surfaces is questionable. An *in situ* ATR FTIR study on planar surfaces study suggested that even trace amount of water in the solvent might be adsorbed by the substrate [21]. It appears that the surface water film is largely determined by the water content of the reaction solution and therefore surface hydration prior to reaction is not important under our conditions.

The role of ambient humidity is suggested by the observation that after extended exposure to ambient environment a white film develops on the surface of the solution. This suggests that the solution-air interface is the preferred location for the OTS molecules to react with moisture and polymerize. This points to the importance of siloxane oligomers in the formation of ODS SAMs. As discussed in 3.2, the presence of oligomers may promote the reaction. The water content (12 mM) in the toluene is sufficient to hydrolyze all the OTS molecules (2.1mM). Since the substrate is equilibrated in the atmosphere, and 12 mM water is present in toluene, a water film on the substrate should be present [36]. Yet the water film alone is not sufficient for self-assembly. If fresh OTS was used, the polymerization process was slow on the time scale of several hours under a dry environment (when the reaction vessels were sealed). We proposed that attachment of single silanol or chlorosilane molecules to the surface is slow. The importance of humidity manifests itself through the promotion of the polymerization process: forming small patches of polymerized silanol that can be subsequently attached to the surface.

Our results suggest that polymerization prior to attachment to the surface, while deemed responsible for multilayer formation [26], may play positive roles in the formation of high quality ODS monolayers. Evidently, large oligomers of siloxane can form ill-defined multilayers, as suggested by Figure 1–6B. However, smaller oligomers may be flexible enough to adopt a geometry that allows all the headgroups attached to the surface, thereby forming a dense monolayer (Figure 1–12). Compared to monomers, siloxane oligomers may adsorb onto the surface much faster than since multiple OH groups are allowed to interact with the water surface. Although many authors assume that hydrolysis occurs at water films on substrate surfaces after chlorosilanes are adsorbed [21, 24, 33], those studies were performed under conditions where the amount of water in the bulk is negligible. Consequently, the reactions may take over 24 hours to complete.

In addition to delivering small, polymerized patches at the air-toluene interface, we cannot completely rule out the possibility that the solvent may absorb moisture when exposed to ambient and consequently the bulk concentration of water may increase. The humidity may change the water concentration in the solvent. However the absorption of moisture by solvent should occur on time scale of hours [21]. To draw a more definitive conclusion, absolute water concentrations with different amount of exposure to ambient humidity need to be measured.

1.3.5. Conclusions and future work.

Our results suggests that the widely varying reported ODS SAM formation kinetics, with reaction time ranging from days to minutes [22-25], can be rationalized by the three roles of water discussed above. We demonstrate that water can be controlled by employing relatively simple procedures and reproducibility can be improved dramatically. If the OTS is not fresh, the coverage may exceed a monolayer within 5mins. This is undesirable since bulk polymerization occurs too rapidly. Under very dry conditions (dry solvent and low humidity), although bulk polymerization is suppressed, the reaction is very slow and the film is not compact. We chose the middle ground for our optimum conditions. By using fresh OTS, 12mM water and 40% ambient humidity, compact SAMs can be performed within an hour or two with no significant bulk polymerization.

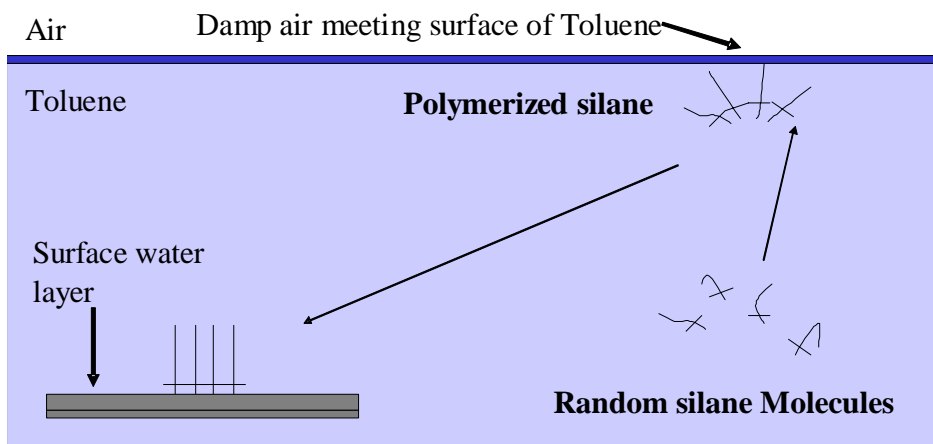


Figure 1–12 The role of humidity in ODS SAM formation.

Our results suggest that small patches of ODS oligomers may allow facile formation of ODS SAMs. Due to the small size and limited degree of cross-linking, formation of dense monolayer may still be possible, in contrast to very large oligomers. Currently the small patches are achieved by exposing the reaction mixture to a controlled ambient humidity. Questions concerning the diffusion of the small patches from liquid air

interfaces and whether the reaction can be scaled up to larger containers remain. On a more fundamental level, more investigations on controlling the processes in the bulk reaction solution as well as those at the surfaces. NMR and light scattering techniques, for example, may help to understand and control crucial steps such as hydrolysis and polymerization of OTS in the bulk solution. To achieve better control over the irreproducible process, we believe that it is also important to use in-situ techniques, especially vibrational spectroscopies, to investigate the adsorption of water, chemical species and bonding on the substrates. Such investigations will help to understand the equilibration between surface water and the degree of cross-linking between siloxane headgroups in the surface plane [48]. Though FT-IR studies of silanization of high surface area materials [32, 33, 38, 49, 50] have advanced our understanding, they cannot substitute for in-situ studies directly on well-defined planar substrates since many conclusions, such as the partition between the water in the surface film and in the solvent, are not necessarily applicable to lower surface area materials.

BIBLIOGRAPHY

1. Biglow, W., D. Pickett, and W. Zisman, *Oleophobic monolayers. I. films adsorbed from solution in non-polar liquids*. Journal of Colloid and Interface Science, 1946. **1**: p. 513-538.
2. Langmuir, I., *The mechanism of the surface phenomena of flotation*. Trans. Faraday Soc., 1920. **15**(3): p. 62-74.
3. Sagiv, J., *Organized monolayers by adsorption. I. formation and structure of oleophobic mixed monolayers on solid surfaces*. Journal of the American Chemical Society, 1980. **102**(1): p. 92-98.
4. Nuzzo, R. and D. Allara, *Adsorption of bifunctional organic disulfides on gold surfaces*. Journal of the American Chemical Society, 1983. **105**: p. 4481-4483.
5. Dubois, L.H. and R.G. Nuzzo, *Synthesis, structure, and properties of model organic surfaces*. Annual Review of Physical Chemistry, 1992. **43**: p. 437-463.
6. Ulman, A., *Formation and structure of self-assembled monolayers*. Chemical Reviews, 1996. **96**: p. 1533-1554.
7. Arkles, B., *Tailoring surfaces with silanes*. Chemtech, 1977. **7**: p. 766-778.
8. Dulcey, C.S., J.H. Georger Jr., V. Krauthamer, D. Stenger, T.L. Fare, and J.M. Calvert, *Deep UV photochemistry of chemisorbed monolayers: patterned coplanar molecular assemblies*. Science, 1991. **252**: p. 551-554.
9. Komeda, T., K. Namba, and Y. Nishioka, *Self-assembled-monolayer film islands as a self-patterned-mask for SiO₂ thickness measurement with atomic force microscopy*. Applied Physics Letters, 1997. **70**(25): p. 3398-3400.
10. Sugimura, H., K. Ushiyama, A. Hozumi, and O. Takai, *Micropatterning of alkyl- and fluoroalkylsilane self-assembled monolayers using vacuum ultraviolet light*. Langmuir, 2000. **16**(3): p. 885-888.
11. Schneeweiss, M.A., H. Hagenstrom, M.J. Esplandiu, and D.M. Kolb, *Electrolytic metal deposition onto chemically modified electrodes*. Applied Physics Materials Science & Processing, 1999. **69**(5): p. 537-551.
12. Moberg, P. and R.L. McCarley, *Electroless deposition of metals onto organosilane monolayers*. Journal of the Electrochemical Society, 1997. **144**(6): p. L151-L153.
13. Zheng, J.W., Z.H. Zhu, H.F. Chen, and Z.F. Liu, *Nanopatterned assembling of colloidal gold nanoparticles on silicon*. Langmuir, 2000. **16**(10): p. 4409-4412.
14. Doppelt, P. and M. Stelzle, *Selective metallization of silica surfaces by copper CVD using a chemical affinity pattern created by gas phase silylation and UV exposure*. Microelectronic Engineering, 1997. **33**(1-4): p. 15-23.
15. Mrksich, M. and G.M. Whitesides, *Using self-assembled monolayers to understand the interactions of man-made surfaces with proteins and cells*. Annual Review of Biophysics and Biomolecular Structure, 1996. **25**: p. 55-78.
16. Lingler, S., I. Rubinstein, W. Knoll, and A. Offenhausser, *Fusion of small unilamellar lipid vesicles to alkanethiol and thiolipid self-assembled monolayers on gold*. Langmuir, 1997. **13**(26): p. 7085-7091.
17. Collet, J., M. Bonnier, O. Bouloussa, F. Rondelez, and D. Vuillaume, *Electrical properties of end-group functionalised self-assembled monolayers*. Microelectronic Engineering, 1997. **36**(1-4): p. 119-122.

18. Vuillaume, D., C. Boulas, J. Collet, J.V. Davidovits, and F. Rondelez, *Organic insulating films of nanometer thicknesses*. Applied Physics Letters, 1996. **69**(11): p. 1646-1648.
19. Fomenko, V., C. Hurth, T. Ye, and E. Borguet, *Second harmonic generation investigations of charge transfer at chemically-modified semiconductor interfaces*. Journal of Applied Physics, 2002. **91**(7): p. 4394-4398.
20. Bumm, L.A., J.J. Arnold, M.T. Cygan, T.D. Dunbar, T.P. Burgin, L. Jones, D.L. Allara, J.M. Tour, and P.S. Weiss, *Are single molecular wires conducting?* Science, 1996. **271**(5256): p. 1705-1707.
21. Imhof, R., X.Y. Xie, and G. Calzaferri, *In situ attenuated total reflection FTIR investigations of thin water films in the silanization of ZnSe and Si*. Spectrochimica Acta Part a-Molecular and Biomolecular Spectroscopy, 1997. **53**(7): p. 981-989.
22. Schwartz, D.K., S. Steinberg, J. Israelachvili, and J.A.N. Zasadzinski, *Growth of a self-assembled monolayer by fractal aggregation*. Physical Review Letters, 1992. **69**(23): p. 3354-3357.
23. Wasserman, S.R., Y.T. Tao, and G.M. Whitesides, *Structure and reactivity of alkylsiloxane monolayers formed by reaction of alkyltrichlorosilanes on silicon substrates*. Langmuir, 1989. **5**(4): p. 1074-87.
24. Lambert, A.G., D.J. Neivandt, R.A. McAloney, and P.B. Davies, *A protocol for the reproducible silanization of mica validated by sum frequency spectroscopy and atomic force microscopy*. Langmuir, 2000. **16**(22): p. 8377-8382.
25. Fadeev, A.Y. and T.J. McCarthy, *Trialkylsilane monolayers covalently attached to silicon surfaces: Wettability studies indicating that molecular topography contributes to contact angle hysteresis*. Langmuir, 1999. **15**(11): p. 3759-3766.
26. Fadeev, A.Y. and T.J. McCarthy, *Self-assembly is not the only reaction possible between alkyltrichlorosilanes and surfaces: Monomolecular and oligomeric covalently attached layers of dichloro- and trichloroalkylsilanes on silicon*. Langmuir, 2000. **16**(18): p. 7268-7274.
27. Jun, Y. and X.Y. Zhu, *Alkoxy monolayers as anti-stiction coatings in Si-based MEMS devices*. Journal of Adhesion Science and Technology, 2003. **17**(4): p. 593-601.
28. Brunner, H., T. Vallant, U. Mayer, H. Hoffmann, B. Basnar, M. Vallant, and G. Friedbacher, *Substrate effects on the formation of alkylsiloxane monolayers*. Langmuir, 1999. **15**(6): p. 1899-1901.
29. Flinn, D.H., D.A. Guzonas, and R.H. Yoon, *Characterization of silica surfaces hydrophobized by octadecyltrichlorosilane*. Colloids and Surfaces a-Physicochemical and Engineering Aspects, 1994. **87**(3): p. 163-176.
30. Inoue, A., T. Ishida, N. Choi, W. Mizutani, and H. Tokumoto, *Nanometer-scale patterning of self-assembled monolayer films on native silicon oxide*. Applied Physics Letters, 1998. **73**(14): p. 1976-1978.
31. Rye, R.R., G.C. Nelson, and M.T. Dugger, *Mechanistic aspects of alkylchlorosilane coupling reactions*. Langmuir, 1997. **13**(11): p. 2965-2972.
32. Angst, D.L. and G.W. Simmons, *Moisture absorption characteristics of organosiloxane self-assembled monolayers*. Langmuir, 1991. **7**(10): p. 2236-42.

33. Tripp, C.P. and M.L. Hair, *Reaction of alkylchlorosilanes with silica at the solid/gas and solid/liquid interface*. Langmuir, 1992. **8**(8): p. 1961-7.
34. Parikh, A.N., D.L. Allara, I.B. Azouz, and F. Rondelez, *An intrinsic relationship between molecular-structure in self-assembled n-alkylsiloxane monolayers and deposition temperature*. Journal of Physical Chemistry, 1994. **98**(31): p. 7577-7590.
35. Vallant, T., J. Kattner, H. Brunner, U. Mayer, and H. Hoffmann, *Investigation of the formation and structure of self-assembled alkylsiloxane monolayers on silicon using in situ attenuated total reflection infrared spectroscopy*. Langmuir, 1999. **15**(16): p. 5339-5346.
36. Vallant, T., H. Brunner, U. Mayer, H. Hoffmann, T. Leitner, R. Resch, and G. Friedbacher, *Formation of self-assembled octadecylsiloxane monolayers on mica and silicon surfaces studied by atomic force microscopy and infrared spectroscopy*. Journal of Physical Chemistry B, 1998. **102**(37): p. 7190-7197.
37. Fairbank, R.W.P. and M.J. Wirth, *Role of surface-adsorbed water in the horizontal polymerization of trichlorosilanes*. Journal of Chromatography A, 1999. **830**(2): p. 285-291.
38. Tripp, C.P. and M.L. Hair, *An infrared study of the reaction of octadecyltrichlorosilane with silica*. Langmuir, 1992. **8**(4): p. 1120-6.
39. Ye, S., S. Nihonyanagi, and K. Uosaki, *Sum frequency generation (SFG) study of the pH-dependent water structure on a fused quartz surface modified by an octadecyltrichlorosilane (OTS) monolayer*. Physical Chemistry Chemical Physics, 2001. **3**(16): p. 3463-3469.
40. Brzoska, J.B., N. Shahidzadeh, and F. Rondelez, *Evidence of a transition-temperature for the optimum deposition of grafted monolayer coatings*. Nature, 1992. **360**(6406): p. 719-721.
41. Carraro, C., O.W. Yauw, M.M. Sung, and R. Maboudian, *Observation of three growth mechanisms in self-assembled monolayers*. Journal of Physical Chemistry B, 1998. **102**(23): p. 4441-4445.
42. Allara, D.L., A.N. Parikh, and F. Rondelez, *Evidence for a unique chain organization in long-chain silane monolayers deposited on 2 widely different solid substrates*. Langmuir, 1995. **11**(7): p. 2357-2360.
43. Richter, A.G., C.J. Yu, A. Datta, J. Kmetko, and P. Dutta, *In situ and interrupted-growth studies of the self-assembly of octadecyltrichlorosilane monolayers*. Physical Review E, 2000. **61**(1): p. 607-615.
44. Ye, T., D. Wynn, R. Dudek, and E. Borguet, *Photoreactivity of alkylsiloxane self-assembled monolayers on silicon oxide surfaces*. Langmuir, 2001. **17**(15): p. 4497-4500.
45. McGovern, M.E., K.M.R. Kallury, and M. Thompson, *Role of Solvent on the Silanization of Glass with Octadecyltrichlorosilane*. Langmuir, 1994. **10**(10): p. 3607-3614.
46. Ulman, A., *Characterization of organic thin films*. 1995, Boston, MA: Butterworth-Heinemann.
47. Parikh, A.N. and D.L. Allara, *Quantitative determination of molecular structure in multilayered thin films of biaxial and lower symmetry from photon*

- spectroscopies .I. reflection infrared vibrational spectroscopy*. Journal of Chemical Physics, 1992. **96**(2): p. 927-945.
48. Stevens, M.J., *Thoughts on the structure of alkylsilane monolayers*. Langmuir, 1999. **15**(8): p. 2773-2778.
 49. Tripp, C.P. and M.L. Hair, *Direct observation of the surface bonds between self-assembled monolayers of octadecyltrichlorosilane and silica surfaces: A low-frequency IR study at the solid/liquid Interface*. Langmuir, 1995. **11**(4): p. 1215-19.
 50. Tripp, C.P. and M.L. Hair, *Reaction of chloromethylsilanes with silica: a low-frequency infrared study*. Langmuir, 1991. **7**(5): p. 923-7.

2. Mechanism of UV photoreactivity of alkylsiloxane self-assembled monolayers.

2.1. Introduction.

There has been intense interest in the growth of Self-Assembled Monolayers (SAMs) [1]. In contrast, much less attention has been paid to the reactivity of SAMs. The stability of SAMs is a prerequisite in their technological applications. Alkanethiol monolayers have been found to have lifetimes ranging from hours to months in ambient environment [2] and degrade in minutes under ultraviolet (UV) irradiation [3]. The reactivity of alkanethiol SAMs has been attributed to the thiolate headgroups, which are prone to oxidation [3]. Even the alkyl chains can degrade under harsh conditions, e.g., under photo or electron irradiation [4, 5]. Knowledge of SAM photoreactivity may help to design and prepare more stable SAMs for technological applications.

While we need to improve the stability of SAMs, controlled degradation can be desirable in some cases. Photoreactivity of SAMs can be exploited to selectively modify SAMs for various applications. As the feature sizes in lithography continue to scale down, there is an increasing demand on the resist films. In the case of photolithography, the thickness of the resist films must reduce as the focus depth of the light decreases with ever decreasing light wavelength [6, 7]. In the case of electron beam-lithography, the reduced thickness is necessary to reduce the scattering of secondary electrons in the resist films, which degrades the resolution [6, 7]. In addition, structural uniformity of the films becomes increasingly more important. SAMs have become an attractive candidate for nanoscale resist due to their molecular thickness and well defined structure [8, 9].

Understanding the photoreactivity of SAMs is important for optimizing photoresist patterning processes involving SAMs [10-12]. In addition, photo-modification of SAMs may serve as a convenient route to attach functional groups to SAMs, enabling one to tailor wettability, adhesion and electrical properties of the monolayers [13].

On a more fundamental level, the molecularly well-defined structures render SAMs a model system to probe the relationship between structure and photoreactivity in condensed phase, which has implications from organic aerosol chemistry to photoresist micropatterning [14-16]. At this stage, the degree of understanding of the complex mechanisms of photooxidation of condensed is far from that achieved for organic compounds in gas phase [16, 17]. It would be challenging or impossible to extract the rate of each individual steps since each step is sensitive to the environment of the reactive sites, which may be highly heterogeneous. Nevertheless SAMs afford the opportunity to systematically vary the structure and composition of organic layers to understand from a molecular level how these factors affect the reactivity.

Due to the unique ordered 2D structures of SAMs, one would expect the reaction kinetics or even reaction pathways of SAMs to depart significantly from gas phase reactions. Indeed, dramatic contrasts have been observed in a limited number of studies. First, the ordered SAM structure may block access to reactive sites. The reactions of ordered organic thin films were found to occur preferentially at the top of the chains [18, 19] or defect sites [2, 20, 21]. However, in some cases, surfaces may significantly enhance the reaction rates. It has been shown that the reactions between hydrocarbon chains in SAMs

and radicals can be enhanced by orders of magnitude compared to gas phase reactions [14, 15, 22]. However, the origin of such enhancement remains unclear. The impinging reactive species may remain on the surface, increasing the probability of reaction, while in gas phase most of the colliding reactants are rapidly separated before reactions can occur. The possibility of crossing of potential energy surfaces was also raised to explain enhanced reactivity. Paz et al. proposed that in the reactions between $O(^3P)$ and methyl groups in SAMs, the long lived collision complex on the surface may result in the crossing to a singlet potential energy surface that results in much higher reactivity [19].

2.1.1. Possible mechanisms of photoreactivity of SAMs.

Depending on the wavelength, the nature of the functional groups in the SAMs, the substrate and the ambient environment, photons can modify the SAMs with different mechanisms. We attempt to categorize the mechanisms according to the active agents involved (Figure 2-1).

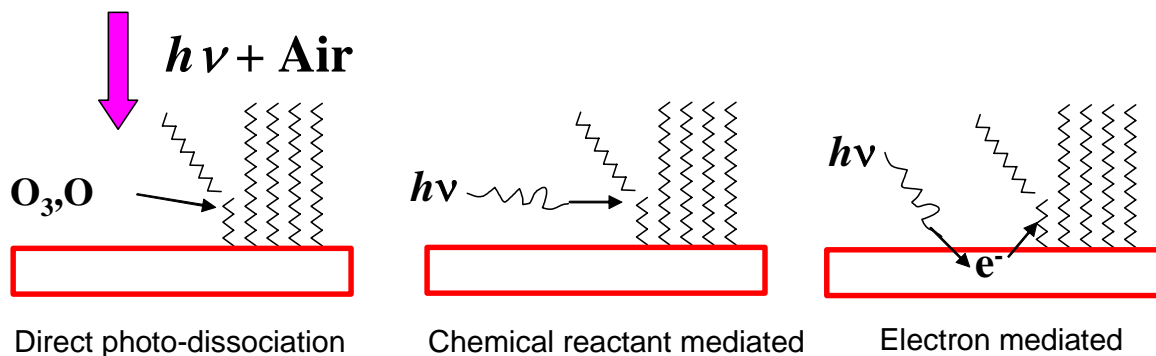


Figure 2-1 Probable mechanisms of SAM photoreactivity.

2.1.1.1. *Direct photodissociation.*

Photons can be directly responsible for the dissociation of the organic molecules in SAMs. UV photons in resonance with electronic transitions in unsaturated SAM layers (such as a π - π^* transition) can induce photolysis [23]. However, photolysis of saturated alkyl SAMs requires a σ - σ^* transition of C-H or C-C bonds induced by absorption of photons in the vacuum UV range ($\lambda < 160$ nm).

2.1.1.2. *Electron-mediated.*

Photons can ionize the underlying substrate or the monolayer, which leads to further chemical transformation and dissociation. X-ray induced modification of SAMs is believed to proceed via this mechanism [24-26]. Whitesides et al. observed that under identical X-ray fluxes, CF_3COO terminated monolayers degraded more rapidly on Au than on Si, which is a less efficient electron emitter [24]. Furthermore, when normalized to photo-emitted electron fluxes, similar amounts of degradation occurred on different substrates [24]. This supports the suggestion that electrons are the primary cause of SAM X-ray degradation. Though there is little absorption of X-rays by organic monolayers, photoelectrons generated from the substrate can interact with the organic monolayers. Indeed, the damage of SAMs by X-ray degradation [25] is remarkably similar to the electron damage of SAMs [27]. Both involve dehydrogenation and cross-linking of the alkyl chains. Both mechanisms result in very little loss of carbon content. Both mechanisms result in the incorporation of oxygenated functional groups upon exposure to air. It is believed that electron impact induces C-H and C-C bond scission, forming radicals [27]. The radicals can undergo cross-linking and oxygenation [27]. The proposed steps are summarized in Table 2-1.

Table 2-1 Proposed mechanism of electron beam degradation of SAMs.

$R-H \rightarrow R\bullet + H\bullet$	R 2-1
$R-R' \rightarrow R\bullet + R'\bullet$	R 2-2
$R\bullet + R''\bullet \rightarrow R-R''$	R 2-3
$R\bullet + O_2 \rightarrow ROO\bullet$	R 2-4
$ROO\bullet \rightarrow -C=O, C-OH, -COOH$	R 2-5

2.1.1.3. *Chemical reactant mediated.*

In an ambient environment, UV light may generate highly oxidative species, such as ozone, atomic oxygen and hydroxyl radicals [28]. The reactive species may subsequently react with the monolayers. A number of studies have attributed the primary degradation pathway of alkanethiol SAMs in ambient and under low UV intensity ($\mu\text{W}/\text{cm}^2$ to mW/cm^2) to ozonolysis [2, 3, 29-31]. In this mechanism, it is suggested that photo-generated ozone attacks the thiolate headgroups to produce solvent-labile species and cleavage of the C-S bond. In contrast, UV photooxidation of alkylsiloxane SAMs has been attributed to the reaction between hydrocarbon chains and atomic oxygen or other oxygen containing radicals [18, 32].

It should be noted that the photoreactivity of SAMs may involve more than one mechanism at the same time. For example, X-ray degradation of SAMs is initiated by electrons, but subsequently chemical reactants may participate in the degradation as well[25].

2.1.2. **Objectives of this study.**

We chose to investigate the reactivity of octadecylsiloxane (ODS) SAMs under UV irradiation in ambient, which has implications in photopatterning applications and heterogeneous chemistry of organic aerosols. The goals of this study are to understand:

1. The active agent for the UV photoreactivity of ODS SAMs.
2. The reactive sites in the photochemical transformation.
3. The nature of reaction intermediates and products.

We found evidence that atomic oxygen is the primary agent for the UV degradation of ODS SAMs. UV degradation results in the scission of alkyl chains instead of the siloxane headgroups. We found that degradation introduces microscopic roughness ODS SAMs. Using a novel highly surface sensitive technique, FLOSS, we identified the presence of submonolayer quantities of chemical functional groups formed by the UV degradation. We proposed a mechanism based on hydrogen abstraction. Deeper molecular level insight into the mechanism of the UV photoreactivity of ODS SAMs has implications in high resolution photopatterning of molecular resists.

2.2. Experimental Section.

2.2.1. SAM preparation.

SAM preparation procedures have been described in detail in Chapter 1.

2.2.2. UV photoreactivity.

The ODS covered samples were irradiated in a home-made pyrex glass UV chamber with a low pressure Hg/Ar lamp (Oriel Instruments) with total intensity of $\sim 2 \text{ mW/cm}^2$ at a working distance of 3 cm. The primary wavelength of the lamp is 254 nm. It is believed

that the UV light at 183 nm, albeit constituting only 3% of total intensity, is responsible for the ozone generation [31]. Before placing the sample in the UV chamber, the UV lamp was powered on for at least 15min to reach stable intensity and steady state ozone concentration in the chamber [29]. The ozone concentration was determined by a direct photometric method [33]. Briefly, the ozone generated in the chamber was captured in a 1cm path length quartz cuvette. Assuming an absorption cross section of $1150 \times 10^{-20} \text{ cm}^2$ at 255 nm, the UV absorbance was used to calculate the concentration [34]. The steady state concentration of ozone in the UV chamber was found to be $100 \pm 10 \text{ ppm}$. A more detailed description can be found in Appendix B.

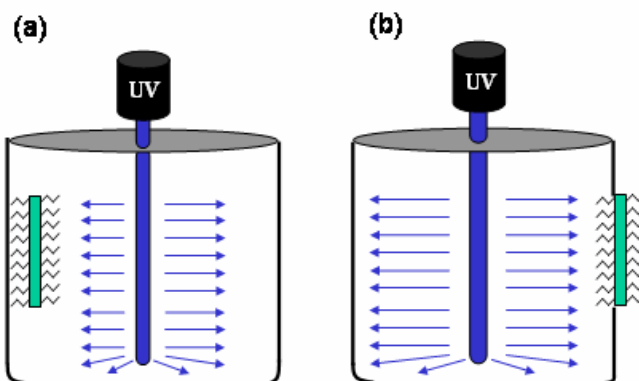


Figure 2-2 UV chamber a: Irradiation configuration 1, where both sides of the sample are exposed to the chamber. b: Irradiation configuration 2, where only a single side is exposed to the reactive species produced in the chamber.

2.2.3. Sample characterization.

2.2.3.1. *Water contact angle and FT-IR measurements.*

These two techniques have been described in Chapter 1. Most FT-IR spectra were obtained from SAMs supported on glass slides. The only exception was the FT-IR measurement in the carbonyl stretch region, which was performed on SAMs supported on oxidized silicon substrates. In that case, the background was N₂ instead of a cleaned substrate.

2.2.3.2. *AFM.*

Details of AFM measurements have been described in the experimental section of Chapter 1.

2.2.3.3. *XPS measurement*

X-ray photoelectron spectra were obtained on a Physical Electronics model 550 apparatus, equipped with a cylindrical, double-pass analyzer. The front of the analyzer was apertured to restrict the acceptance angle to $\pm 6^\circ$. The energy resolution of the apparatus was determined to be 1 eV. X-ray photoelectron spectra were taken using an Al K α X-ray source (1486.3 eV) and all the spectra were taken at 30° take-off angle. The pressure in the analytical chamber was $\sim 10^{-9}$ Torr during analysis. Spectra of C(1s) (binding energy: 280 - 292 eV) region were collected.

2.2.3.4. *Fluorescence labeling of surface species (FLOSS).*

Chromophore labeling: μ M solutions were prepared of either triphenylmethylchloride (98%, Aldrich) in dimethylformamide (DMF, ACS grade, Baker), 1-pyrenemethylamine (95%, Aldrich) in ethanol (ACS grade, Pharmaco) or 1-naphthaleneethanol (99%, Aldrich) in methylenechloride (ACS grade, Fisher). The trityl and pyrene labeling reactions were carried out at room temperature for two hours. The naphthalene labeling reaction was refluxed for two hours with a catalytic amount of hydrochloric acid (CMOS grade,

Baker). Fluorescence measurements were performed on a Jobin Yvon Horiba Spex Fluorolog 3 with 5 nm bandpass and 5 scan averages with samples situated at a 45° incident angle. Excitation and emission monochromators are double grating and detection is accomplished using a PMT. Fluorescent signals for all samples were corrected for lamp fluctuations by recording the ratio of the fluorescence signal to a source reference photodiode.

Post Reaction Cleaning Procedure: Following the chromophore grafting, sample surfaces were rinsed with neat solvent. The samples were then sonicated in successively less polar solvents (methanol or acetone, then CH₂Cl₂, and finally hexane) to remove residual reactant species from the surface.

The calibration sample was marked with a diamond scribe defining the boundaries of the spot (4mm × 6mm) illuminated by the fluorometer. This facilitated realignment of the sample and ensured that the solution spread only in the defined area. A 5 μL drop of dilute solution was placed on the marked area of the sample and the solvent was allowed to evaporate.

2.3. Results.

2.3.1. Contact angle results.

The ODS SAMs are known to be remarkably stable in ambient over extended periods of time. There was no measurable change in the contact angles of the monolayers stored

under ambient in our laboratory over several months. The water contact angles of the ODS monolayers on glass irradiated for different amounts of time in the UV chamber are shown in Figure 2-3 . The contact angle of SAMs dropped significantly following a few minutes of UV irradiation in air. The increasing hydrophilicity of the surface can be explained by conversion of alkyl chains to hydrophilic groups, e.g. OH, aldehydes or carboxylic acids, or increasing coverage of the hydrophilic substrate due to loss of the alkyl chains during the UV irradiation. When the UV irradiation chamber was flushed with argon, there was little change in the contact angle after irradiation. This suggests that the UV alone cannot directly dissociate the alkyl chains. Remarkably, the side of the slides facing away from the irradiation source displayed very low reactivity. The lifetime of ozone is sufficient to maintain a roughly uniform concentration across the UV chamber [35]. This long lifetime is confirmed by experiments described in Appendix B. As the glass slides are opaque to UV wavelengths below 300 nm (Figure 2-4), the backside of the sample is exposed to ozone but not UV with wavelength below 300 nm. This result suggests that UV and O₂ are both necessary for the reaction to proceed. In agreement with Moon et al. [32], we conclude that ozone alone was not the active reagent in our system.

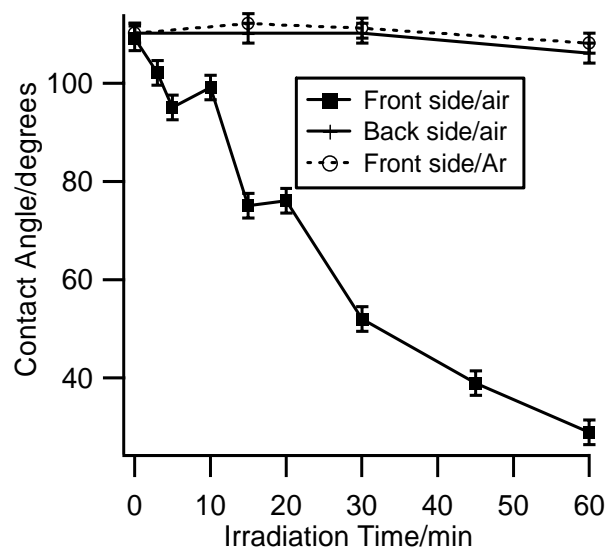


Figure 2-3 Contact angles of irradiated ODS SAMs on glass as a function of time under different ambient environments.

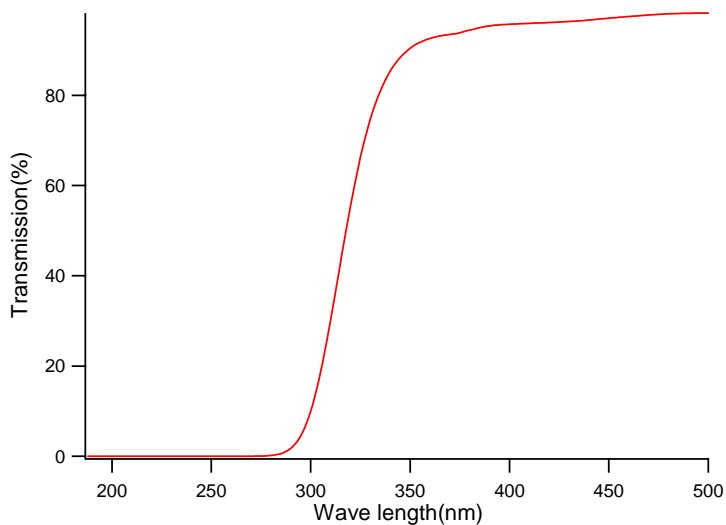


Figure 2-4 UV-vis spectrum of a 1mm thick microscope cover glass slide (VWR).

2.3.2. FT-IR results.

2.3.2.1. UV irradiation configuration.

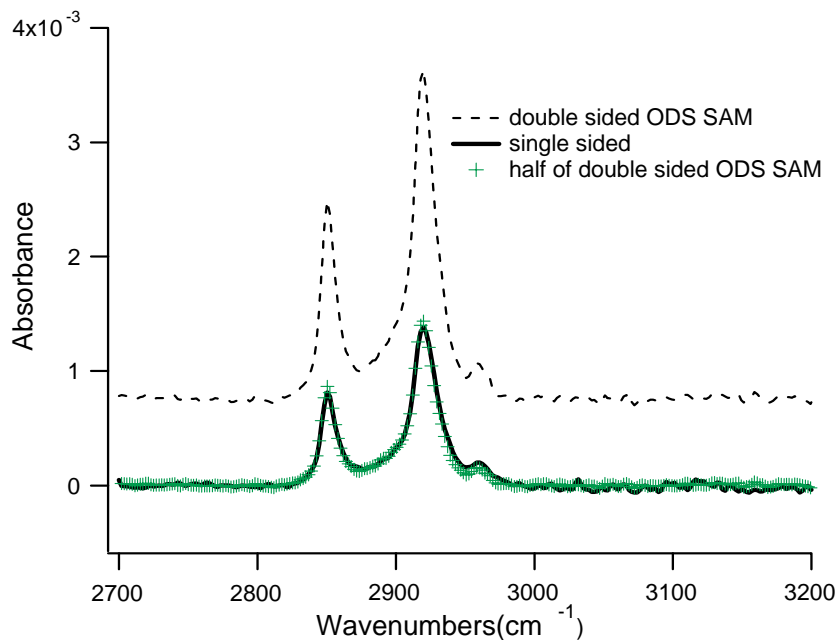


Figure 2-5 FT-IR spectra of double sided ODS sample and single sided ODS sample on glass.

The degradation kinetics on the two sides of the sample is not uniform as indicated in Figure 2-3. The two sides, with different kinetics, contribute to the transmission FT-IR spectra, making the results difficult to interpret. In order to isolate the kinetics of the side that faces the UV light using FT-IR, we employed a different irradiation configuration. We exposed only one side of the ODS glass slide to UV for a desired period of time using irradiation configuration 2 in Figure 2-2 and then exposed the other side to UV, which was originally outside the chamber for the same period of time. Since the glass substrate blocks the UV light below 300 nm (Figure 2-3), responsible for monolayer photoreactivity, both sides received the same amount of irradiation and hence degradation. This method allows us to study the kinetics of the SAM degradation directly exposed to UV. Extended UV irradiation (>2 hr) of one side of a sample resulted in the decrease in FT-IR intensity to almost precisely half the initial IR intensity (Figure

2-5). This indicates that the side that was exposed to UV was completely degraded while the other side of the slide was still covered with a full monolayer ODS. Having the assurance that the SAM outside the UV chamber was not degraded during irradiation, the FTIR spectra of the monolayer on glass were recorded following UV degradation on each side for identical amount of time.

2.3.2.2. *Degradation kinetics.*

The FT-IR spectra in the CH stretch region of the ODS SAMs as a function of irradiation time on glass are shown in Figure 2-6. $\nu_{\text{as}}\text{CH}_3$ (CH_3 asymmetric stretch mode near 2960 cm^{-1}), $\nu_{\text{as}}\text{CH}_2$ (CH_2 antisymmetric stretch mode near 2920 cm^{-1}) and $\nu_{\text{s}}\text{CH}_2$ (CH_2 symmetric stretch near 2850 cm^{-1}) modes were resolved. The spectra were in good agreement to those reported for compact monolayers in the literature [36, 37]. To perform a more quantitative analysis, we deconvoluted the spectra to calculate the integrated absorbance of $\nu_{\text{as}}\text{CH}_2$ and $\nu_{\text{s}}\text{CH}_2$. 80% reduction of the $\nu_{\text{as}}\text{CH}_2$ and $\nu_{\text{s}}\text{CH}_2$ band is observed in Figure 2-7 after 1 hour of UV irradiation in air. The reduction in absorbance suggests conversion of CH_2 groups to other functional groups as well as loss of carbon from the surface. In sharp contrast to the reaction between organic thin films and atomic oxygen under vacuum[19], which displayed first order kinetics, the decay rate of the $\nu_{\text{s}}\text{CH}_2$ $\nu_{\text{as}}\text{CH}_2$ mode absorbance did not decrease significantly as the UV degradation proceeds until . Instead, the reaction displays roughly zeroth-order kinetics until most of the CH groups are depleted, indicating that the reaction rate does not depend on the concentration of CH_2 groups. This result also stands in contrast with previous studies of ambient UV degradation alkanethiol monolayers, which display a decrease in

the CH₂ decay rate as the oxidation proceeds [31]. Further discussion on the degradation kinetics can be found in 2.4.4.2.

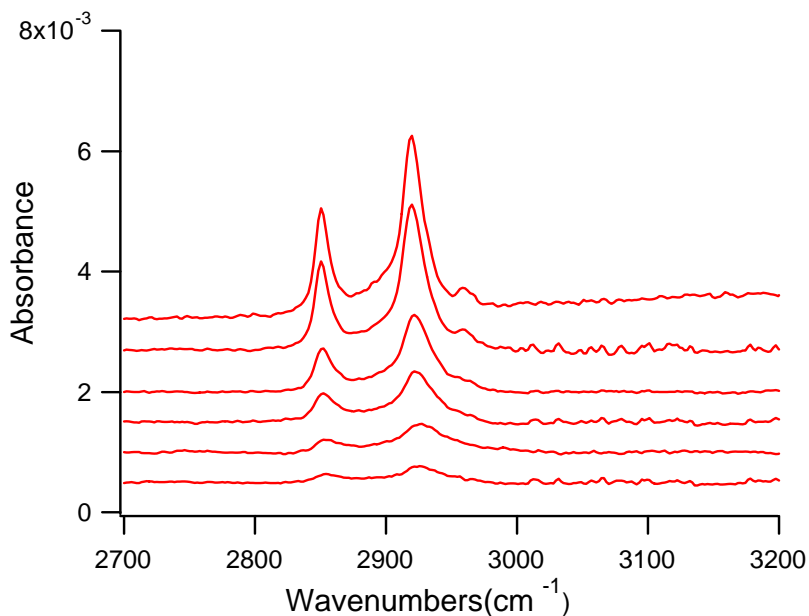


Figure 2-6 FT-IR spectra of ODS SAMs on glass irradiated for different amount of time, 0, 5 min, 20 min, 30 min, 45 min to 60 min in descending order. Spectra are offset for clarity.

2.3.2.3. Compactness of irradiated SAMs.

The peak frequencies of the CH stretch modes are sensitive to the local chemical environment [37]. The CH₂ peak frequency is considered to be a measure of degree of ordering in SAMs [37]. The ν_{as} CH₂ peak frequency is at 2927 cm⁻¹ for liquid OTS and 2917 cm⁻¹ for solid OTS [37]. At full monolayer coverage, the monolayer has to adopt an ordered configuration to accommodate the maximum number of molecules. The peak frequency of the SAMs we used is 2920 cm⁻¹, indicating that the film is largely compact but contains slight amount of disordering. Our results suggested that the molecules became more disordered as degradation proceeds as indicated by the blue shift of the CH

stretch modes (Figure 2-8). After 45 min of reaction the peak frequency was at 2926 cm^{-1} , close to that in liquid phases.

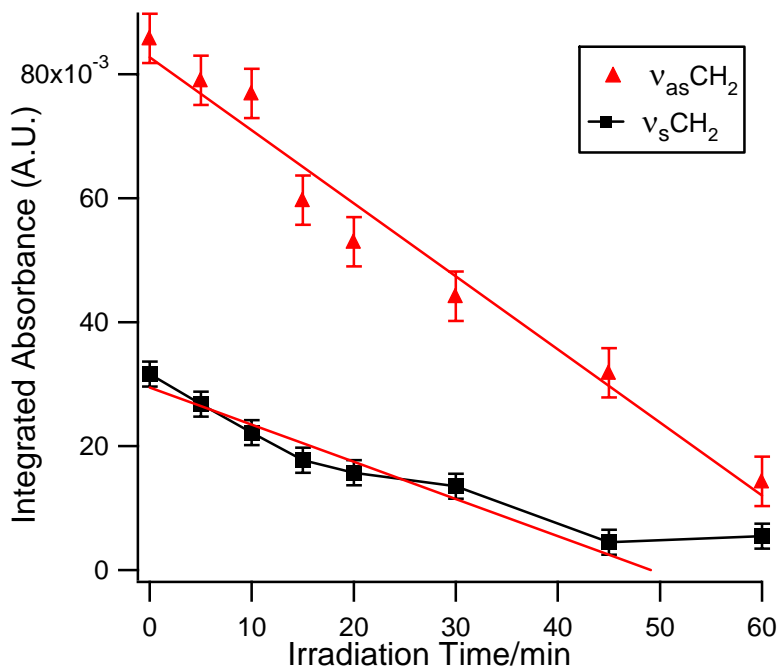


Figure 2-7 Integrated absorbance of $\nu_{as}CH_2$ and ν_sCH_2 vs UV irradiation time (min).

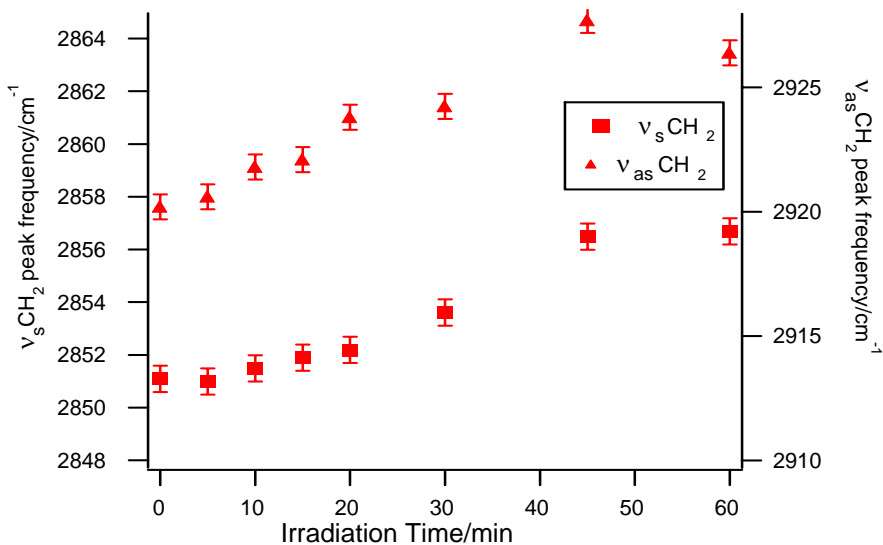


Figure 2-8 $\nu_{as}CH_2$ and ν_sCH_2 peak frequencies of ODS SAMs as a function of UV irradiation time.

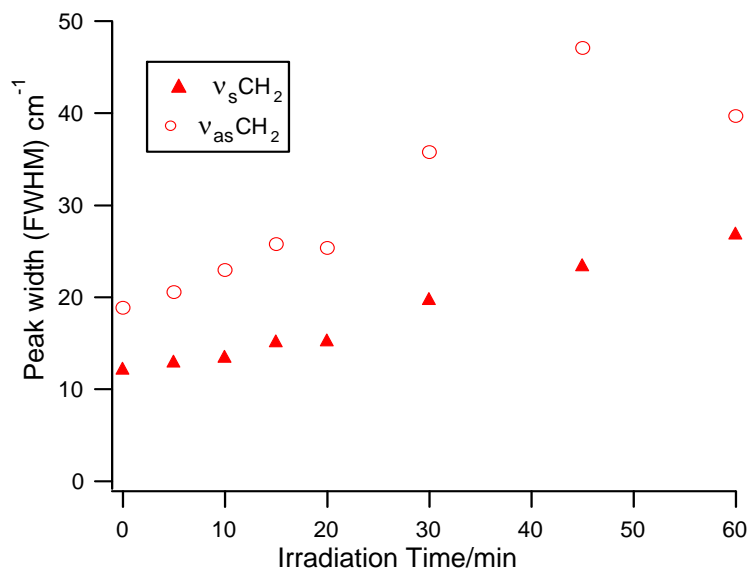


Figure 2-9 $\nu_{as}\text{CH}_2$ and $\nu_s\text{CH}_2$ peak width (full width at half maximum) of ODS SAMs as a function of UV irradiation time.

2.3.2.4. Effect of rinsing

Rinsing the irradiated SAMs in solvent does not change the FT-IR spectra significantly (Figure 2-10). The robustness of SAMs against rinsing indicates that all remaining CH chains in irradiated SAMs are firmly attached to the surface. It also suggests that the photo cleaved species are volatile and therefore removed during the irradiation (prior to rinsing). In contrast, dramatic differences in the CH stretch mode intensity are often observed on irradiated alkanethiol SAM samples before and after rinsing [3]. In the photooxidation of alkanethiol SAMs, the thiolate headgroups react to weaken the bonds to the substrate, forming weakly bonded long alkyl chains that do not evaporate easily and can only be rinsed off with solvent. This suggests lack of reactivity in the siloxane headgroups of the ODS monolayers.

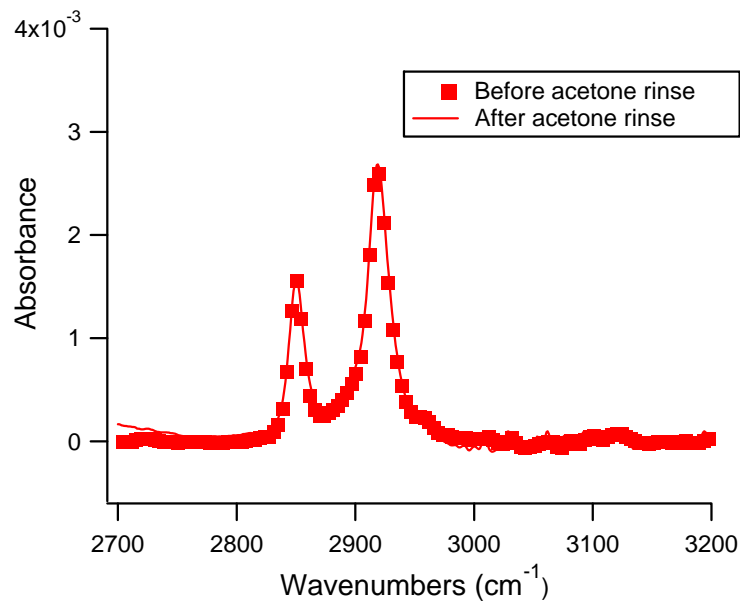


Figure 2-10 Effect of acetone rinsing on a SAM exposed to 15 min of UV irradiation.

2.3.2.5. Effect of humidity.

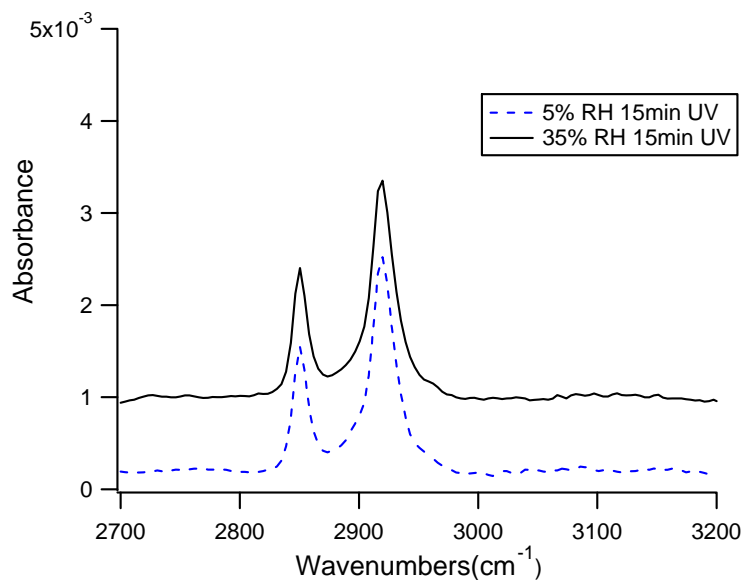


Figure 2-11 FT-IR spectra of ODS monolayers on glass irradiated with UV for 15 min under 35% and 5% relative humidity.

To understand the role of water in the system, the UV ozone chamber was placed in a glove bag continuously purged with dry air to reduce the humidity to 5%. Remarkably, the FT-IR spectrum was similar to the spectrum of monolayer irradiated under 35%

ambient humidity (Figure 2-11). The integrated absorbance in the CH₂ asymmetric mode was 0.065 in both cases. This suggests that the changes in concentrations of water vapor and presumably OH radicals do not alter the reaction kinetics. Further discussion on the role of humidity can be found in 2.4.2.

2.3.2.6. *Detection of other functional groups.*

So far we have focused on CH stretch region (2800-3000 cm⁻¹), in principle, FT-IR should be capable of detecting the resulting hydrophilic functional groups formed on the SAM surface as well. Carbonyls such as ketones, aldehydes and carboxylic acids have absorbance near 1700 cm⁻¹. However, the FTIR spectra were inconclusive as to their presence. No peaks can be clearly assigned to carbonyls (Figure 2-12). Difficulties associated with the detection of carbonyl groups include: 1. A gas phase IR water adsorption band near 1700 cm⁻¹ overlaps with the carbonyl stretch modes. It is difficult to completely subtract out the background due to the presence of water vapor even with good purging in FT-IR spectrometers [38]. 2. The signal level from submonolayer species is very small. Assume that the minimum detectable carbonyl signal in an IR experiment is 0.1 mOD. A typical IR cross-section for an C=O is 8.4×10^{-19} cm², calculated from IR data for acetone [39]. Using these two pieces of information we can calculate that there would have to be 2.7×10^{14} cm⁻² carbonyl groups at the surface to achieve this magnitude of signal². A full compact OTS monolayer corresponds to approximately 4.2×10^{14} molecules cm⁻². The surface coverage of carbonyls must be greater than 65% to achieve a detectable signal level by FT-IR. This suggests that the

² The surface concentration c is calculated by $c = 2.303A/\sigma$, where σ is the absorption cross section and A is the absorbance.

surface concentration of carbonyls is less than monolayer coverage and other more sensitive tools are necessary to detect the surface functionalities.

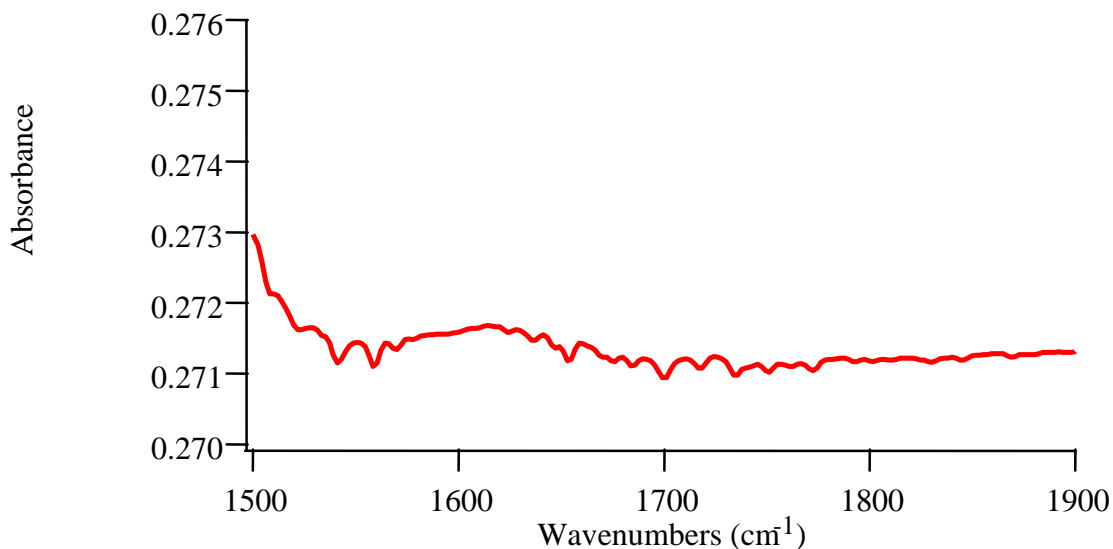


Figure 2-12 FTIR spectrum of ODS SAM irradiated for 30 minutes in the carbonyl stretch region. Substrate SiO₂/Si.

2.3.3. AFM results.

To probe the details of alkylsiloxane surface photoreactivity, the evolution of the SAM morphology was investigated by AFM. The unirradiated surface with ODS monolayer was flat with RMS roughness less than 0.3 nm on an oxidized Si substrate. We found that there was no evidence that pinholes had been created during after various periods of irradiation up to 30 min. This suggests that the degradation doesn't proceed via the development of defects. Indeed it was difficult to detect any changes in the samples on the sole basis of AFM images of full monolayers.

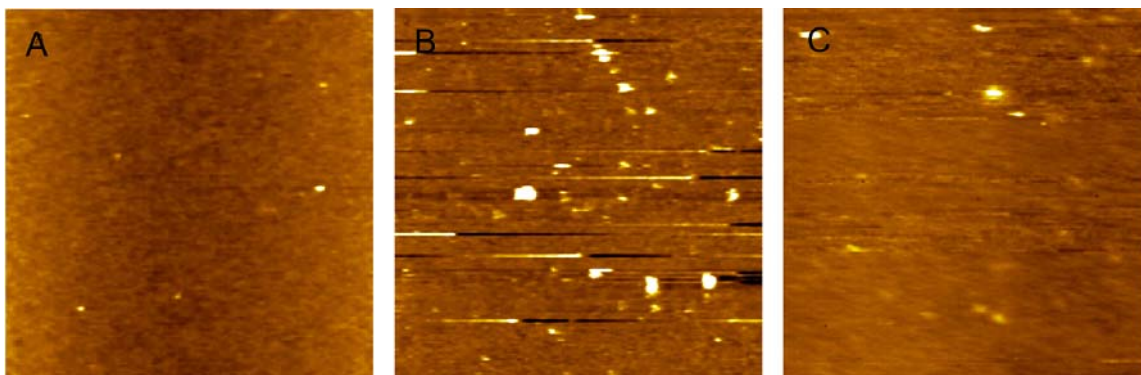


Figure 2-13 Contact mode AFM images of ODS on SiO₂/Si irradiated (from left to right) for a: 0 min, b: 15 min and c: 30 min. Height scale 2 nm.

In another experiment, ODS samples with sub-monolayer coverage were investigated with AFM. It was convenient to study flat substrates partially covered with high density SAM islands [40]. This made morphological changes easier to follow as well as facilitating accurate repositioning of samples after ex-situ irradiation. This type of sample was successfully prepared by reducing the immersion time to about 30 sec and lowering the reaction temperature to 10°C. Images of a sub-monolayer coverage ODS sample are shown in Figure 2-14. The ODS molecules aggregated into flower-shaped islands that were 1.5-2 nm high. A higher resolution image showed that the islands were porous. It had been proposed that under certain conditions OTS molecules cross-linked to form small patches in bulk solution [41]. Subsequently the patches aggregate on the surface to form islands. There is space between the patches that cannot be filled other monomers or patches in a short period. Therefore lots of open space appeared on the surface.

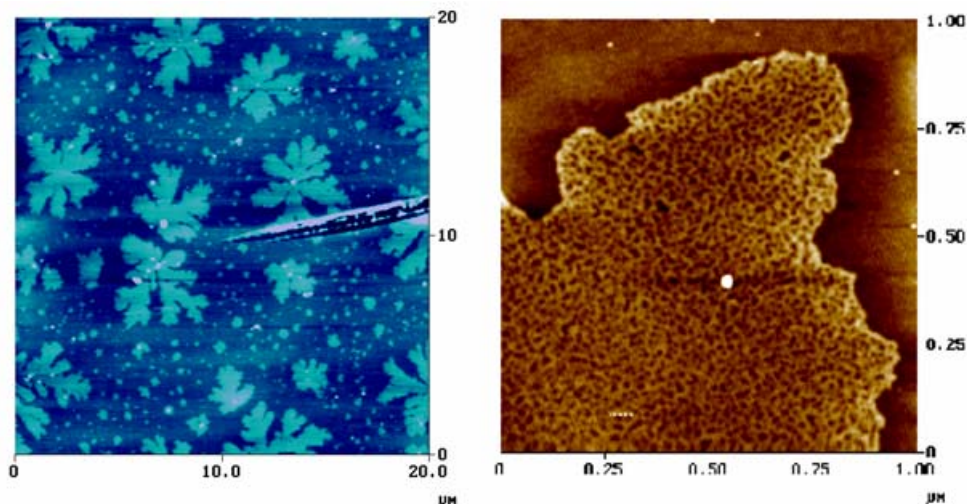


Figure 2-14 Tapping mode AFM images of a submonolayer ODS SAM on SiO₂/Si.

The surface covered with submonolayer islands was imaged with tapping mode AFM before UV irradiation (Contact mode AFM is not suitable for the surface with high frictional contrast. We observed significant frictional cross-talk on the surface especially on the irradiated surface. See Appendix A for more details.). Tapping mode was found to be effective in eliminating the frictional cross-talk and allowed us to obtain reliable topographic information on the surface. After irradiation, AFM images were acquired at the identical region. A uniform reduction in the height of monolayer ODS islands from 1.7 ± 0.2 nm to 0.8 ± 0.2 nm occurred after 15 minutes of UV/ozone exposure. Figure 2-16 shows that after 60 min of irradiation, the ODS islands disappeared almost completely, the residual island height is about 0.2 ± 0.2 nm. The island height of the ODS monolayer dropped to $45 \pm 17\%$ of original value after 15 min of irradiation and to $10 \pm 10\%$ of original value after 1 hr of irradiation. This qualitatively agrees with the integrated $\nu_{\text{as}}\text{CH}_2$ absorbance in FT-IR which are $69 \pm 6\%$ of original value after 15 min of irradiation and $20 \pm 6\%$ after 1 hour of irradiation. The drop of the absorbance in FT-IR

may be explained by the conversion of C-H to other groups such as C-OH as in the atomic oxygen degradation of ODS monolayer [19]. However, the reduction of the island height measured by AFM suggests that chain scission indeed occurred during the degradation process.

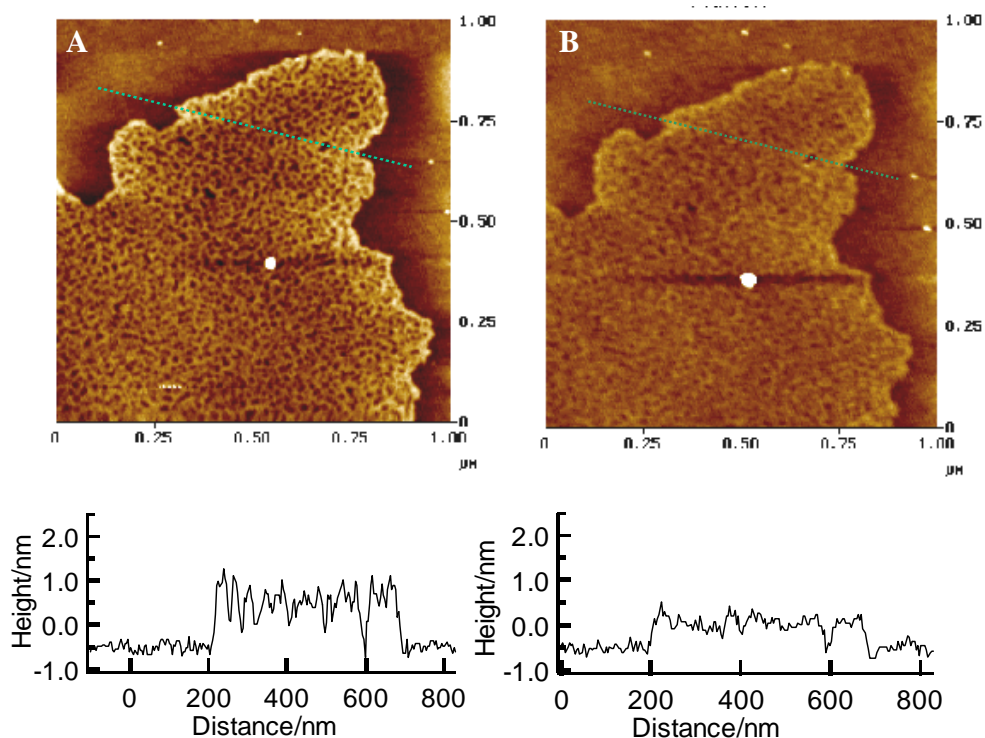


Figure 2-15 Tapping mode AFM images and cross sections of ODS SAM on SiO_2/Si surface. (A) No UV irradiation. SAM height=1.7 nm (B) 15 min UV irradiation. SAM height=0.8 nm

Interestingly, our AFM results in Figure 2-15 indicate that defect sites do not appear to nucleate the degradation of ODS SAM. The cross sectional AFM segment shows that the pinholes in the SAM did not widen during irradiation within the limit of AFM resolution (10 nm). They do not appear to be sites of enhanced reactivity. There is little evidence that the holes grew within the islands. Furthermore, the shape of the islands remained remarkably uniform, suggesting that the island perimeter does not display enhanced reactivity. The AFM results provide direct evidence that the domain boundaries between

the ODS covered and bare substrate do not play a significant role in the degradation process. On the contrary, we see a uniform reduction in the height of monolayer ODS islands.

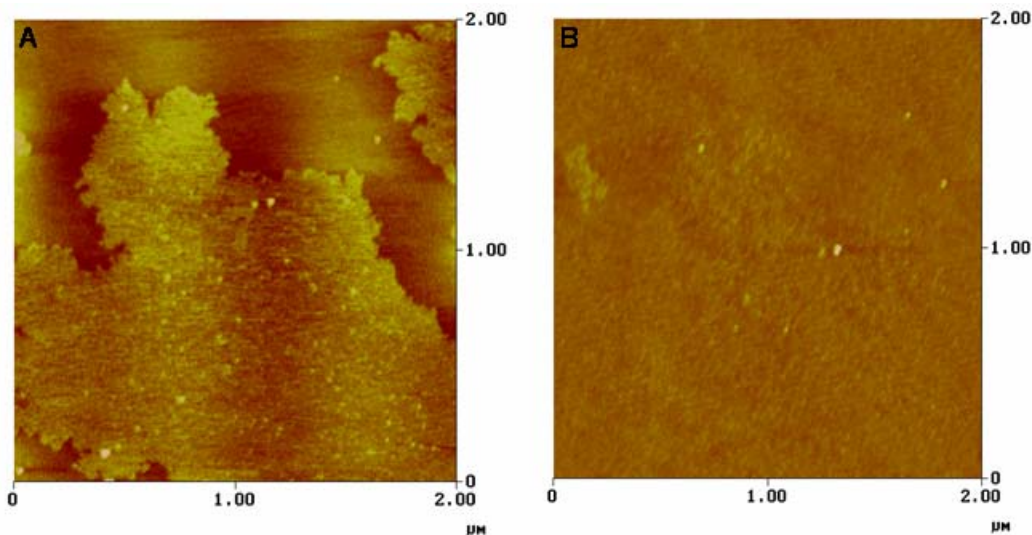


Figure 2-16 Tapping mode AFM images of ODS on SiO₂/Si at an identical location (A) without UV irradiation (B) 60 min UV.

2.3.4. XPS results.

To determine the chemical nature of irradiated SAMs, XPS spectra were collected on ODS SAMs with and without UV irradiation. After 15 min of irradiation, the C(1s) intensity was reduced by 12±4%. FT-IR suggests that 31±6% of CH₂ groups were lost after 15 min of irradiation. It should be noted that due to the attenuation in photoelectrons, the photoelectron intensity is a sublinear function of the carbon content, i.e., the percentage reduction in the surface concentration of carbon should be higher than 12%. The photoelectrons from thicker the films experience greater attenuation [42]. The attenuation of photoelectrons from atoms covered by a film with a thickness x , can be described by the following equation [42].

$$i = i_0 e^{-x / \lambda \sin \theta} \quad \text{Equation 2-1}$$

where i is the intensity after attenuation per unit depth, i_0 correspond to the unattenuated intensity, λ is the attenuation length of photoelectrons, and θ is the take off angle with respect to the surface.

For a uniform organic film consisting of n alkyl chains with thickness d , the total photoelectron intensity of the film can be obtained by integrating the intensity at different depths x (distance from the vacuum air interface) [42].

$$C = \int_0^d i_0 e^{-x / \lambda \sin \theta} dx = i_0 \lambda \sin \theta (1 - e^{-d / \lambda \sin \theta}) = C_\infty (1 - e^{-d / \lambda \sin \theta}) \quad \text{Equation 2-2}$$

where C_∞ corresponds to the intensity of an organic film with infinite thickness.

We assumes that the thickness of the hydrocarbon layer of the unirradiated ODS SAM to be 25 Å and the λ of C(1s) photoelectron to be 32 Å [42] and θ is 60°. According to Equation 2-2, a decrease of total intensity of 12±4% after UV irradiation corresponds to a reduction of the layer thickness by 18±5%. It should be mentioned that there is significantly uncertainty of the λ of C(1s) photoelectrons in hydrocarbon films [42, 43]. Therefore, we are unable to conclude whether the difference of loss of carbon measured by XPS and the loss of methylene groups measured by FT-IR is significant.

Part of the difference between XPS and FTIR results may be accounted for by the appearance of several % coverage of various oxygen containing groups (CO₂H, COH and

CO). There were some indications of shoulder peaks at C-O (286.5 eV) and C=O (290 eV). However, the peaks were too low for quantitative measurement. The upper limit of oxygenated carbon is estimated to be 8 % by integrating the fitting residue of a Voigt function centered at 285 eV. In addition, as the SAM degrades, it may be less resistant to contamination. Therefore, we cannot exclude the possibility that the adsorption of hydrocarbon contamination from the ambient during the time window after UV irradiation and before loading the sample to the XPS chamber³. (Our fluorescence labeling of surface groups indicated that small amount of alcohol and carbonyl groups (on the order of a few percent of monolayer coverage) are present on the surface [44].) Overall, our results suggest that the oxygenated content is small. In contrast, Paz. et al. found a pronounced shoulder peak in the C(1s) region after treating ODS SAMs with O(³P), suggesting more than 20% of the carbon is converted to oxygen when similar total amount of carbon is lost [19]. Similarly the shoulder peaks for oxygenated carbon of ODS SAMs were significantly more pronounced under the X-ray or electron beam irradiation in vacuum or low pressure oxygen [5, 26]. It suggests that once formed, the oxygenated functional groups are more readily cleaved under the UV/oxygen environment. By comparison, due to the lack of ambient oxidants, the oxygenated functional groups may accumulate on the surface under low oxygen environments, such as in vacuum chambers [19].

³ To more unambiguously identify the surface functional groups, we used fluorescence labeling to identify functional groups chemically attached to SAMs. Physisorbed functional groups do not contribute to the fluorescence signal in this case.

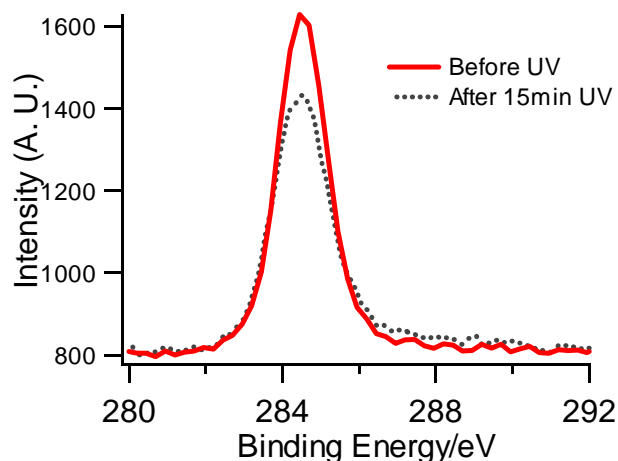


Figure 2-17 XPS spectra of ODS SAMs with no irradiation and after 15 min of UV irradiation. Substrate: SiO₂/Si.

2.3.5. Fluorescence labeling of surface species (FLOSS).

Though we suspected the presence of oxygen containing functionality in UV irradiated siloxane SAMs, these could not be detected with FTIR or XPS. UV/ O₃ irradiation may produce surface densities of the OH, CHO and COOH functional groups in the range of 0.01 ML, (ML is defined as the maximum surface concentration of packed alkyl chains, $4.2 \times 10^{14} \text{ cm}^{-2}$ [45]). The sensitivity of IR and XPS was insufficient to detect such low concentration species. In the area of biological [46-50] and polymer chemistry [51-54] fluorescent labeling has long been used to both qualitatively and quantitatively monitor functionality. Fluorescent probes have also been used study the structure and reactivity of self-assembled monolayers (SAMs) [55-58]. A question is whether the inherent sensitivity of fluorescence can be exploited to identify and quantify low concentration surface functionalities.

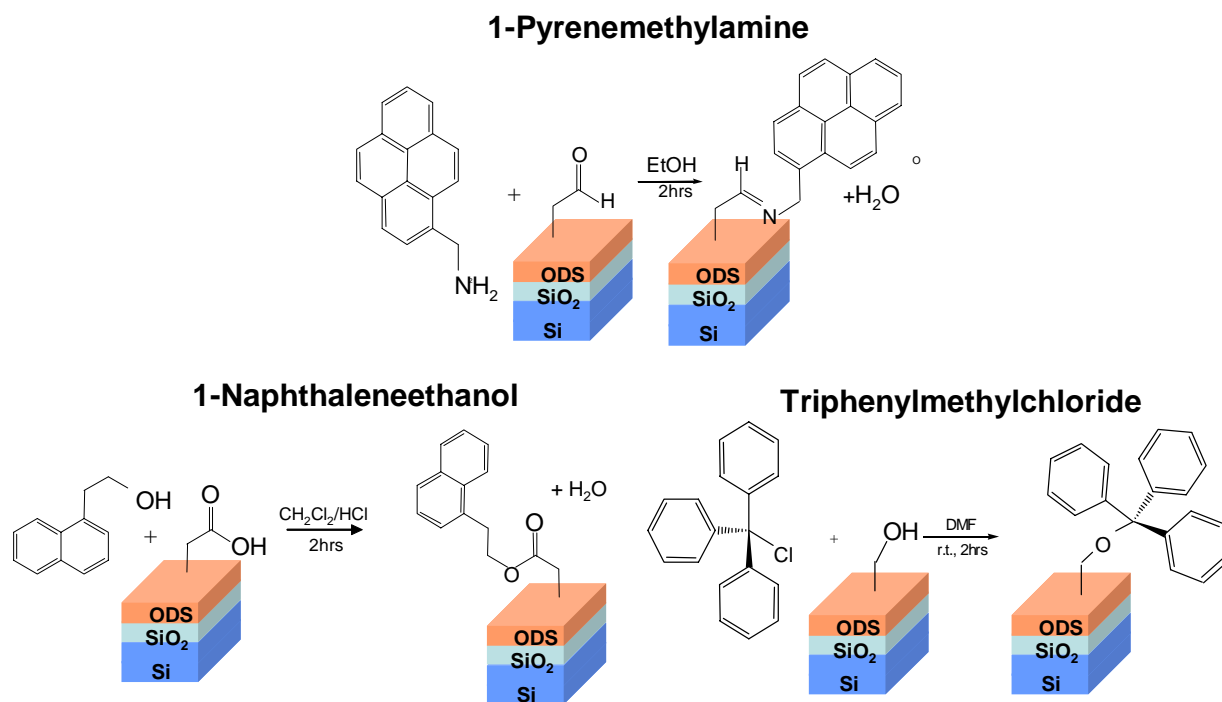


Figure 2-18 Schematic of fluorescence labeling of CHO, COOH, and OH surface functional groups.

As shown in Figure 2-18, 1-pyrenemethylamine was selected to label aldehyde surface groups by formation of imine linkages. (Formation amide by a reaction between carboxylic acid and amine groups can not occur at room temperature. [59]) 2-naphthaleneethanol was used to label carboxylic acid surface groups by formation of esters. Triphenylmethylchloride was selected to identify surface OH groups. In all cases the fluorescence from irradiated monolayers, that presumably contained oxygen functionality, was more intense than from the unirradiated monolayer, which underwent the same labeling reactions. In all these cases, control experiments on unirradiated SAMs, exhibited only small residual non-specific adsorption.

The specificity of the detection is demonstrated explicitly in the case of the OH groups (Figure 2-19). The bare silicon control substrate displayed specific reactivity due to the existence of silanol groups, SiOH, present on the native silicon oxide [45]. The presence of OH groups on the UV irradiated SAM is also detected (Figure 2-19). In addition, the presence of CHO and CO₂H on UV irradiated SAMs was indicated by the covalent attachment of 1-pyrenemethylamine (Figure 2-20) and 2-naphthaleneethanol (Figure 2-21). Reinhoudt et al. found that the fluorescence from ~0.3 ML pyrene attached to a NH₂ terminated SAM is dominated by excimer emission around 480 nm [58]. While in Figure 2-20, the emission is dominated by monomer emission near 390 nm. This provides evidence that the surface coverage of the attached pyrene is less than 0.1 ML, and that there is no clustering of surface aldehyde groups. Due to the large distances between the covalent attached chromophores, little aggregation can occur.

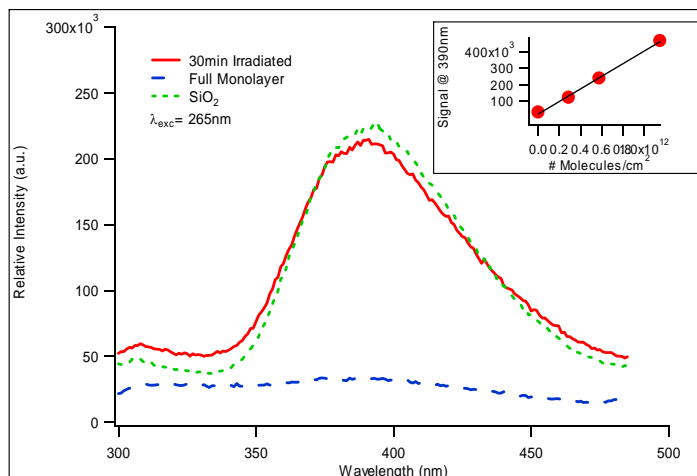


Figure 2-19 Detection of surface alcohol groups by covalent surface attachment of triphenylmethylchloride to a SAM surface irradiated for 30 minutes in UV/ O₃ as well as SiO₂ and unirradiated monolayer controls. Inset: calibration plot.

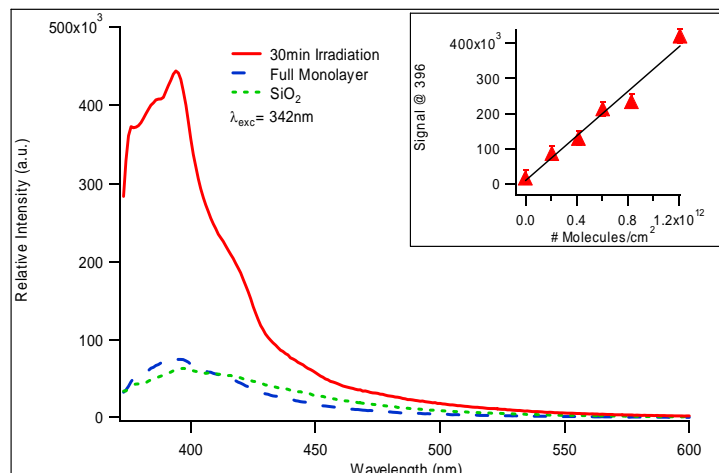


Figure 2-20 Detection of surface aldehyde groups by covalent surface attachment of 1-pyrenemethylamine to a SAM surface irradiated for 30 minutes in UV/ O₃ and controls. Inset: calibration plot.

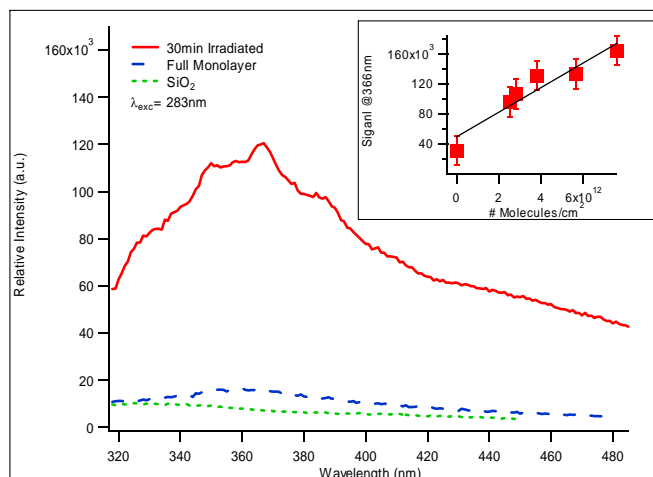


Figure 2-21 Detection of surface carboxylic acid groups by covalent surface attachment of 2-naphthaleneethanol to a SAM surface irradiated for 30 minutes in UV/ O₃ and controls. Inset: calibration plot.

To quantify the amount of chemisorbed chromophores corresponding to OH, CHO and COOH groups, calibration curves were obtained by measuring the peak fluorescence intensities for known amounts of chromophores deposited on an unirradiated SAM surface. Deposition of chromophores was achieved by uniformly spreading a predetermined volume of chromophore solution on the surface and letting the solvent

evaporate. By measuring the peak intensity of the surface labeled by the corresponding chromophores, the surface concentrations of the CHO, OH, and CO₂H were determined from the calibration plots (insets of Figure 2-19, Figure 2-20 and Figure 2-21)

To gain a better understanding of the UV photo-oxidation process and the evolution of surface groups, the surface concentrations of the CHO, OH, and CO₂H were determined as a function of UV irradiation in Figure 2-22. Up to 4.3% of the ML was functionalized by CO₂H groups and 0.5% by OH groups. CHO groups peaked at about 1.3% ML at 30 min, consistent with Figure 2-20 that little chromophore aggregation occurred. The CHO concentration dropped after 50min of UV. This trend is expected since the concentrations of the intermediates produced by the photooxidation of CH groups should also decrease as 80% of the hydrocarbon groups in the SAM are depleted after 50min UV.

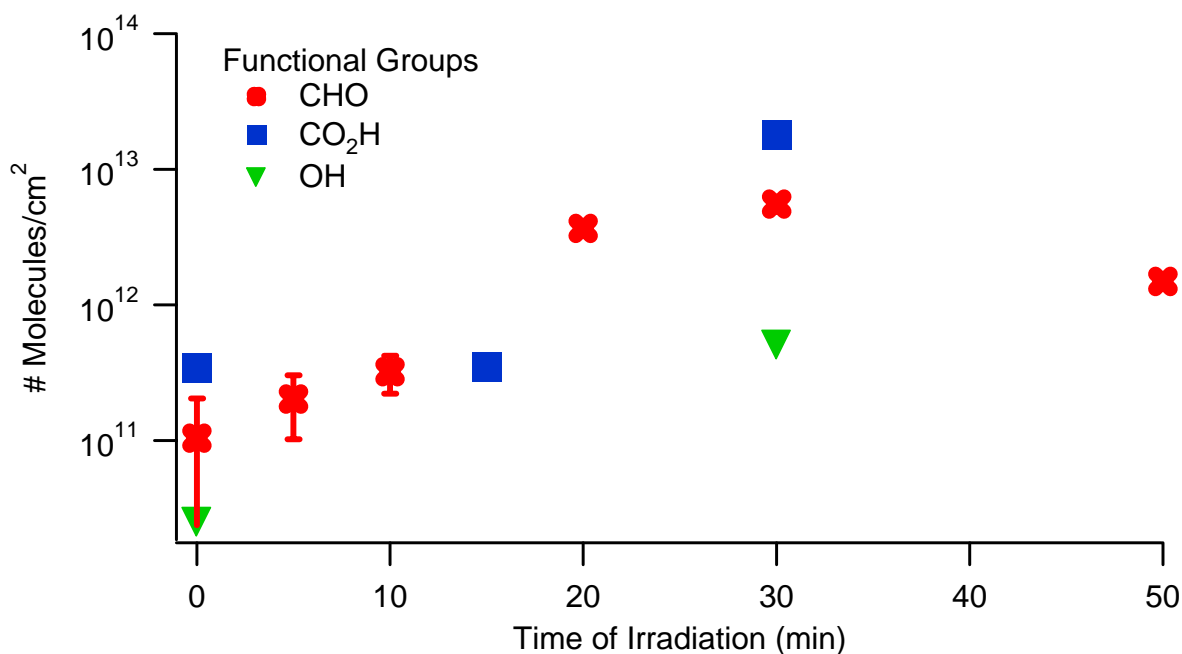


Figure 2-22 Surface concentration of oxygen containing functionality (\blacktriangledown OH, \blacksquare CO₂H, \times CHO) at the SAM surface as a function of UV irradiation time.

It should be noted that FLOSS detects the functional groups on the top of SAMs. Functional groups buried deep in the monolayer may not be accessible to chromophores. In addition, the chromophores used are large enough to occupy 3-4 surface sites of close packed alkyl chains. This approach is not suitable for measuring high concentration surface species (>0.1 ML). If the surface functional groups are closely packed, the chromophores may not be able to attach to all the closely packed surface groups [58]. In addition chromophore aggregation and fluorescence quenching at high concentrations makes quantification complicated [58]. Therefore, the concentration of functional groups may be underestimated.

By adding a long alkyl chain linker between the functional group and the chromophore, one may be able to label groups deeper in the monolayer. In addition, the esterification reaction to label COOH groups may not be very efficient. A more efficient approach to label COOH groups is amide formation, which requires converting the COOH groups to acid chloride or anhydride, then reacting with amine linked chromophores [58]. These questions will need to be addressed to achieve more reliable surface concentrations with FLOSS.

On the other hand, this steric limitation can potentially be an advantage of FLOSS, since one may use chromophores with different geometries to access information about lateral and vertical spatial distributions of functional groups (e.g., phase segregation [38]), which is difficult to achieve with XPS or SIMS.

2.4. Discussion.

2.4.1. Summary of results.

- UV degradation requires the combination of UV and oxygen. Ozone alone does not degrade alkylsiloxane SAMs.
- Contact angle results suggest that the SAMs become increasingly more hydrophilic. However, water does not completely wet the surface even after several monolayers of CH₂ groups are removed. This suggests that the coexistence of hydrophilic and hydrophobic groups on the top of irradiated SAMs.
- FT-IR results show decrease of CH groups, consistent with AFM and contact angle results. The kinetics is complicated. It is more consistent with zeroth order kinetics than first order kinetics. The less compact monolayer showed blue shift (gauche defects) as degradation proceeds.
- XPS results showed a loss of carbon. However, the concentration of oxygenated carbon is too low to unambiguously identify.
- FLOSS was able to identify and quantify small amount of functional groups formed during the UV irradiation. We estimate that the surface coverage of OH COOH and CHO groups is at most a few percent of a monolayer.

2.4.2. Active agents.

Our results clearly showed that UV alone does not degrade ODS SAMs. Photolysis of saturated SAMs requires $\sigma\text{-}\sigma^*$ transition induced by absorption of photons in the vacuum UV range (<160 nm). Since our UV source (mainly 254 nm and small amount of 183 nm) falls short of the required range, the UV light cannot dissociate the saturated hydrocarbon chains directly. This explains the lack of reactivity when the UV chamber is purged with inert gas. The requirement of the combination of UV and oxygen suggests that UV generated reactive species, such as OH or O, are responsible for the degradation.

The photochemistry of O₃, O and OH are well known [28]. Under UV irradiation in ambient, ozone is produced in reactions illustrated in R 2-6 and R 2-8. Singlet atomic oxygen O(¹D) is produced by photolysis of ozone. OH is mainly produced by the reaction between O(¹D) and H₂O (R 2-9). Most of the O(¹D) is rapidly quenched by collision with inert molecules (M) such as N₂ R 2-7 [60]. In the ambient environment, the concentration of N₂ 1.9×10^{19} molecule/cm³ reduces the lifetime of O(¹D) to ~1ns (R 2-7). Only a small fraction (~1%) of O(¹D) is able to form OH under ambient (R 2-9). The production rate of OH is proportional to the humidity. The insensitivity of ODS degradation kinetics to humidity (from 5% to 35%) is surprising because OH is widely recognized as the major oxidant of hydrocarbons in the atmosphere [17]. It may suggest that under our conditions, due to higher concentrations or rate constants, other reactive species such as atomic oxygen play dominant roles in hydrogen abstraction and the contribution from OH is negligible. Further investigations, such as quantitative measurements of the OH concentration, are necessary to clarify the role of OH radicals.

Table 2-2 Reactions to generate atmospheric oxidants [34].

$O_2 + hv(185 \text{ nm}) \rightarrow 2 O$		R 2-6
$O_3 + hv(254 \text{ nm}) \rightarrow O_2 + O(^1D)$	k_1	R 2-7
$O(^1D) + M \rightarrow O(^3P) + M$	$k_2 = 5 \times 10^{-11} \text{ cm}^3 \text{ molecule}^{-1} \text{ s}^{-1}$	R 2-8
$O(^1D) + H_2O \rightarrow 2HO\bullet$	$k_3 = 2.2 \times 10^{-10} \text{ cm}^3 \text{ molecule}^{-1} \text{ s}^{-1}$	R 2-9
$O(^3P) + O_2 + M \rightarrow O_3 + M$	$k_4 = 2 \times 10^{-33} \text{ cm}^6 \text{ molecule}^{-2} \text{ s}^{-2}$	R 2-10

From the preceding discussion, atomic oxygen is a plausible oxidant in ambient UV oxidation of ODS SAMs. More insights on the role of atomic oxygen can be gained if the concentration of atomic oxygen can be estimated. The production rate of atomic oxygen is shown in R 2-7, where I_0 is the UV light intensity, σ is the absorption cross section $1150 \times 10^{-20} \text{ cm}^2$ [34] and $h\nu$ is the photon energy at 254 nm. k_1 is calculated to be $3.2 \times 10^{-2} \text{ s}^{-1}$.

$$\frac{d[O_3]}{dt} = \frac{I_0 \sigma}{h\nu} [O_3] = k_1 [O_3] \quad \text{Equation 2-3}$$

$$k_1 [O_3] = k_4 [O_2] [M] [O(^3P)] \quad \text{Equation 2-4}$$

R 2-7 and R 2-10 dominate the equilibrium between ozone and $O(^3P)$ [28]. Under a steady-state condition,

$$[O(^3P)]/[O_3] = \frac{k_1}{k_4 [O_2] [M]} = 1.3 \times 10^{-7} \quad \text{Equation 2-5}$$

The ozone concentration in the UV chamber is 100ppm (2.4×10^{15} molecule/cm³), [O(³P)] is estimated to be 3.2×10^8 molecule/cm³.

The flux[61] of O(³P) is

$$f_{O(3P)} = [O(^3P)] \times \left(\frac{k_B T}{2\pi m} \right)^{\frac{1}{2}} \quad \text{Equation 2-6}$$

where k_B is the Boltzmann constant and T is the temperature (300K) and m is the mass of atomic oxygen. The flux of O(³P) is calculated to be 5.2×10^{12} molecule cm⁻² s⁻¹. Similarly, the flux of O(¹D) is calculated to be 9.8×10^8 molecule cm⁻² s⁻¹. Assuming the area of a hydrocarbon chain to be 0.225 nm² [37], the total surface concentration of hydrocarbon groups (CH₂ and CH₃) in a compact ODS SAM is equivalent to 7.6×10^{15} groups.cm⁻². The time to completely oxidize the ODS SAM is observed to be 4200 s. Therefore, the average reaction rate R_{CH} is 1.8×10^{12} molecule cm⁻² s⁻¹. The flux of O(¹D) is too low to account for the oxidation of ODS. However, the flux of O(³P), 5.2×10^{12} molecule cm⁻² s⁻¹ compares favorably to R_{CH} , considering the high reaction probability of hydrogen abstraction by O or OH on organic surfaces [15, 19].

2.4.3. Probable reaction pathways.

The hydrocarbon chains are gradually shortened during photooxidation. AFM and FT-IR results point to a microscopic reaction pathway that involves the reactivity of hydrocarbon chains instead of siloxane headgroups. We assume that the mechanism of UV degradation of alkyl chains in SAMs also involves hydrogen abstraction as it does in

gas phase [62]. It is to be noted that even in the gas phase, photooxidation of compounds as simple as butane can have extremely complex reaction pathways [16]. It is much more difficult to access information about the individual steps in the condensed phase such as SAMs. However, given the evidence of the role of atomic oxygen in the UV degradation of ODS SAMs and the detection of reaction intermediates such as alcohol, aldehyde, and carbonyl groups by FLOSS [44], we can propose probable reaction pathways. The first step probably involves hydrogen abstraction to form alkyl radicals (R 2-11). The alkyl radicals rapidly react with O₂ to form peroxide radicals (R 2-12). As illustrated in R 2-13 and R 2-14, the peroxide has a number of pathways to form alkoxy radicals, which can be oxidized to form carbonyls (R 2-15). The aldehyde groups can dissociate via photolysis (R 2-16) or further hydrogen abstraction at the α carbon (R 2-17 and R 2-18), finally resulting in loss of carbon. Hydrogen abstraction in the CHO group (R 2-19) results in the formation of peroxyacids (R 2-19), a precursor of carboxylic acids.

Table 2-3 Formation of alkoxy radical

$R-H + O \rightarrow R\bullet + HO\bullet$	R 2-11
$R\bullet + O_2 \rightarrow ROO\bullet$	R 2-12
$ROO\bullet + h\nu \rightarrow RO\bullet + O$	R 2-13
$ROO\bullet + HO\bullet \rightarrow RO\bullet + HOO\bullet$	R 2-14

Table 2-4 Further oxidation.

$R-CH_2O\bullet + O_2 \rightarrow RCHO + HOO\bullet$	R 2-15
$RCHO + h\nu \rightarrow R\bullet + CHO\bullet$	R 2-16



2.4.4. Reactive sites.

2.4.4.1. Headgroups vs. alkyl chains.

Our results stand in contrast to the degradation mode of alkanethiol SAMs, revealed by STM experiments which suggest the nucleation role of defects [2]. The contrasting roles of defects in alkanethiol/Au and alkylsiloxane/SiO₂ provide insight into the reactive site of the SAM degradation. The thiolate headgroups of alkanethiol SAMs are known to be reactive [4]. It is difficult for the reactive species to penetrate the densely packed alkyl chains of a full monolayer to reach the thiolate groups. The impinging reactive species can easily access the thiolate group from defect sites in the monolayer. By contrast, the siloxane headgroups in the ODS SAM do not appear to be the reactive site judging from the lack of growth of defect sites in the monolayer. Both AFM and FT-IR results point to a microscopic reaction pathway that involves the reactivity of hydrocarbon chains instead of headgroups. The hydrocarbon chains are gradually shortened during photooxidation. This also explains why morphological changes in full monolayers could not be observed. UV irradiation reduces the SAM thickness, but AFM can only detect this change if there are regions of bare substrate from which SAM height can be determined. Because of the lack of reactivity of the headgroups, the coverage of SAM domain remains unchanged

throughout the reaction, resulting in the constant decay rate of CH₂ groups deduced from FT-IR (Figure 2-7).

Our observation that the hydrocarbon chains are the reactive sites of in the photooxidation of alkylsiloxane SAMs, stands in contrast to the UV degradation of alkanethiol SAMs, in which the thiolate headgroups are reported to be the vulnerable groups. Unlike UV degradation of alkanethiol SAMs, ozone is not the reactive species in alkylsiloxane degradation. The difference can be explained by the different chemical reactivity of the two systems. The terminal thiolate group, with its lone pairs, can be oxidized without cleavage of other bonds. In fact, gas-phase oxidation of thiols with atomic oxygen showed nearly zero reaction activation barrier [63]. By contrast, in order to oxidize the valence saturated siloxane group, cleavage of the Si-C bond (bond energy $\approx 300\text{kJ/mol}$ [64]) is required. This renders the oxidation of the siloxane headgroup kinetically unfavorable.

2.4.4.2. *Preferential reactive sites in the CH chains.*

Having settled that the degradation of ODS proceeds via the photooxidation of alkyl chains instead of headgroups, and that the reaction is initiated by a series hydrogen abstraction reactions, we can focus on the molecular scale mechanism of alkyl chain oxidation. The pseudo zeroth-order CH₂ decay kinetics under ambient contrasts with the first order reaction between O(³P) and alkyl organic thin films under vacuum [19]. This suggests the role of dioxygen in the ambient and the role of structures of SAMs. The kinetics may be a consequence of a complex oxidation mechanism. However, a more straightforward interpretation is the constant effective surface concentration of CH₂ on

the surface as degradation proceeds. This requires that the monolayer degradation preferentially initiates from the top of a SAM, which is more accessible to reactive species. Paz et al. found that the reaction between O(³P) and hydrocarbon chains in SAMs is limited by the penetration of O(³P) [19]. The loss of CH₂ signal is mainly due to the loss of carbon, exposing the underlying groups for hydrogen abstraction. Although a group on the top of a chain is cleaved, the effective surface concentration of CH₂ remains the same as long as all the 17 carbon groups in a chain are not cleaved. In contrast, in the reaction between O(³P) and hydrocarbon chains, the oxygenated functional groups may accumulate on the surface under vacuum, blocking the access of reactive species to the underlying hydrocarbon groups[19].

$$R = \frac{d[\text{CH}_2]}{dt} = k[\text{CH}_2] \quad \text{Equation 2-7}$$

$$[\text{CH}_2] \equiv \text{ML} \quad \text{Equation 2-8}$$

From this pseudo-zeroth order kinetics (Equation 2-7 Equation 2-8), we can extract the nominal reaction rate constant of CH₂ groups by assuming the effective surface concentration to be a monolayer. From the slope in Figure 2-7, k_{CH₂} is calculated to be 4.1×10⁻³ s⁻¹.

More careful analysis of contact angle results affords additional information about the microscopic mechanism. The contact angle results indicate that the hydrophobic CH₃ and CH₂ groups (contact angle ~ 110°) are converted to hydrophilic groups such as CHO, OH and COOH (contact angle ~0°) during degradation. However, even after 30min of degradation, when half of the CH₂ groups are lost, the contact angle still has not dropped

to zero. This suggests that the surface is still not completely covered with hydrophilic groups. The contact angle of a composite surface mixed on molecular level is described by [65].

$$(1 + \cos \theta)^2 = f_1(1 + \cos \theta_1)^2 + f_2(1 + \cos \theta_2)^2 \quad \text{Equation 2-9}$$

where θ , θ_1 , and θ_2 are the contact angles on the composite surface, hydrophilic surface and hydrophobic surface respectively. f_1 is the fractional coverage of the hydrophilic groups and f_2 is the fractional coverage of the hydrophobic groups. Assuming θ_1 to be 0 and θ_2 to be 110 degrees, the fractional coverage of the hydrophilic groups can be calculated from the measured contact angle θ . It is to be noted that the fractional coverage does not necessarily correspond to the physical surface composition because it does not take into account the effect of surface reconstruction during wetting, as well as the degree of probe molecular penetration [65]. Nevertheless, this approach provides qualitative insights into the relative contribution of different surface groups to the overall wetting. According to FT-IR results in Figure 2-7, 25% of CH_2 groups are lost after 15min of UV irradiation, corresponding to more than 4 monolayers of CH_2 groups since each ODS molecule contains 17 CH_2 units. Yet the effective fractional coverage indicated by contact angle is only about 30% when more than 4 ML of CH_2 groups are lost. This suggests that the top of the reacted monolayer is not entirely covered with hydrophilic groups.

There are several possible explanations.

1. The oxygenated groups are buried in the monolayer therefore not accessible to the probe water molecules.
2. Even if all the top of the monolayer is completely converted to hydrophilic groups, the surface may be rough and the water used to measure the contact angle is in contact with the hydrophilic top as well as the hydrophobic side chains.
3. The reaction of the CH groups does not necessarily lead to conversion to hydrophilic groups. Some of the radicals may recombine, leading to cross-linking (R 2-2).

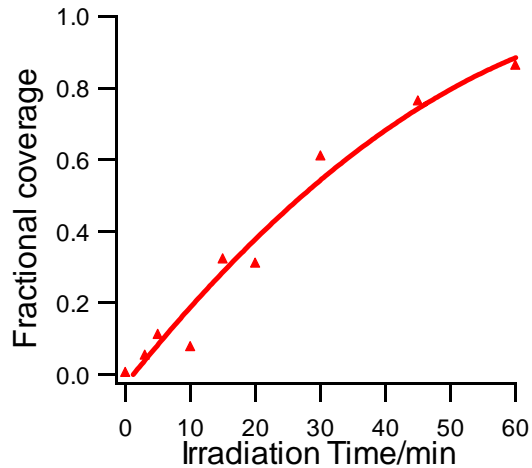


Figure 2-23 Estimated fractional coverage of hydrophilic groups as determined by contact angle results.

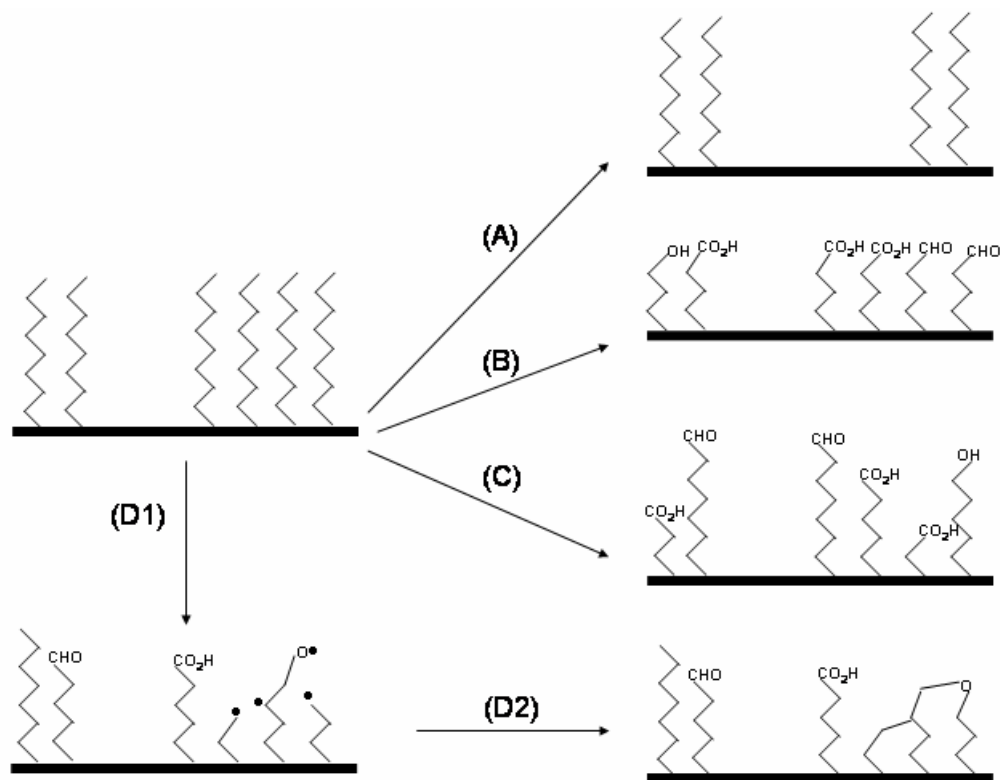


Figure 2-24 Possible microscopic mechanisms of alkylsiloxane degradation.

With the information we have about the reactive sites in the ODS SAMs, four possible mechanisms are listed (Figure 2-24).

Mechanism A: Chain scission occurs at the Si-C bond and reaction nucleates from the defect sites.

Mechanism B: The hydrocarbon chain scission occurs exclusively at the top of the monolayer and the degree of chain scission is uniform. Consequently, the top of the monolayer is uniformly terminated with hydrophilic groups.

Mechanism C: The reaction is restricted to the top of the hydrocarbon chains, loss of carbon occurs randomly.

Mechanism D: The chain scission is not limited to the top of the CH chains. Atomic oxygen and other reactive species may penetrate a few groups deep into the monolayer

and react with the side of the CH chains. Radicals resulted from hydrogen abstraction may recombine (cross-link).

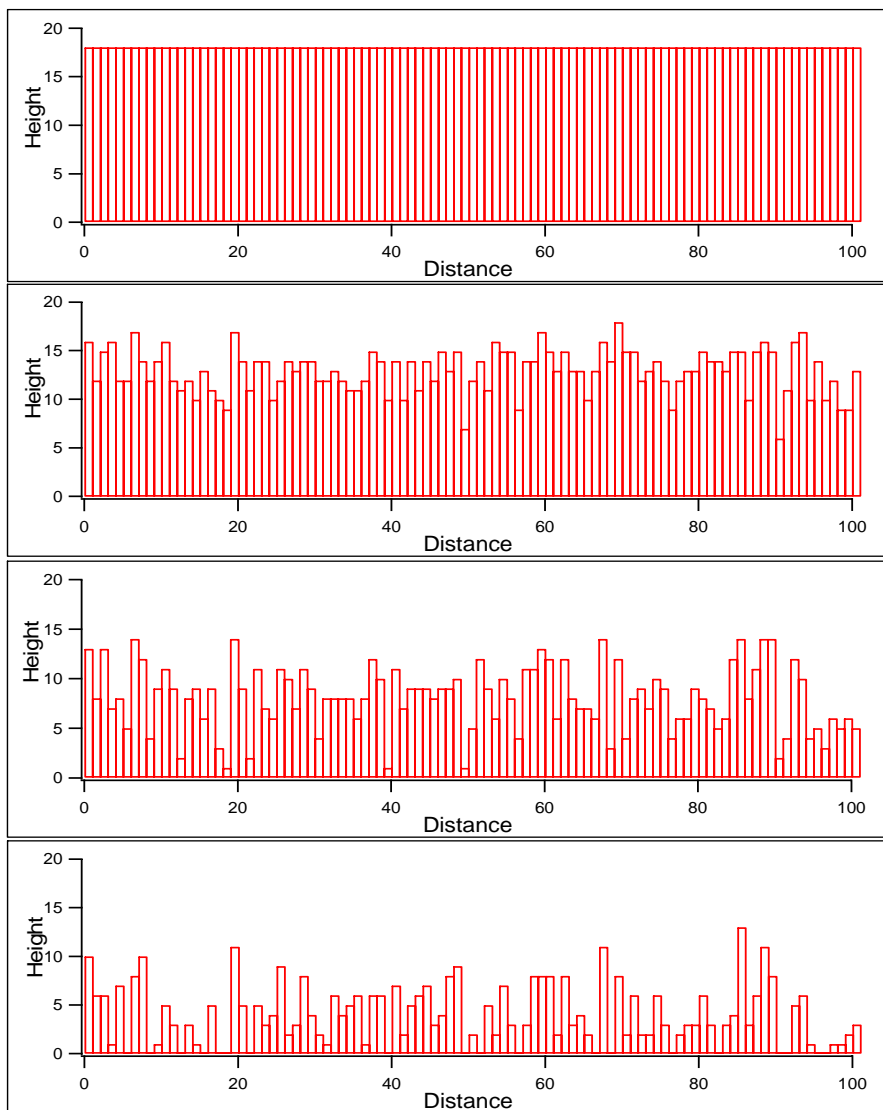


Figure 2-25 Simulated evolution (top to bottom) of a cross section of ODS SAM. Each bar represents an individual ODS chain. Height is in the unit of the height of a CH₂ group (~0.14 nm). Horizontal distance is in unit of the lateral spacing between chains (~0.5 nm).

Mechanism A can be easily excluded as discussed. Mechanism B is not consistent with the observation that the contact angle does not drop to zero even after several monolayers

of CH_2 is removed. If the top of the SAM is uniformly terminated with hydrophilic groups, the contact angle should be close to zero within 10 min.

To better understand the resultant nanometer scale morphology of Mechanism C, we carried out a computer simulation assuming that

1. Only the top of a CH chain can react.
2. The reaction result in the loss of one CH group (CH_2 or CH_3) each time.
3. The reaction on the top of CH chains occurs with equal probability (totally random) regardless of the local environment.

The simulated cross section is shown in Figure 2-25. It is apparent that such random chain scission introduced significantly roughness, i.e., different chains lose different number of CH groups.

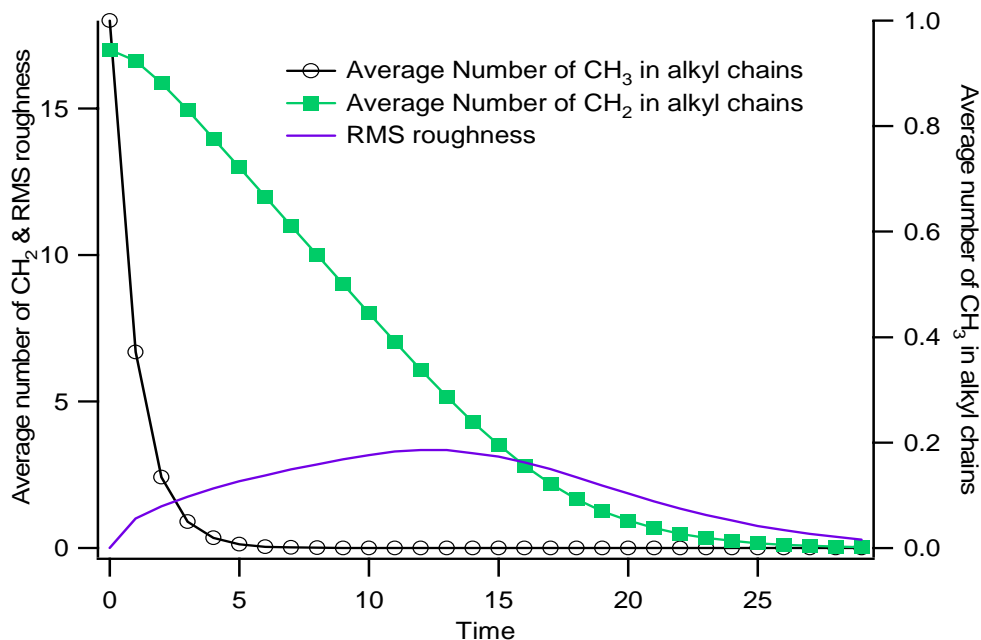


Figure 2-26 Evolution of simulated morphology assuming that chain scission is restricted to the top of chains. Each time increment represents the time it takes to react 1 ML of surface sites.

The average fractional coverage of hydrocarbons groups and the RMS roughness are shown in Figure 2-26. The decay rate of CH₂ group is mostly constant except the initial and final stage. The zeroth order kinetics is due to the constant effective surface concentration of CH₂ groups. When a CH₂ group is cleaved, the underlying CH₂ group is exposed. Therefore, the effective surface concentration remains the same. The initial slower rate is attributed to the presence of CH₃ groups, blocking the access of reactive species to the underlying CH₂ groups. The decreased rate at the later stage is due to the depletion of CH₂ groups. Once the all the CH₂ groups in a surface site are reacted, this site can no longer participate in the chain scission reaction. Hence the effect surface concentration of CH₂ groups decreases. The reaction kinetics from the simulation is consistent with the IR results in Figure 2-7 in reproducing the roughly constant decay rate of CH₂ stretch modes. However, due to the limited precision of the measured absorbance, it is difficult to conclude from the IR data whether the reaction rate is slower at the initial and the late stages the irradiation, as suggested by Mechanism C.

The RMS roughness can be as much as the height of 5 CH₂ groups (Figure 2-26). Although the non-uniform chain scission introduces microscopic scale roughness, the roughness is on nm scale and consequently can not be observed with the limited lateral resolution of AFM (10 nm). However, such microscopic scale roughness is consistent with the fact that the water contact angle does not drop to zero after 20min (Figure 2-3), when several monolayers of CH₂ groups are removed. During the contact angle measurement, water is in contact with morphologically and chemically heterogeneous surfaces. The hydrophilic top as well as the hydrophobic side of chains of the UV

irradiated SAMs are exposed to water during contact angle measurements. This roughness may also explain the blue shift in the CH stretch region in the IR spectrum of irradiation SAMs (Figure 2-8) and broadening of the peak widths (Figure 2-9). Due to the roughness on the surface, the top portion of CH chains has more free space, similar to a liquid environment. However, this mechanism does not explain the observation that the hydrophilic groups cover only a fraction of monolayer, as suggested by FLOSS. It may be caused by the microscopic roughness of SAMs as the bulky chromophores can not label the functional groups at the bottom of the pinholes produced by UV irradiation. Or it may indeed suggest only a small fraction of the monolayer is functionalized by those oxygenated functional groups. This raises the possibility of Mechanism D.

It is also possible that the reactive species penetrate a few groups deep into the ODS SAM as suggested by Mechanism D (Figure 2-24). Also the radicals formed during hydrogen abstraction process may recombine, leading to cross-linking. Cross-linking is believed to be prevalent in electron beam or X-ray induced degradation of SAMs [25, 27]. Mechanism D generates a surface with even lower coverage of hydrophilic groups due to the presence of cross-linking. Therefore, not all chain scission events result in the formation of hydrophilic groups. This appears to be consistent with the FLOSS results that only a fraction of a monolayer is functionalized. Further investigations need to be carried out to test the validity of Mechanisms C and D. For example, to test how much the reactive species penetrate into SAMs, one can deuterate the groups at the top or bottom of the alkyl chains. IR can then be used to differentiate the reactivity in different sites in the SAMs.

2.4.5. Implications on photopatterning.

A key requirement for photopatterning is to limit oxidation to the irradiated areas. This requirement can be easily fulfilled if the photons can excite the SAMs directly [23]. However, we observed chemical reactants, such as $O(^3P)$, are necessary for the UV degradation of ODS SAMs. These chemical reactants may not be confined to irradiated areas. From the right side of Equation 2-4, the life time of $O(^3P)$, τ , is calculated to be 4.2×10^{-6} s. The diffusion coefficient of $O(^3P)$ under 1 atm is $D = 1 \text{ cm}^2 \text{ s}^{-1}$ [15].

The free mean path of $O(^3P)$ can be estimated by

$$l = \sqrt{D\tau} = 17 \mu\text{m} \quad \text{Equation 2-10}$$

Therefore, the reactive species $O(^3P)$, which is mainly responsible for hydrogen abstraction, can diffuse tens of μm away from the irradiated areas, resulting in poor resolution in projection photopatterning of SAMs. Therefore, if the degradation process is dominated by chemical reactions, to achieve good resolution, proximity masks are necessary to reduce the diffusion of reactants to undesired areas.

However, at 5 W/cm^2 intensity, projection UV photopatterning of alkyl based SAMs has been reported to achieve sub micron resolution [12]. Clearly, photolysis is involved in that case. Though the hydrogen abstraction, the first step of oxidation of aliphatic chains, involves radicals that may not have high spatial confinement. Photolysis, whose spatial resolution is only limited by the spatial confinement of irradiation, may occur on reaction intermediates. The loss of carbon is probably due to the removal of CHO groups by hydrogen abstraction at the α carbon or the photolysis of CHO. The effective rate

constant of caused by photolysis of aldehydes can be estimated from the intensity of the UV light assuming unity quantum yield.

$$\frac{d[CHO]}{dt} = \frac{I_0 \sigma}{h\nu} [CHO] = k'[CHO]$$

Equation 2-11

Where I_0 (2 mW/ cm²) is the incident intensity of UV irradiation, σ is the absorption cross section (2×10^{-20} cm² [66]) and $h\nu$ is the photon energy (7.2×10^{-19} J).

We found that the rate constant to be 5.6×10^{-5} s⁻¹, nearly two orders of magnitude lower than k_{CH_2} (4.1×10^{-3} s⁻¹). Therefore, photolysis is not the dominant channel for dissociation of carbonyls at this low intensity. Rather, we suggest that the loss of carbon mainly results from the reaction of chemical reactive species, e.g., hydrogen abstraction at the α carbon site (R 2-17). Another important step, that photolysis may significantly contribute to, is the photodissociation of peroxide radicals into alkoxy radicals (R 2-13). The reported cross section is 360×10^{-20} cm² at 254 nm [67], which results in a rate constant of 1×10^{-2} s⁻¹. However, the contribution from competing chemical reactions such as R 2-14, is unknown. Therefore, it is not clear whether the photolysis channel dominates (R 2-13).

A better understanding of the mechanism of ODS photoreactivity can provide insight into how to favor the reaction pathways that have better spatial confinement during photopatterning processes. One can envision that even if the light is not in the range of photolysis of alkyl chains, by increasing light intensity and other reaction conditions, the

contribution from photolysis can be increased relative to the contribution from chemical reactions.

2.4.6. Conclusions.

In conclusion, by combining different surface characterization techniques, we gain more molecular level insight into the mechanism of the UV photoreactivity of ODS SAMs. Our results suggest that atomic oxygen is the primary agent for the UV degradation of ODS SAMs. UV degradation results in the scission of alkyl chains instead of the siloxane headgroups. We found that degradation introduces microscopic roughness to ODS SAMs. Using a novel, highly surface sensitive technique, FLOSS, we identified the presence of submonolayer quantities chemical functional groups formed by the UV degradation. We proposed a mechanism based on hydrogen abstraction.

2.4.7. Future work.

Due to their molecularly well-defined structures, SAMs is a model system to probe the relationship between structure and reactivity. By controlling concentrations of different reactive species and reactions on well defined SAMs terminated with different oxygenated functional groups, more insight into the possible elementary steps of the photochemical reaction on SAMs can be obtained. To further explore the effect of SAM structure, SAMs of various degrees of compactness will need to be prepared. Placing deuterated groups at different locations in SAMs will provide direct information about the effect of structure of SAMs on the photoreactivity as well as more microscopic details of the hydrogen abstraction. FLOSS affords a unique opportunity to access information

about lateral and vertical spatial distributions of functional groups produced in the UV degradation, by using chromophores with different geometries. We believe that more molecular level understanding of SAM reactivity will emerge from such systematic investigations.

BIBLIOGRAPHY

1. Ulman, A., *Formation and structure of self-assembled monolayers*. Chemical Reviews, 1996. **96**: p. 1533-1554.
2. Poirier, G.E., T.M. Herne, C.C. Miller, and M.J. Tarlov, *Molecular-scale characterization of the reaction of ozone with decanethiol monolayers on Au(111)*. Journal of the American Chemical Society, 1999. **121**(41): p. 9703-9711.
3. Zhang, Y.M., R.H. Terrill, T.A. Tanzer, and P.W. Bohn, *Ozonolysis is the primary cause of UV photooxidation of alkanethiolate monolayers at low irradiance*. Journal of the American Chemical Society, 1998. **120**(11): p. 2654-2655.
4. Huang, J.Y. and J.C. Hemminger, *Photooxidation of thiols in self-assembled monolayers on gold*. Journal of the American Chemical Society, 1993. **115**(8): p. 3342-3343.
5. Lercel, M.J., C.S. Whelan, H.G. Craighead, K. Seshadri, and D.L. Allara, *J. Vac. Sci. Tech. B*, 1996. **14**(4085-4090).
6. Xia, Y.N., X.M. Zhao, and G.M. Whitesides, *Pattern transfer: Self-assembled monolayers as ultrathin resists*. Microelectronic Engineering, 1996. **32**(1-4): p. 255-268.
7. Xia, Y.N., J.A. Rogers, K.E. Paul, and G.M. Whitesides, *Unconventional methods for fabricating and patterning nanostructures*. Chemical Reviews, 1999. **99**(7): p. 1823-1848.
8. Lercel, M.J., R.C. Tiberio, P.F. Chapman, H.G. Craighead, C.W. Sheen, A.N. Parikh, and D.L. Allara, *Self-Assembled Monolayer electron-beam resists on GaAs and SiO₂*. Journal of Vacuum Science & Technology B, 1993. **11**(6): p. 2823-2828.
9. Yang, X.M., R.D. Peters, T.K. Kim, P.F. Nealey, S.L. Brandow, M.S. Chen, L.M. Shirey, and W.J. Dressick, *Proximity X-ray lithography using self-assembled alkylsiloxane films: Resolution and pattern transfer*. Langmuir, 2001. **17**(1): p. 228-233.
10. Tarlov, M.J., D.R.F. Burgess, and G. Gillen, *UV photopatterning of alkanethiolate monolayers self-assembled on gold and silver*. Journal of the American Chemical Society, 1993. **115**(12): p. 5305-5306.
11. Huang, J.Y., D.A. Dahlgren, and J.C. Hemminger, *Photopatterning of self-assembled alkanethiolate monolayers on gold - a simple monolayer photoresist utilizing aqueous chemistry*. Langmuir, 1994. **10**(3): p. 626-628.
12. Behm, J.M., K.R. Lykke, M.J. Pellin, and J.C. Hemminger, *Projection photolithography utilizing a Schwarzschild microscope and self-assembled alkanethiol monolayers as simple photoresists*. Langmuir, 1996. **12**(8): p. 2121-2124.
13. Roberson, S.V., A.J. Fahey, A. Sehgal, and A. Karim, *Multifunctional ToF-SIMS: combinatorial mapping of gradient energy substrates*. Applied Surface Science, 2002. **200**(1-4): p. 150-164.
14. Moise, T. and Y. Rudich, *Uptake of Cl and Br by organic surfaces - a perspective on organic aerosols processing by tropospheric oxidants*. Geophysical Research Letters, 2001. **28**(21): p. 4083-4086.

15. Bertram, A.K., A.V. Ivanov, M. Hunter, L.T. Molina, and M.J. Molina, *The reaction probability of OH on organic surfaces of tropospheric interest*. Journal of Physical Chemistry A, 2001. **105**(41): p. 9415-9421.
16. Ravishankara, A.R., *Heterogeneous and multiphase chemistry in the troposphere*. Science, 1997. **276**(5315): p. 1058-1065.
17. Atkinson, R., *Gas-phase tropospheric chemistry of organic compounds*. J. Phys. Chem. Ref. Data, 1994. **Monograph 1**: p. 1-216.
18. Ye, T., D. Wynn, R. Dudek, and E. Borguet, *Photoreactivity of alkylsiloxane self-assembled monolayers on silicon oxide surfaces*. Langmuir, 2001. **17**(15): p. 4497-4500.
19. Paz, Y., S. Trakhtenberg, and R. Naaman, *Reaction between $O(^3P)$ and organized organic thin films*. Journal of Physical Chemistry, 1994. **98**(51): p. 13517-13523.
20. Maoz, R. and J. Sagiv, *Penetration-controlled reactions in organized monolayer assemblies. I. aqueous permanganate interaction with monolayer and multilayer films of long-chain surfactants*. Langmuir, 1987. **3**: p. 1034.
21. Schonherr, H., V. Chechik, C.J.M. Stirling, and G.J. Vancso, *Monitoring surface reactions at an AFM tip: An approach to follow reaction kinetics in self-assembled monolayers on the nanometer scale*. Journal of the American Chemical Society, 2000. **122**(15): p. 3679-3687.
22. Thomas, E.R., G.J. Frost, and Y. Rudich, *Reactive uptake of ozone by proxies for organic aerosols: Surface-bound and gas-phase products*. Journal of Geophysical Research-Atmospheres, 2001. **106**(D3): p. 3045-3056.
23. Dulcey, C.S., J.H. Georger Jr., V. Krauthamer, D. Stenger, T.L. Fare, and J.M. Calvert, *Deep UV photochemistry of chemisorbed monolayers: patterned coplanar molecular assemblies*. Science, 1991. **252**: p. 551-554.
24. Laibinis, P.E., R.L. Graham, H.A. Biebuyck, and G.M. Whitesides, *X-ray damage to CF_3CO_2 -terminated organic monolayers on silicon/gold supports is due primarily to x-ray induced electrons*. Science, 1991. **254**: p. 981.
25. Frydman, E., H. Cohen, R. Maoz, and J. Sagiv, *Monolayer damage in XPS measurements as evaluated by independent methods*. Langmuir, 1997. **13**(19): p. 5089-5106.
26. Kim, T.K., X.M. Yang, R.D. Peters, B.H. Sohn, and P.F. Nealey, *Chemical modification of self-assembled monolayers by exposure to soft X-rays in air*. Journal of Physical Chemistry B, 2000. **104**(31): p. 7403-7410.
27. Seshadri, K., K. Froyd, A.N. Parikh, D.L. Allara, M.J. Lercel, and H.G. Craighead, *Electron-beam-induced damage in self-assembled monolayers*. Journal of Physical Chemistry, 1996. **100**(39): p. 15900-15909.
28. Finlayson-Pitts, B. and J. Pitts, *Atmospheric chemistry: Fundamentals and experimental techniques*. 1986, New York: John Wiley & Sons.
29. Ferris, M.M. and K.L. Rowlen, *Direct evidence of ozone as the active oxidant in "photooxidation" of alkanethiols on SERS-active silver*. Applied Spectroscopy, 2000. **54**(5): p. 664-668.
30. Lewis, M., M. Tarlov, and K. Carron, *Study of the photooxidation process of self-assembled alkanethiol monolayers*. Journal of the American Chemical Society, 1995. **117**(37): p. 9574-9575.

31. Norrod, K.L. and K.L. Rowlen, *Ozone-induced oxidation of self-assembled decanethiol: Contributing mechanism for "photooxidation"?* Journal of the American Chemical Society, 1998. **120**(11): p. 2656-2657.
32. Moon, D.W., A. Kurokawa, S. Ichimura, H.W. Lee, and I.C. Jeon, *Ultraviolet-ozone jet cleaning process of organic surface contamination layers.* Journal of Vacuum Science & Technology a-Vacuum Surfaces and Films, 1999. **17**(1): p. 150-154.
33. Horvath, M., L. Bilitzky, and J. Huntner, *Ozone.* 1985, New York: Elsevier Science Publishing.
34. Jet Propulsion Laboratory, C., *Chemical kinetics and photochemical data for use in stratospheric modeling.* 1997.
35. Zhukov, V., I. Popova, and J.T. Yates, Jr., *Delivery of pure ozone in ultrahigh vacuum.* Journal of Vacuum Science & Technology a-Vacuum Surfaces and Films, 2000. **18**(3): p. 992-994.
36. Parikh, A.N., D.L. Allara, I.B. Azouz, and F. Rondelez, *An intrinsic relationship between molecular-structure in self-assembled n-alkylsiloxane monolayers and deposition temperature.* Journal of Physical Chemistry, 1994. **98**(31): p. 7577-7590.
37. Flinn, D.H., D.A. Guzonas, and R.H. Yoon, *Characterization of silica surfaces hydrophobized by octadecyltrichlorosilane.* Colloids and Surfaces a-Physicochemical and Engineering Aspects, 1994. **87**(3): p. 163-176.
38. Atre, S.V., B. Liedberg, and D.L. Allara, *Chain length dependence of the structure and wetting properties in binary composition monolayers of OH-Terminated and CH₃-Terminated alkanethiolates on gold.* Langmuir, 1995. **11**(10): p. 3882-3893.
39. Stein, S.E., *Infrared spectra*, in *NIST Chemistry WebBook, NIST Standard Reference Database Number 69* (<http://webbook.nist.gov>), P.J. Linstrom and W.G. Mallard, Editors. 2003, National Institute of Standards and Technology: Gaithersburg MD, 20899.
40. Carraro, C., O.W. Yauw, M.M. Sung, and R. Maboudian, *Observation of three growth mechanisms in self-assembled monolayers.* Journal of Physical Chemistry B, 1998. **102**(23): p. 4441-4445.
41. Doudevski, I., W.A. Hayes, and D.K. Schwartz, *Submonolayer island nucleation and growth kinetics during self-assembled monolayer formation.* Physical Review Letters, 1998. **81**(22): p. 4927-4930.
42. Bain, C.D. and G.M. Whitesides, *Attenuation lengths of photoelectrons in hydrocarbon films.* Journal of Physical Chemistry, 1989. **93**(4): p. 1670-3.
43. Lamont, C.L.A. and J. Wilkes, *Attenuation length of electrons in self-assembled monolayers of n-alkanethiols on gold.* Langmuir, 1999. **15**(6): p. 2037-2042.
44. McArthur, E., T. Ye, and E. Borguet, *Fluorescence detection of surface bound intermediates produced from UV photoreactivity of alkylsiloxane SAMs.* Submitted to JACS.
45. Fairbank, R.W.P. and M.J. Wirth, *Role of surface-adsorbed water in the horizontal polymerization of trichlorosilanes.* Journal of Chromatography A, 1999. **830**(2): p. 285-291.

46. Apostolova, E., S. Krumova, N. Tuparev, M.T. Molina, T. Filipova, I. Petkanchin, and S.G. Taneva, *Interaction of biological membranes with substituted 1,4-anthraquinones*. Colloids and Surfaces B-Biointerfaces, 2003. **29**(1): p. 1-12.
47. Chu, S.S. and S.H. Reich, *NPIT - a new reagent for quantitatively monitoring reactions of amines in combinatorial synthesis*. Bioorganic & Medicinal Chemistry Letters, 1995. **5**(10): p. 1053-1058.
48. Malicka, J., I. Gryczynski, Z. Gryczynski, and J.R. Lakowicz, *Effects of fluorophore-to-silver distance on the emission of cyanine-dye-labeled oligonucleotides*. Analytical Biochemistry, 2003. **315**(1): p. 57-66.
49. Marchi-Artzner, V., B. Lorz, C. Gosse, L. Jullien, R. Merkel, H. Kessler, and E. Sackmann, *Adhesion of Arg-Gly-Asp (RGD) peptide vesicles onto an integrin surface: Visualization of the segregation of RGD ligands into the adhesion plaques by fluorescence*. Langmuir, 2003. **19**(3): p. 835-841.
50. Singh, Y., A. Gulyani, and S. Bhattacharya, *A new ratiometric fluorescence probe as strong sensor of surface charge of lipid vesicles and micelles*. Febs Letters, 2003. **541**(1-3): p. 132-136.
51. Hayashi, Y. and K. Ichimura, *Movement of polymer segments by exciplex emission of pyrene and N,N-dimethylaniline at the polymer-silica interface*. Journal of Fluorescence, 2003. **13**(2): p. 129-137.
52. Herold, M., H. Brunner, and G.E.M. Tovar, *Polymer nanoparticles with activated ester surface by using functional surfmers*. Macromolecular Chemistry and Physics, 2003. **204**(5-6): p. 770-778.
53. Lee, K.B., K.R. Yoon, S.I. Woo, and I.S. Choi, *Surface modification of poly(glycolic acid) (PGA) for biomedical applications*. Journal of Pharmaceutical Sciences, 2003. **92**(5): p. 933-937.
54. Wang, W.L., Q.G. He, J. Zhai, J.L. Yang, and F.L. Bai, *Self-assembled hyperbranched poly(para-phenylene vinylene) monolayers: Fabrication and characterization*. Polymers for Advanced Technologies, 2003. **14**(3-5): p. 341-348.
55. Sagiv, J., *Organized monolayers by adsorption. 1. formation and structure of oleophobic mixed monolayers on solid surfaces*. Journal of the American Chemical Society, 1980. **102**(1): p. 92-98.
56. Fox, M.A., W.J. Li, M. Wooten, A. McKerrow, and J.K. Whitesell, *Fluorescence probes for chemical reactivity at the interface of a self-assembled monolayer*. Thin Solid Films, 1998. **329**: p. 477-480.
57. Montalti, M., L. Prodi, N. Zaccheroni, R. Baxter, G. Teobaldi, and F. Zerbetto, *Kinetics of place-exchange reactions of thiols on gold nanoparticles*. Langmuir, 2003. **19**(12): p. 5172-5174.
58. Flink, S., F.C.J.M. van Veggel, and D.N. Reinhoudt, *Functionalization of self-assembled monolayers on glass and oxidized silicon wafers by surface reactions*. Journal of Physical Organic Chemistry, 2001. **14**(7): p. 407-415.
59. Brown, W., *Introduction to organic chemistry*. 1982, Boston: Willard Grant Press.
60. Zahr, G.E., R.K. Preston, and W.H. Miller, *Theoretical treatment of quenching in atomic oxygen(1D) + molecular nitrogen collisions*. Journal of Chemical Physics, 1975. **62**(3): p. 1127-35.

61. Atkins, P. and J. Paula, *Physical chemistry*. 7th ed. 2002, New York: W. H. Freeman and Company.
62. Cox, R., K. Patrick, and S. Chant, *Mechanism of atmospheric photooxidation of organic compounds. reactions of alkoxy radicals in oxidation of n-butane and simple ketones*. Environmental Science and Technology, 1981. **15**(5): p. 587-592.
63. Tevault, D.E., R.L. Mowery, and R.R. Smardzewski, *Ozone and oxygen atom reactions with dimethylsulfide and methanethiol in argon matrixes*. Journal of Chemical Physics, 1981. **74**(8): p. 4480-7.
64. Colvin, E.W., *Silicon in organic synthesis*. 1985, Malabar, Florida: Robert E Krieger Publishing Co.
65. Israelachvili, J.N. and M.L. Gee, *Contact angles on chemically heterogeneous surfaces*. Langmuir, 1989. **5**(1): p. 288-9.
66. Martinez, R.D., A.A. Buitrago, N.W. Howell, C.H. Hearn, and J.A. Joens, *The near UV absorption spectra of several aliphatic aldehydes and ketones at 300K*. Atmospheric Environment Part a-General Topics, 1992. **26**(5): p. 785-792.
67. Maricq, M.M. and T.J. Wallington, *Absolute ultraviolet cross-sections of methyl and ethyl peroxy radicals*. Journal of Physical Chemistry, 1992. **96**(2): p. 986-992.

3. Introduction to electrochemical interfaces.

3.1. Electrochemical interfaces: structure of the double layer.

3.1.1. The electrochemical interface and the electric double layer.

The electrochemical interface is the interface between an electrode and an electrolyte. It has been long recognized that a layer of charge resides in the electrode while in the electrolyte, a layer of ionic excess charge balances the electrode charge [1, 2]. These two layers collectively are commonly referred as electric double layer. Helmholtz proposed a simplistic model of the electric double layer; the double layer consists of two sheets of charge, equal in magnitude, of opposite sign and separated by a distance d [1, 2]. The capacitance can be described by a parallel-plate capacitor. The charge density σ is related to the voltage drop across the double layer ϕ by:

$$\sigma = \frac{\epsilon\epsilon_0}{d} \phi \quad \text{Equation 3-1}$$

The differential capacitance is the derivative of the charge density with respect to ϕ .

$$C_H = \frac{d\sigma}{d\phi} = \frac{\epsilon\epsilon_0}{d} \quad \text{Equation 3-2}$$

where d is the separation between the two layers, ϵ is the dielectric constant of the medium, and ϵ_0 is the vacuum permittivity. A more sophisticated model, the Gouy-Chapman model takes into account that the ionic charge in the electrolyte is not confined to the surface despite the attractive force of charge residing at the electrode surface [1, 2]. Instead, the ionic charge density ρ along one dimensional coordinate x follows a Boltzmann distribution and forms a diffuse layer near the electrode interface.

$$\rho(x) = \sum_i n_i Z_i e \times \exp\left(\frac{-z_i e \phi}{kT}\right) \quad \text{Equation 3-3}$$

where n is the number density of ions, Z_i is the number of electronic charge on ion i , k is the Boltzman constant and T is the absolute temperature.

The charge densities ρ and the potential in the double layer are described by Poisson equation:

$$\rho(x) = -\epsilon\epsilon_0 \frac{d\phi^2}{dx^2} \quad \text{Equation 3-4}$$

By combining the two equations and further transformation [1, 2], one can obtain the differential capacitance of the diffuse layer, C_D .

$$C_D = \frac{d\sigma^M}{d\phi_0} = ze \left(\frac{2\epsilon\epsilon_0 n^0}{kT}\right)^{1/2} \cosh\left(\frac{ze\phi_0}{2kT}\right) \quad \text{Equation 3-5}$$

The Gouy-Chapman model is successful in describing the behavior of the double layer at low electrolyte concentrations. However, the capacitance deviates significantly at higher concentrations [1, 2]. It has been found that the values of calculated capacitance are significantly higher than experimentally determined values at higher electrolyte concentrations.

A more refined model takes into account that unlike true point charges, which can be infinitely close to the surface, the finite size of solvated ions implied a minimum distance d of approach, defined by the ionic radius. Stern treated the electrolyte side of the electric double layer as comprising a compact layer (outer Helmholtz layer) and a diffuse layer [1]. Consequently the differential capacitance corresponds to the overall capacitance of two capacitors connected in series [1].

$$\frac{1}{C_d} = \frac{1}{C_D} + \frac{1}{C_H}$$

Equation 3-6

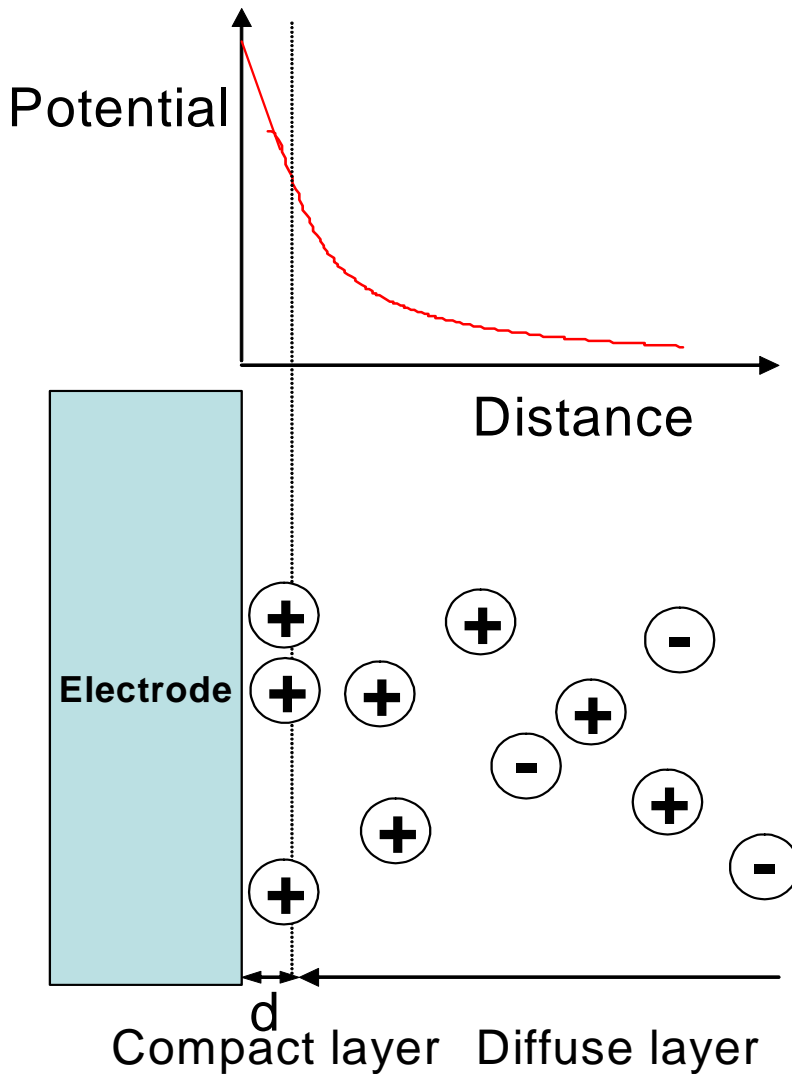


Figure 3-1 Structure of double layer and the potential drop across double layer.

A salient feature of the electric double layer is the extremely high capacitance [1], a consequence of the small thickness of double layer capacitors. Assuming the thickness of the Helmholtz compact layer to be 0.3 nm, the dielectric constant of the water to be 80, the capacitance of the layer is calculated to be $240 \mu\text{F}/\text{cm}^2$ according to Equation 3-7. However, a typical observed value is about $30 \mu\text{F}/\text{cm}^2$, suggesting that the dielectric constant of the interfacial water is significantly smaller, 5-10, as opposed to 80, the value

observed for the bulk water. The smaller value is attributed to the limited structural flexibility of water at interfaces [2]. The capacitance of the Helmholtz layer is $30 \mu\text{F}/\text{cm}^2$. The high capacitance is responsible for the high surface charge density (up to 0.1-0.2 charge/surface atom) and the high electric field (10^6 - 10^8 V/cm) present in the double layer [3]. If the potential drop at the double layer is 0.3 V, the effective electric field is 10^8 V/cm at a thickness of 0.3 nm. Such a high electric field can profoundly affect the structure and chemistry of species present at the electrochemical interfaces. Therefore, by tuning the electrode potential, the fundamental variable at electrochemical interfaces, we have opportunities to drive not only electron transfer processes, but also surface processes, such as, adsorption and 2D phase transitions.

3.1.2. Electrode surfaces.

Electrochemical processes are heavily dependent on the structure and electronic properties of the electrode surfaces. Most of our investigations have been performed on gold electrodes. Therefore it is necessary to briefly mention the surface crystallography of single crystal Au electrodes, which, in addition to FCC packing, may have surface reconstructions. In general, surface reconstruction is the deviation of the position of surface atoms from the bulk termination, a consequence of the imbalance of surface forces at the surface, a highly asymmetric environment [3]. Due to the abrupt surface termination, surface atoms have less interaction with other atoms than bulk atoms. Therefore, the surface atoms tend to adopt a more close packed structure to minimize surface energy.

Au is a FCC metal with an atomic radius of 0.288 nm [4, 5]. Au(111) has two stable phases: an unreconstructed (1×1), which has the bulk termination, and a reconstructed phase (Figure 3-2). The reconstructed phase on Au(111) is a $(22 \times \sqrt{3})$ super structure consists of 23 surface atoms compressed along $[\bar{1}\bar{1}0]$ orientation into a space of 22 atoms (63 \AA) for the bulk phase [4, 5]. The $(22 \times \sqrt{3})$ phase is rather similar to the (1×1) phase, as the surface compression is only about 4.5% (Figure 3-2). The surface compression along $[\bar{1}\bar{1}0]$ direction results in double stripes with vertical corrugation of 0.1 \AA [4, 5] (Figure I-2). In addition, the compression results in the displacement of atoms from a straight line along $[\bar{1}\bar{1}0]$. The displacement along $[1\bar{1}\bar{2}]$ (perpendicular to $[\bar{1}\bar{1}0]$) is about 0.8 \AA (Figure 3-2).

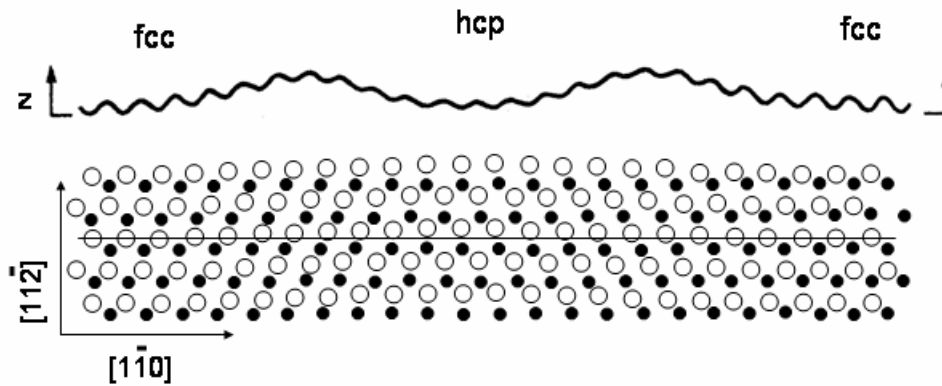


Figure 3-2 Model for the Au(111) reconstruction. The solid dots denote the positions of atoms in the second layer, whereas open circles denote the positions of atoms in the reconstructed top layer. C and A mark the regions of ABC (fcc) and ABA (hcp) stacking. The displacement of atoms from the straight line along the $[1\bar{1}\bar{0}]$ direction of about 0.8 \AA is apparent [4].

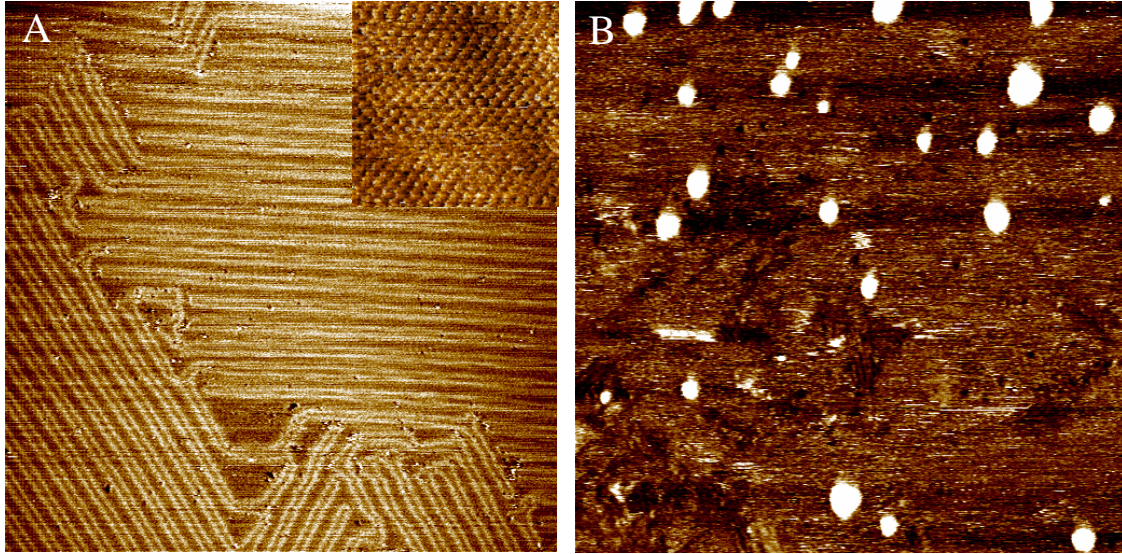


Figure 3-3 STM images of Au(111) surface under 0.1M H_2SO_4 at different electrode potentials, image size: $160 \text{ nm} \times 160 \text{ nm}$. A: reconstructed surface is observed at 0.05V. The double reconstruction stripes are rotated by 120° , reflecting the symmetry of the (111) surface. Inset: atomic resolution image of the reconstructed surface ($4.5 \text{ nm} \times 4.5 \text{ nm}$). The lattice constant is about 3 \AA , which is in good agreement of the lattice constant of gold 2.88 \AA . B: The reconstruction is lifted at 0.36V. The 4-5% extra gold atoms are released to form the monolayer islands.

By contrast, the reconstructed phase of Au(100) differs from the bulk termination dramatically. The reconstructed phase (commonly denoted as (hex) phase) has hexagonal packing while the unreconstructed phase, (1×1) , has the square lattice (Figure 3-4). The packing density of the (hex) phase is 20% higher than the (1×1) phase [6]. The mismatch between the top hexagonal lattice and the underlying square lattice causes 14.5 \AA wide stripes with corrugation of 0.3 \AA (Figure 3-4)[6]. In addition, along the stripes, the mismatch causes alternating appearance of single and double stripes (The cross section view of Figure 3-4) with a periodicity of 39 \AA .

The reconstructed phases are the thermodynamically favored phases at room temperature in vacuum [3]. In an electrochemical environment, a phase transition can be induced by

changing the electrode potential [3]. It is now well established that a negative surface charge density favors the reconstructed phase and that a positive surface charge density lifts the surface reconstruction [3]. This trend can be rationalized by suggesting that the more close-packed reconstructed surface is stabilized by higher electron density [3]. Another cause for lifting of reconstruction is the chemisorption of anions [3]. Chemisorption reduces the imbalance of surface forces by forming chemical bonds with surface atoms. Therefore it favors the unreconstructed phase.

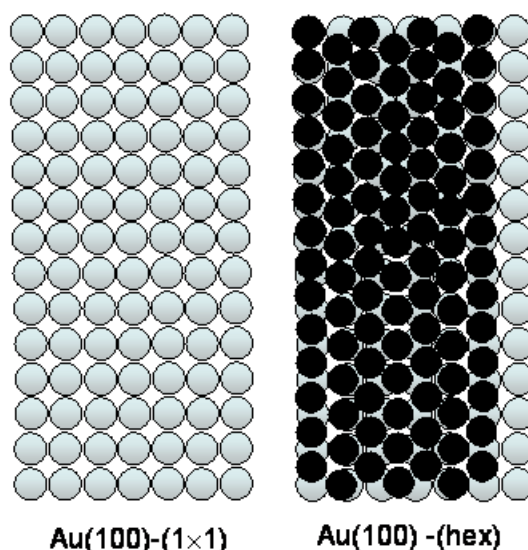


Figure 3-4 Models for the unreconstructed Au(100) and the reconstructed Au(100) surfaces [6].

3.2. Adsorption and self-assembly of molecular adsorbates at electrochemical interfaces.

Molecular adsorbates at charged interfaces afford opportunities in molecular level engineering of surfaces for applications ranging from electrocatalysis [7], sensors [8], to corrosion protection [9]. Central to successful implementation of those applications is to the ability to understand and control how molecules arrange at charged interfaces. The

question is two fold. First, one needs to understand the stability of adsorbate structures at different surface charge densities. Second, one may utilize the charge dependence to achieve desired structures.

3.2.1. Molecular adsorbates at vacuum-solid and gas-solid interfaces.

To understand the behavior of molecular adsorbates at electrochemical interfaces, it is often instructive to discuss the relevant work carried out on molecular adsorbates at the vacuum-solid and gas-solid interfaces. While electrochemical interfaces have additional complexity due to the influence of the electrolyte and the electric field present, the information from vacuum-solid and gas-solid studies can often serve as a starting point to understand the structures of molecular adsorbates at electrochemical interfaces.

3.2.1.1. Adsorbate-substrate interactions.

At vacuum-solid interfaces, it is recognized that the structures of the adsorbates are determined by the interplay between surface interactions, such as adsorbate-substrate interaction and adsorbate-adsorbate interactions [10]. According to the strength of the interactions, the adsorbate-substrate interactions can be categorized as physisorption interactions and chemisorption interactions. Physisorption is caused by van der Waals interactions. Thus the interaction is relatively weak (the adsorption energy is typically less than 40 kJ/mol for small molecules). In contrast, chemisorption involves actual chemical bond formation between the adsorbate and substrate. Hence the adsorbates are much more tightly bonded to the surface. The adsorbate-substrate interaction may play a number of roles [11]. First, it confines the adsorbates to the surface, a prerequisite for the stability of the self-assembled structures. Second, the periodic corrugation along the

surface imposed by the symmetry of the substrate atomic lattice plays important roles in the long range order of adsorbates. Third, to form ordered structures, the adsorbate must be allowed to reorganize laterally to reach the minimum energy position. The surface diffusion barrier is related to the strength of adsorbate-substrate interaction. A stronger adsorbate-substrate interaction typically results in higher diffusion barrier and therefore hinders surface diffusion.

3.2.1.2. Adsorbate-adsorbate interactions.

Depending on the nature of the functional groups on the adsorbates and their geometry, the adsorbate-adsorbate interactions may result from van der Waals [11], hydrogen bonding [12], dipole-dipole [13], and π stacking interactions [14]. The adsorbate-adsorbate interactions often play crucial roles in the lateral arrangement of molecular adsorbates. For example, the weak van der Waals interaction between the alkyl chains is largely responsible for the compactness and lattice spacing alkanethiol self-assembled monolayers [11]. To create more sophisticated two dimensional self-assembled structures on surfaces, non-covalent intermolecular interactions including hydrogen bonding [12], weak electron donor-acceptor [15, 16], and dipole-dipole interactions [13] have been employed.

3.2.2. Molecular adsorbates at electrochemical interfaces.

Adsorbate-substrate and adsorbate-adsorbate interactions remain important in determining the structure of adsorbates at an electrochemical interface. However, one needs to consider the additional effect of the electrolyte and surface charge.

3.2.2.1. Thermodynamics.

The most fundamental equation governing the equilibrium at electrochemical interfaces is the electrocapillary equation [1]. An electrochemical interface, consisting of an electrode under a solution of an electrolyte, CA and a surface active neutral species M, the infinitesimal change of surface tension, $d\gamma$, is given by

$$-d\gamma = \sigma dE_- + \Gamma_{C^+} d\mu_{CA} + \Gamma_M d\mu_M \quad \text{Equation 3-8}$$

where E is the electrode potential, Γ_{C^+} and Γ_M are surface excesses of C^+ and M, and μ_M and μ_{CA} are the chemical potentials of CA and M.

On a mercury electrode, γ is a directly measurable quantity. Even for solid surfaces, change in γ can be obtained by integration, when the chemical potentials, μ_M and μ_{CA} , determined by the concentrations in the bulk electrolyte are held constant [1].

$$\Delta\gamma = \int_{E_{pzc}}^E -\sigma dE \quad \text{Equation 3-9}$$

One of the most important applications of electrocapillary equation is the measurement of the surface excess of the adsorbed species M, by taking the derivative of γ with respect to the bulk concentration of M, C_M [17]. From the surface excess, other thermodynamic quantities such as free energy of adsorption can be calculated [17].

$$\Gamma_M = \frac{-d\gamma}{RT d \ln C_M} \quad \text{Equation 3-10}$$

The electrocapillary equation also provides a thermodynamic description of two dimensional phase transitions [18]. Consider two phases, α and β at the electrode surface with surface tensions, γ_α and γ_β . The stability of the two phases on electrode surfaces is

determined by the tendency to minimize surface tension γ . A phase transition from α to β occurs when γ_β becomes less than γ_α . The variation of surface tension is described by:

$$d\gamma_\alpha = -S_\alpha dT - C_\alpha (E - E_\alpha^{pzc}) dE - RT\Gamma_\alpha d \ln C_M \quad \text{Equation 3-11}$$

$$d\gamma_\beta = -S_\beta dT - C_\beta (E - E_\beta^{pzc}) dE - RT\Gamma_\beta d \ln C_M \quad \text{Equation 3-12}$$

where S_α S_β are the entropies of the two phases, Γ_α and Γ_β are the surface excesses of the two phases, C_α and C_β correspond to the differential capacitances of α and β , and E^{pzc} is the potentials of zero charge for α and β . From the equation, it is apparent that three parameters, temperature T , electrode potential E and the bulk concentration C_M can affect the surface tension of the two phases and consequently controls the stability of the different phases.

Although the electrocapillary equation provides a macroscopic description of the electrochemical interface, it does not take into account the properties of adsorbates and the role of electric fields. To understand how electric fields affect the microscopic structure of adsorbates, one needs to take into account surface interactions such as electrostatic interactions and chemical interactions. According to the statistical mechanical treatment assuming a 2D Ising lattice gas model [18, 19], the free energy change, $\Delta G(F)$, when the adsorbate M displaces the solvent molecules and forms an ordered layer, is given by

$$\Delta G(F) = \Delta G(0) + RT \ln C - N_A \Delta P_s F - 1/2 N_A \Delta \alpha_s F^2 = 0 \quad \text{Equation 3-13}$$

where $\Delta G(0)$ is a field independent term, C is the concentration of adsorbates in the bulk, N_A is the Avogadro number, F is the electric field present at the interface, ΔP_s is the

difference between the permanent dipole moments of the adsorbate and the solvent molecules, and $\Delta\alpha_s$ is the difference between the polarizabilities of the adsorbates and the solvent. Since F is not a measurable quantity, to test this model, one needs to make assumptions of the correlation between the electric field and the electrode potential [19]. A linear relationship between the electric field and electrode potential can be assumed. Indeed, this model is in qualitative agreement with experimental results in reproducing the quadratic dependence of ΔG on the electrode potential [18]. However, agreement between the model and the experimental data must be achieved through fitting of many adjustable parameters. It remains a challenge to correlate these parameters to real physical quantities such as polarizability [19].

3.3. SPM study of molecular self-assembly.

Electrochemical techniques, such as AC impedance, have provided macroscopic quantities such as the coverage and adsorption energies of adsorbates at electrochemical interfaces from the electrocapillary equation [17, 18]. *Ex situ* techniques, in which the electrode is immersed from the electrolyte and transferred to a ultra high vacuum environment for structural analysis, have provided valuable structural information on the adsorbed molecules [20, 21]. However, a persisting challenge in *ex situ* techniques is that one must establish the relevance of the information acquired *ex situ* to the real processes under the electrochemical environment [20, 21]. To gain more direction microscopic information, a number of *in situ* techniques, such as electro-reflectance, second harmonic generation, surface enhanced Raman spectroscopy, Infrared spectroscopy, surface X-ray

scattering have been used to directly probe various aspects of the structure and properties of adsorbates under electrochemical environments [21]. Electrochemical scanning probe microscopy (EC-SPM) has advanced significantly our understanding of electrochemical interfaces by *in situ* “visualization” of the real space arrangement of atoms and molecules. Over the past decade, *in situ* EC-SPM has played a pivotal role in the studies of potential driven surface reconstruction [3], electrodeposition [22], and molecular adsorption [23].

3.3.1. Principles of electrochemical SPM.

3.3.1.1. Scanning probe microscopy

All scanning probe microscopy techniques involve a local probe in proximity to the surface [24]. The position of the probe is controlled by a piezoelectric with sub Å precision. A feedback is necessary to probe the local information of the surface. In Scanning Tunneling Microscopy (STM), a bias is applied between a conductive probe and the substrate. The tunneling current, which is sensitive to the tip-surface distance as well as the electronic properties of the surface, is used to probe the topographic and electronic information of the surface [24]. In Atomic Force Microscopy (AFM) (Figure 3-6), the force between the probe and the surface is sensed by the deflection of the cantilever and used to map the topography and local adhesion of the surface [24].

3.3.1.2. SPM under electrochemical environments

Although originally developed for studies under vacuum and ambient environments [25, 26], SPM quickly found applications in in-situ probing of electrochemical interfaces [27]. Electrochemical AFM requires virtually no modification of the regular ambient AFM to

image under electrochemical environments except connection to an external potentiostat. For electrochemical STM (EC-STM), the tip generates a faradaic current that is dependant on the tip potential. The faradaic current from a bare metallic tip overwhelms the tunneling current. Therefore, it is necessary to coat the tip, except the apex, with an insulating material (Figure 3-5) [27]. Another important feature of EC-STM is that a bipotentiostat is required to independently control the potential of the tip and the potential of the surface (Figure 3-5). The tip bias is therefore the difference between the potentials of the tip and the surface. It turns out that if cleanliness of samples and electrolytes is maintained, EC-SPM is often capable of resolution significant better than that under ambient environments or even comparable to that achieved under UHV [27].

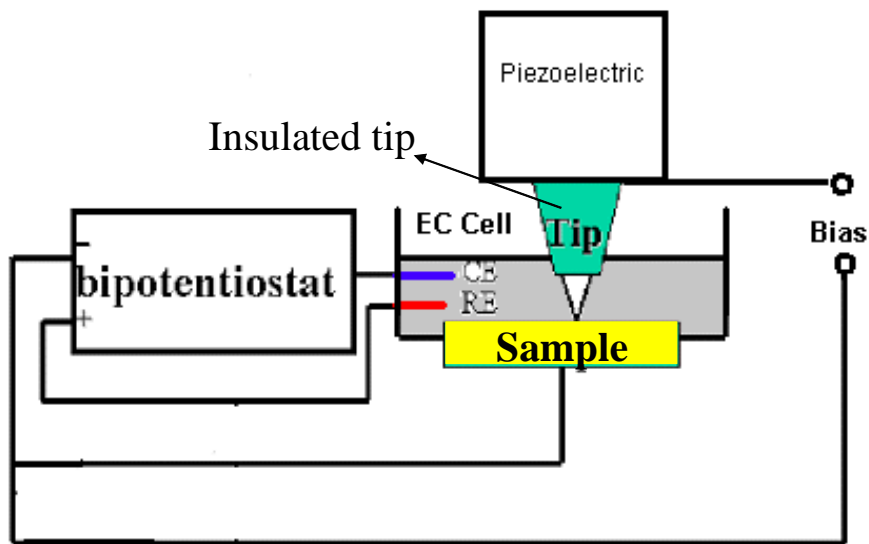


Figure 3-5 Schematic of EC-STM. A bipotentiostat is used to control electrode potential in four electrode setup, including CE: counter electrode, RE: reference electrode.

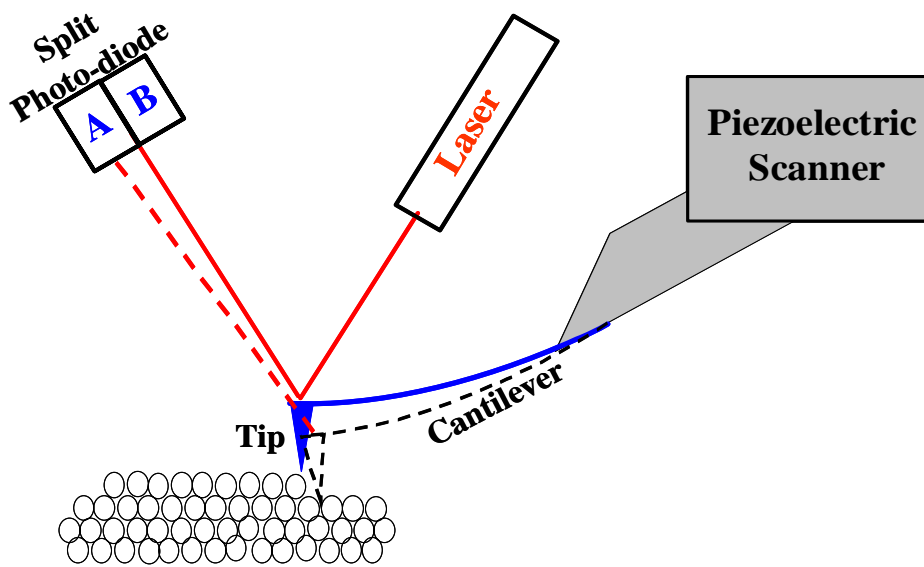


Figure 3-6 Schematic of AFM. The force between the tip and the surface is sensed by the deflection of a cantilever. Reflection of a laser beam from the cantilever, measured by a split photodiode, monitors the deflection of the cantilever.

3.3.2. EC-SPM study of molecular self-assembly.

In addition to studying substrates and atomic adsorbate [3], SPM has become an indispensable tool in elucidating the self-assembly of organic molecules at electrochemical interfaces [28]. Unlike most other *in situ* techniques, which can only provide average information of ensembles, EC-SPM has allowed unprecedented levels of insight into how molecules self-assemble on electrode surfaces by providing the real space structure of adsorbates on an individual molecule basis.

A wide range of molecular adsorbates, such as DNA and its bases [29-31], alkanethiols [32, 33], ionic surfactants [34], small aromatic compounds such as, bipyridine [14, 35], benzene and naphthalene [36, 37], and macrocycles such as porphyrins [38-40], have been imaged under electrochemical conditions.

A particularly interesting question is how the microscopic details of potential-induced 2D phase transitions, whose existence is suggested by many electrochemical and spectroscopic investigations in [17, 18]. Indeed, consistent with capacitance measurements, ordered physisorbed guanine structures on HOPG formed near the potential of zero charge were observed by STM to desorb at higher surface charge densities [29]. Cunha and Tao's STM study of 2,2'-bipyridine (22BPY) on an Au(111) electrode revealed microscopic details of a potential induced order-disorder phase transition [14]. The ordering observed at more positive potentials has been attributed to the screening of dipole-dipole repulsion between adsorbates by the positive surface charge [14, 23]. Therefore, 22BPY can form long polymeric chains like stacked coins due to the π stacking interaction. In some cases, impressive details of the dynamic processes of phase transitions, the nucleation and growth process, have been followed by EC-SPM at a molecular level [23, 35, 38, 41]. The effect of the substrate has also been studied. Itaya et al., found that for substrates with excessive molecule-substrate interaction, iodine modification can reduce the interaction and facilitate the ordering processes of adsorbates [39, 42, 43].

3.4. Overview of the EC-STM section of this dissertation.

Our investigations are aimed at understanding the rules governing self-assembly at electrochemical interfaces and how they can be exploited to control the self-assembly processes. Most of the organic adsorbates have a hydrophobic component. In Chapter 4, we focus on the effect of hydrophobic interactions in molecular self-assembly by studying a completely hydrophobic molecule, hexadecane. Our EC-STM study provides

molecular level details of the potential induced transformation of a completely hydrophobic molecule, hexadecane, at electrochemical interfaces. A variety of charge dependant structures of the hydrophobic phase at the interfaces, including the surface charge induced order-disorder phase transitions as well as the formation of nanometer-sized alkane aggregates, are demonstrated. In Chapter 5, we demonstrated that we can exert active control over the self-assembled structure of porphyrin adsorbates, which are much more polarizable than hexadecane molecules and more strongly adsorbed on Au(111) electrode. Our results suggest that the electrode potential, adsorbate surface mobility and ordering process are correlated. Ordered porphyrin adlayers can be prepared by adsorption at potentials between 0.2 to $-0.2V_{SCE}$. In this potential range, molecule substrate interaction is strong enough to confine molecules in ordered array but also weak enough to allow facile lateral reorganization of adsorbates, a key requirement for self-assembly [11]. In Chapter 6, we performed more systematic STM and electrochemical studies to understand the interplay between the redox properties of TPyP, the adsorption and self-assembly processes on Au surfaces. We found that the irreversible adsorption of TPyP has a dramatic effect on its electrochemistry. We attribute the distinct reactivity to the strong interaction between TPyP molecules and the Au substrate. Our investigation also shows how redox reactions can influence the formation of multilayers, which is probably related to the π stacking interactions of porphyrins. In Chapter 7, we studied the potential dependant structures of surface micelles of sodium dodecylsulfate. We have demonstrated that the intrinsic length scales of self-assembled structures may be exploited to grow metal nanostructures of controlled spacing.

BIBLIOGRAPHY

1. Grahame, D.C., *The electrical double layer and the theory of electro-capillarity*. Chemical Reviews, 1947. **41**: p. 441-501.
2. Parsons, R., *The electrical double layer: recent experimental and theoretical developments*. Chemical Reviews (Washington, DC, United States), 1990. **90**(5): p. 813-26.
3. Kolb, D.M., *Reconstruction phenomena at metal-electrolyte interfaces*. Progress in Surface Science, 1996. **51**(2): p. 109-173.
4. Woll, C., S. Chiang, R.J. Wilson, and P.H. Lippel, *Determination of atom positions at stacking-fault dislocations on gold (111) by scanning tunneling microscopy*. Physical Review B: Condensed Matter and Materials Physics, 1989. **39**(11): p. 7988-91.
5. Gao, X., A. Hamelin, and M.J. Weaver, *Atomic relaxation at ordered electrode surfaces probed by Scanning Tunneling Microscopy: Au(111) in aqueous solution compared with ultrahigh-vacuum environments*. J. Chem. Phys., 1991. **95**: p. 6993.
6. Gao, X.P., A. Hamelin, and M.J. Weaver, *Elucidating Complex Surface Reconstructions with Atomic-Resolution Scanning Tunneling Microscopy - Au(100)-Aqueous Electrochemical Interface*. Physical Review B, 1992. **46**(11): p. 7096-7102.
7. Collman, J.P., P. Denisevich, Y. Konai, M. Marrocco, C. Koval, and F.C. Anson, *Electrode catalysis of the four-electron reduction of oxygen to water by dicobalt face-to-face porphyrins*. Journal of the American Chemical Society, 1980. **102**(19): p. 6027-36.
8. Flink, S., F.C.J.M. van Veggel, and D.N. Reinhoudt, *Sensor functionalities in self-assembled monolayers*. Adv. Mater. (Weinheim, Ger.), 2000. **12**(18): p. 1315-1328.
9. Laibinis, P.E. and G.M. Whitesides, *Self-assembled monolayers of n-alkanethiolates on copper are barrier films that protect the metal against oxidation by air*. Journal of the American Chemical Society, 1992. **114**(23): p. 9022-9028.
10. Somorjai, G.A., *Chemistry in two dimensions : surfaces*. 1981, Ithaca,NY: Cornell University Press.
11. Poirier, G.E., *Characterization of organosulfur molecular monolayers on Au(111) using scanning tunneling microscopy*. Chemical Reviews, 1997. **97**(4): p. 1117-1127.
12. Barth, J.V., J. Weckesser, C.Z. Cai, P. Gunter, L. Burgi, O. Jeandupeux, and K. Kern, *Building supramolecular nanostructures at surfaces by hydrogen bonding*. Angewandte Chemie-International Edition, 2000. **39**(7): p. 1230-+.
13. Yokoyama, T., S. Yokoyama, T. Kamikado, Y. Okuno, and S. Mashiko, *Selective assembly on a surface of supramolecular aggregates with controlled size and shape*. Nature, 2001. **413**: p. 619-621.
14. Cunha, F. and N. Tao, *Surface charge induced order-disorder transition in an organic monolayer*. Physical Review Letters, 1995. **75**(12): p. 2376.

15. Leininger, S., B. Olenyuk, and P.J. Stang, *Self-assembly of discrete cyclic nanostructures mediated by transition metals*. Chemical Reviews, 2000. **100**(3): p. 853-907.
16. Schwab, P.F.H., M.D. Levin, and J. Michl, *Molecular rods. 1. simple axial rods*. Chem. Rev., 1999. **99**(7): p. 1863-1933.
17. Lipkowski, J., L. Stolberg, D.-F. Yang, B. Pettinger, S. Mirwald, F. Henglein, and D.M. Kolb, *Molecular adsorption at metal-electrodes*. Electrochimica Acta, 1994. **39**(8-9): p. 1045.
18. De Levie, R., *The dynamic double layer: Two-dimensional condensation at the mercury-water interface*. Chemical Reviews, 1988. **88**(4): p. 599-609.
19. Trasatti, S., *Charge of maximum adsorption of organic compounds at electrodes. Separation of induced and permanent dipole effects*. Journal of Electroanalytical Chemistry and Interfacial Electrochemistry, 1978. **91**(1): p. 1-9.
20. Hubbard, A.T., *Surface electrochemistry*. Langmuir, 1990. **6**(1): p. 97-105.
21. Lipkowski, J., P.N. Ross, and Editors, *Structure of electrified interfaces*. 1993, New York: VCH. 406 pp.
22. Herrero, E., L.J. Buller, and H.D. Abruna, *Underpotential Deposition at Single Crystal Surfaces of Au, Pt, Ag and Other Materials*. Chemical Reviews, 2001. **101**(7): p. 1897-1930.
23. Cunha, F., N.J. Tao, X.W. Wang, Q. Jin, B. Duong, and J. D'Agnesse, *Potential-induced phase transitions in 2,2'-bipyridine and 4,4'-bipyridine, monolayers on Au(111) studied by in situ scanning tunneling microscopy and atomic force microscopy*. Langmuir, 1996. **12**(26): p. 6410.
24. Wiesendanger, R., H.J. Guentherodt, and Editors, *Scanning Tunneling Microscopy III. Theory of STM and related scanning probe methods*. 1993, New York: Springer. 375 pp.
25. Binnig, G., H. Rohrer, C. Gerber, and E. Weibel, *Surface studies by scanning tunneling microscopy*. Physical Review Letters, 1982. **49**(1): p. 57-61.
26. Binnig, G., C. Quate, and C. Gerber, *Atomic force microscope*. Phys. Rev. Lett, 1986. **56**(9): p. 930-933.
27. Gewirth, A.A. and B.K. Niece, *Electrochemical applications of in situ scanning probe microscopy*. Chemical Reviews, 1997. **97**(4): p. 1129-1162.
28. Itaya, K., *In situ scanning tunneling microscopy in electrolyte solutions*. Progress in Surface Science, 1998. **58**(3): p. 121-247.
29. Srinivasan, R., J.C. Murphy, R. Fainchtein, and N. Pattabiraman, *Electrochemical STM of condensed guanine on graphite*. Journal of Electroanalytical Chemistry and Interfacial Electrochemistry, 1991. **312**(1-2): p. 293-300.
30. Brown, G.M., D.P. Allison, R.J. Warmack, K.B. Jacobson, F.W. Larimer, R.P. Woychik, and W.L. Carrier, *Electrochemically induced adsorption of radiolabeled DNA on gold and HOPG substrates for STM investigations*. Ultramicroscopy, 1991. **38**(3-4): p. 253-64.
31. Tao, N.J., J.A. DeRose, and S.M. Lindsay, *Self-assembly of molecular superstructures studied by in situ scanning tunneling microscopy: DNA bases on gold (111)*. Journal of Physical Chemistry, 1993. **97**(4): p. 910-19.

32. Pan, J., N. Tao, and S.M. Lindsay, *An Atomic-Force Microscopy Study of a Self-Assembled Octadecyl Mercaptan Monolayer Adsorbed on Gold(111) under Potential Control*. Langmuir, 1993. **9**(6): p. 1556-1560.
33. Schneeweiss, M.A., H. Hagenstrom, M.J. Esplandiu, and D.M. Kolb, *Electrolytic metal deposition onto chemically modified electrodes*. Applied Physics a-Materials Science & Processing, 1999. **69**(5): p. 537-551.
34. Burgess, I., C.A. Jeffrey, X. Cai, G. Szymanski, Z. Galus, and J. Lipkowski, *Direct visualization of the potential-controlled transformation of hemimicellar aggregates of dodecyl sulfate into a condensed monolayer at the Au(111) electrode surface*. Langmuir, 1999. **15**(8): p. 2607-2616.
35. Dretschkow, T., D. Lampner, and T. Wandlowski, *Structural transitions in 2,2'-bipyridine adlayers on Au(111) - an in-situ STM study*. Journal of Electroanalytical Chemistry, 1998. **458**(1-2): p. 121-138.
36. Yau, S.L., Y.G. Kim, and K. Itaya, *In situ scanning tunneling microscopy of benzene adsorbed on Rh(111) and Pt(111) in HF solution*. Journal of the American Chemical Society, 1996. **118**(33): p. 7795-7803.
37. Yau, S.L., Y.G. Kim, and K. Itaya, *High-resolution imaging of aromatic molecules adsorbed on Rh(111) and Pt(111) in hydrofluoric acid solution: In situ STM study*. Journal of Physical Chemistry B, 1997. **101**(18): p. 3547-3553.
38. Ogaki, K., N. Batina, M. Kunitake, and K. Itaya, *In situ scanning tunneling microscopy of ordering processes of adsorbed porphyrin on iodine-modified Ag(111)*. Journal of Physical Chemistry, 1996. **100**(17): p. 7185-7190.
39. Kunitake, M., U. Akiba, N. Batina, and K. Itaya, *Structures and dynamic formation processes of porphyrin adlayers on iodine-modified Au(111) in solution: In situ STM study*. Langmuir, 1997. **13**(6): p. 1607-1615.
40. Tao, N.J., *Probing potential-tuned resonant tunneling through redox molecules with scanning tunneling microscopy*. Physical Review Letters, 1996. **76**(21): p. 4066-4069.
41. Dretschkow, T., A.S. Dakkouri, and T. Wandlowski, *In-situ scanning tunneling microscopy study of uracil on Au(111) and Au(100)*. Langmuir, 1997. **13**(10): p. 2843-2856.
42. Kunitake, M., N. Batina, and K. Itaya, *Self-organized porphyrin array on iodine modified Au(111) in electrolyte solutions in situ Scanning Tunneling-Microscopy study*. Langmuir, 1995. **11**(7): p. 2337-2340.
43. Sashikata, K., T. Sugata, M. Sugimasa, and K. Itaya, *In situ scanning tunneling microscopy observation of a porphyrin adlayer on an iodine-modified Pt(100) electrode*. Langmuir, 1998. **14**(10): p. 2896-2902.

4. The role of hydrophobic chains in self-assembly at electrified interfaces: Observation of potential induced transformation of two dimensional crystals of hexadecane by in-situ scanning tunneling microscopy.

4.1. Introduction.

4.1.1. Role of hydrophobic tails in the structure of amphiphilic monolayers.

Adsorbed organic thin films, often residing at charged interfaces, afford opportunities in molecular level engineering of surfaces for applications ranging from sensors [1], corrosion protection [2] to bio-membrane functions and colloidal systems[3, 4]. The interfacial charge may affect the structure and properties of thin films. Understanding and controlling the charge dependant structures and properties are important for preparing and controlling the properties of organic thin films on electrode surfaces for various applications [5-8].

Most organic thin films at charged interfaces are composed of amphiphilic molecules, consisting of hydrophobic tails and hydrophilic head groups, whose potential dependant structure is a result of complex interactions between the hydrophobic tails, the head groups, the electrolyte and the substrate. Changes in molecular orientation and packing [9, 10], desorption [9] and formation of surface aggregates such as micelles [11, 12] may occur in adsorbed amphiphilic molecules upon modulation of the surface charge. The competitive adsorption of electrolyte and hydrocarbon chains on electrodes is recognized as a dominant factor in the structure of weakly adsorbed amphiphilic molecules [9]. Near the potential of zero charge (pzc) in aqueous environments, hydrophobic repulsion orients

the hydrophobic hydrocarbon chains of physisorbed amphiphilic molecules toward the metal surface while the hydrophilic head groups point toward the aqueous electrolyte [9]. However, at sufficiently high surface charge density, hydrophobic hydrocarbon chains on electrode surfaces are displaced by the electrolyte, resulting in a change in orientation or desorption [9]. Even for self-assembled monolayers, formed by molecules with headgroups binding strongly to the substrate through chemisorption, in which one would expect diminishing influence from the weakly interacting tails, the hydrophobic tails remain critical in determining the formation and stability of the monolayers at electrified interfaces. For example, increasing the length of the alkyl chains has been found to improve the stability at negative potential of alkanethiols monolayers [6, 7, 13]. Hatchett et al. found that the adsorption free energies of n-alkanethiols under aqueous solution increased by 1 kcal/mol with each additional methylene unit in the chain[7]. The increased stability has been attributed to increasing hydrophobic interactions under aqueous solution, improved screening of ions, and the increased stabilization by Van der Waals interactions between the chains [6, 7, 13]. It was proposed that for alkanethiols with chain length longer than ten carbons, the contribution from alkyl chains to the adsorption energy (10-20 kcal/mol) is comparable to that from the chemisorbed sulfur head groups (20-30 kcal/mol) [7].

4.1.2. Studies of alkanes at electrified interfaces.

2D hydrophobic phases, such as normal alkanes confined at electrified interfaces, represent an interesting model system to understand the role of hydrophobic tails of amphiphilic molecules. Although the hydrophobic tails are frequently invoked to explain

the structure and properties of amphiphilic molecules at solid-liquid interfaces, there has been little experimental effort to separately study the structure and dynamics of completely hydrophobic molecules, such as alkanes, at these interfaces. Wu et al. studied the penetration of ions across hydrophobic phases in the presence of electric fields by depositing hydronium ions on alkane films on Pt(111) [14]. The activation barrier for the ion penetration through 3-methylpentane was determined to be 38kJ/mol [14]. Ivosevic et al. studied the spreading of hydrocarbon droplets at the dropping mercury electrode (DME) [15]. It was found that various hydrocarbons could spread on the DME within a potential range near the pzc. Longer alkanes spread more readily than shorter ones, presumably due to higher molecule-substrate interactions. However, the existing studies are mostly limited to the thermodynamic description of the interfaces, e.g. measurement of interfacial tension. What is largely unexplored and of particular interest is the surface charge driven microscopic structure and dynamics that correspond to the spreading or aggregation of alkanes on metal electrodes. In this respect, STM, capable of tracking the evolution of individual molecules, provides a particularly powerful approach to tackle this complex problem.

4.1.3. Summary of previous investigations of the structure of alkanes on Au surfaces.

To understand the largely unexplored alkane thin film structures at electrified interfaces, it is instructive to review existing studies of alkanes adsorbed on metal surfaces in UHV or under nonpolar solvents. Such studies can elucidate the role of intermolecular and molecule-substrate interactions, which should be relevant in determining the structures of

alkanes at electrified interfaces despite the additional complexity arising from the electric field dependant electrolyte-substrate and electrolyte-adsorbate interactions.

The physisorption of alkanes on single crystal metal surfaces has served as a model system. For long-chain n-alkanes ($>C_6$), the physisorption energy on Au increases linearly with the chain length by 6.2 ± 0.2 kJ/mol per additional methylene unit [16]. Solvation force measurements, temperature programmed desorption, molecular dynamics and Monte Carlo simulations suggest the formation of alkane layered structures near solid surfaces due to adsorbate-substrate interactions [17-19]. Reflection absorption infrared spectroscopy [20-22] and low energy electron diffraction (LEED) [23] reveal that adsorbed linear alkanes adopt an all trans conformation in ordered layers, with the zig-zag plane of the molecules aligning parallel to the substrate surfaces.

Scanning tunneling microscopy (STM) studies have provided structural details about the physisorbed alkanes adsorbed on metal surfaces [24-30] It was found that the structure of the 2D alkane crystals depends on the substrate crystallography [26, 27]. The long molecular axis of the alkane molecules was preferentially oriented along the $[01 \bar{1}]$ or $[1 \bar{1}0]$ direction of the substrate, i.e. at 30° with respect to the stripes of the reconstruction on Au(111) [26, 27]. Thus a relatively complete picture of alkane adsorption has emerged in UHV and under non-polar solvents, enabling us to address the additional complexities that the aqueous electrolyte and electric fields can introduce.

4.1.4. Summary of this work.

We report a high resolution STM investigation of potential dependant structures of hexadecane on Au(111) under an electrochemical environment. The experiments reported here afford a molecular level understanding of the structure of the hydrophobic phase at electrified interfaces. A variety of charge dependant structures of the hydrophobic phase at the interfaces, including the surface charge induced order-disorder phase transitions as well as the formation of nanometer-sized alkane aggregates, are demonstrated. Consideration of the role of competitive adsorption between the hydrophobic alkane molecules and aqueous electrolyte enables the structures to be rationalized. The observation of rich dynamic behavior, such as the propagation of domains, and flipping of molecular orientations, offer insight into the role of intermolecular interactions in the dynamics of 2D phase transitions. In addition, the observation of 2D hexadecane crystal on unreconstructed Au(111) under electrochemical environment, which could not be observed under non-polar solvent [27], suggests that the aqueous electrolyte may promote the ordering of the hydrophobic thin film. It is hoped that such molecular level understanding of the hydrophobic phase under electrolyte will contribute to the elucidation of the structure and dynamics of amphiphilic molecules at electrified interfaces.

4.2. Experimental.

4.2.1. Sample preparation.

The Au(111) single crystal substrate, a disc 1 cm in diameter and 2 mm thick (Monocrystals Co., Ohio), was cleaned by immersion in hot piranha solution (1:3 H₂O₂ (reagent grade, J. T. Baker) and H₂SO₄ (reagent grade, J. T. Baker)) for 1 hour, and

immersion in hot HNO_3 (reagent grade, EM science) for 30 minutes. (Caution! The piranha solution is a very strong oxidizing reagent and extremely dangerous to handle. Protective equipment including gloves and goggles should be used at all times.) After each step the sample was rinsed by ultrasonication in ultrapure water ($>18 \text{ M}\Omega\cdot\text{cm}$). The crystal was hydrogen flame annealed, and allowed to cool down to room temperature in air. A drop of hexadecane (Acros, 99%) was placed on the surface and rinsed with decane, then allowed to dry in air. The crystal was transferred to the STM electrochemical cell and immersed under potential control ($0.25 \text{ V}_{\text{SCE}}$) in 0.1 M HClO_4 (Optima grade, Fisher Scientific) solution[31]. A Teflon STM cell ensured that only the (111) facet was exposed to electrolyte. The substrate was occasionally electropolished at 3 V potential in $1 \text{ M H}_2\text{SO}_4$ solution [32]. All electrode potentials are quoted relative to the SCE potential.

4.2.2. STM experiments.

STM images were obtained with a PicoScan STM system (Molecular Imaging). A bi-potentiostat (Molecular Imaging) was used to control the sample and tip potential independently. The electrochemical cell was made of Teflon. A silver wire and a platinum wire were used as a quasi-reference electrode and counter electrode, respectively. All cell components were chemically cleaned in the same way as the crystal. Electrochemically etched STM tips, coated with paraffin wax, yielded less than 10 pA Faradic current. All the STM images were obtained under constant current mode at 1.1 nA . The tip potential was kept at 0V_{SCE} , so that the tip-sample bias tracked the

sample potential in the range from 0.05 to 0.65 V. Additional details of the tip fabrication and reference electrode can be found in Appendices C and D.

4.3. Results and discussion.

4.3.1. Structure of Hexadecane monolayers on reconstructed Au(111) surface.

STM images of hexadecane at the Au(111)/0.1 M HClO₄ solution interface at 0.25 V_{SCE} (Figure 4-1) show a molecular row structure crossing the substrate double stripes. The underlying double stripe structure, 0.1 to 0.2 Å high, is due to the reconstruction of the Au(111) surface [33, 34] and is clearly visible even in the presence of adsorbed molecules. The Au(111) surface has two stable phases; the unreconstructed (1×1), consistent with a bulk termination, and the reconstructed (22×√3), where the surface atoms are slightly compressed in [110] directions [33]. In an electrochemical environment, a transition between the two phases can be induced by changing the electrode potential [34]. The reconstructed surface is stable at potentials when the surface has a negative excess charge. It is now well established that the reconstructed Au(111)-(22×√3) surface transforms to the Au(111)-(1×1) phase at potentials above ~440 mV_{SCE}, and that the reverse transition occurs for potentials below ~220 mV_{SCE} in HClO₄ solution [35]. The density of the reconstructed phase is estimated to be about 4.5% higher than the unreconstructed phase [34]. The periodicity of the double stripes of the alkane covered reconstruction is about 63 Å, nearly identical to that observed on a bare Au(111) under electrolyte [34].

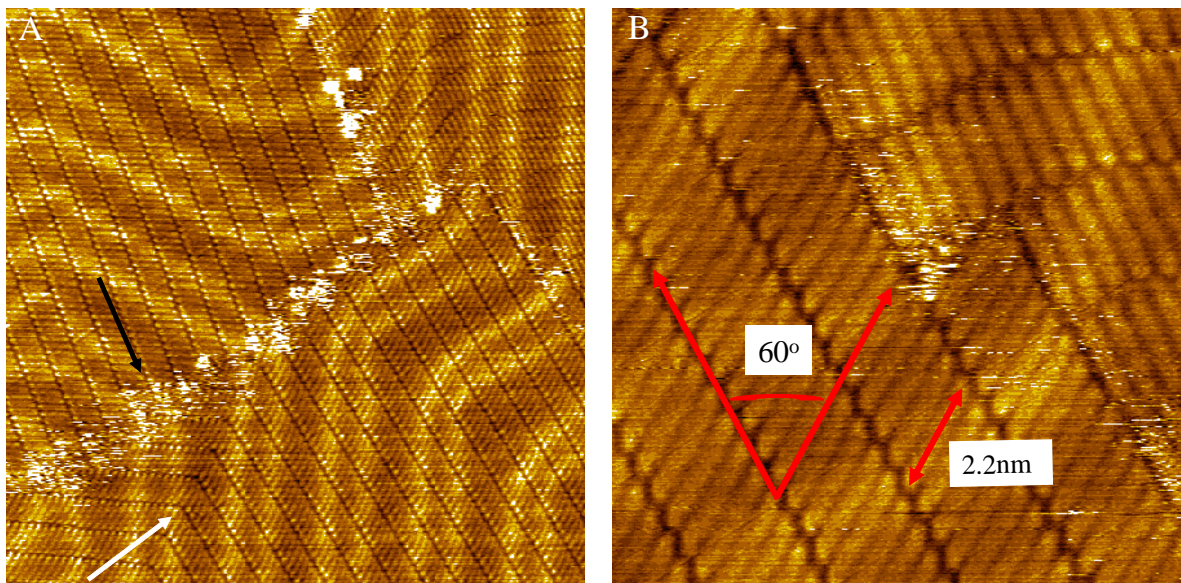


Figure 4-1 Hexadecane on reconstructed Au(111)/ 0.1 M HClO₄ interface at 0.25 V_{SCE}. Molecules adopt extended conformation as 2.2 nm long, and 0.45 nm wide rods parallel to the surface. The molecular axes cross the rows at about 60°. The domain boundaries of the molecular rows are pinned by the domain structure of the reconstruction stripes of the gold surface, as indicated by a black arrow. Scan area (A) 42×42 nm²; (B) 10×10 nm².

A high resolution image, Figure 4-1B, shows that the molecular rows consist of rods 2.2 nm in length, separated by 0.45±0.02 nm, measured perpendicular to the molecular axis. The molecular axes cross the rows at about 60°. The 2.2 nm length is in agreement with the calculated length of hexadecane in an all-trans conformation [36], suggesting that the rods in the STM images correspond to individual hexadecane molecules in an all-trans conformation with the molecular axis parallel to the surface plane. The clear observation of the double stripe substrate structure in the present work indicates that adsorption of alkanes does not lift the Au(111) reconstruction.

The molecular layers adopt a well-defined structure with respect to the underlying substrate. The molecular axis was preferentially oriented at 30° with respect to the stripes

of the gold reconstruction. This result is in agreement with the reported STM result for hexadecane adsorbed on Au(111) under neat hexadecane, where the preferential orientation of the molecular axis is along nearest neighbor (NN) direction (the $[01 \bar{1}]$ or $[1 \bar{1}0]$ direction of the substrate), i.e., at 30° with respect to the stripes of gold reconstruction [24, 25, 27] (Figure 4-2). A consequence of this arrangement is the existence of two equivalent directions of the molecular rows, at $+30^\circ$ and -30° with respect to the double stripes of the Au(111) reconstruction. It should be noted that the hexadecane molecules are not observed on NN(90) $[\bar{1}01]$, which is perpendicular to stripes of reconstruction. Uosaki et al. proposed that the linear alkane chains perpendicular to the stripes of reconstruction experience the greatest corrugation of the double row reconstruction (Figure 4-2B) and therefore this configuration is unfavorable [25].

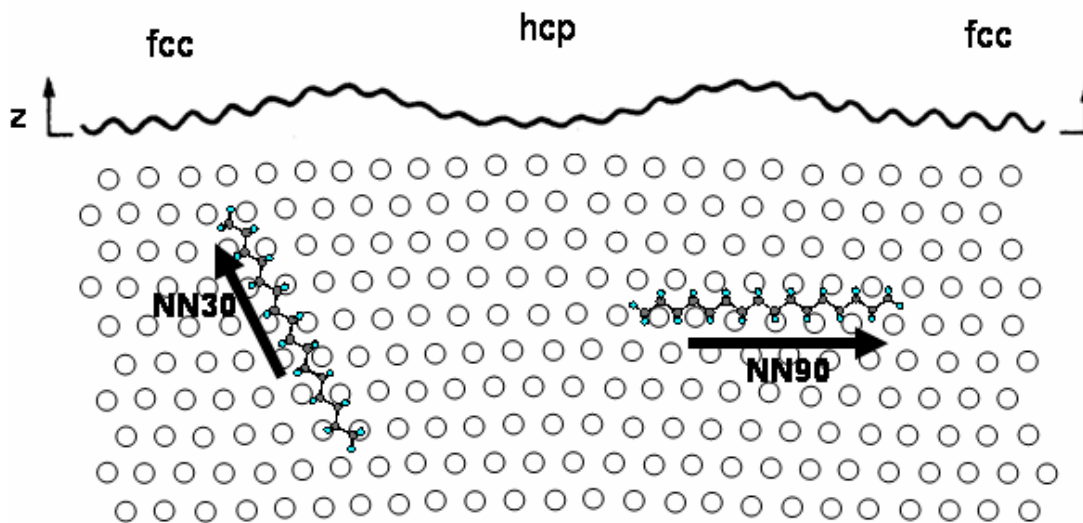


Figure 4-2 Schematic model of the reconstructed gold surface and the relative arrangement of alkanes: (a) NN(30) and (b) NN(90).

The influence of the Au(111) surface reconstruction on the structure of the 2D alkane crystal is apparent as shown in Figure 4-1A and B. Noisy domain boundaries indicated by a black arrow in Figure 4-1A, are formed between molecular rows with different molecular axis orientations. The noise suggests mobility of molecules at the edges of the domains. Interestingly, the domain boundaries of the molecular rows are located at the substrate reconstruction domain boundaries, i.e., the elbows in the double rows of the herringbone structure. Within the same domain, even if the molecular rows change direction, the molecular axis direction does not change (Figure 4-1A as indicated by a white arrow). These results are in good agreement with those reported by Uosaki et al. under non-polar solvent [24, 25].

4.3.2. Potential-induced transformation of 2D hexadecane crystals on Au(111).

4.3.2.1. Order-disorder transitions at potentials positive of the pzc

In order to study the effect of the substrate potential, and the morphology of the Au(111) substrate, on the ordered structures, the electrode potential was changed step by step and STM images were recorded. The row structure and the Au(111) reconstruction were observed as shown in Figure 4-1A even as the electrode potential was stepped as high as 0.55 V_{SCE}. However, when the electrode potential was stepped to 0.65 V_{SCE}, the reconstruction was lifted. The characteristic double stripe structure of the reconstructed Au(111) disappeared, and characteristic monoatomic high Au islands, resulting from the lifting of the reconstruction at positive potential [33], appeared as seen in Figure 4-3A and B.

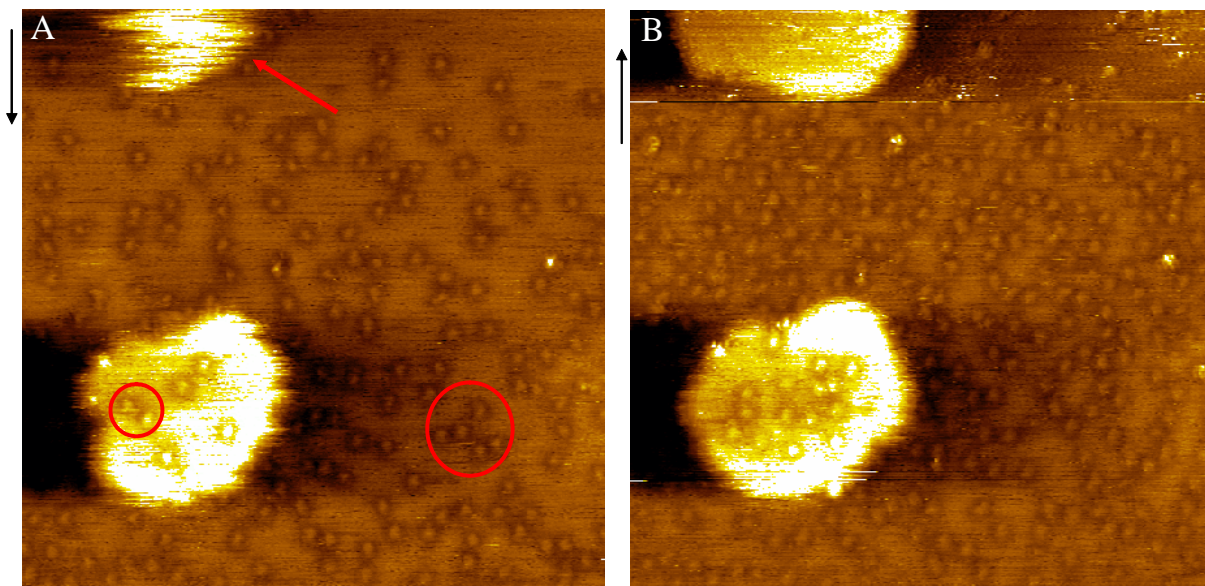


Figure 4-3 Hexadecane on Au(111) in 0.1 M HClO_4 solution at $0.65 V_{\text{SCE}}$. The reconstruction is lifted and Au islands appear. At the same time, ordered hexadecane rows have disappeared, and dots, about 1 nm in diameter appeared on the surface and grew in number with time. (A) after 0-95 seconds after potential step to $0.65 V_{\text{SCE}}$, (B) after 96-190 seconds after potential step. Scan area: $32 \times 32 \text{ nm}^2$. Scan direction is indicated by black arrows at the top left side of each image.

At the same time, the ordered hexadecane layers disappeared, and rings, about 1 nm in diameter, appeared on the surface. These rings are depressions $0.3\text{-}0.5 \text{ \AA}$ deep and are present on the Au islands. We attribute these rings to hexadecane molecules adopting vertical or tilted orientations. Hexadecane molecules lying flat on the surface enhance tunneling as evidenced by the imaging of the 2.2 nm long rods as protrusions in the STM images. The enhancement of tunneling of physisorbed insulating molecules has been rationalized by the weak coupling between states in the adsorbate and states in the substrate near the Fermi level [37]. The coupling of these states, which obviously requires geometric proximity, renders the adsorbate an antenna to receive tunneling electrons [37]. The flat orientation of hexadecane molecules allows maximum coupling to the substrate and therefore enhances tunneling. However, if the hexadecane molecules

adopt another orientation, e.g., vertical or tilted, in which only a small part of the chain is in van der Waals contact with the substrate, coupling between the molecules and the substrate may be significantly weakened. Tunneling through the molecules may be suppressed to the extent that the tunneling probability through nearby solvent molecules is greater, reversing the contrast. Consequently, the molecules may be imaged in STM as depressions on the surface. Therefore, we speculate that the dark ring structures, enclosing a bright core, are Au clusters surrounded by hexadecane molecules. The density of the rings increased with time after the lifting of the reconstruction from less than 20/100 nm² to about 50/100 nm² after 95 seconds.

The Au islands grew slowly, adopting hexagonal shapes and their edges became more well-defined, as shown in Figure 4-3A and Figure 4-3B, as a function of time. This result differs from our previous studies of the growth and dissolution of nanoscale Au islands in pure 0.1 M HClO₄ solutions, where the Au islands created by the lifting of the Au(111) reconstruction formed almost immediately and adopted a shape that was more circular than polygonal [31]. Closer inspection of the images reveals that the island edges are fuzzy, suggesting that the islands are in the process of dynamic evolution [38]. Atoms are continuously attaching, detaching or diffusing along the island edges. Clearly the presence of the hexadecane molecules affects the structures and dynamics of the gold islands. Au adatoms are ejected onto the surface upon lifting of the reconstruction. The growth of Au islands is a consequence of the aggregation of the adatoms. We suggest that the adsorption of alkanes hinders the surface diffusion of these adatoms, which is necessary for their incorporation into islands, slowing down the growth the islands. In

pure 0.1 M HClO₄ solutions, the Au(111) reconstruction lifts at a significantly lower potential, 0.4-0.45 V_{SCE} [33, 35]. The STM results presented here suggest that the 2D molecular crystals stabilize the reconstructed herringbone structure of the reconstructed Au(111) to a higher potential than in neat HClO₄.

When the potential was stepped back from 0.65 V_{SCE} to 0.25 V_{SCE}, the ring structures disappeared and small clusters, imaged as protrusions appeared. Simultaneously, the ordered 2D molecular structures recovered on the unreconstructed Au(111) surfaces as shown in Figure 4-4A. The correlation between the disappearance of the rings and the appearance of ordered molecular rows, suggests that the rings may be composed of aggregated molecules. Therefore, as the alkanes incorporate into the molecular rows, the rings disappeared and the Au clusters left behind are imaged as protrusions. This is consistent with the finding that alkanes form droplets at potentials far away from the pzc but spread out on the metal surface near the pzc [15]. The monoatomic high Au islands are observed to assume a hexagonal shape, in sharp contrast to the round shape observed in neat 0.1 M HClO₄ [31]. This is presumably due to the pinning of the island perimeter atoms by hexadecane molecules. Monoatomic Au islands of similar shape have been reported by Lipkowski et al. in their STM study of surfactants adsorbed on Au [12].

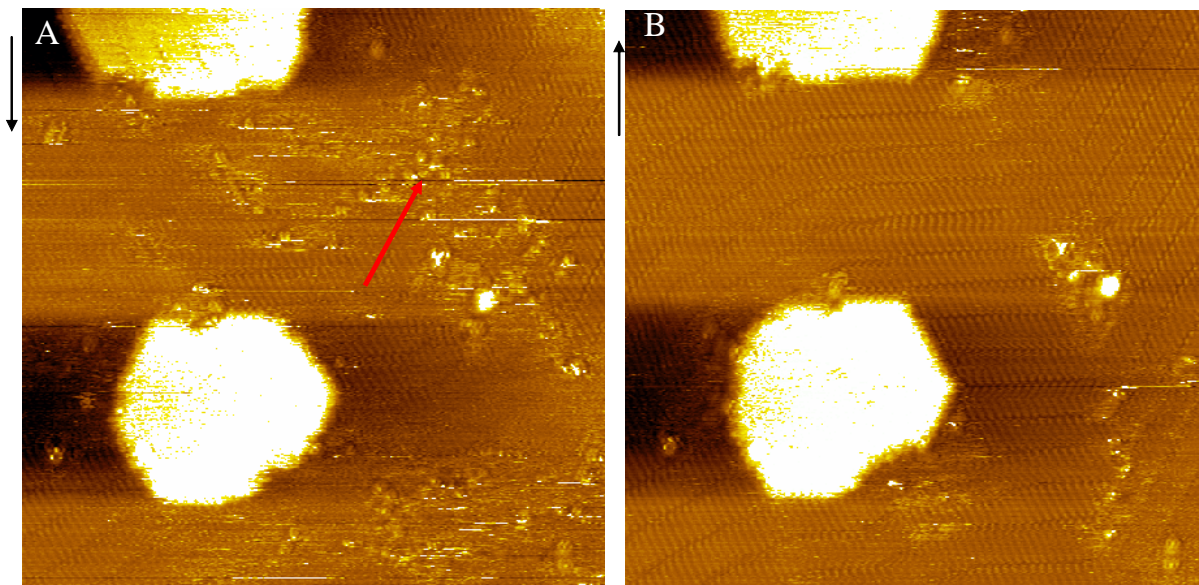


Figure 4-4 Hexadecane on Au(111) in 0.1 M HClO₄ solution, at 0.25 V_{SCE} after potential was stepped back from 0.65 V_{SCE}. The dots begin to disappear and the ordered molecular row structures recover on the unreconstructed Au(111) surface. (A) after 0-95 seconds after potential step to 0.25 V_{SCE}, (B) after 96-190 seconds after potential step. Scan area: 32 × 32 nm².

At the potential of 0.65 V_{SCE}, the surface is positively charged, attracting the polar aqueous solvent that presumably displaces the non-polar hexadecane molecules. Hexadecane is insoluble in water. Hence the adsorbed hexadecane begins to aggregate to minimize hydrophobic interactions. In the SPM study of potential dependant structure of dodecyl sulfate on Au(111), Lipkowski et al. observed that dodecyl sulfate forms hemimicelles near the pzc but desorbs at negative potential [12]. Unlike surfactant molecules, which are soluble in water, the hexadecane molecules cannot leave the surface by desorbing into the bulk aqueous phase. The hexadecane aggregates are probably quite mobile as the area of interaction with the surface is reduced, to allow the electrolyte access to the surface, with a concomitant reduction in the binding energy of hexadecane to the surface. However, when the potential was stepped back to 0.25 V_{SCE}, close to the

pzc, the aggregated molecules can re-assemble into ordered layers to maximize the adsorbate-substrate interaction. This releases the gold atoms trapped in the clusters.

It is worth noting that hexadecane molecules can form ordered structures on an unreconstructed Au(111) surface. This is in contrast to the result reported in a nonpolar solvent, that, hexadecane molecules can not form ordered structures on the unreconstructed Au(111) surface [27]. Comparison with Figure 4-1A, acquired before the lifting of reconstruction, allows the determination of the substrate orientations. It can be concluded that the molecular axes are again aligned along nearest neighbor (NN) direction (the $[01\bar{1}]$ or $[1\bar{1}0]$ direction of the unreconstructed Au(111)). The similarity of the molecule orientation with respect to lattice on reconstructed (Figure 4-1A) and unreconstructed (Figure 4-4B) suggests that the orientation of the molecular axes is determined by the hexagonal packing of the Au lattice. However, the reconstruction plays a role in pinning domain boundaries (Figure 4-1A).

4.3.2.2. *Order-disorder transitions negative of the pzc.*

A reversible order-disorder transition is also observed at potentials lower than the pzc. When the electrode potential was stepped from 0.15 V_{SCE} to 0.05 V_{SCE}, the ordered molecular structures disappeared as shown in Figure 4-5, indicating that the ordered adlayer transformed into a disordered structure. However, no aggregates, dots or rings similar to the ones in Figure 4-3 were observed when the potential induced order-disorder phase transition was triggered. It is assumed that this is due to the lack of Au adatoms, which can only be produced during the lifting of the Au reconstruction at high potentials. These adatoms may be required to form and stabilize the molecule-encapsulated

aggregates (rings). The surface becomes more negatively charged as the potential stepped from 0.15 V_{SCE} to 0.05 V_{SCE}. (The pzc of unreconstructed Au(111) is about 0.35 V_{SCE} [33].) The more negative the surface charge, the greater the interaction between the substrate and the polar solvent molecules and positive ions. As a result, the alkane molecules are displaced by the electrolyte at potentials significantly negative of the pzc (Figure 4-8).

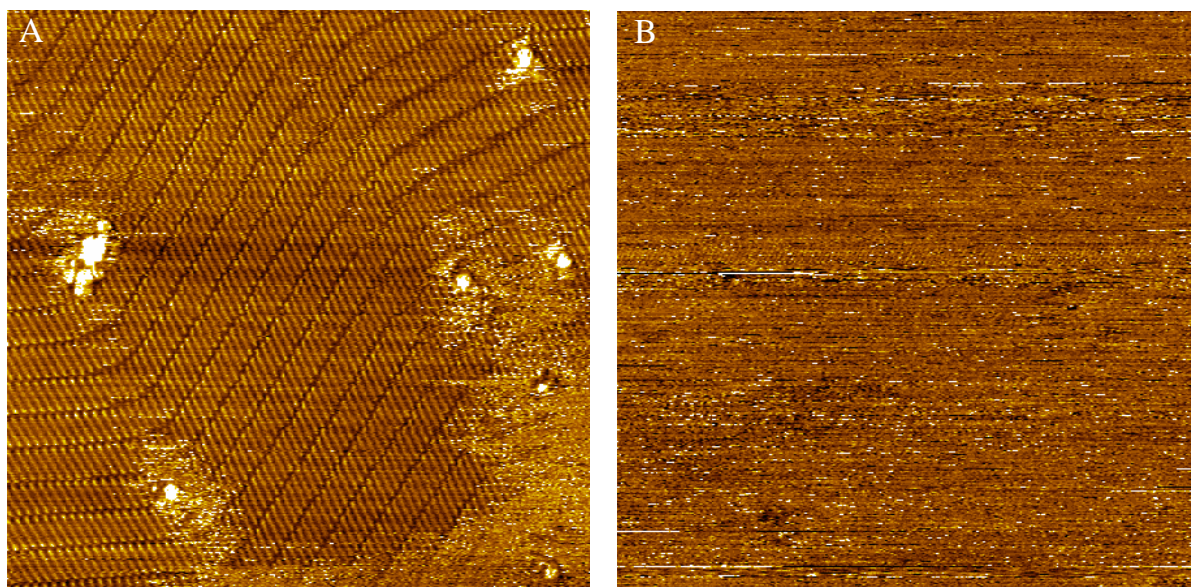


Figure 4-5 Hexadecane on Au(111) in 0.1 M HClO₄ solution. When potential was stepped from 0.15 V_{SCE} (A) to 0.05 V_{SCE} (B), the ordered molecular rows disappeared. Scan area: 32 × 32 nm².

The potential induced order-disorder transitions are quite reversible. Stepping the potentials back to 0.25 V, results in the appearance of ordered molecular domains that initially grew rapidly as evidenced by the almost immediate appearance of molecular rows as shown in Figure 4-6B. Subsequently, the ordered domain grew slowly at the expense of the disordered domain. The boundary between the ordered and the disordered domains moved in the direction of the ordered molecular rows. It is estimated that the

2D crystal grew at a rate of about 0.2 nm/sec by comparing the position of the domain boundary in Figure 4-6C with Figure 4-6B.

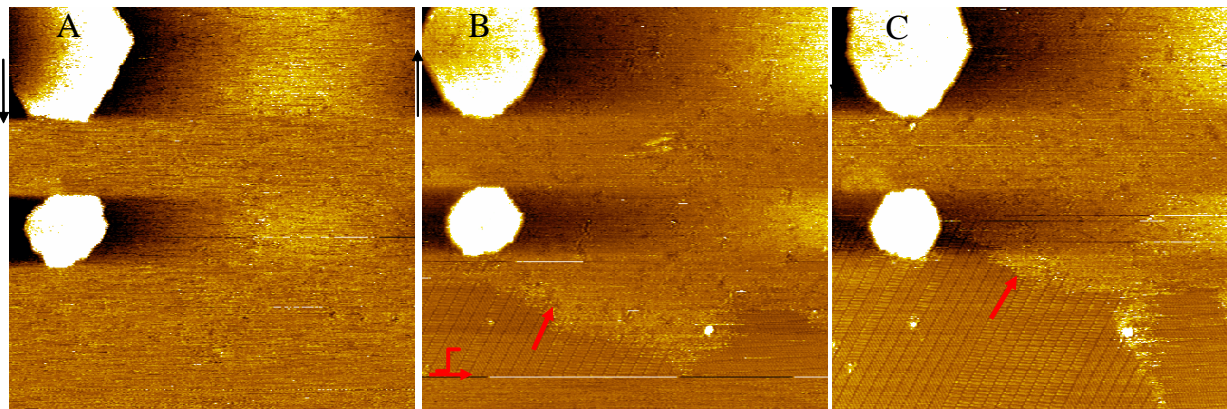


Figure 4-6 Hexadecane on Au(111) in 0.1 M HClO₄ solution (A) obtained at 0.05 V_{SCE}. (B) after potential step to 0.25 V_{SCE}, the ordered molecular rows reappear immediately; (C) 96-190 seconds after potential step, ordered molecular layers domain continue to grow. Scan area: 65 × 65 nm².

We also note that the order-disorder transitions are reversible. This suggests that the molecules displaced by the electrolyte on charged surface remain in the vicinity of the surface instead of being completely desorbed into the electrolyte and diffusing away from the surface (Figure 4-8). When the potential returns to the pzc, the displaced molecules are immediately available to form the 2D molecular crystal. This is not surprising considering the hydrophobicity of the hexadecane molecules, manifested by negligible solubility in bulk water.

4.3.3. Spontaneous molecular domain flipping.

There are two different possible molecular orientations in a row. In one domain, the molecules are tilted +60° with respect to the molecular rows. In the other they are tilted at -60°. The tilt angles are probably related to the symmetry of the Au(111) substrate,

indicating the role of adsorbate-substrate interactions in determining the molecular orientation. The presence of two different molecular orientations in a single row is sometimes observed as indicated by arrows in Figure 4-7A. The boundary between two domains is the line where the molecular 2D crystals show different orientations of molecules in the rows. The images also reveal features that we attribute to the sudden change of molecular orientation that occurs while the image is being acquired. The "partial" molecules observed in Figure 4-7A are in fact molecules "caught" in the action of changing orientation.

We suggest that the change of molecular orientation is caused by the merging of domains. When two domains merge (Figure 4-7D), the rows from different domains merge to form a single row, as can be seen in the bottom right hand corner of Figure 4-7D. If two rows, each containing molecules with a different orientation, are to merge seamlessly then the molecules in one of the rows will have to change orientation upon merging so that the new row will contain molecules with a single orientation to minimize repulsion. This reorientation presumably initiates at the domain boundary and travels down the row, a kind of "domino effect", resulting in the observation of "partial" molecules as the reorientation propagates down the row while the STM scans upward. This occurs rapidly as the STM scans because only parts of the flipped molecules are imaged.

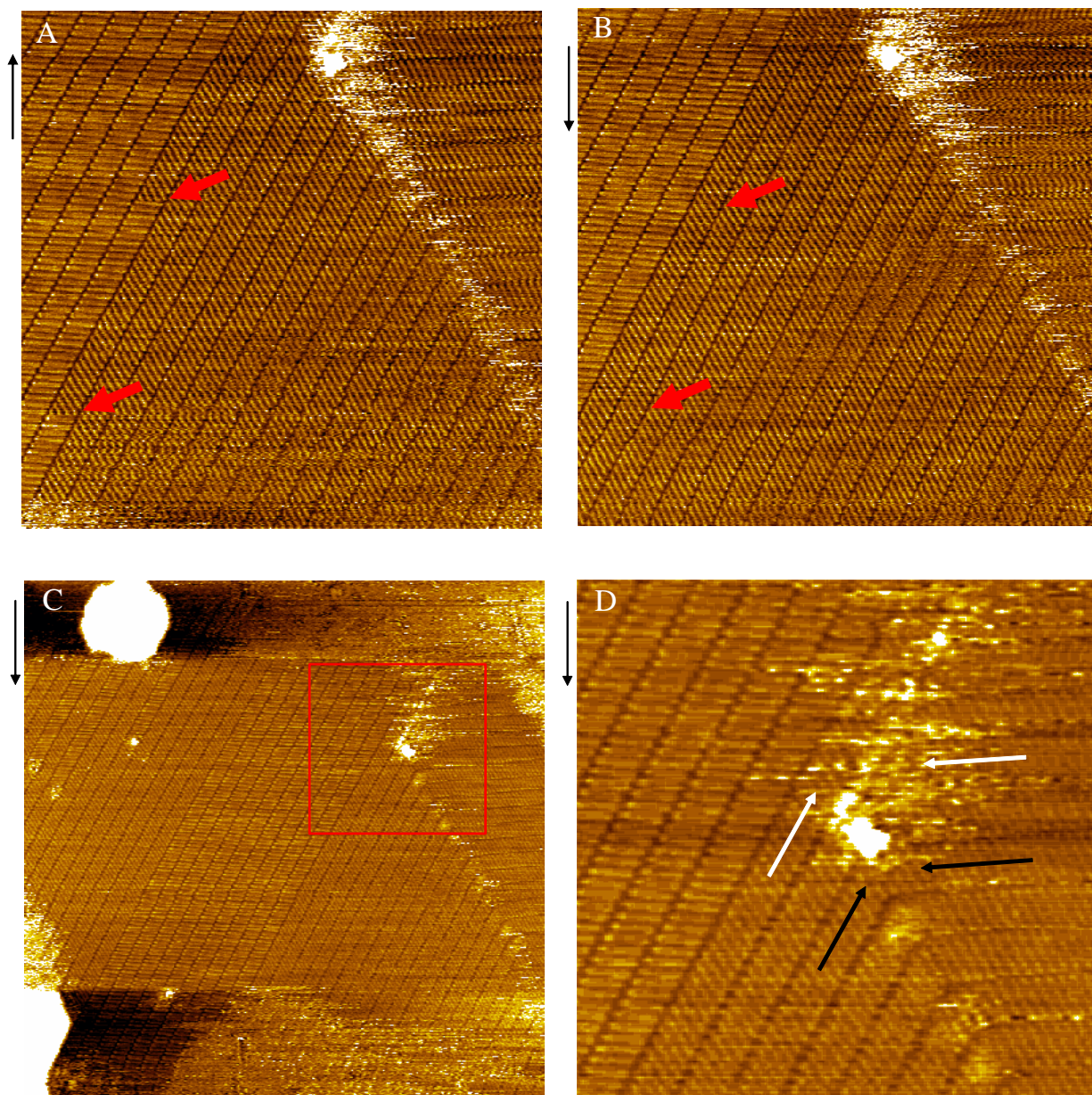


Figure 4-7 Spontaneous molecular domain flipping; Hexadecane on Au(111) in 0.1 M HClO₄ solution at 0.25 V_{SCE}. Two different molecular orientations in a single row are indicated by arrows. (A) Sudden change of molecular orientation during scanning results in a single orientation. (B) The likely cause is the merging of domains, indicated by arrows in D. Scan area (A-B) 34.5 × 34.5 nm², (C) obtained before (A), 65 × 65 nm², (D) Zoom in of Figure 6 C, 20 × 20 nm².

The rows indicated by black arrows in Figure 4-7D have merged, i.e. the molecules in the two rows assume the same orientation. The white arrows in Figure 4-7D indicate rows that have not yet merged. The domain boundary is noisy, probably reflecting mobile molecules attempting to find the lowest energy configuration. When the merging is complete, molecules in one of the rows must change orientation in order to minimize the repulsion in the new merged row. When two rows containing molecules with different orientations merge, a single orientation ultimately prevails. This indicates the critical role of intermolecular interactions for molecular self-assembly in this system.

The upper limit of the time scale of flipping can be estimated. The clarity of the imaged partial molecules suggest that the flipping of molecules in a row is concerted within the time scale of a scan cycle along the fast axis (~0.1 sec). If all the molecules did not flip within a short period of time, the horizontal and tilted molecules would coexist in a row. Due to the stress induced by the molecules with different orientations, the molecules in the row would not be locked in a stable configuration, and would not be clearly imaged by STM. Therefore, the area indicated by arrows in Figure 4-7A would appear noisy, which it does not. Tip interactions are discounted because (1) the molecules change orientation away from parallel to the fast scanning direction of the tip, the direction one would expect to be favored if tip induced effects were occurring as reported by Stevens et al. [39], to a direction that makes an angle with the scan direction; (2) Further transitions were not observed in subsequent images, although there is still a boundary between the molecular rows with different orientations, and the tip is still interacting with the molecules.

4.3.4. Stabilization of substrate by molecular overlayers.

It should be noted that there is no sign of reconstruction of the Au substrate, from Figure 4-4 to Figure 4-7, even though the substrate is in a potential range where the Au(111) surface should be reconstructed in the absence of adsorbed hexadecane molecules. This indicates that the adsorption of hexadecane stabilizes the unreconstructed Au(111). This is in contrast with the result shown in Figure 4-3, where the assembled hexadecane molecules stabilize the reconstructed Au(111). The results presented here show that the adsorption of a physisorbed hexadecane stabilizes both the reconstructed structure and unreconstructed structure over a wider potential range than in neat 0.1 M HClO₄. In addition to slower diffusion of Au adatoms (discussed in section 3.2.1), another possible reason for the observed stabilization is that the adsorption of insoluble alkane molecules screens the polar H₂O molecules and electrolyte ions from the gold surface, reducing the capacitance and charge density of the double layer. Therefore, in the presence of hexadecane, a more positive potential is required to lift the reconstruction and a more negative potential is required to form reconstruction. As a consequence, both the reconstructed surface and the unreconstructed surface are stable over a wider potential range. It is worth noting the contrasting role in substrate reconstruction played by specifically adsorbed anions, such as Cl⁻, [33] that destabilize the reconstruction, shifting the (1x1) - (22x√3) phase transition potential to more negative values. These anions are believed to facilitate the phase transition between the reconstructed and unreconstructed phase of Au(111) by weakening the bond between the bulk and Au surface atoms [33].

The insoluble hexadecane layer on the contrary probably prevents interactions between the electrolyte and the substrate, until the solvent actually displaces the alkanes.

4.3.5. Discussion.

4.3.5.1. Nature of the potential induced order-disorder phase transition.

The principal interactions that determine the structure of the molecular monolayer at the surface are molecule-substrate interactions and molecule-molecule interactions[40]. If only molecule-solvent interactions were important one would not expect a strong effect of potential on the observed structures. Physisorbed alkanes interact with the Au surface through weak dispersion forces. In electrochemical systems, one needs to consider the additional effect of surface charge and the electrolyte. Due to the low polarizability of alkanes, any modulation of alkane-substrate interaction by the electric field is expected to be much less important than the effect of surface charge in enhancing the adsorption of the aqueous electrolyte. When the electrode potential is at the pzc, the surface is free of charge. It is near this potential that the adsorption of alkane molecules results in the long range ordered structures observed in Figure 4-1. Higher or lower potentials will charge the surface with positive or negative charge, attracting ions and water molecules. This eventually results in the displacement of hexadecane molecules, which leads to the disordering of the adlayer (Figure 4-8).

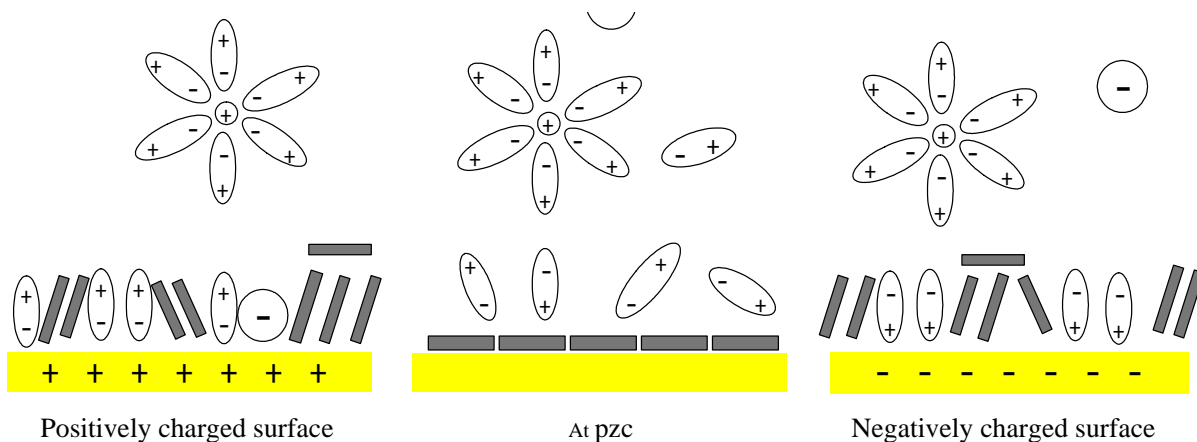


Figure 4-8 The effect of surface charge on molecular adsorption. At low surface charge density, hexadecane lies flat, forming an ordered domain. At high surface charge density, positive or negative, the solvent is attracted to the substrate, displacing hexadecane molecules.

4.3.5.2. Observation of ordered structures on unreconstructed surface.

It is worth noting that hexadecane molecules can form ordered structures on an unreconstructed Au(111) surface. This is in contrast to the result reported in a nonpolar solvent, that, STM did not observe ordered structures of hexadecane on unreconstructed Au(111) surface. The inability to form ordered structures was attributed to a slight lattice mismatch between the van der Waals diameter of alkyl chains and the atomic troughs along $[01\bar{1}]$ [27]. It suggests that electrochemical interfaces may promote the ordering of hydrophobic adlayers. An important origin of the ordering is 2D confinement on the surface [17]. To adopt a maximum coverage, adsorbates must form an ordered structure. Under an aqueous environment, due to the hydrophobic interaction, segments of adsorbed alkane molecules may have less tendency to desorb than under a non polar solvent (Figure 4-9). This confinement effect may lead to the formation of more ordered structures. This effect suggests the role of hydrophobic interactions in self-assembly.

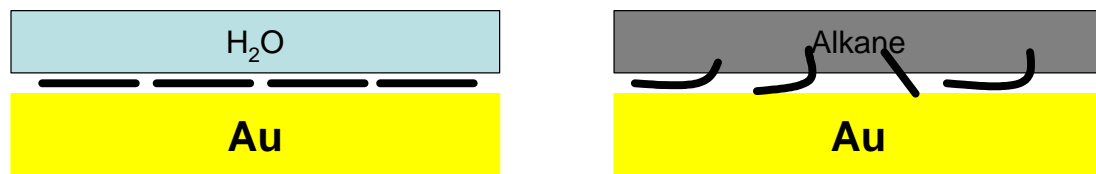


Figure 4-9 Alkane adsorbates confined at water/ Au interface and alkane/Au interface.

4.3.5.3. Possible structure of alkane aggregates.

However, questions concerning the structure of the displaced hexadecane molecules arise. The rings observed in Figure 4-3 can be ascribed to alkane aggregates surrounding Au nanoclusters. So far we only observed the ring structures, that we assign to hexadecane containing aggregates, on the surface at positive potential when mobile adatoms are also present due to the lifting of the reconstruction. It is well known that amphiphilic surfactant molecules can form well-defined aggregates such as hemimicelles at charged interfaces [3]. However, the surfactant hemi-micelle aggregates requires the presence of hydrophilic headgroups as well as hydrophobic tails. The nature of the interactions that might hold the alkane molecules together in the well-defined nm-sized aggregates is unclear, but is probably driven by hydrophobic effects. We suggest the aggregates result from the concerted effect of repulsion by aqueous electrolyte and the preferred incorporation of isolated small Au clusters in the core of the aggregate. The nanometer sized Au clusters formed from the lifting of reconstruction may adsorb alkanes more strongly due to the lower coordination number of Au atoms in the clusters. Therefore Au nanoclusters may nucleate and stabilize the presumed alkane aggregates. Despite the high spatial resolution of STM, it is noted that due to the nature of the contrast mechanism, which relies on electron tunneling probabilities, it will probably not be possible to image aggregates adopting conformations characterized by low

conductivity, e.g., vertical orientations. Therefore, it will be useful to use AFM to study the structures of alkane aggregates at high surface charge density.

4.4. Summary.

This study provides the first direct visualization of potential dependant structures of adsorbed alkanes at an electrochemical interface. Near the pzc, hexadecane monolayers under electrolyte remarkably resemble those observed under non-polar solvents in forming ordered monolayers, consisting of molecular rows, on Au surfaces [24, 27]. One major difference is the observation of ordered monolayers on unreconstructed Au(111). The structure of molecular adlayers were found to be heavily dependant on electrode potential. Molecular layers at the Au(111) surface can be reversibly switched between ordered and disordered structures by driving the electrode potential away from the pzc. Rings, 1 nm in diameter, were observed when the potential was stepped to 0.65 V on a reconstructed surface previously covered with an ordered hexadecane monolayer. The rings are tentatively assigned to aggregates of hexadecane molecules. When the electrode potential is lower than 0.15 V, the ordered molecular rows disappeared from the negatively charged electrode surface. The ordered molecular rows recovered when the electrode potential returned to voltages close to the pzc of Au(111). The ordered hexadecane rows are observed to stabilize both the reconstructed and unreconstructed Au(111) surfaces. This behavior is assumed to result from the screening of the polar H₂O molecules and electrolyte ions from the gold surface as well as the hindrance of adatom diffusion by adsorbed alkane molecules.

BIBLIOGRAPHY

1. Flink, S., F.C.J.M. van Veggel, and D.N. Reinhoudt, *Sensor functionalities in self-assembled monolayers*. Adv. Mater. (Weinheim, Ger.), 2000. **12**(18): p. 1315-1328.
2. Laibinis, P.E. and G.M. Whitesides, *Self-assembled monolayers of n-alkanethiolates on copper are barrier films that protect the metal against oxidation by air*. Journal of the American Chemical Society, 1992. **114**(23): p. 9022-9028.
3. Evans, D. and H. Wennerstrom, *The colloidal domain*. 1999, New York: Wiley-VCH. 295.
4. De Levie, R., *Electrochemistry of artificial ultrathin lipid membranes. A review*. J. Electroanal. Chem. Interfacial Electrochem., 1976. **69**(3): p. 265-97.
5. Ulman, A., *An introduction to ultrathin organic films : from Langmuir- Blodgett to self-assembly*. 1991, Boston: Academic Press.
6. Walczak, M.M., D.D. Popenoe, R.S. Deinhammer, B.D. Lamp, C. Chung, and M.D. Porter, *Reductive desorption of alkanethiolate monolayers at gold: a measure of surface coverage*. Langmuir, 1991. **7**(11): p. 2687-93.
7. Hatchett, D.W., R.H. Uibel, K.J. Stevenson, J.M. Harris, and H.S. White, *Electrochemical measurement of the free energy of adsorption of n-alkanethiolates at Ag(111)*. Journal of the American Chemical Society, 1998. **120**(5): p. 1062-1069.
8. Kurtyka, B. and R. de Levie, *The hydrophobic electrode*. J. Electroanal. Chem., 1995. **397**(1-2): p. 311-14.
9. Lipkowski, J. and L. Stolberg, *Adsorption of molecules at metal electrodes*, ed. J. Lipkowski and P. Ross. 1992, New York: VCH. 171.
10. Gao, X.P., H.S. White, S.W. Chen, and H.D. Abruna, *Electric-Field-Induced Transitions of Amphiphilic Layers on Mercury-Electrodes*. Langmuir, 1995. **11**(11): p. 4554-4563.
11. Bizzotto, D. and J. Lipkowski, *Electrochemical and spectroscopic studies of the mechanism of monolayer and multilayer adsorption of an insoluble surfactant at the Au(111)/electrolyte interface*. Journal of Electroanalytical Chemistry, 1996. **409**(1-2): p. 33-43.
12. Burgess, I., C.A. Jeffrey, X. Cai, G. Szymanski, Z. Galus, and J. Lipkowski, *Direct visualization of the potential-controlled transformation of hemimicellar aggregates of dodecyl sulfate into a condensed monolayer at the Au(111) electrode surface*. Langmuir, 1999. **15**(8): p. 2607-2616.
13. Esplandiu, M.J., H. Hagenstrom, and D.M. Kolb, *Functionalized self-assembled alkanethiol monolayers on Au(111) electrodes: 1. Surface structure and electrochemistry*. Langmuir, 2001. **17**(3): p. 828-838.
14. Wu, K., M.J. Iedema, and J.P. Cowin, *Ion penetration of the water-oil interface*. Science, 1999. **286**(5449): p. 2482-2485.
15. Ivosevic, N., V. Zutic, and J. Tomaic, *Wetting equilibria of hydrocarbon droplets at an electrified interface*. Langmuir, 1999. **15**(20): p. 7063-7068.

16. Wetterer, S.M., D.J. Lavrich, T. Cummings, S.L. Bernasek, and G. Scoles, *Energetics and kinetics of the physisorption of hydrocarbons on Au(111)*. Journal of Physical Chemistry B, 1998. **102**(46): p. 9266-9275.
17. Xia, T. and U. Landman, *Molecular Dynamics of adsorption and segregation from an alkane mixture*. Science, 1993. **261**(5126): p. 1310.
18. Wang, J.-C. and K.A. Fichthorn, *Molecular configurations and solvation forces in confined alkane films*. Mater. Res. Soc. Symp. Proc., 1999. **543**(Dynamics in Small Confining Systems IV): p. 63-68.
19. Balasubramanian, S., M.L. Klein, and J.I. Siepmann, *Simulation studies of ultrathin films of linear and branched alkanes on a metal substrate*. Journal of Physical Chemistry, 1996. **100**(29): p. 11960-11963.
20. Bishop, A.R., M.J. Hostetler, G.S. Girolami, and R.G. Nuzzo, *Transport dynamics in ordered bilayer assemblies of the n- alkanes on Pt(111)*. Journal of the American Chemical Society, 1998. **120**(14): p. 3305.
21. Yamamoto, M., Y. Sakurai, Y. Hosoi, H. Ishii, K. Kajikawa, Y. Ouchi, and K. Seki, *Structures of a long-chain n-alkane, n-C44H90, on a Au(111) surface: An infrared reflection absorption spectroscopic study*. Journal of Physical Chemistry B, 2000. **104**(31): p. 7363-7369.
22. Yamamoto, M., Y. Sakurai, Y. Hosoi, H. Ishii, E. Ito, K. Kajikawa, Y. Ouchi, and K. Seki, *Physisorption of a long-chain eta-alkane on Ag(111) surface: an infrared reflection absorption spectroscopic study*. Surface Science, 1999. **428**: p. 388-392.
23. Firment, L.E. and G.A. Somorjai, *Surface structures of normal paraffins and cyclohexane monolayers and thin crystals grown on the (111) crystal face of platinum. A low-energy electron diffraction study*. J. Chem. Phys., 1977. **66**(7): p. 2901-13.
24. Uosaki, K. and R. Yamada, *Formation of two-dimensional crystals of alkanes on the Au(111) surface in neat liquid*. Journal of the American Chemical Society, 1999. **121**(16): p. 4090-4091.
25. Yamada, R. and K. Uosaki, *Two-dimensional crystals of alkanes formed on Au(111) surface in neat liquid: Structural investigation by scanning tunneling microscopy*. Journal of Physical Chemistry B, 2000. **104**(25): p. 6021-6027.
26. Yamada, R. and K. Uosaki, *In situ observation of the two-dimensional crystals of alkanes on a reconstructed Au(100) surface in neat liquid by scanning tunneling microscopy*. Langmuir, 2000. **16**(10): p. 4413-4415.
27. Xie, Z.X., X. Xu, J. Tang, and B.W. Mao, *Reconstruction-dependent self-assembly of n-alkanes on Au(111) surfaces*. Journal of Physical Chemistry B, 2000. **104**(49): p. 11719.
28. Xie, Z.X., X. Xu, J. Tang, and B.W. Mao, *Molecular packing in self-assembled monolayers of normal alkane on Au(111) surfaces*. Chemical Physics Letters, 2000. **323**(3-4): p. 209-216.
29. Marchenko, O. and J. Cousty, *Molecule length-induced reentrant self-organization of alkanes in monolayers adsorbed on Au(111)*. Physical Review Letters, 2000. **84**(23): p. 5363-5366.

30. Marchenko, A., Z.X. Xie, J. Cousty, and L.P. Van, *Structures of self-assembled monolayer of alkanes adsorbed on Au(111) surfaces*. Surface and Interface Analysis, 2000. **30**(1): p. 167-169.
31. He, Y. and E. Borguet, *Dynamics of Metastable Nanoscale Island Growth and Dissolution at Electrochemical Interfaces by Time-Resolved STM*. Journal of Physical Chemistry B, 2001. **105**: p. 3981-3986.
32. Whitton, J.L. and J.A. Davies, *An electrochemical technique for removing thin uniform layers of gold*. J. Electrochem. Soc., 1964. **111**: p. 1347-1349.
33. Kolb, D.M., *Reconstruction phenomena at metal-electrolyte interfaces*. Prog. Surf. Sci., 1996. **51**(2): p. 109-73.
34. Gao, X., A. Hamelin, and M.J. Weaver, *Atomic relaxation at ordered electrode surfaces probed by Scanning Tunneling Microscopy: Au(111) in aqueous solution compared with ultrahigh-vacuum environments*. J. Chem. Phys., 1991. **95**: p. 6993.
35. Tao, N.J. and S.M. Lindsay, *Kinetics of a potential induced $23x\text{-root-3}$ to $1x1$ transition of Au(111) studied by in situ scanning tunneling microscopy*. Surface Science, 1992. **274**(2): p. L546-L553.
36. Hentschke, R., B. Schurmann, and J. Rabe, *Molecular Dynamics simulations of ordered alkane chains physisorbed on graphite*. Journal of Chemical Physics, 1992. **96**(8): p. 6213.
37. Giancarlo, L.C. and G.W. Flynn, *Scanning tunneling and atomic force microscopy probes of self- assembled, physisorbed monolayers: Peeking at the peaks*. Annual Review of Physical Chemistry, 1998. **49**: p. 297.
38. Giesen, M., M. Dietterle, D. Stapel, H. Ibach, and D.M. Kolb, *Step fluctuations on metals in contact with an electrolyte: a new access to dynamical processes at the solid/liquid interface*. Surface Science, 1997. **384**(1-3): p. 168-178.
39. Stevens, F., D. Buehner, and T.P. Beebe, *Ordering of adsorbed organic monolayers confined in molecule corrals during scanning tunneling microscopy observation*. Journal of Physical Chemistry B, 1997. **101**(33): p. 6491-6496.
40. VanHove, M.A., *Surface crystallography at the metal-gas interface*, in *Structure of Electrified Interfaces*, J. Lipkowski and P.N. Ross, Editors. 1993, VCH Publishers, Inc.: New York.

5. Porphyrin self-assembly at electrochemical interfaces: Role of potential modulated surface mobility.

5.1. Introduction.

5.1.1. Molecular self-assembly on surfaces.

Controlled assembly of individual molecules on surfaces has the potential to supplement lithographic techniques in manufacturing, as nanoscale molecular engineering becomes an integral part of miniaturization in electronic and photonic devices [1]. However, precise control of supramolecular structures on surfaces requires that a number of fundamental questions be resolved regarding the nature of the controlled assembly process, including the roles of adsorbate-adsorbate and adsorbate-substrate interactions as well as related phenomena such as surface diffusion and adsorption. Non-covalent intermolecular interactions including hydrogen bonding [2], weak electron donor-acceptor [3, 4], and dipole-dipole interactions [5] have been employed to control two dimensional molecular self-assembly. In addition, adsorbate-substrate interactions, and resulting surface mobility, play pivotal roles in forming ordered structures. Strong adsorbate-substrate interactions result in low surface mobility, hindering the assembly of the ordered structures that are favored by adsorbate-adsorbate interaction.

Common strategies to tune surface mobility at vacuum-solid and gas-solid interfaces include annealing at elevated temperature [6, 7] and weakening the adsorbate-substrate interaction through surface modification with a passivating layer [6, 8]. Recently, Hipps et al. formed ordered adlayers of coadsorbed phthalocyanines, CoPc and F₁₆CoPc. F₁₆CoPc, which has sixteen electron-withdrawing fluorine substituents, alone cannot

form ordered adlayers due to strong electrostatic interaction with the surface [9]. The coexistence of electron-withdrawing $F_{16}CoPc$ and electron-donating $CoPc$ may adjust surface partial charges, therefore achieving optimum adsorbate-substrate interaction required by self-assembly processes [9]. Under electrochemical conditions, it is known that the adsorbate-substrate interaction can be modulated by the surface charge density [10]. Therefore electrochemical environments offer additional possibilities to control surface dynamics via the surface charge. Indeed, Cunha and Tao have demonstrated that the electrode potential can drive the order-disorder phase transition of 2-2' bipyridine (2,2'-BP) on Au(111) [11]. The ordering of 2,2'-BP at high potential was attributed to a charge induced reduction in dipole-dipole repulsion between adsorbates and consequent increase in the adsorbate coverage [11]. This raises the question as to whether one can tune the surface mobility to achieve optimum self-assembly via potential control under electrochemical conditions.

5.1.2. Motivation.

We chose to investigate the self-assembly of porphyrins for two reasons.

1. Porphyrins are polarizable due to the large π systems. Therefore, it may be possible to substantially modulate the adsorbate-substrate interaction via the surface charge density. In turn the surface mobility, mainly determined by the adsorbate-substrate interaction, may be controlled by the surface charge density. Moreover, the large planar π systems are expected to assume a flat orientation due to their tendency to maximize the π bonding to the surface. Due to the absence of dipoles normal to the surface for porphyrins, we do not expect significant deviation from the flat orientation when surface charge density is

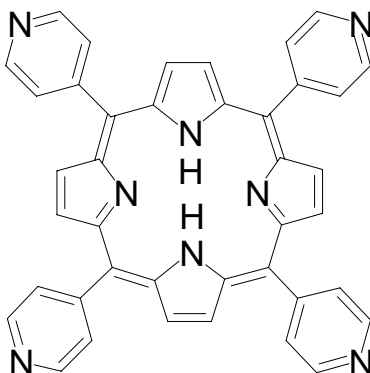
altered. By contrast, polar molecules may undergo significant orientational transitions. A Second Harmonic Generation study, for example, reveals that 2,2'-BP assumes a flat orientation, with the two N pointing to the surface in a dipolar configuration, on negatively charged electrode and vertical orientation at positively charged surface [12]. The change in orientation may fundamentally alter the nature of the adsorbate-adsorbate interaction, as illustrated by the vertical orientation induced π stacking interaction between the 2,2'-BP, which is impossible under a flat orientation [11]. The consistent flat orientation of the large planar π systems may allow one to tune the binding energy, without altering the nature of intermolecular interactions at electrochemical interfaces. Therefore, by turning surface charge density, one may understand self-assembly on surface in a more simplified way and control it in a more predictable fashion.

2. The second motivation arises from the technological importance of self-assembled thin films of porphyrins. The unique electronic properties and reactivities of porphyrins have been recognized and utilized in applications ranging from organic electronics, to solar cells and electrocatalysis [13, 14]. The four peripheral groups and metal centers can be tailored to precisely control the lateral and vertical spacing and connections between porphyrin molecules [3-5]. The combined electronic properties, chemical reactivity and structural versatility render porphyrins promising building blocks for the rational design of self-assembled supramolecular structures in nano-electronics applications [15]. Ordered structures of porphyrin thin films have been extensively investigated in UHV[9][16-18]. However, successful preparation of highly ordered porphyrin adlayers directly on metal surfaces from the solution phase, more convenient and compatible with

further wet chemistry such as attachment of ligands, has not been reported to our knowledge. Itaya et. al. found that 5,10,15,20-tetrakis(N-methylpyridinium-4-yl)-21H,23H-porphine (TMPyP) can only form a disordered monolayer on Au(111), presumably due to the slow surface diffusion resulting from strong adsorbate-substrate interactions [19]. However, ordered TMPyP monolayers can be formed on iodine modified metal surfaces that provide weakened adsorbate to substrate binding energies [19-21].

We demonstrate that robust ordered porphyrin monolayers can be prepared by adsorption at potentials between 0.2 to $-0.2V_{SCE}$. In this potential range, enhanced surface diffusion allows the adsorbate to assemble in ordered arrays, reminiscent of annealing in vacuum at elevated temperatures to prepare 2D crystalline structures [7]. Our results reveal the control over 2D self-assembly one may exert via the modulation of surface charge density.

Scheme 1 5,10,15,20-Tetra(4-Pyridyl)-21H,23H-Porphine (TPyP)



5.2. Experimental.

An Au(111) single crystal (Monocrystals Co., Ohio) and an Au(111) facet of a single crystalline bead were used as substrates. Prior to the experiments the substrate was cleaned by immersion in hot piranha solution [1:3 H₂O₂ (J. T. Baker, CMOSTM) and H₂SO₄ (J. T. Baker, CMOSTM)] for 1 hour, and immersion in hot HNO₃ (EM SCIENCE GR) for 30 minutes. (Caution! The piranha solution is a very strong oxidizing agent and extremely dangerous. Eye protection and gloves should be used during handling.) After each step the sample was rinsed by ultrasonication in ultrapure water (>18MΩ•cm) produced by a Barnstead, Nanopure Infinity system. After chemical cleaning, the crystal was hydrogen flame annealed, and allowed to cool down in air. The crystal was transferred to the STM electrochemical cell and immersed under potential control (0.1 V) in 0.1 M H₂SO₄ solution (Fisher Scientific Co., Trace metal grade).

5,10,15,20-Tetra(4-Pyridyl)-21H,23H-Porphine (TPyP) was purchased from Aldrich Chem. Co., and used without further purification. The 0.2 mM TPyP solution was prepared in 0.1 M H₂SO₄ solution. After the bare gold surface was imaged under neat 0.1 M H₂SO₄ solution, a drop of the TPyP solution was added to the STM cell, to produce a final concentration of about 10⁻⁵M TPyP. In some cases, as indicated in the text, preadsorbed TPyP was studied in a porphyrin-free solution. Preadsorption was achieved by holding the Au(111) crystal in 0.1 M H₂SO₄ solution with 2×10⁻⁴M TPyP at a potential of -0.25 V for 5 minutes. The electrode was then withdrawn from the cell, rinsed with DI water and immersed in a 0.1 M H₂SO₄ blank solution under potential control (-0.25 V).

The electrochemical cell was made of Teflon. All potentials were quoted against SCE, though a silver wire or a Pt wire was actually used as the quasi-reference electrode (Appendix D). A platinum wire was used as the counter electrode. All cell components were chemically cleaned in the same way as the crystal.

STM images were obtained with a PicoScan STM system (Molecular Imaging). A bi-potentiostat (Molecular Imaging) was used to control the sample and tip potential independently, as well as to perform cyclic voltammetry. STM tips were electrochemically etched Tungsten STM Tips insulated with paraffin wax (Appendix C). The Faradaic current of the insulated tips under imaging condition is less than 10 pA. All the STM images were obtained under constant current mode, 0.2-0.3nA. The tip potential was maintained at 0.0V to minimize the Faradaic current.

5.3. Results and discussions:

5.3.1. Potential dependant mobility of TPyP.

Adsorption of 5,10,15,20-Tetra(4-Pyridyl)-21H,23H-Porphine (TPyP) at high electrode potential (>0.5 V) typically results in a disordered structure, Figure 5-1A. Each molecule is imaged individually as a square with four bright lobes. The four bright lobes are due to the pyridine rings, as reported for NiTPP on Au(111)[9] and TMPyP on I--Au(111)[19]. The equivalent appearance of the lobes suggest that the molecule is lying flat on the Au(111) surface. No significant displacement of the molecules was observed for up to an hour. This result is consistent with the observation that immobilized TMPyP molecules

adsorb on bare Au(111) at high potential with a disordered structure [19]. The large bright structures are Au islands that result from the lifting of the Au(111) reconstruction, a process that occurs at high electrode potential ($>0.3 V_{SCE}$) in neat 0.1 M H_2SO_4 [22, 23].

In order to probe the effect of the electrode potential on the binding of TPyP to the Au surface, and the resulting structures, the electrode potential was stepped from 0.5 V to $-0.3 V$ in the middle of the image (Figure 5-1B). While isolated species, resolved as disordered TPyP molecules, were observed at 0.5 V, the TPyP molecules can no longer be observed on the surface at $-0.3 V$. These STM images suggest two possibilities: (1) the TPyP molecules cannot be imaged because they desorb from the surface at negative potentials; (2) the TPyP molecules remain on surface, but the adsorbate-substrate interaction is too weak for the molecules to remain sufficiently immobilized to be imaged by STM. To test whether TPyP is adsorbed on Au(111) at negative potential, Au(111) was immersed in the TPyP solution at $-0.25 V$ for a few minutes. Then the electrode was emmersed and rinsed with water before immersion in TPyP free 0.1 M H_2SO_4 at $-0.25 V$. The first scan of the CV (Figure 5-2), shows a peak, associated with the oxidation of TPyP from Au(111) at a potential of 0.17 V. This provides evidence that the TPyP is adsorbed on the surface at $-0.25 V$. The inability to image the molecules at low potential ($< -0.2V$) suggests that they are highly mobile.

The adsorbate-substrate interaction is clearly potential dependent. At 0.5 V, the interaction between the molecules and the substrate is so strong that it hinders surface

diffusion, preventing the formation of an ordered adlayer structure. However, at a lower potential, -0.3 V, the adsorbate-substrate interaction is too weak and the molecules are too mobile to be imaged by STM. The process is quite reversible. When the potential was stepped back to 0.5 V in the middle of Figure 5-1C, disordered molecules appeared rapidly. At -0.3 V, TPyP molecules are disordered because the binding energy is not sufficient to confine molecules in 2D ordered structures. Upon applying a potential step to 0.5 V, the increased binding energy “freezes” the TPyP molecules rapidly in a disordered state. Due to the low surface mobility, the ordering process is kinetically hindered.

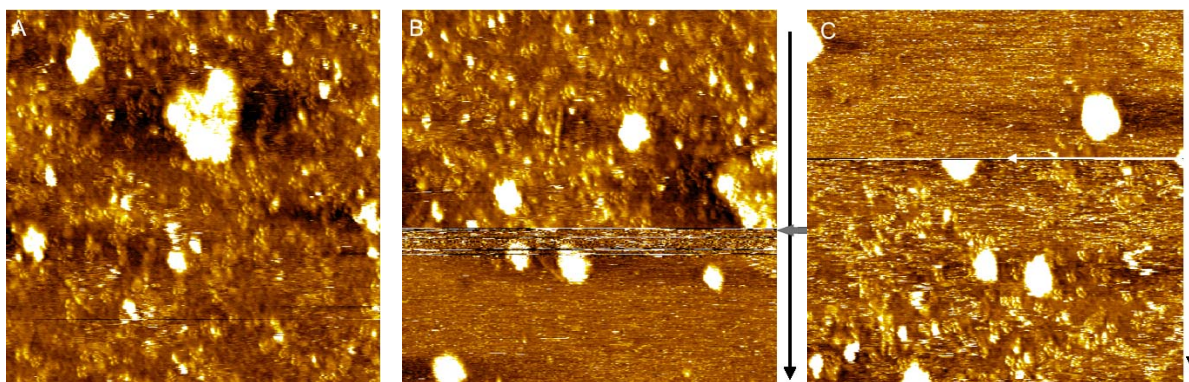


Figure 5-1 In-situ STM images ($50 \times 50 \text{ nm}^2$) of TPyP on Au(111) in $0.1 \text{ M H}_2\text{SO}_4 + 10^{-5} \text{ M TPyP}$ solution. Scan directions are indicated by black arrows. Tip locations when potential step occurred are indicated by white arrows. (A) Electrode potential 0.5 V. (B) Electrode potential 0.5 V (upper part), -0.3 V (lower part). (C) -0.3 V (upper part) 0.5 V (lower part).

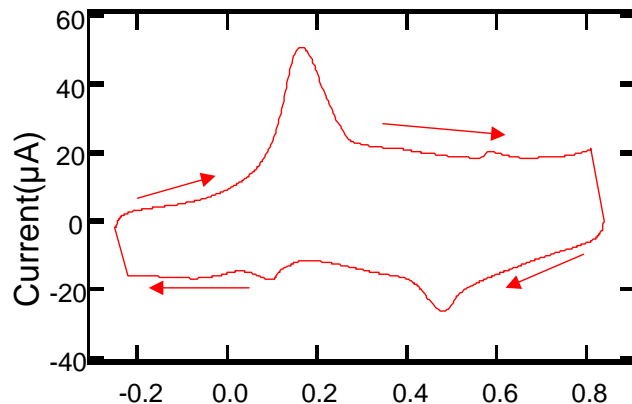


Figure 5-2 Cyclic voltammogram of Au(111) with pre-adsorbed TPyP in a blank 0.1 M H_2SO_4 solution, initially held at -0.25 V, scan rate 2V/s.

The preceding results, namely low mobility at high potential and high mobility at low electrode potential, suggest that by tuning the electrode potential one can control the mobility of the adsorbates and ultimately the self-assembly process. Indeed, ordered structures of TPyP molecules were observed by STM on Au(111) at -0.05 V. These typically consisted of several domains, rotated by 120 degrees with respect to each other (Figure 5-3A). Concurrent with the formation of ordered adlayers, continuous motion of adsorbates at the domain boundaries was observed in STM images, suggesting that the molecules can move at this potential.

To further prove that surface mobility is a critical factor in forming ordered structures, and that the disordered adlayer at high potential (Figure 5-1A) is a result of the strong adsorbate-substrate interaction that hinders surface diffusion, molecules were adsorbed on the surface at 0.1 V, by adding TPyP to the neat electrolyte, and observed to form ordered adlayers. Then the electrode potential was increased by increments of 0.1 V at intervals of several minutes. Even at 0.5 V ordered structures are still observed (Figure

5-3B). In fact we observed that the ordered structures were stable up to 0.8V. The ordered structure seen in Figure 5-3B is in contrast to Figure 5-1A, in which molecules are adsorbed at the same potential (0.5 V), but where a disordered structure was observed. This is also in remarkable contrast with Figure 5-1C, where disordered structure was observed after potential step from -0.3 V to 0.5 V. The fact that the adlayer structure depends on the sample history provides strong evidence that the ordering process can be kinetically limited by the low surface mobility at positive potential (>0.5 V). If the potential is gradually increased to 0.5 V, the molecules have the opportunity to self-assemble into ordered structure at intermediate potentials (from -0.2 to 0.2 V). Once they are locked into ordered arrays, the molecules remain ordered at potentials as high as 0.8V. However, if the potential is stepped quickly to 0.5 V, the suddenly increased binding energy “freezes” the TPyP molecules rapidly in a disordered state. This suggests the crucial role of potential dependant surface mobility in determining the formation of an ordered adlayer.

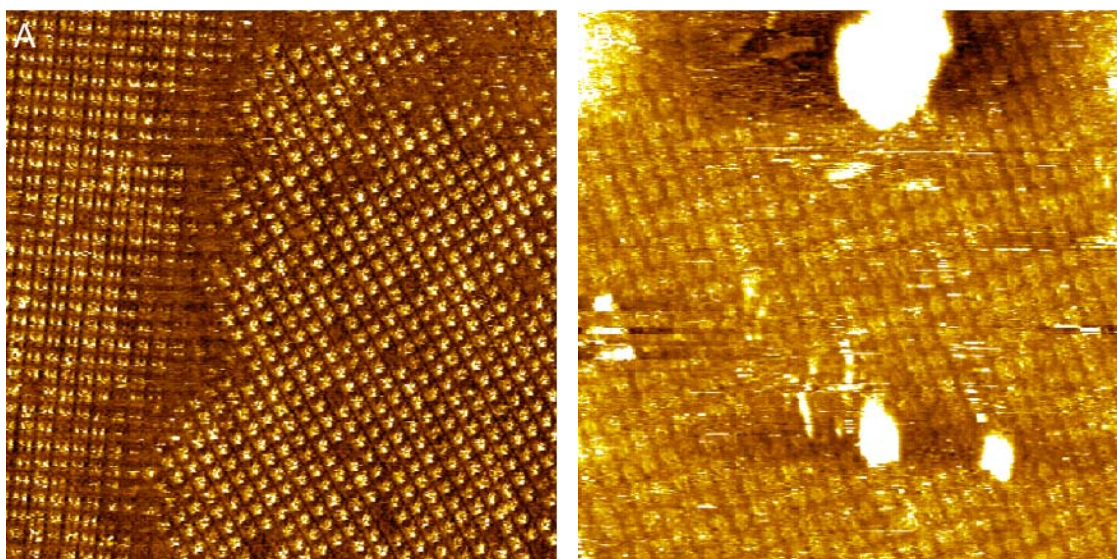


Figure 5-3 STM images of TPyP adlayers on reconstructed Au(111) in 0.1 M H₂SO₄ solution. (40×40 nm²) (A) electrode potential –0.05 V. (B) The electrode potential was stepped progressively to 0.5 V after the ordered monolayer was formed at 0V.

5.3.2. Dynamics of the preadsorbed TPyP adlayer

One may expect to study the growth of ordered adlayer after addition of TPyP to the electrochemical cell. However this study is rather complicated and not instructive for the following reasons. Upon injection of TPyP solution into the electrochemical cell, one has to allow some time (ca. 10min) for the drift of the STM to settle before one can monitor the dynamics in-situ. However, typically 10min after injection, we found that the adlayer had already reached equilibrium. Therefore no dynamics information can be achieved in this experiment. Reducing the TPyP concentration is no more helpful because the adsorption is more likely to be the rate-limiting factor, obscuring the role of surface mobility in the growth process. To further understand the role of potential dependant adsorbate-substrate interactions and surface mobility in the dynamics of self- assembly processes, we instead chose to study the preadsorbed TPyP adlayer in blank electrolyte. We applied potential perturbations to the system, expecting to extract dynamics information concerning the ordering process.

TPyP molecules were preadsorbed on Au(111) as described in the experimental section. Subsequently, the TPyP covered Au(111) was imaged under TPyP free H₂SO₄ solution. The surface packing of TPyP in the presence of neat electrolyte is similar to that in the presence of TPyP containing solution, Figure 5-4A. This proved that ordered adlayer endured emersion from the cell and cycles of rinsing with water or H₂SO₄ solution. This observation highlights the robustness of the supramolecular surface structure formed in

this potential controlled manner. At a potential of -0.05 V, ordered domains of TPyP molecules, separated by domain boundaries (Figure 5-4A), are clearly resolved. The presence of multiple domains may result from different nucleation sites from which the molecules adsorbed to the surface crystallize into two-dimensional structures. A sequential image, Figure 5-4B, suggests that the domain edges were moving significantly at this potential. Part of the molecular domain indicated by a circle is converted to a domain rotated by 60 degrees. Also there is significant noise in the domain edges, suggesting higher mobility of molecules in those areas. This intermediate potential significantly enhanced the mobility of molecules compared to 0.5 V, where no motion of molecules was observed over extended periods of time, Figure 5-1A.

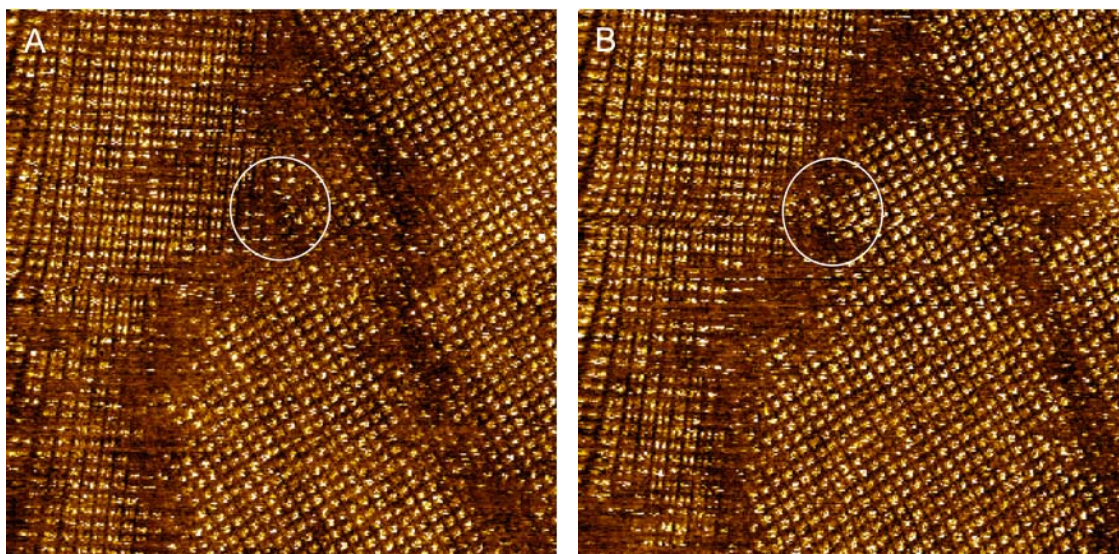


Figure 5-4 Sequential STM images (62×62 nm²) of TPyP on reconstructed Au(111) in 0.1 M H₂SO₄ solution at -0.05 V. A circle highlights a domain that recrystallized between images.

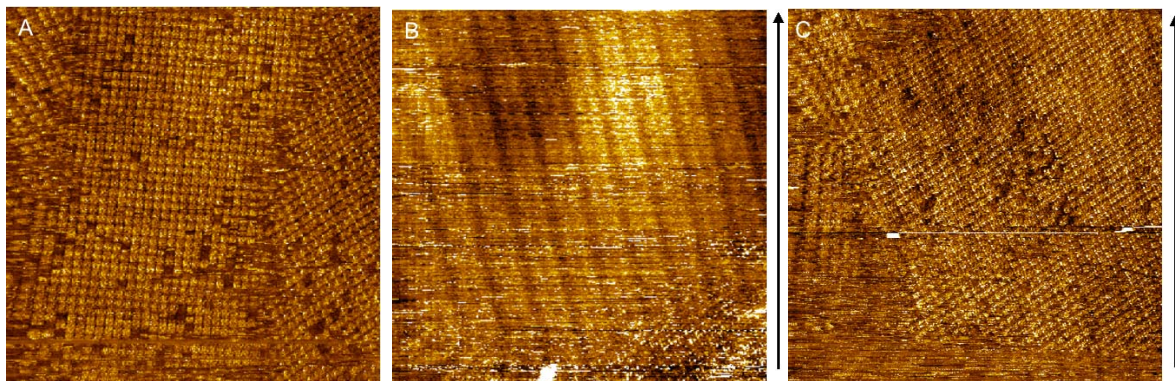


Figure 5-5 In-situ STM images ($62 \times 62 \text{ nm}^2$) sequence of TPyP on reconstructed Au(111) in neat 0.1 M H_2SO_4 solution. Scanning directions are indicated by the black arrows. (A) electrode potential -0.05 V . (B) obtained after electrode potential was stepped to -0.25 V . (C) was obtained after electrode potential was stepped back to -0.05 V .

In order to probe the stability of the ordered structure at negative potentials, the potential was stepped from -0.05 V to -0.25 V . The ordered TPyP molecules disappeared rapidly. The image (Figure 5-5B) showed clearly the double row reconstruction features of Au(111), that were 0.2 \AA high and separated from the next pair by 6.3 nm . We postulate that the TPyP molecules remain adsorbed on Au(111) surface at the potential of -0.25 V , as verified in the CV experiment discussed above, but that the adsorbate-substrate interaction is too weak to form an ordered phase.

As a probe of the dynamics of self assembly, the potential was stepped from -0.25 V back to -0.05 V , and ordered molecular domains grew almost immediately (Figure 5-5C). The time scale of the ordering process is estimated to be within seconds. It should be noted that the new molecular domain, imaged in the same area, was rotated with respect to the domain observed in Figure 5-5A. This result suggests that the TPyP molecules form a new ordered phase, distinct from the structure seen in Figure 5-5A, after the

potential returned to -0.05 V. Once the potential was stepped to -0.05 V, the TPyP molecules self-assembled into an ordered phase from the reservoir of molecules in the disordered phase (liquid-like) that had been produced at -0.25 V. Furthermore, the rapid appearance of molecular domains at -0.05 V under clean electrolyte requires the availability of high concentration TPyP molecules near the surface. Since this experiment was performed under TPyP free electrolyte, this provides further direct evidence that the molecules remain adsorbed on the surface at -0.25 V even in TPyP free electrolyte, supporting the CV results in Figure 5-2. Had the molecules been desorbed by stepping the potential from -0.05 V to -0.25 V, the molecules would have diffused away into solution, slowing down, or more likely preventing the appearance of ordered structures observed in Figure 5-5C. However, the high concentration of adsorbates is not the only prerequisite for such rapid formation of ordered phases. The enhanced surface mobility at -0.05 V (demonstrated in Figure 5-4) ensures facile lateral reorganization of disordered molecules, promoting the ordering process.

5.3.3. Summary.

From our present results, it is clear that TPyP forms ordered or disordered structures at the Au(111)/0.1 M H₂SO₄ solution interface depending on the potential at which the molecules self-assembles. We attributed this to the potential dependant binding energy and surface mobility. An alternative explanation for the disordered structure for Figure 5-3A is unfavorable adsorbate-adsorbate interaction. Instead, an ordered adlayer was observed in Figure 5-3B. Therefore, the disordered TPyP at high potential (0.5 V), A, is

kinetically limited by slow surface diffusion/strong adsorbate-substrate interaction rather than an equilibrium structure caused by unfavorable adsorbate-adsorbate interaction.

A plausible explanation for the modulation of the TPyP-substrate interaction is electron donation from the π orbitals of TPyP. The strong electric field across the double layer (10^7V/m to 10^9V/m) may significantly modulate the electron donating effect to the substrate. The electron donating effect may be enhanced at high electrode potential (positive surface charge density) and reduced at low electrode potential (negative surface charge density). We note that while the electrode potential modulates electrostatic interactions between molecules and the substrate, potential induced change of redox state of porphyrins may also change the adsorbate-substrate interaction. A thorough understanding of the nature of the potential dependant adsorbate-substrate interaction requires further spectroscopic and theoretical investigations. Notwithstanding of the exact origin of potential modulation, the role of potential-dependant surface mobility is highlighted in the formation of ordered self-assemblies under electrochemical conditions.

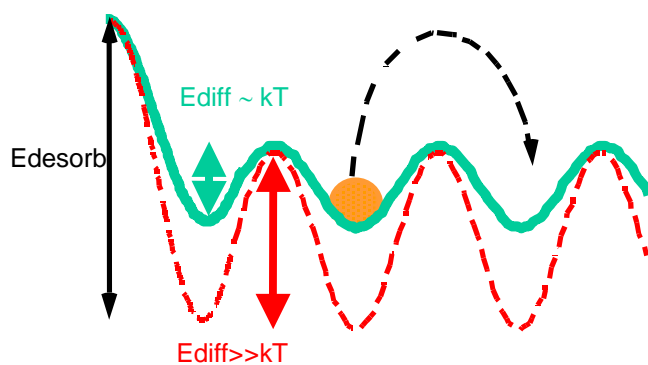


Figure 5-6 Influence of adsorbate binding energy E_{desorb} on surface diffusion.

Our results are in agreement with Itaya's investigation in that the surface diffusion play a critical role in formation of highly ordered structure of porphyrins [19]. However, the major difference between our result and that of Itaya et al., is that TMPyP molecules, structurally similar to TPyP, do not form ordered structures on bare Au(111). Highly ordered adlayers of TMPyP could only prepared on iodine modified Au [19]. Our results suggest that it may be a consequence of the higher potential ($0.57V_{SCE}$), at which TMPyP on bare Au(111) was adsorbed. High electrode potentials result in a strong adsorbate-substrate interaction, hindering surface diffusion. The present investigation suggests a convenient approach to form ordered porphyrin structures directly on Au surfaces. One can control the adsorbate-substrate interactions by adjusting electrode potential. Figure 5-6 illustrates a simplistic view of the relationship between surface diffusion and binding energy. The reduction of binding energy E_{desorb} is accompanied by a decrease in diffusion barrier E_{diff} . Once E_{diff} is reduced to be comparable to thermal energy kT , the surface mobility is significantly enhanced. This is reminiscent of the thermal annealing commonly employed at vacuum-solid and gas-solid interfaces to facilitate the surface diffusion required for molecular self-assembly. The difference is that enhanced surface mobility in thermal annealing is achieved via increasing the thermal energy (kT) relative to a constant diffusion barrier E_{diff} while the increase in adsorbate diffusivity in potential modulation approach is achieved via a lowering of the diffusion barrier E_{diff} relative to a constant thermal energy (kT). Future spectroscopic and theoretical investigations into the nature of the adsorbate-substrate interaction and how it is modulated by the electrode potential will be of great interest. From a technological point of view, it will be interesting to utilize the electrode potential to tune surface processes, such as surface

diffusion, to direct the growth of self-assembled structures of large planar aromatic molecules.

BIBLIOGRAPHY

1. Giancarlo, L.C. and G.W. Flynn, *Scanning tunneling and atomic force microscopy probes of self- assembled, physisorbed monolayers: Peeking at the peaks*. Annual Review of Physical Chemistry, 1998. **49**: p. 297.
2. Barth, J.V., J. Weckesser, C.Z. Cai, P. Gunter, L. Burgi, O. Jeandupeux, and K. Kern, *Building supramolecular nanostructures at surfaces by hydrogen bonding*. Angewandte Chemie-International Edition, 2000. **39**(7): p. 1230-+.
3. Leininger, S., B. Olenyuk, and P.J. Stang, *Self-assembly of discrete cyclic nanostructures mediated by transition metals*. Chemical Reviews, 2000. **100**(3): p. 853-907.
4. Schwab, P.F.H., M.D. Levin, and J. Michl, *Molecular rods. 1. simple axial rods*. Chem. Rev., 1999. **99**(7): p. 1863-1933.
5. Yokoyama, T., S. Yokoyama, T. Kamikado, Y. Okuno, and S. Mashiko, *Selective assembly on a surface of supramolecular aggregates with controlled size and shape*. Nature, 2001. **413**: p. 619-621.
6. Zhang, Z.Y. and M.G. Lagally, *Atomistic processes in the early stages of thin-film growth*. Science, 1997. **276**(5311): p. 377-383.
7. Poirier, G.E., *Characterization of organosulfur molecular monolayers on Au(111) using scanning tunneling microscopy*. Chemical Reviews, 1997. **97**(4): p. 1117-1127.
8. Heringdorf, F.J.M.Z., M.C. Reuter, and R.M. Tromp, *Growth dynamics of pentacene thin films*. Nature, 2001. **412**(6846): p. 517-520.
9. Hipps, K.W., L. Scudiero, D.E. Barlow, and M.P. Cooke, *A self-organized 2-dimensional bifunctional structure formed by supramolecular design*. Journal of the American Chemical Society, 2002. **124**(10): p. 2126-2127.
10. Lipkowski, J., L. Stolberg, D.-F. Yang, B. Pettinger, S. Mirwald, F. Henglein, and D.M. Kolb, *Molecular adsorption at metal-electrodes*. Electrochimica Acta, 1994. **39**(8-9): p. 1045.
11. Cunha, F. and N. Tao, *Surface charge induced order-disorder transition in an organic monolayer*. Physical Review Letters, 1995. **75**(12): p. 2376.
12. Yang, D.F., D. Bizzotto, J. Lipkowski, B. Pettinger, and S. Mirwald, *Electrochemical and 2nd-Harmonic Generation studies of 2,2'-bipyridine adsorption at the Au(111) electrode surface*. Journal of Physical Chemistry, 1994. **98**(28): p. 7083-7089.
13. Forrest, S.R., Chem. Rev., 1997. **97**: p. 1793.
14. Dolphin, V.D., ed. *The Porphyrins*. 1979, Academic Press: New York.
15. Weiss, P.S., *Nanotechnology - Molecules join the assembly line*. Nature, 2001. **413**(6856): p. 585-586.
16. Fritz, T., M. Hara, W. Knoll, and H. Sasabe, *STM investigations on heteroepitaxially grown overlayers of Cu-phthalocyanine on Au(111) surfaces*. Molecular Crystals and Liquid Crystals Science and Technology Section a-Molecular Crystals and Liquid Crystals, 1994. **252**: p. 561.
17. Scudiero, L., D.E. Barlow, U. Mazur, and K.W. Hipps, *Scanning tunneling microscopy, orbital-mediated tunneling spectroscopy, and ultraviolet*

- photoelectron spectroscopy of metal(II) tetraphenylporphyrins deposited from vapor.* Journal of the American Chemical Society, 2001. **123**(17): p. 4073.
18. Chizhov, I., G. Scoles, and A. Kahn, *The influence of steps on the orientation of copper phthalocyanine monolayers on Au(111).* Langmuir, 2000. **16**(9): p. 4358-4361.
 19. Kunitake, M., U. Akiba, N. Batina, and K. Itaya, *Structures and dynamic formation processes of porphyrin adlayers on iodine-modified Au(111) in solution: In situ STM study.* Langmuir, 1997. **13**(6): p. 1607-1615.
 20. Kunitake, M., N. Batina, and K. Itaya, *Self-organized porphyrin array on iodine modified Au(111) in electrolyte solutions in situ Scanning Tunneling-Microscopy study.* Langmuir, 1995. **11**(7): p. 2337-2340.
 21. Ogaki, K., N. Batina, M. Kunitake, and K. Itaya, *In situ scanning tunneling microscopy of ordering processes of adsorbed porphyrin on iodine-modified Ag(111).* Journal of Physical Chemistry, 1996. **100**(17): p. 7185-7190.
 22. Tao, N.J. and S.M. Lindsay, *Kinetics of a potential induced 23XSQRT3 to 1X1 transition of Au(111) studied by in-situ scanning tunneling microscopy.* Surf. Sci. Lett., 1992. **274**: p. L546-L553.
 23. He, Y. and E. Borguet, *Dynamics of metastable nanoscale island growth and dissolution at electrochemical interfaces by time-resolved scanning tunneling microscopy.* Journal of Physical Chemistry B, 2001. **105**(18): p. 3981-3986.

6. In-situ STM study of electrode reactions and potential induced adsorption-desorption of porphyrin adsorbates.

6.1. Introduction.

The unique electronic properties and reactivity of porphyrins have been recognized and utilized in applications ranging from organic electronics, to solar cells and electrocatalysis.[1, 2] Often central to these applications are the questions on how to control the structures and chemical reactivity of porphyrin thin films on surfaces.

Much attention has been paid to the electrocatalytic properties due to the metal centers in the adsorbed porphyrins [2]. It has been recognized that adsorption can affect the electrochemistry of porphyrins dramatically. For example, it remains unclear why the most potent oxygen reduction electrocatalyst, cobalt cofacial diporphyrin, displays high four electron reduction reactivity only on edge plane graphite [3]. Unlike in bulk solution, cobalt porphyrins adsorbed on HOPG does not display well defined redox peaks in cyclic voltammetry [4]. The adsorption was suggested to change the energetics of redox states and therefore affect the redox potential significantly [4].

The electrochemistry of water soluble free base porphyrins investigated by Wilson and Neri is summarized in (Figure 6-1)[5, 6]. The unreduced form P(0) exists as free base P(0)H₂ or diacid, P(0)H₄²⁺. At about -0.2 V, P(0) can undergo a two electron reduction process to form phlorin, P(-II) via a chemical intermediate, iso-P(-II)H₄. At potentials lower than -0.4 V, further reduction of P(-II) occurs.

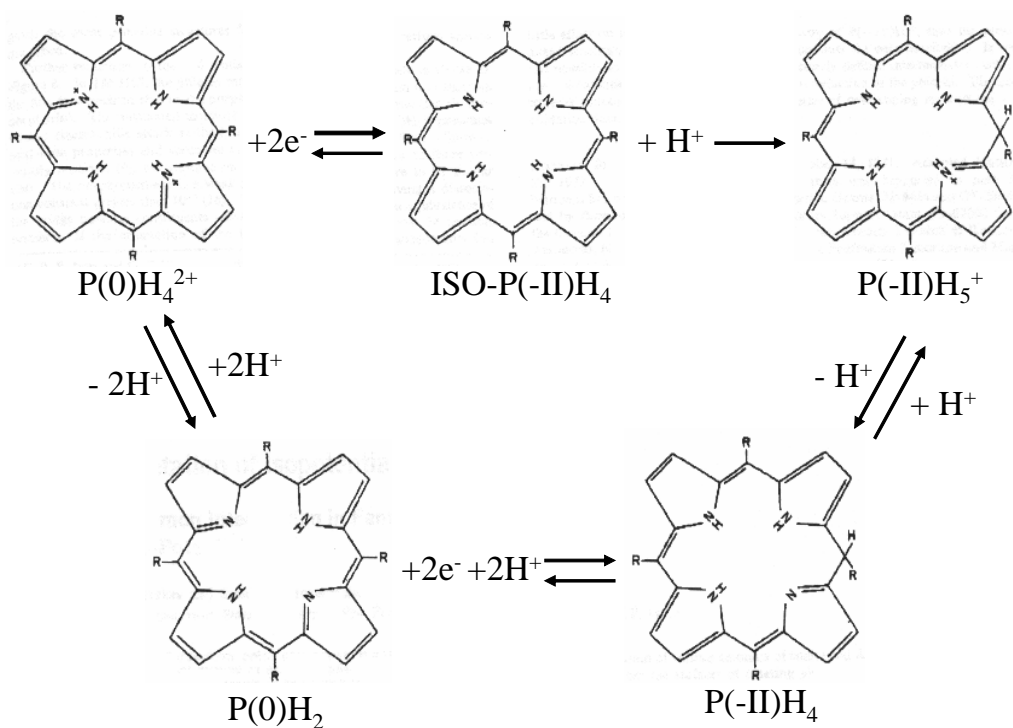


Figure 6-1 Possible electrochemical reaction mechanism of TMPyP under acidic medium [5, 6].

Compared to solution phase porphyrins, the reactivity of adsorbed water soluble porphyrins is much less understood. Very sensitive tools are required to study the reaction intermediates and products of the redox reactions on surfaces. Itoh's surface-enhanced resonance Raman scattering spectroscopy (SERRS) studies suggested that a water soluble porphyrin, meso-tetrakis(4-N-methylpyridyl)porphine (TMPyP), adsorbed as diacid form, P(0)H_4^{2+} on a roughened silver electrode [7]. The diacid is reduced to phlorin (P-II) at a more negative potential [7]. However, the roughened surface, which is necessary for surface enhancement, causes additional complications as the small silver clusters present on the surface may reduce the adsorbed molecules [7]. Therefore questions remain on how the SERRS results correlate to the electrochemical behavior on a well defined surface. Devynck et al. reported that in an acidic medium, the TMPyP

irreversibly adsorbed on Au displayed no redox peaks between -0.4 V to 0.7V_{SCE} in cyclic voltammogram [8], in contrast with the bulk electrochemistry.

Not only is the electrochemistry of adsorbed, water soluble porphyrins poorly understood, their adsorbed structures have been largely unknown until the development of STM. STM found that on well defined surfaces such as HOPG and single crystal Au surface, porphyrins typically adopt a flat orientation to maximize the interaction between the π rings and the substrate [9, 10].

In the proceeding chapter, we reported our studies of the structures of a water soluble porphyrin, 5,10,15,20-Tetra(4-Pyridyl)-21H,23H-Porphine (TPyP) on the Au(111) surface. We found that TPyP was irreversibly adsorbed on the Au surface. We demonstrated that under an electrochemical environment, 5,10,15,20-Tetra(4-Pyridyl)-21H,23H-Porphine (TPyP) adsorbing on positively charge surfaces forms a disordered layer, that is metastable with respect to the thermodynamically more stable ordered layer, on positively charge surfaces due to excessive molecule-substrate interaction. Ordered porphyrin monolayers can be prepared by adsorption at potentials between 0.2 to -0.2 V_{SCE}. In this potential range, enhanced surface diffusion allows the adsorbate to assemble in ordered arrays, reminiscent of annealing in vacuum at elevated temperatures to prepare 2D crystalline structures [11]. Once formed the ordered 2D structures are stable up to 0.8 V_{SCE}.

In this chapter, we report a more systematic STM and electrochemical study designed to understand the interplay between the redox properties, adsorption, and self-assembly processes of TPyP on Au surface. We found the irreversible adsorption of TPyP had a dramatic effect on its electrochemistry. We attribute the distinct reactivity to the strong interaction between TPyP molecules and the Au substrate. Our investigation also shows how redox reactions can influence the formation of multilayers. The multilayer formation is probably related to the π stacking interactions of porphyrins. Our results suggest that by controlling the electrochemistry, one can either promote or suppress the formation of multilayers. This may be useful for the ongoing efforts to build 3D supramolecular structures from the surface.

6.2. Experimental section.

The experimental procedures have been described in the experimental section of the preceding chapter.

6.3. Results and discussion.

6.3.1. Cyclic voltammetry results.

6.3.1.1. Cyclic voltammograms (CVs) of TPyP in solution.

Cyclic voltammetry was performed to investigate the redox state of the TPyP in solution.

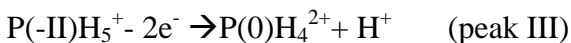
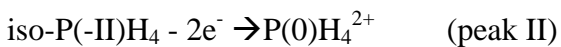
The CVs of Au(111) in 0.1 M H₂SO₄ solution with 2×10^{-4} M TPyP at different scan rates (0.02 V/s-2 V/s) show several new peaks, one cathodic peak(I) and two anodic peaks(II) and (III) (Figure 6-2). At a scan rate of 1 V/s, the redox peaks I, II, and III, appeared at –

0.05 V, 0.03 V and 0.14 V respectively. Peak(II) was not apparent at low scan rates, but as the scan rate was increased, the anodic peak current associated with peak(II) increased. This result suggests that there are two kinds of reduced species that are active in the oxidation reaction [5, 6].

The electrochemical reaction mechanisms of porphyrins in the solution phase have been extensively investigated as shown in (Figure 6-1) [5, 6]. In acid solution below pH 2, the porphyrin molecule $P(0)H_2$ is believed to be protonated to form porphyrin diacid $P(0)H_4^{2+}$. The reduction of $P(0)H_2$ probably involves a heterogeneous electron transfer followed by a homogeneous protonation reaction.



Accordingly, we suggest that the two oxidation peaks correspond to the oxidation of iso-P(-II)H₄ and P(-II)H₅⁺.



At a low scan rate, sufficient time exists for the protonation reaction to occur before oxidation. All the iso-P(-II)H₄ is converted to P(-II)H₅⁺, and peak II, associated with

oxidation of iso-P(-II)H₄ is negligible. As the scan rate is increased, insufficient time is allowed for the conversion of iso-P(-II)H₄ to P(-II)H₅⁺. Thus the increased amount of remaining iso-P(II)H₄ results in a increase of peak II.

Overall, our cyclic voltammograms of TPyP in solution phase are in good agreement with Wilson and Nerri's [5, 6]. This provides a baseline to discuss the redox chemistry of TPyP adsorbed on Au(111) electrodes.

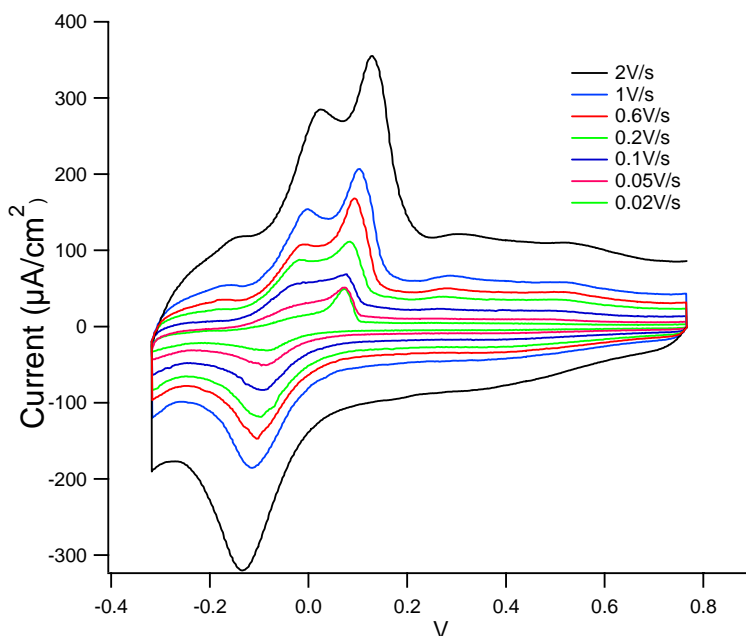


Figure 6-2 Cyclic voltammograms of Au(111) in 0.1 M H₂SO₄ solution with 2×10^{-4} M TPyP. The electrode potential scan rates were 0.02, 0.05, 0.1, 0.2, 0.6, 1, 2 V/s.

6.3.1.2. Cyclic voltammograms of TPyP preadsorbed at negative potentials.

To study the redox chemistry of TPyP adsorbed on Au(111) electrodes without the interference of TPyP from the bulk solution, we first immersed the Au(111) electrode in TPyP solution at -0.25 V, rinsed the Au electrode with water and 0.1 M H₂SO₄, and then

transferred the Au electrode covered with adsorbed TPyP into an electrochemical cell containing 0.1 M H₂SO₄ for electrochemical measurements.

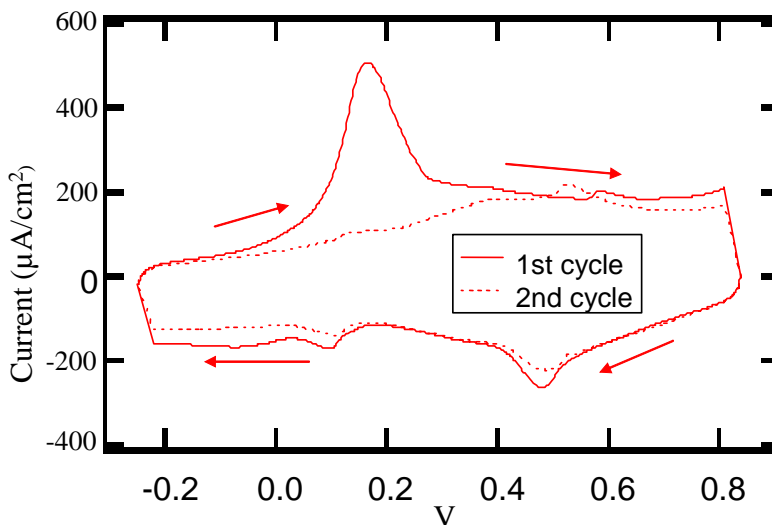


Figure 6-3 Cyclic voltammograms of Au(111) with pre-adsorbed TPyP in a blank 0.1 M H₂SO₄ solution, initially held at -0.25 V, scan rate 2 V/s (first cycle —, second cycle).

The first scan of the CV (Figure 6-3) of the preadsorbed TPyP showed a peak, at a potential of 0.15 V. Since it appeared at the same potential as the oxidation of P(-II) in Figure 6-2, we assign this peak to the oxidation of P(-II) species. Using the second scan as the background, which displays no peak near 0.15V, the total amount of charge per unit area consumed for the surface oxidation reaction is calculated to be about 30 $\mu\text{C}/\text{cm}^2$. Dividing the total number of electrons by 2 (number of electrons involved in the oxidation) yields a TPyP coverage of 9.4×10^{13} molecule/ cm^2 , which corresponds to 2.2 monolayers assuming that each molecule occupies an area of $1.55 \times 1.55 \text{ nm}^2$ as determined by STM. Clearly multiple layers of TPyP can be adsorbed on Au(111) and survive the rinsing and transfer to another electrochemical cell. Another pair of redox peaks at 0.46 and 0.53 V appear and may reveal the adsorption/desorption of SO_4^{2-} at Au(111) [12].

However, in sharp contrast to the CV of TPyP solution, on the TPyP covered Au(111), the oxidation of P(-II) is irreversible, i.e., the cathodic peak at -0.05 V is absent. Instead a much smaller cathodic peak appeared at 0.08 V. Moreover, in the second cycle, the anodic peak disappeared as well. In another experiment to test the reversibility of oxidation, the electrode was held at a positive potential, 0.8 V, before the CV scans. Only small peaks were observed (Figure 6-4). The irreversibility of the redox reaction suggests two possibilities:

1. The anodic peak at 0.15 V, is accompanied by significant desorption. Once the TPyP molecules are desorbed from the electrode and diffuse into the bulk solution, they can no longer contribute to the electron transfer processes at the electrode surface.
2. The oxidation of P(-II) forms a P(0) species that is difficult to reduce.

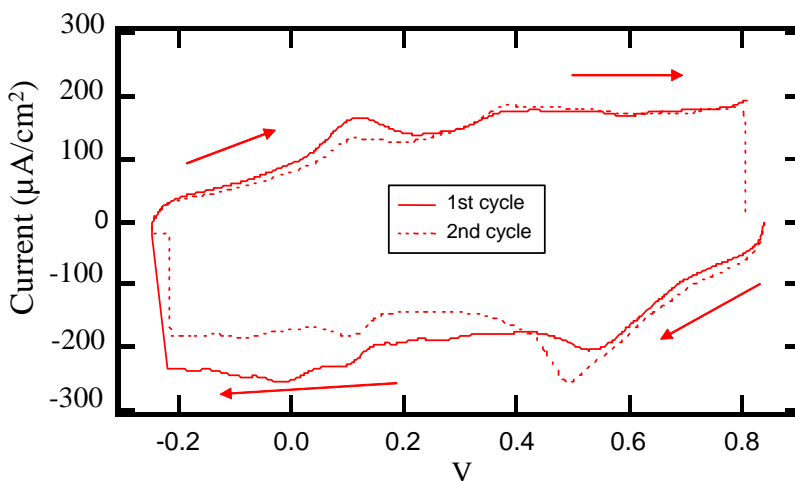


Figure 6-4 Cyclic voltammograms of Au(111) with pre-adsorbed TPyP in a blank 0.1 M H_2SO_4 solution, initially held at 0.8 V, scan rate 2 V/s (first cycle —, second cycle - - -).

6.3.1.3. *Cyclic voltammograms of preadsorbed TPyP: Preadsorbed at positive potentials.*

To understand in more detail the electrochemical reactivity of irreversibly adsorbed TPyP, another series of CVs were carried out. TPyP molecules were preadsorbed at a positive potential (0.6 V) before the Au electrode was rinsed and transferred to an electrochemical cell containing neat 0.1 M H₂SO₄. The electrode was held at 0.6 V for 5 min to ensure that only P(0) species are present. Then the electrode was held at a negative potential -0.05 V for a duration τ , after which a CV scan was initiated (Figure 6-5). The anodic peak grew with increasing time spent at -0.05 V. Though the growth appeared to slow for times longer than 5min, there is no clear sign of reaching a plateau. Therefore the time constant for the reduction of P(0) should be significantly higher than 5min. Similar CVs are obtained after many cycles, suggesting that minimal desorption is involved. This provides evidence that at least some porphyrins adsorbates remain adsorbed throughout the electrochemical experiments.

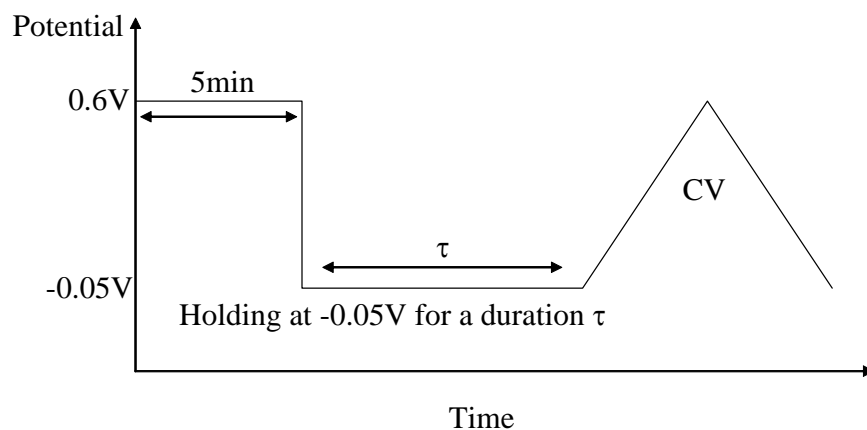


Figure 6-5 Waveform for the cyclic voltammetric experiment of TPyP preadsorbed at a positive electrode potential.

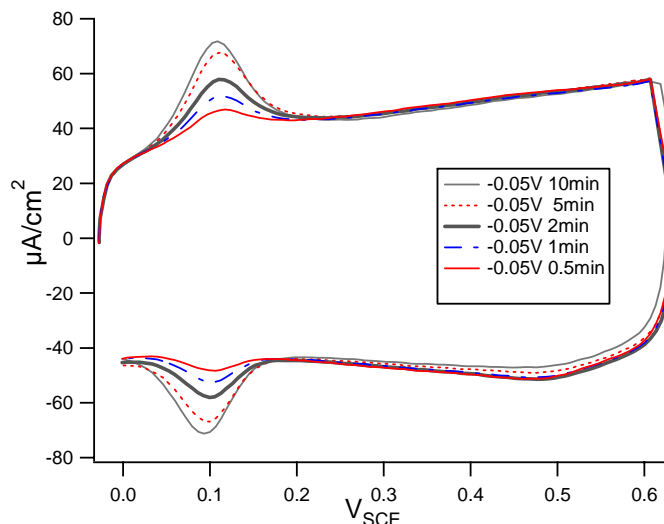


Figure 6-6 Cyclic voltammograms of preadsorbed TPyP on Au(111). The electrode surface was equilibrated at -0.05 V for different durations. Scan rate 1 V/s.

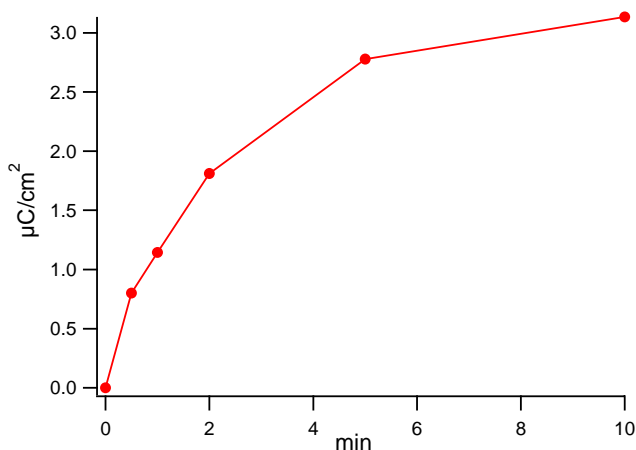


Figure 6-7 Integrated charge of preadsorbed TPyP as a function of duration at -0.05 V extracted from the CVs in Figure 6-6.

The presence of redox peaks in Figure 6-6 suggests that at least some of the P(0) molecules remain adsorbed at positive potentials. Therefore the absence of an electrochemical signal in the second cycle of Figure 6-3, does not mean that the TPyP molecules completely desorb from the surface after oxidation in the first cycle. Rather, the reduction of P(0) adsorbed on the surface is much slower than in the solution. After 10min at -0.05 V, only 0.22 ML of TPyP is reduced, based on the integrated charge

density⁴. Therefore the reduction of adsorbed P(0) is not rapid enough to produce a cathodic peak. The cathodic peak appeared to be greatly suppressed (by several orders of magnitude) when the TPyP is adsorbed. This provides direct evidence that the electrochemical reactivity of the preadsorbed TPyP is distinct from that of TPyP in solution phase. The different electrochemical activity of TPyP adsorbed on the Au(111) surface is probably due to the interaction with the Au substrate. Differences in the electrochemical behavior of adsorbed and solution phase species have been noted previously [4] [8].

In addition, after holding the electrode at a low potential, there is a cathodic peak that is symmetric to the anodic peak along the x axis. It is noteworthy that at a scan rate of 1 V/sec, the cathodic and anodic peaks are separated by 0.17 V in the CV under TPyP containing solution while the peak separation for the preadsorbed TPyP is negligible. The symmetry of anodic and cathodic peaks is characteristic of a reversible redox reaction of adsorbed species [13, 14]. The reversibility observed in Figure 6-6 appears in contradiction with Figure 6-3, Figure 6-4 and Figure 6-7, which all suggest that the P(0) species is slow to reduce. Therefore it is unreasonable to observe a cathodic peak as large as the anodic peak at relatively high scan rate (1 V/sec).

However, the TPyP covered electrode was held at a positive potential (0.6 V) for 5min before stepping to the negative potential. Evidently holding the electrode at positive potentials reduces the reduction rate of TPyP. The apparent contradiction can be

⁴ The charge density was integrated from 0.02 to 0.25V and subtracted by a straight line background.

explained by the presence of two kinds of P(0) species depending on the time spent at positive potentials. P(0)a has reactivity similar to that in the bulk solution and P(0)b has suppressed reactivity (Figure 6-8). P(0)a is an intermediate that is produced by the oxidation of P(-II). P(0)a is readily reduced to P(-II), resulting in a cathodic peak that is similar to the anodic peak in Figure 6-6. P(0)a is converted to P(0)b after staying at a high potential, e.g. 0.6 V, for a sufficient period of time. Therefore, after staying at a positive potential for a sufficient period of time, the cathodic peak diminishes.

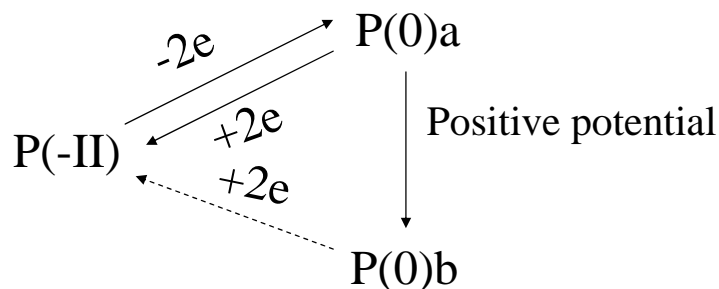


Figure 6-8 Proposed surface species of TPyP.

6.3.2. STM results.

6.3.2.1. Adsorbed TPyP under neat 0.1 M H₂SO₄.

To directly answer the question whether the TPyP molecules desorb at positive potentials (>0.3 V) in TPyP free solution, we preadsorbed TPyP onto the Au(111) surface at -0.25V (see 6.3.1.2) and imaged the TPyP covered surface under neat 0.1 M H₂SO₄ with EC-STM (Figure 6-9).

When the electrode potential was stepped from 0.05 to 0.15 V, where the adsorbed TPyP molecules were oxidized as suggested by the CV (Figure 6-3), a white linear island

appeared, indicated by an arrow at bottom of Figure 6-9 B. In addition, the image is very noisy. The noise in the STM images is most probably due to diffusive motion as has been reported by several groups [15-18]. The noisy areas and ordered molecular domains are imaged at the same time (Figure 6-9C). Accordingly, we suggest that the noise in the STM images is due to diffusive motion of adsorbates, instead of tip perturbation, which should affect the entire image. Figure 6-9C, taken at about 170 seconds after Figure 6-9 B, shows several domains containing ordered molecular arrays. There are still some noisy areas between the ordered molecular domains. The reconstruction stripes can now be resolved clearly under the adsorbed molecular adlayer. In next image, Figure 6-9D, the noisy areas have almost completely disappeared. Both the ordered molecular lattice and the reconstruction stripes under the adlayer are resolved clearly. Compared with Figure 6-9B, the domains in Figure 6-9D have assumed different orientations, suggesting that the molecules have rearranged. Furthermore an island, presumably resulting from the lifting of the Au(111) reconstruction, has appeared at the bottom right-hand corner. Usually, the Au(111) reconstruction does not lift until 0.3 V under sulfuric acid [19]. The partial lifting of the reconstruction in some areas is assumed to result from the adsorption of P(0) molecules, which may interact with Au(111) surface via a chemisorption interaction. Chemisorption may destabilize Au reconstruction and lift the substrate reconstruction [19].

The adsorbed TPyP molecules and the underlying corrugation of the Au(111) reconstruction can be observed clearly at even higher potential (0.25 V), Figure 6-9 C. After the electrode potential was stepped from 0.25 to 0.35 V (Figure 6-9 E), more

unreconstructed areas appeared. However, some reconstruction stripes were still present. When the potential was stepped to 0.45 V (Figure 6-9 F), the surface reconstruction was lifted completely.

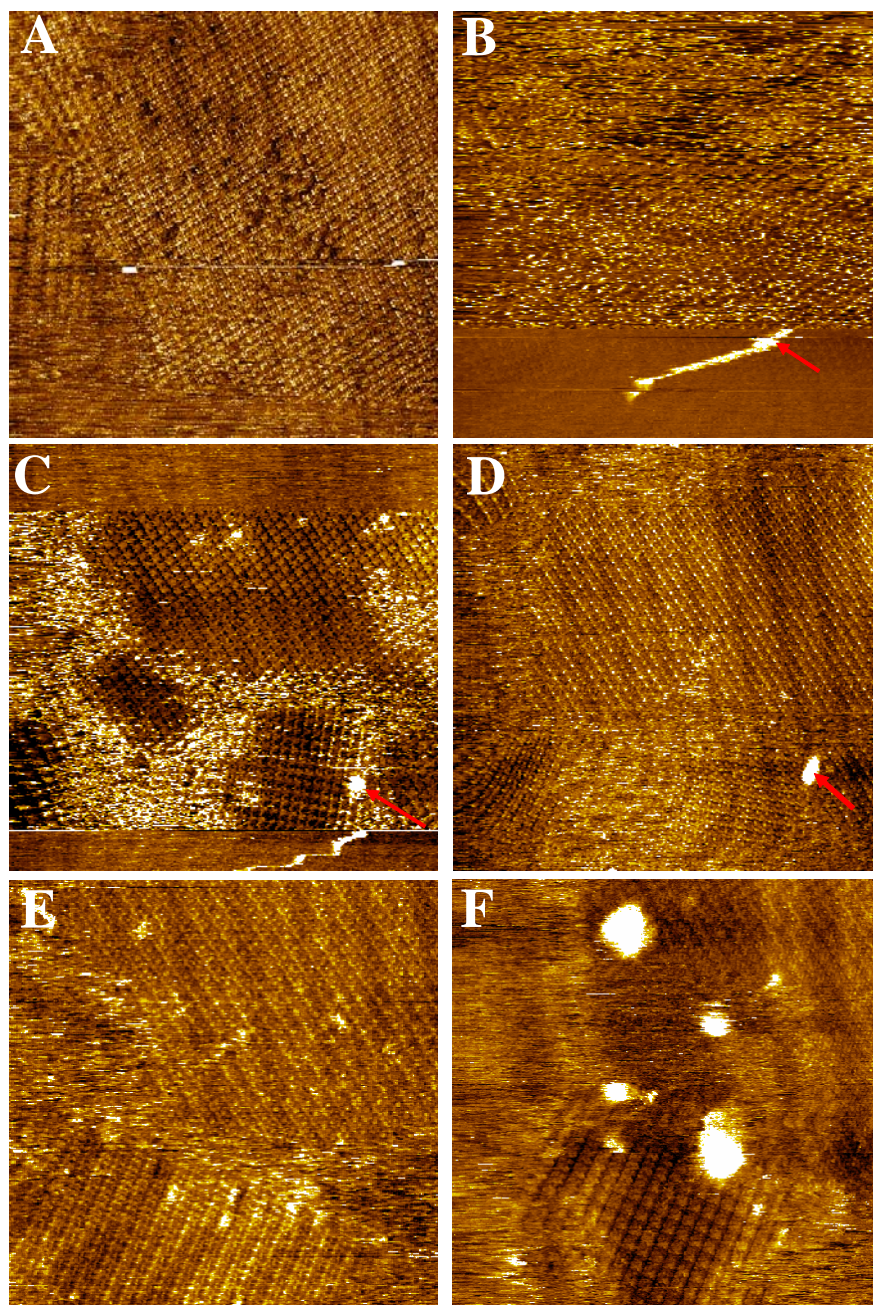


Figure 6-9 In situ STM images of preadsorbed TPyP on reconstructed Au(111) in 0.1 M H_2SO_4 solution. (A) obtained at electrode potential -0.05 V, setpoint $I = 0.2$ nA. (B-D)

obtained after electrode potential was stepped to 0.15 V from -0.05 V, setpoint $I = 0.2$ nA. E obtained at electrode potential 0.25 V. F obtained at electrode potential 0.35 V. Image size: 62 nm \times 62 nm. Scan direction: upward.

6.3.2.2. *Growth dynamics under TPyP solution.*

To understand the redox reactions and ordering process of TPyP, the potential dependence of adlayer structure on the unreconstructed Au(111) was studied in 0.1 M H_2SO_4 solution with 10^{-5} M TPyP. A disordered surface was prepared at by stepping the surface from -0.2 V to 0.5 V (see Figure 5-7C). Then the potential was stepped to 0.1 V, where the ordering should start.

Apart from the Au islands resulting from the lifting of Au(111) reconstruction [19], clusters containing porphyrin adsorbates can be resolved (Figure 6-10). Again the size of the molecules is between 1.5-1.6 nm. Interestingly the distribution of island height is binary. The majority of the molecular clusters are 2.5-3.1 Å higher than island free areas while some of the molecular clusters are only 1.2-1.5 Å high. This suggests the presence of monolayer and bilayer islands. However, height in the STM images does not always correspond to the physical height of the features. These STM images are acquired in constant current mode. The higher clusters may correspond to porphyrin molecules that have a higher tunneling probability, therefore displaying larger protrusion. However, close inspection of the boundaries between the layer with more apparent height and the layer with less apparent height provides evidence that former is adsorbed on top of the latter. The STM image shows that in the boundaries the layer with more apparent height sometimes blocks the view of molecules in the layer with less apparent height (Figure

6-11). Only parts of molecules in the “lower” layers are resolved in the STM while without exception, the entire molecules in the “higher” layers are resolved. This provides evidence that the molecules at the perimeter of a molecular cluster with higher apparent height partially overlap with the molecules at the underlying layer. Therefore the “higher” layer is assigned to bilayer adsorbed on top of a monolayer.

Figure 6-9 in the previous section suggests that monolayer coverage TPyP remain adsorbed between -0.05 V to 0.45 V under neat 0.1 M H₂SO₄. Therefore, in a TPyP containing solution, where the tendency for adsorption is even stronger, we expect TPyP molecules to fully cover the electrode surface. Therefore, we assume that TPyP molecules are present even in the areas where no molecules are resolved by STM (Figure 6-10). There are probably disordered TPyP molecules in those areas. Unlike molecules at 0.5 V (Chapter 4), where the binding energy is high enough to immobilize disordered molecules, the disordered molecules at 0.1 V are not sufficiently immobilized to be imaged. At this potential, only after incorporation into ordered domains can the TPyP molecules be resolved by STM.

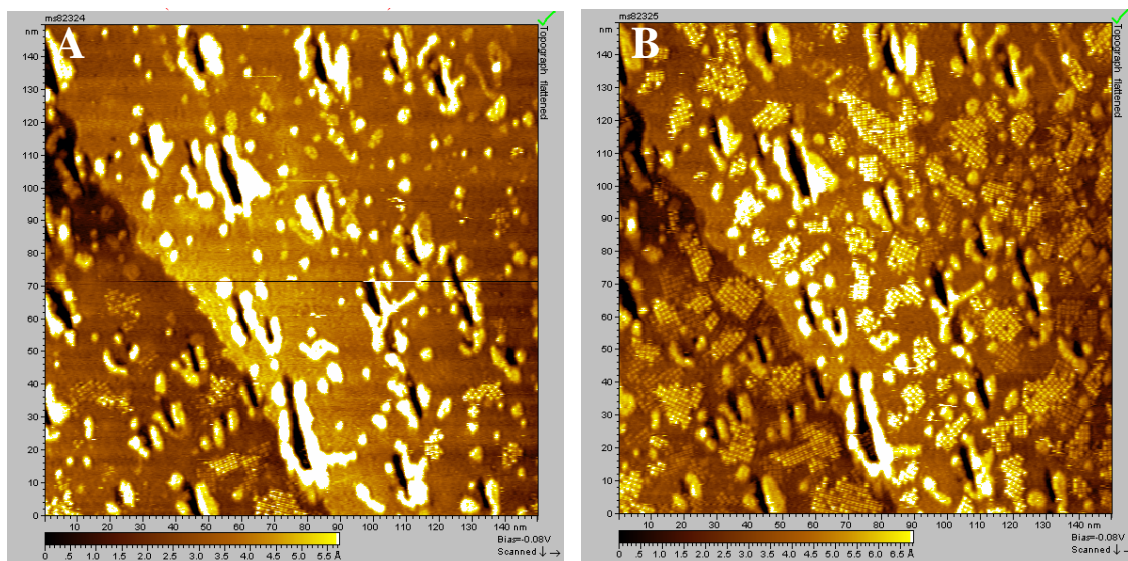


Figure 6-10 Time dependant STM images of TPyP adsorption onto Au(111). Solution: 1×10^{-5} M TPyP in 0.1 M H_2SO_4 . A 0-109 sec after potential step from 0.5 V to 0.1 V. B 109-218 sec after potential step from 0.5 V to 0.1 V. Image size: $62 \times 62 \text{ nm}^2$. Scan direction: downward.

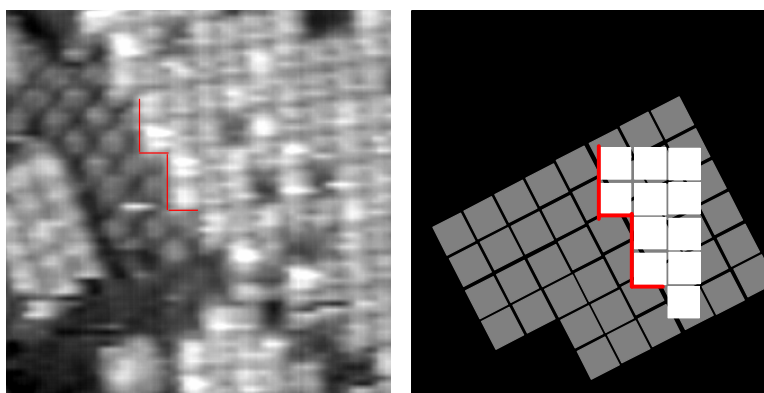


Figure 6-11 A: STM image ($20 \times 20 \text{ nm}^2$) of a TPyP domain boundary under 1×10^{-5} M / 0.1 M H_2SO_4 solution. Molecular layer 2.5-3.1 Å high coexists with molecular layer 1.2-1.5 Å high. The molecules in the layer which has higher apparent height are fully resolved while only partial molecules in the lower layer are resolved at the boundary highlighted by the red line. B: A model for the proposed multilayer structure.

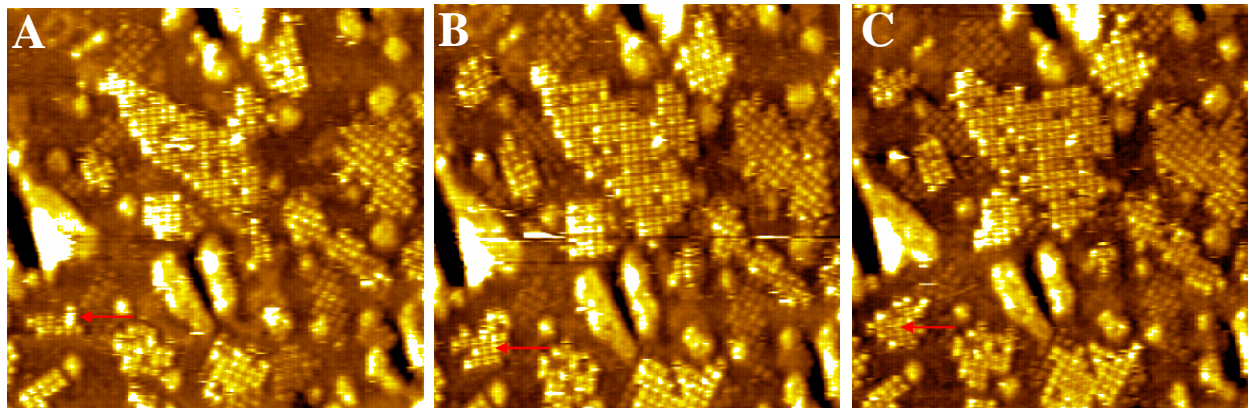


Figure 6-12 Time dependant STM images of TPyP adsorption onto Au(111) after potential step from 0.5 V to 0.1 V. Solution: 1×10^{-5} M TPyP in 0.1 M H_2SO_4 . A. 109-218 sec. B. 218-327 sec. C. 327-436 sec. The red arrows point to the same domain which grew after potential step. Image size: $40 \times 40 \text{ nm}^2$. Scan direction: downward.

The fractional coverage of bilayer, θ , is estimated by counting the number of molecules N . By assuming that each molecule occupies 2.4 nm^2 , θ can then be calculated in Equation 1, where A is the total area of the image.

$$\theta = \frac{N \times 2.4 \text{ nm}^2}{A(\text{nm}^2)} \quad \text{Equation 6-1}$$

In the coverage calculation, the image of the first scan (0-109sec) (Figure 6-10A) is divided into halves along the slow scan axis, with the top half representing the scan of 0-55 sec and the bottom half representing 55-109 sec. This increases the effective time resolution to about 1 min and allows better understanding of the time dependant growth of ordered domains.

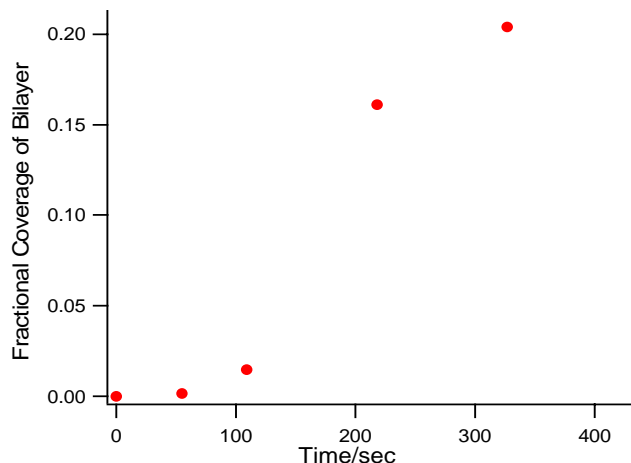


Figure 6-13 Fractional coverage of TPyP bilayer as a function of time after potential step from 0.5 V to 0.1 V.

By combining time dependant images and calculated fractional coverage (Figure 6-10, Figure 6-12, and Figure 6-13), one can recognize that the ordering of TPyP proceeds via the nucleation and growth mode. During the first 55 sec (Top half of Figure 6-10A), only a few molecules were resolved. Only after about 1min did clusters start to appear (lower part of Figure 6-10A), but the coverage remained very low (2%). There was an induction period of about 100 sec. Only after the induction period did the ordered domains grow rapidly. The overall coverage of bilayer domains rapidly increased to 0.16 between 109-218 sec.

This behavior is characteristic of nucleation and growth [20]. The growth of ordered domains proceeds via the radial expansion of nuclei that reach a critical size [20]. Once nucleation centers are formed, they can serve as templates for rapid growth. It is also evident that the orientations of the domains are largely determined by the nucleation stage. A careful inspection found that most of the domains imaged in Figure 6-10A

remained at the same orientation as their nucleation centers. However, the growth slowed down in the subsequent frames. The coverage increased to 0.2 between 209 and 318 sec and remained about 0.2 after 400 sec. The reduction in the growth rate may suggest that the coverage of bilayer has reached an equilibrium coverage. It may also suggest that the some other factors limit the growth of bilayer. The ordering process is dependant on the lateral organization of adsorbates. At the initial stage of growth, lateral reorganization is rapid due to large free volume of adsorbates. At a later stage, the free volume decreases and it is more difficult for the adsorbates reorganize laterally to form ordered domains.

6.3.2.3. *Dissolution of TPyP multilayers.*

When the potential was stepped to 0.15 V, the coverage of the bilayer was reduced slightly (Figure 6-14B). However, once the potential reached 0.2 V, the dissolution accelerated dramatically (Figure 6-14C,D). Most of the monolayer and bilayer clusters disappeared. Ordered domains as high as the surrounding, which should consist of disordered TPyP domains, appeared at the same locations as the clusters. The ordered domains are stable up to 0.6 V. We assume that the domains correspond to monolayer for the following reasons:

1. The STM images no longer display different levels of height.
2. The TPyP molecules are positively charged. All pyridine units can be protonated, therefore each molecule, in principle, carries up to four unit charges.

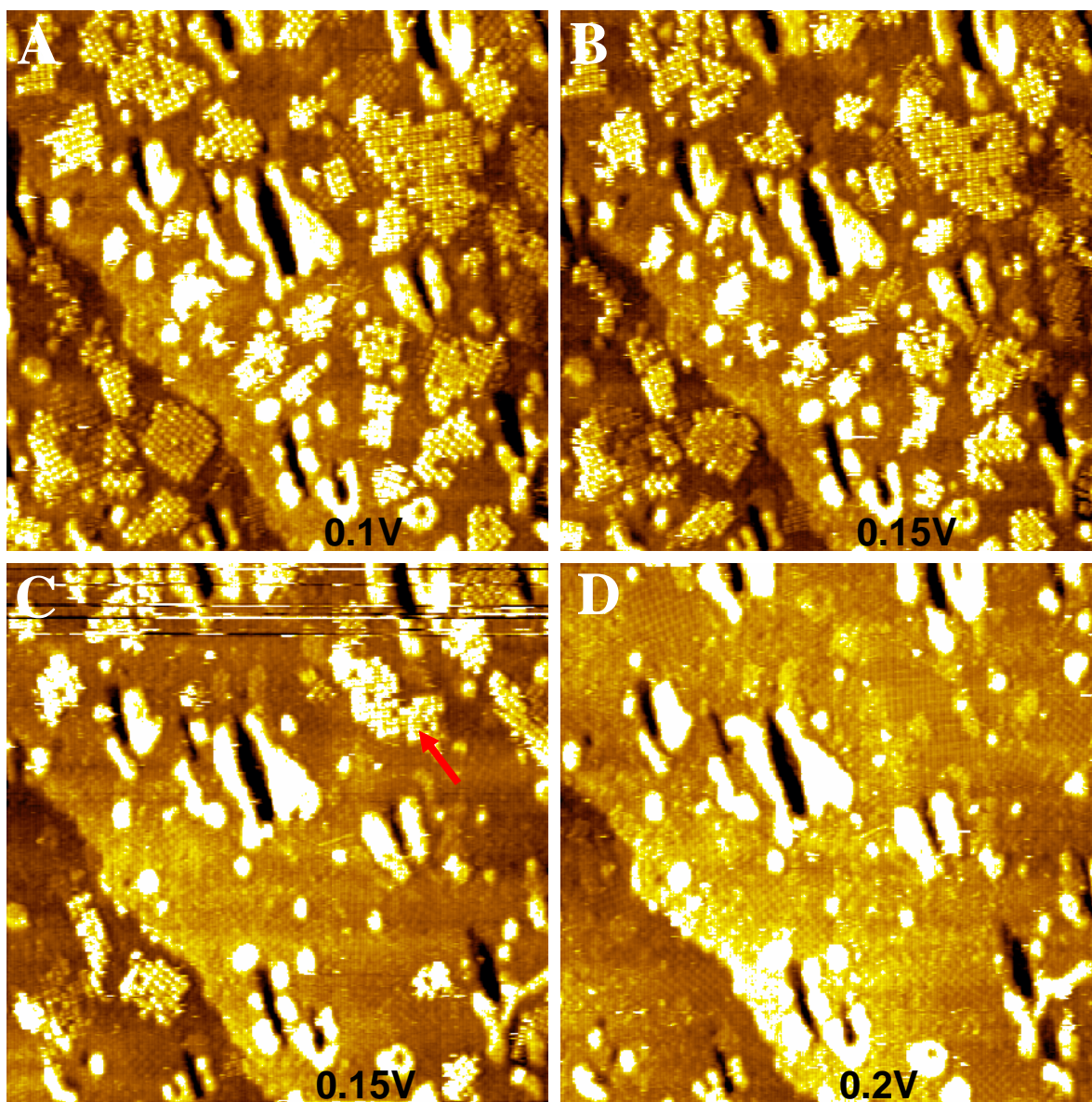


Figure 6-14 In situ STM images of TPyP on unreconstructed Au(111) under 1×10^{-5} M/0.1 M H_2SO_4 solution. (A) obtained at electrode potential 0.1 V. (B-C) obtained after potential step to 0.15 V 0-109 sec and 109-218 sec respectively. (D) after potential step to 0.2 V., 0-109 sec. Image size: $62\text{nm} \times 62\text{ nm}^2$. Scan direction: downward.

The electrostatic repulsion energy E is

$$E = nF\phi \quad \text{Equation 6-2}$$

where ϕ is the potential drop across the double layer, n is the number of unit charge and F

is the Faraday constant. Assuming ϕ to be 0.2 V and n to be 4, the electrostatic repulsion energy is 80 kJ/mol. Therefore, the positively charged surface is unlikely to adsorb multilayers of TPyP because the π stacking interaction is unlikely to be strong enough to compensate for the electrostatic repulsion.

The disappearance of the clusters was not due to the change in imaging contrast caused by an increase in bias because at least some of the bilayer clusters with similar height are still resolved in (Figure 6-14B,C). Cyclic voltammograms suggest only P(0) should exist at potentials higher than 0.2 V. The similar height of ordered and disordered domains reinforces our previous hypothesis that the disordered domains consist of adsorbed P(0). The potential of disappearance of clusters in STM images coincides with the potential of the anodic peak of P(-II) in CVs (Figure 6-6). Therefore we assume that after oxidation of P(-II), the top layer is oxidized and desorbed, leaving behind a monolayer that has lower apparent height.

6.3.3. Surface interactions.

Our previous STM results on the dynamics of TPyP on Au(111) in Chapter 5 indicated that the interaction between the TPyP adsorbate and the Au(111) substrate increased with increasing electrode potential [21]. Our results suggest that TPyP molecules are strongly adsorbed at positive potentials. In an acid solution, the pyridine groups of TPyP will be

protonated and the molecule will be positively charged. One would suppose that the positively charged TPyP monolayer would tend to desorb on a positively charge electrode surface. A possible explanation for the observation of adsorbed TPyP is that the strong contribution from π bonding interaction of the large π system exceeds the effect of electrostatic repulsion. The other reason is that the counter ions near the pyridinium units may screen some of the electrostatic repulsion.

Our STM results also suggest that TPyP has a tendency to form multilayers at potentials between -0.20 V to 0.15 V, where the surface charge density is moderately negative. It is well known in the solution phase that macrocycles tend to aggregate due to the π stacking interaction [22]. Multilayer adsorption of coronene onto a electrode surface was observed by Kunitake et al [23]. Coronene monolayers were stable over a wider potential range than the multilayers. The desorption of the insoluble neutral aromatic compound occurred when the surface became significantly charged. While not suggested by Kunitake et al., we believe that at a higher surface charge density, the water and ions are attracted to the surface, displacing the insoluble neutral adsorbate in the multilayers, consistent with our studies of order-disorder phase transitions of insoluble hexadecane at charged solid-liquid interfaces [24].

In the case of TPyP, the redox reaction may play an additional important role since the disappearance of multilayers in STM images coincided with the oxidation of P(-II). The P(0) species produced by oxidation may experience greater electrostatic repulsion (from the neighboring adsorbates as well as from the substrate) to form multilayers because, by

assuming a diacid form, the P(0) may have two more positive charges due to the protonation of the macrocycle. The increased repulsion may result in the desorption of multilayers at more positive surface charge density. It is to be noted that STM can only resolve immobilized multilayers. Below -0.25 V (Chapter 5), STM could not resolve porphyrin molecules. Reduced molecule-substrate interaction becomes insufficient to confine molecules into ordered 2D structures. However, CV suggests the multilayers are still present on Au surface (Figure 6-3) at -0.25 V. The multilayers were not sufficiently ordered to be resolved by STM. The presence of multilayers may be caused by electrostatic attraction of positively charged TPyP and the electrode surface.

6.3.4. The reactivity of adsorbed species.

One important question concerns the irreversibility of the oxidation of adsorbed TPyP (Figure 6-3). The irreversibility can be explained by desorption of oxidized species. Consequently the species are no longer available to be reduced. An alternative explanation is that the oxidized species remains adsorbed, but it is not readily reduced. By combining the STM and CV results, we find that both explanations are correct to some degree. STM results provide definitive evidence that even under a neat 0.1 M H₂SO₄, monolayer TPyP remains adsorbed on Au(111) over a wide range of potential (Figure 6-9). Therefore the lack of a reduction peak in the CV is due to the adsorbed P(0) species with distinct reactivity from P(0) present in solution. However, the irreversibility also has a contribution from the desorption of multilayers upon oxidation. Both STM and CV results suggest that multilayers are formed at potentials below 0.15 V. STM shows that the multilayers are desorbed above the oxidation potential, 0.2 V.

A more complete interpretation of the irreversibility takes into account a monolayer and multilayers that have different chemical reactivity. Due to strong interaction with the substrate, the electrochemical reactivity of the monolayer is greatly suppressed. Chemisorption may destabilize Au reconstruction and lift the substrate reconstruction [19]. STM results suggest that the interaction between P(0) and Au(111) has chemisorption character since P(0) partially lifts Au reconstruction (Figure 6-9B,C). Therefore, the redox properties of TPyP may be profoundly influenced by adsorption. The molecules in the more weakly adsorbed multilayers have reactivity similar to those in bulk solution. The oxidation of preadsorbed P(-II) causes the desorption of the physisorbed multilayer. In contrast, the chemisorbed monolayer remains on the surface and cannot be oxidized easily.

Another surprising result is that adsorbed P(-II) is oxidized to another P(0) intermediate (P(0)a) that has high reactivity as suggested by Figure 6-6. At a positive potential, P(0)a is converted to P(0)b, which does not display a reduction peak at the potential range we investigated (-0.25 to 0.6 V).

The nature of these species is unclear for the moment. The P(0)a intermediate with enhanced reactivity may have the same chemical composition as the P(0)b. The difference in reactivity may originate from the interaction with the substrate. P(-II) is assumed to be a physisorbed species since its reactivity is similar to P(-II) in the bulk.

Therefore, it is reasonable that after oxidation, the P(-II) is converted to another weakly adsorbed species, P(0)a, which is a precursor to a chemisorbed species, P(0)b.

Another possibility is that the P(0)a and P(0)b may correspond to two different chemical species. For example, P(0)a may correspond to a protonated species such as $P(0)H_4^{2+}$ and P(0)b may correspond to an unprotonated species such as $P(0)H_2$ (Figure 6-8). The reduction of $P(0)H_4^{2+}$ should be more facile than $P(0)H_2$ due to the presence of additional positive charges. $P(0)H_4^{2+}$ is clearly unfavorable at positively charged surface. To minimize electrostatic repulsion, it may deprotonate to form $P(0)H_2$ at positive potential. However, this hypothesis contrasts with the Itoh's SERRS investigation, which suggests that porphyrins always assume $P(0)H_4^{2+}$ adsorption state under acidic mediums [7]. We nevertheless note that the substrate used for their study, electrochemically roughened Ag electrodes, may differ dramatically from the planar Au(111) electrode we use and the chemical states of adsorbed species may differ substantially.

6.4. Conclusions and future work.

Our findings can be summarized as following.

- TPyP is irreversibly adsorbed at Au(111) over a wide range of potential, from -0.25 V to 0.8 V.
- Adsorbed TPyP forms monolayers and multilayers with distinct electrochemical reactivity. The monolayer is present at a wide range of potentials (-0.25 V to 0.6 V), suggesting that TPyP is irreversibly adsorbed

at Au(111). However, multilayers desorb near the oxidation potential of TPyP. The desorption of multilayers may be caused by the electrostatic repulsion.

- TPyP adsorbates in the monolayer display distinct electrochemical reactivity from TPyP in solution. By holding the TPyP covered electrode at a lower potential, we demonstrate that TPyP adsorbed at positive potentials is reduced significantly more slowly.
- CVs of preadsorbed TPyP suggest the oxidation of reduced TPyP P(-II) forms at least two P(0) species. Immediately after oxidation, a P(0)a intermediate is produced, which is readily reduced. At positive potential, P(0)a may be converted to P(0)b, which has suppressed reactivity.
- Time dependant STM images suggest that the self-assembly of TPyP follows a nucleation and growth mode. The orientations of the nucleation centers determine the orientations of molecular domains. This suggests that strategies that reduce nucleation centers may result in the formation of larger molecular domains.
- This study further reinforces our conclusion in Chapter 5 that the potential dependant surface interaction can be exploited to control the ordering of adsorbates [25]. We have demonstrated that we can induce the ordering and study its kinetics by potential perturbation. We can also direct the formation of multilayers.

Our combined CV and STM investigation reveals a complex interplay between redox reactions, monolayer and multilayer adsorption, and lateral organization of molecules. Many studies have shown that adsorption suppresses the electrochemical reactivity of porphyrins [26]. In situ STM studies can afford more insight into the origin of the distinct electrochemical reactivity of adsorbed species. The distinct redox chemistry of TPyP adsorbates is clearly influenced by their interaction with the substrate, as revealed by in situ STM. On the other hand, the change of chemical nature of adsorbed species changes the surface interactions and the resultant surface structures. This is supported by the potential of desorption of multilayers coinciding with the oxidation potential.

Future work includes further investigations of the chemical nature of adsorbed species. More systematic electrochemical studies, including the effect of potential and duration at positive potentials, as well as the pH dependence, may clarify the chemical nature of P(0)b. It will be very instructive if STM can provide spectroscopic contrast on porphyrins with different redox states. In general it is challenging under an electrochemical environment because the contrast may heavily depend on the tip condition, which is difficult to reproduce. However, by controllably varying the chemical composition of adsorbates, the ability to differentiate different porphyrin species has been demonstrated [27].

Another important area is the self assembly process at electrode surfaces where more elaborate control may be possible once the molecular scale dynamics of the ordering process is better understood. Currently our understanding of the dynamics of molecular

self-assembly at electrochemical interfaces is largely limited to macroscopic measurements such as differential capacitance on weakly adsorbed molecules [28]. Chapters 5 and 6 suggest the critical role of electrode potential in ordering of porphyrin adsorbates. Our results suggest that the electrode potential can trigger the nucleation and growth process of self-assembly. More real space STM studies of the dynamics of ordering over a wide range of potentials may help to understand how electrode potentials may affect different stages of the ordering process. It is common in nanoparticle synthesis to create a controlled amount of nucleation centers and trigger controlled growth of nanoparticles [29]. It should be possible to design potential perturbations that control the density of nucleation centers and hence the size of ordered molecular domains.

BIBLIOGRAPHY

1. Forrest, S.R., *Ultrathin organic films grown by organic molecular beam deposition and related techniques*. Chemical Reviews, 1997. **97**(6): p. 1793-1896.
2. Dolphin, V.D., ed. *The Porphyrins*. 1979, Academic Press: New York.
3. Hutchison, J.E., T.A. Postlethwaite, C.H. Chen, K.W. Hathcock, R.S. Ingram, W. Ou, R.W. Linton, R.W. Murray, D.A. Tyvoll, L.L. Chng, and J.P. Collman, *Electrocatalytic activity of an immobilized cofacial diporphyrin depends on the electrode material*. Langmuir, 1997. **13**(7): p. 2143-2148.
4. Ni, C.L. and F.C. Anson, *Relation between the potentials where adsorbed and unadsorbed cobalt(III) tetrakis(N-methylpyridinium-4-yl)porphyrin is reduced and those where it catalyzes the electroreduction of dioxygen*. Inorganic Chemistry, 1985. **24**(26): p. 4754-6.
5. Wilson, G.S. and B.P. Neri, *Cyclic voltammetry of porphyrins and metalloporphyrins*. Annals of the New York Academy of Sciences, 1973. **206**: p. 568-578.
6. Neri, B.P. and G.S. Wilson, *Electrochemical studies of meso-tetra(4-methylpyridyl)porphyrin in acid solution*. Analytical Chemistry, 1972. **44**(6): p. 1002-1009.
7. Koyama, T. and K. Itoh, *Comparison of electrochemical redox processes on silver electrode surfaces between meso-tetrakis(2-N-methylpyridyl)porphine and meso-tetrakis(4-N-methylpyridyl)porphine. Study by surface-enhanced resonance Raman scattering spectroscopy*. Journal of Electroanalytical Chemistry and Interfacial Electrochemistry, 1986. **215**(1-2): p. 209-222.
8. Bedioui, F., J. Devynck, C. Hinnen, A. Rousseau, C. Bied-Charreton, and A. Gaudemer, *In situ characterization of redox properties of water-soluble porphyrins irreversibly adsorbed on gold electrode using the electroreflectance technique*. Journal of the Electrochemical Society, 1985. **132**(9): p. 2120-4.
9. Kunitake, M., N. Batina, and K. Itaya, *Self-organized porphyrin array on iodine modified Au(111) in electrolyte solutions in situ Scanning Tunneling-Microscopy study*. Langmuir, 1995. **11**(7): p. 2337-2340.
10. Tao, N.J., G. Cardenas, F. Cunha, and Z. Shi, *In-situ STM and AFM study of protoporphyrin and Iron(III) and Zinc(II) protoporphyrins adsorbed on graphite in aqueous- solutions*. Langmuir, 1995. **11**(11): p. 4445-4448.
11. Poirier, G.E., *Characterization of organosulfur molecular monolayers on Au(111) using scanning tunneling microscopy*. Chemical Reviews, 1997. **97**(4): p. 1117-1127.
12. Angerstein-Kozłowska, H., B.E. Conway, A. Hamelin, and L. Stoicoviciu, *Elementary steps of electrochemical oxidation of single-crystal planes of gold - I. Chemical basis of processes involving geometry of anions and the electrode surfaces*. Electrochimica Acta, 1986. **31**(8): p. 1051-61.
13. Brown, A.P., C. Koval, and F.C. Anson, *Illustrative electrochemical behavior of reactants irreversibly adsorbed on graphite electrode surfaces*. Journal of Electroanalytical Chemistry and Interfacial Electrochemistry, 1976. **72**(3): p. 379-87.
14. Bard, A.J. and L.R. Faulkner, *Electrochemical Methods: Fundamentals and Applications*. 1980. 718 pp.

15. Poensgen, M., J. Wolf, J. Frohn, M. Giesen, and H. Ibach, *Step dynamics on Ag(111) and Cu(100) surfaces*. Surface Science, 1992. **274**(3): p. 430.
16. Sumetskii, M. and K. Aa, *Noise in STM due to atoms moving in the tunneling space*. Physical Review B, 1993. **48**(23): p. 17493.
17. Sumetskii, M., A. Kornyshev, and U. Stimming, *Adatom diffusion characteristics from STM noise - Theory*. Surface Science, 1994. **309**: p. 23.
18. Dunphy, J., P. Sautet, D. Ogletree, O. Dabbousi, and M. Salmeron, *Scanning-Tunneling-Microscopy study of the surface-diffusion of sulfur On Re(0001)*. Physical Review B, 1993. **47**(4): p. 2320.
19. Kolb, D.M., *Reconstruction phenomena at metal-electrolyte interfaces*. Progress in Surface Science, 1996. **51**(2): p. 109-173.
20. Buess-Herman, C., *Dynamics of adsorption and two-dimensional phase transitions at electrode surfaces*, in *Adsorption of Molecules at Metal Electrodes*, J. Lipkowski and P.N. Ross, Editors. 1992, VCH: New York. p. 77 pp.
21. He, Y., T. Ye, and E. Borguet, in preparation.
22. Akins, D.L., H.R. Zhu, and C. Guo, *Absorption and raman-scattering by aggregated meso-tetrakis(p-sulfonatophenyl)porphine*. Journal of Physical Chemistry, 1994. **98**(14): p. 3612-3618.
23. Uemura, S., M. Sakata, I. Taniguchi, C. Hirayama, and M. Kunitake, *In situ observation of coronene epitaxial adlayers on Au(111) surfaces prepared by the transfer of Langmuir films*. Thin Solid Films, 2002. **409**(2): p. 206-210.
24. He, Y., T. Ye, and E. Borguet, *The role of hydrophobic chains in self-assembly at electrified interfaces: Observation of potential-induced transformations of two-dimensional crystals of hexadecane by in-situ scanning tunneling microscopy*. Journal of Physical Chemistry B, 2002. **106**(43): p. 11264-11271.
25. He, Y., T. Ye, and E. Borguet, *Porphyrin self-assembly at electrochemical interfaces: Role of potential modulated surface mobility*. Journal of the American Chemical Society, 2002. **124**(40): p. 11964-11970.
26. Shi, C.N. and F.C. Anson, *A simple method for examining the electrochemistry of metalloporphyrins and other hydrophobic reactants in thin layers of organic solvents interposed between graphite electrodes and aqueous solutions*. Analytical Chemistry, 1998. **70**(15): p. 3114-3118.
27. Tao, N.J., *Probing potential-tuned resonant tunneling through redox molecules with scanning tunneling microscopy*. Physical Review Letters, 1996. **76**(21): p. 4066-4069.
28. De Levie, R., *The dynamic double layer: Two-dimensional condensation at the mercury-water interface*. Chemical Reviews, 1988. **88**(4): p. 599-609.
29. Steigerwald, M.L. and L.E. Brus, *Semiconductor crystallites: a class of large molecules*. Accounts of Chemical Research, 1990. **23**(6): p. 183-8.

7. Electrodeposition onto molecular scale templates.

7.1. Introduction.

This chapter describes the effect of surface micelles on the nanoscale metal structures created by electrodeposition. Relevant background information concerning electrodeposition and organic-metal interactions is provided below.

7.1.1. Electrodeposition.

Compared to other metallization techniques, vapor deposition [1] and electroless deposition [2], electrodeposition is a simple process that allows good control of surface morphology and surface coverage through control of parameters such as electrode potential, current density, additives, and plating time [3, 4]. During electrode deposition, an electrode is in contact with an electrolyte containing metal ions to be reduced and deposited on the electrode. Electrochemistry distinguishes between bulk deposition and underpotential deposition [5-7]. Bulk electrodeposition refers to the electrochemical deposition of a metal on a substrate made of the same metal. The equilibrium electrode potential E of bulk deposition is controlled by the well known Nernst equation (Equation 7-1) [8], where E_0 is the standard electrode potential, n is the number of unit charge on the metal, F is the Faradaic constant and $a_{M^{n+}}$ is the activity of the metal ions [8].

$$E = E_0 + \frac{RT}{nF} \ln(a_{M^{n+}}) \quad \text{Equation 7-1}$$

At potentials lower than E , the metal ions are reduced to elemental metal which is deposited on the electrode surface.

Underpotential deposition (UPD) [5-7] occurs when metal is deposited on a foreign substrate that has higher affinity for the metal than the interaction between atoms of the metal to be deposited. As a consequence, the metal starts to form atomic layers on the foreign substrate at a potential less negative than E . UPD is a self-limiting process since the enhanced interaction with the substrate is limited to a few atomic layers near the surface. As the number of layers increases, the deposition potential quickly approaches the bulk deposition value.

7.1.2. Organic molecules as resists.

One of the most versatile methods to fabricate metal patterns on surfaces is to deposit metals in the presence of organic resists. There have been considerable interests in using well defined organic monolayers as resists. The monolayers can either act as masks to block metal deposition or, with metallophilic functional groups, act as the preferential sites for metal deposition [9]. Evidently, the organic layers must be patterned, which is typically achieved with photolithography, E-beam lithography, scanning probe lithography or soft lithography [10]. Photolithography and soft lithography have limited resolution (~ 100 nm). E-beam and SPM lithography, though capable of nm resolution, write structures in serial fashion and therefore are not suitable for large scale fabrication [10]. Molecular self-assembly, in which molecules self-organized into defined patterns, is a parallel process and may potentially compliment traditional lithography processes in defining nm scale structures [11]. By careful design of molecular building blocks, the achieved self-assembled structures are growing in complexity [12-14].

An interesting question is whether the features in the 2D self-assembled structures can define the lateral placement of metal nanostructures. Self-assembled structures of diblock polymers can act as templates to form perpendicular electrodeposited nanowires tens of nm in diameter [15]. In addition to macromolecules, features of truly molecular dimension are exploited to create various metal nanostructures. Hatzor and Weiss showed that self-assembled multilayers can act as masks to form gaps as small as several nanometers. The gap width is controlled by the thickness of self-assembled multilayers [16]. Kim et al. used self-assembled organic nanotubes to grow atomic silver wires perpendicular to the substrate [17]. A recent study suggests that the electrodeposited copper oxide grown on achiral surfaces in the presence of chiral molecules can be imparted with enantioselectivity [18]. However, little is known how metal atoms are deposited on preferential surface sites in these molecular scale templates and how the templates are perturbed by the deposited metal atoms. Studies capable of interrogating the structural evolution during deposition process will be helpful to understand and optimize formation of nanostructures in these templates.

7.1.3. Metal-organic interfaces.

In addition to creating lateral metal patterns, metallization on organic structures is also an important means to create well-defined metal-organic interfaces. Molecular electronics applications require connecting organic molecules to two or three conducting terminals [19]. A common approach to create metallic contacts with organic molecules is to deposit metal on top of self-assembled monolayers [1, 20, 21] or Langmuir Blodgett films [22]. To achieve good performance, the top metal electrode must only be in contact with

the top of the monolayers. However, in reality, this interface is typically poorly defined. Metal atoms tend to penetrate the voids or inter-chain free volumes in monolayers and create shorts during metal evaporation [1, 19-21] or electrodeposition [23]. SIMS and XPS studies showed that the resulting structures of metal-organic interfaces are very sensitive to interactions between metal atoms and functional groups in the monolayers [20, 21]. More microscopic details of the interactions need to be understood and controlled to form well defined metal-organic-metal contact.

7.1.4. Self-assembled 2D structures of surfactants.

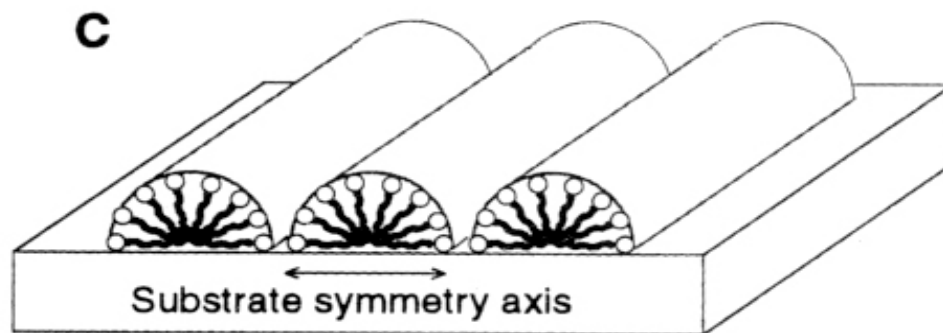


Figure 7-1 Proposed model of hemicylindrical structure of CTAB surface aggregates on hydrophobic surfaces [24].

Although surfactants have long been recognized to form micellar structures in bulk solutions [25] and evidence also suggested the presence of micelle-like surface aggregates when surfactant molecules are adsorbed [26], direct evidence of micelle-like surface structures only appeared less than a decade ago [24, 27]. Using AFM, Manne et al. observed that cetyltrimethylammonium bromide (CTAB) formed hemicylinders on

graphite [27]. The hydrophobic chains aggregate while the hydrophilic head groups are exposed to the aqueous environment.

Surface micelles have also been observed by AFM on metal surfaces [28]. The effect of surface charge density at metal electrodes on the surface structures of SDS has long been suggested by differential capacitance measurement [29, 30]. The Lipkowski group applied in situ AFM and STM to study the potential dependant structures of surface aggregates on Au(111) [31]. The observed structures of SDS on Au resembles those of CTAB on graphite (Figure 7-1). STM results suggest that on the surface, the molecules in the first layer lie flat on the surface to form rows with head to head, tail to tail configuration (Figure 7-1). The unit cell of the ordered structure is 4.4 nm long and 0.5 nm wide. The sulfate head groups are about 0.8 nm apart. On top of monolayer rows, the SDS molecules aggregate to form hemicylinders. On the surface of the hemicylinders are hydrophilic sulfate groups, thereby shielding the hydrophobic core from the aqueous environment. It was found that the hemicylindrical structure formed by 16 mM SDS was stable at a potential range of $-0.2 V_{SCE}$ to $0.3 V_{SCE}$, under which the electrode is moderately charged [31]. SDS molecules desorb at a sufficiently negatively charged surface. If the electrode potential is increased to a point where the positive surface charge density becomes equal to or exceeds the negative charge of adsorbed SDS, the repulsion between the sulfate groups is completely screened and SDS molecules form a condensed film [31]. The exact structure of the condensed film at positive potential remains unclear. It is not clear, for example, if SDS molecules form a monolayer or a bilayer [32].

7.1.5. Motivation.

Electrodeposition of metals such as tin [33] and copper [34, 35] in the presence of cationic or anionic surfactants has been investigated. The adsorbed surfactants were observed to hinder metal deposition [33-35]. It has been proposed that surface aggregates block the diffusion of metal ions to the surface, which is necessary for reduction. In addition, the adsorbed surfactants can promote the layer by layer deposition by reducing the [33-35].

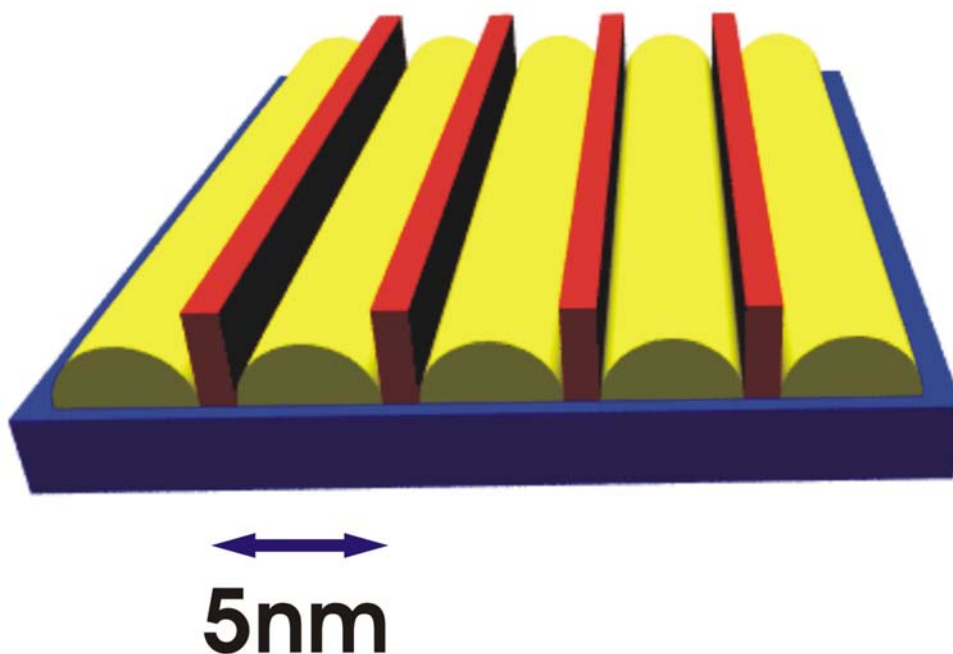


Figure 7-2 Hypothetical formation of silver nanowires on the hemicylindrical surface micelles. Parallel silver wires may be preferentially formed at the trench site, the surface site between the hemicylinders.

Our hypothesis is that, under optimal conditions, metal atoms may preferentially be electrodeposited certain sites in self-assembled molecular templates, such as the trench sites between the hemicylindrical surface micelles (Figure 7-2) or space between the

hexadecane molecular rows (Chapter 4). These sites allow interaction with the bare substrate as well as the neighboring sulfate groups. In addition to patterning metal on surface, we believe the surface micelles are a model system to understand the interaction between organic molecules and the deposited metal. By imaging the deposition process of metals on the two dimensional structure, we can obtain direct information about the affinity between the metal atoms and functional groups.

We have demonstrated that the intrinsic length scales of molecular assemblies may be exploited to grow metal nanostructures of controlled spacing. We observed evidence for preferential deposition of metals in molecular templates. We found that the concentration of the metal ions is critical for the selective metal deposition on to the templates. The observed metal structures provide insight into the interaction between metal atoms and organic functional groups. We hope that understanding and tailoring the interactions will lead to more precise control of over the placement of new strategies to connect organic molecules to metal nanostructures.

7.2. Experimental.

An Au(111) single crystal disc (Monocrystals Co., Ohio) was used as the substrate. Prior to the experiments the substrate was cleaned by immersion in hot piranha solution [1:3 H₂O₂ (J. T. Baker, CMOSTM) and H₂SO₄ (J. T. Baker, CMOSTM)] for 1 hour, and immersion in hot HNO₃ (EM SCIENCE GR) for 30 minutes. (Caution! The piranha solution is a very strong oxidizing agent and extremely dangerous. Eye protection and

gloves should be used during handling.) After each step the sample was rinsed by ultrasonication in ultrapure water ($>18\text{M}\Omega\cdot\text{cm}$) produced by a Barnstead, Nanopure Infinity system equipped with a UV lamp to further reduce trace amounts of organic impurity. After chemical cleaning, the crystal was hydrogen flame annealed, and allowed to cool down under Argon purging. The crystal was quickly covered with a drop of water and transferred to an STM electrochemical cell to be filled with electrolyte.

The electrochemical cell was made of Teflon. To prevent the leakage of the surfactant solution, an O-ring (Chemraz, Ace glassware) was used to seal the gap between the cell and the Au single crystal. A silver wire was used as the reference electrode. The potential is quoted against SCE. A platinum wire was used as the counter electrode. All cell components (with the exception of silver wire) were chemically cleaned in the same way as the crystal. The silver wire was sonicated in methanol and water.

All chemicals: sodium dodecylsulfate (Fluka, $>99\%$) and silver perchlorate monohydrate (Aldrich, 99.999%) were used as received. Sodium dodecylsulfate undergoes slow hydrolysis in aqueous solution [36]. Therefore sodium dodecylsulfate solution was prepared within 24 hrs prior to each experiment.

STM and AFM images were obtained with a PicoScan SPM system (Molecular Imaging). A bi-potentiostat (Molecular Imaging) was used to control the sample and tip potential independently, as well as to perform cyclic voltammetry. STM tips were etched tungsten tips coated with polyethylene, since we found that our paraffin wax coating used

previously was unstable in surfactant solutions. More details of the tip fabrication procedure can be found in Appendix C.

Oxide sharpened Si_3N_4 AFM tips were purchased from Digital Instruments. The cantilever with a nominal spring constant of 0.06 N/m was selected for imaging. The tips were cleaned in hot piranha solution (1:3 H_2O_2 (J. T. Baker, CMOSTM) and H_2SO_4 (J. T. Baker, CMOSTM)) prior to imaging.

7.3. Results.

7.3.1. Potential dependant structures of SDS at electrochemical interfaces.

7.3.1.1. Structure of surface micelles on Au(111).

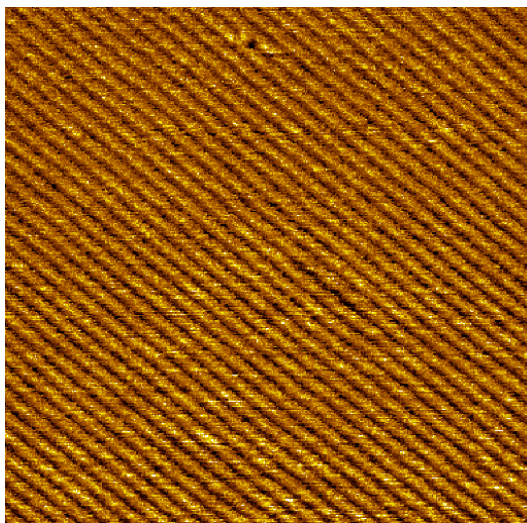


Figure 7-3 Deflection mode AFM image of surface aggregates on Au(111) under 10 mM SDS. Image size $150 \times 150 \text{ nm}^2$. Electrode potential: $0.3 \text{ V}_{\text{SCE}}$.

AFM images suggest that SDS can form uniformly spaced strips on Au(111) surface (Figure 7-3). The stripes in the AFM image have a periodicity of 4.4 nm, in good agreement with Lipkowski et al. [31]. The force-distance curve displays an exponential

increase of repulsive force as the tip approaches the surface until the repulsion force is higher than 0.2nN, beyond which the tip jumps into contact with the surface.

Manne et al. explained the jump-to-contact behavior to the presence of surface micelles [27]. The SDS solution has a pH about 6-7. At this pH, the Si_3N_4 AFM tip is negatively charged [37]. The negatively charged tip experiences electrostatic repulsion from the negatively charged top of surface micelles. When the force is higher than a certain value, the surface micelles collapse. This is reflected in the drop of the force. The force sharply increases after the tip is in contact with the hard surface. Manne et al. pointed out that the surface micelles are only imaged by AFM when the delicate force does not perturb the surface micelles but has sufficient force gradient proximity to discriminate the surface structures [27]. It has been pointed out by Wanless and Dukker that the apparent height of surface micelles, defined as the height difference (0.1-0.2 nm) between the top of surface micelles and the trench site between the neighboring surface micelles in AFM images does not reflect the true topography of surface micelles[38]. The resolution of AFM is largely determined by the force gradient around the local structures. Compared to typical AFM imaging conditions when the tip is in hard contact with the surface, the tip is mapping the contour of double layer force, which decays more slowly with increasing distance [38]. In addition, due to the finite size of the tip, the tip may not reach able to reach the bottom of the “trenches” between the surface micelles [38]. A better way to extract the height information is to measure the distance between the jump-to-contact point, where the micelles begin to collapse, and the hard contact point [27]. The distance is about 2.5 nm, which is about the length of a SDS molecule.

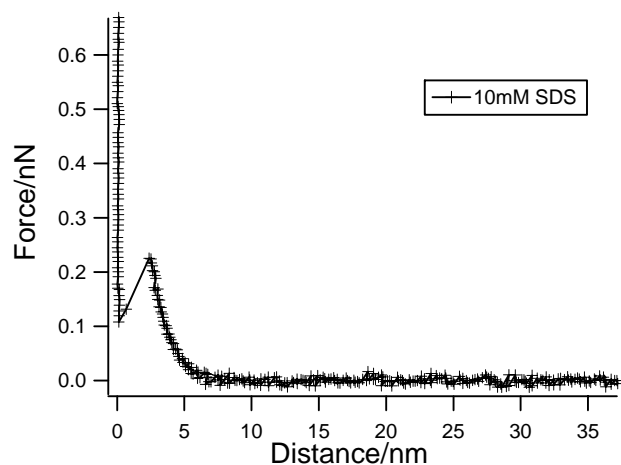


Figure 7-4 Approach force-distant curve of Au(111) under 10 mM SDS at open circuit potential. The force is calculated using the nominal spring constant of the cantilever, 0.06 N/m.

7.3.1.2. *Potential dependant structures.*

Our primary objective is to deposit metal on the templates formed by surface micelles. Therefore it is important to study the stability of these structures at different electrode potential. In agreement with Lipkowski et al. [31], AFM images suggest that the highly ordered stripes are only present within a certain potential range (Figure 7-5). The ordered structure disappeared at potentials below -0.3 V. As discussed in Chapter 4, if the surface charge density is sufficiently negative, the electrolyte displaces the alkyl chains [39]. The sulfate ions also experience greater repulsion by the surface charge. Therefore the SDS molecules are desorbed. Above 0.35 V, the structures become more disordered. The stripes are no longer continuous. The surface aggregates become more spherical instead of elongated.

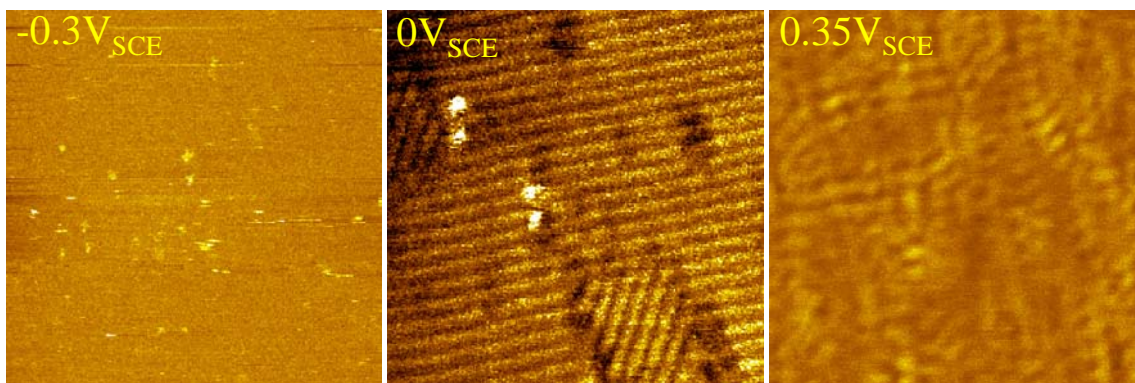


Figure 7-5 Surface charge dependant structure of SDS on Au(111). 10 mM SDS. Image size: $100 \times 100 \text{ nm}^2$.

As mentioned in the introduction, the structure of SDS at positively charged surface is unclear. Capacitance measurement suggest that the onset of the abrupt capacitance drop occurs when the positive surface charge density exceeds the charge density of a monolayer of closely packed sulfate groups [30, 31]. Therefore, it is assumed that SDS molecules form a closely packed monolayer with head groups anchored to the gold surface and hydrocarbon tails pointing towards the aqueous environment (Figure 7-6A). However, AFM force curves suggest that the surface remains negatively charged after the formation of the condensed film [31]. If there were only a monolayer present, the positive surface charge should be sufficient to cancel the negative charge of the head groups and consequently the force curve should display attraction instead of repulsion. Evidently, there is more than a single monolayer on the surface.

A single monolayer exposes the hydrophobic tails to the electrolyte. This is an unfavorable situation. Wang et al. hypothesized that SDS forms a lipid-like bilayer at the positively charged Au surface (Figure 7-6B)[32]. The second layer minimizes exposure

of the hydrophobic monolayer surface to the aqueous environment. In the end, only the hydrophilic head groups are exposed to the aqueous environment.

Supporting the bilayer model is the STM observation of closely packed hexagonal structure with spacing of 0.5nm [32]. It was assumed that the top of the bilayer was imaged. However, it is unlikely that the STM can image the headgroups of the bilayer. To resolve the headgroups on top of the bilayer by STM, electrons must tunnel through 24 insulating hydrocarbon groups (CH₂ and CH₃ groups), which would be extremely difficult. In the literature, the longest alkanethiol successfully imaged by STM has 18 CH groups at ultra low tunneling current (pA or less) [40]. Therefore, we believe in that case, it is unlikely that STM can image the insulating bilayer adsorbed on top of the monolayer. The tip may penetrate the bilayer to image the alkyl chains in the monolayer of SDS [32]. From a theoretical point of view, bilayer formation is unlikely because of the repulsion between the charged sulfate groups on top of the bilayer. The excessive positive charge density (higher than the charge density of SDS monolayer) is unlikely to promote the formation of lipid-like bilayer structures because the positive surface charge would attract the sulfate groups in the bilayer toward the monolayer instead of pointing away from the monolayer.

We suggest that the SDS molecules form micelle like structures on the hydrophobic monolayer surface (Figure 7-6C).

1. This model can explain the micelle like structure at positively charged surface (Figure 7-5).

2. In this model, only the hydrophilic head groups are exposed to electrolyte.
3. This model takes into consideration the repulsion between the sulfate groups on top of the monolayer.

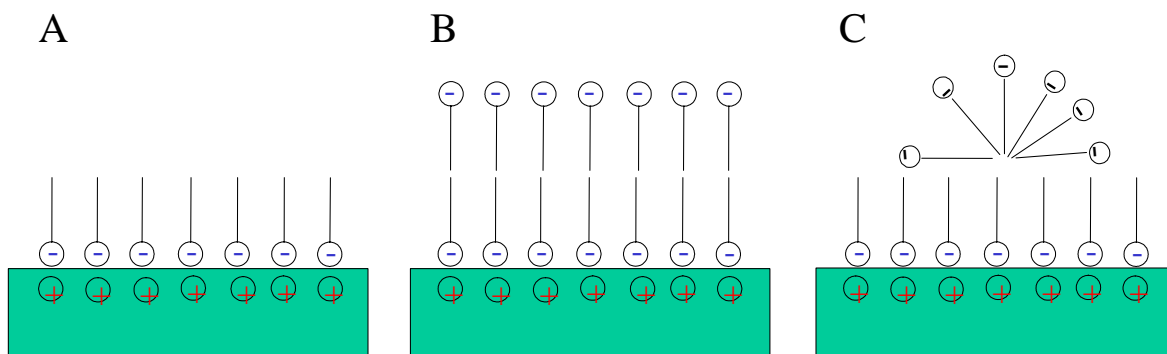


Figure 7-6 Hypothetical structures of adsorbed SDS at positively charged Au(111). A: SDS forms a compact monolayer with sulfate groups attached to the positively charged surface. B. A bilayer structure. C. Micelle like structure on top of a monolayer

7.3.2. Electrodeposition on molecular-scale templates.

7.3.2.1. Growth of electrodeposited islands.

After $1\mu\text{M}$ AgClO_4 was added to the 10 mM SDS solution, in addition to stripes due to the surface micelles, islands appeared (Figure 7-7). These islands are clearly anisotropic, i.e., all the islands are elongated along the direction of hemicylinders. The preferential locations of the elongated islands are less clear. Some of the islands appear at the Y joints, defect sites in the micelles. Other islands appear to center at the spacing between the hemicylinders. The apparent width of these islands is about 5-10 nm. As we discussed before, the contrast mechanism limits the spatial resolution. Therefore, it is difficult to conclude more precisely the physical width of the islands from the AFM results. We will return to this issue in the discussion of STM results. The potential at

which islands start to appear is about 0.1 V higher than the bulk deposition potential of silver. Therefore, the deposition is an underpotential deposition process. This suggests that certain sites in the surface micelles have strong interaction with electrodeposited silver.

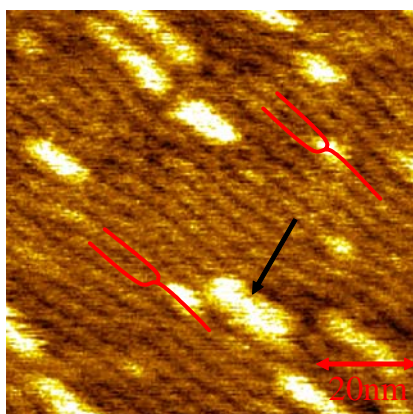


Figure 7-7 Anisotropic electrodeposition on Au(111) under 1 μM AgClO_4 and 10 mM SDS. Electrode potential 0.3 V. Elongated islands were observed to grow along the surface micelles.

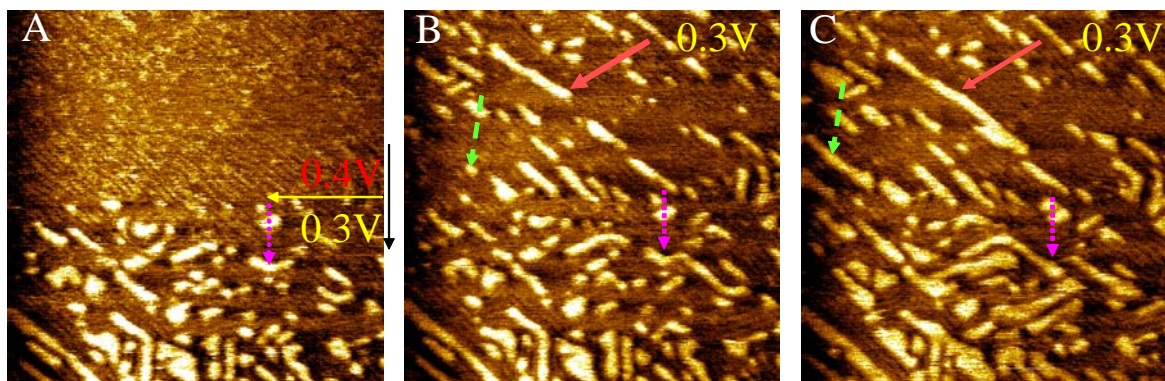


Figure 7-8 Time dependant electrodeposition on Au(111) under 1 μM AgClO_4 and 10 mM SDS. Image size $225 \times 225 \text{ nm}^2$. The electrode potential was stepped from 0.3 V to 0.2 V at the lower half of the image A. (Scan direction: downward.) B and C are sequential frames of A. Image acquisition speed 80 sec/frame. Solid, dashed and dotted arrows identify the same spots in different images.

Figure 7-8A, a time dependant image suggests that after stepping the potential from 0.4 V to 0.3 V, when the tip is scanning in the middle of the image, islands appear immediately. The sequential images of Figure 7-8 suggest that the electrodeposition of Ag^+ in the presence of SDS surface micelles also follows a nucleation and growth mechanism. The island identified by a dashed arrow in Figure 7-8B is elongated into a 40nm line in Figure 7-8C. Some islands merge as coverage increases as indicated by the solid arrows in Figure 7-8 B and C. However, the growth is also accompanied by reorganization. The right segment of an elbow marked by a dotted arrow in Figure 7-8 disappears in C, whereas the left segment merges with a wire with the same orientation.

At a longer time scale (>30 min at 0.3 V), much larger islands are resolved. Some of the islands are 100 nm wide, suggesting that the deposited silver islands merged. However, these islands remain elongated and their long axes orient along the direction of hemicylinders in the island free area. Height mode images suggest these islands are more than 1 nm high.

We speculate that these islands are not purely silver on Au substrate. The electrode potential is 0.1 V above the bulk deposition potential. Only underpotential deposition can occur. Therefore, the thickness silver should be at most a monolayer (2-3 Å). To explain the height difference, we suggest that silver and surface micelles form adducts which are higher than the neighboring silver free surface micelles. The microscopic structure of the adducts is unclear. Silver may form wires between the hemicylinders, the silver may also cover part of the top of hemicylinders, joining the hemicylinders together

(Figure 7-10A). Alternatively, the silver may form elongated monolayer islands, which stabilize the surface micelles on the top (Figure 7-10B). We don't think silver deposited at the bottom of the surface micelles can cause the islands to be more than 1 nm higher. A silver monolayer would simply increase the physical height of the surface micelles by 2-3 Å. It should be noted that the AFM tip is mapping the double layer force of surface micelles, the apparent height difference in the AFM images does not necessarily agree with the physical height if the nature of the force and the force gradient differ in different area. However, in this particular case, the AFM tip should experience similar double layer repulsion on the top of surface micelles whether a layer of silver is present under the surface micelles or not. Therefore, silver deposited between Au and the surface micelles would simply increase the apparent height by 2-3 Å, which is still insufficient to account for the actual height difference observed. Model A may cause such difference in height since additional SDS may be adsorbed on the top of deposited silver. More evidence of the microscopic adducts is shown in the next section.

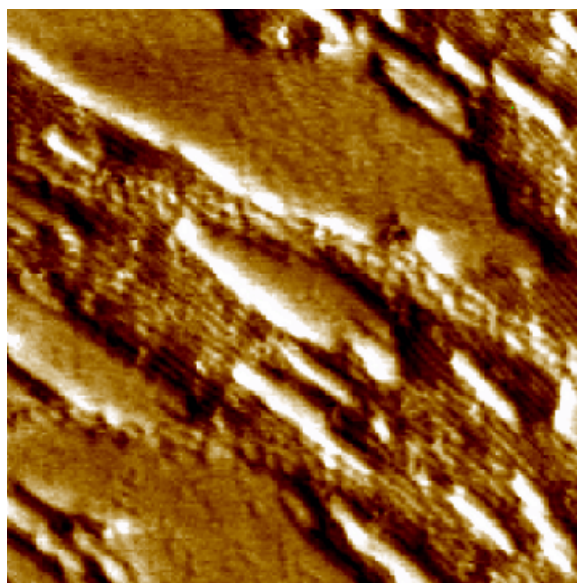


Figure 7-9 AFM image of anisotropic electrodeposition on Au(111) under 1 μM AgClO_4 10 mM SDS. Electrode potential 0.3 V. Image size: $300 \times 300 \text{ nm}^2$.

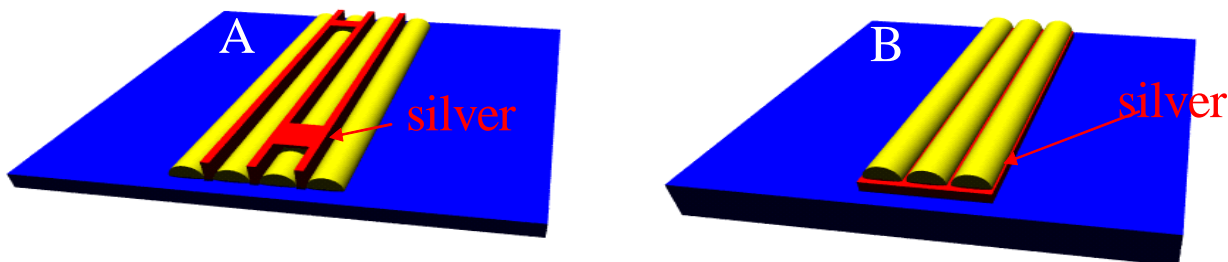


Figure 7-10 Proposed models for Ag-surface micelle adduct. A: silver grows in the trench sites and on top of surface micelles. B. Silver forms monolayer islands on the Au substrate. Surface micelles grow on the silver monolayer.

7.3.2.2. *Stability of Ag islands at negative surface charge density.*

At 0.1 V, AFM images suggest that the large Ag islands are porous (Figure 7-11).

These islands consist of interconnected stripes with a periodicity of 4-5 nm, suggesting the presence of hemicylindrical surface aggregates. However, these stripes appear isolated. Surface micelles could not be resolved in other regions, in sharp contrast to surface micelles observed without Ag^+ (Figure 7-5B). Without the stabilization by neighboring surface micelles, some other interactions must be present to stabilize the isolated micelles. This provides further evidence that Ag and micelles can form adducts. The presence of Ag may stabilize the surface micelles so they are stable even if they are isolated.

When the electrode potential was stepped to 0 V, the stripes collapsed and more circular features appeared at the same location (Figure 7-12). This again supports our previous assumption that the stripes contain both surface micelles and silver. Without the support of the surface micelles, the silver nanowires collapsed to form circular islands. The area of the islands is less than 50% of the area occupied by the stripes. If there were a

monolayer of silver under the surface micelles, the coverage of the circular silver islands would be equal to the coverage of the stripes. We previously argued against Model B in Figure 7-10 from the stand point of height difference. The coverage is again inconsistent with Model B, in which Ag forms only monolayer islands under the surface micelles.

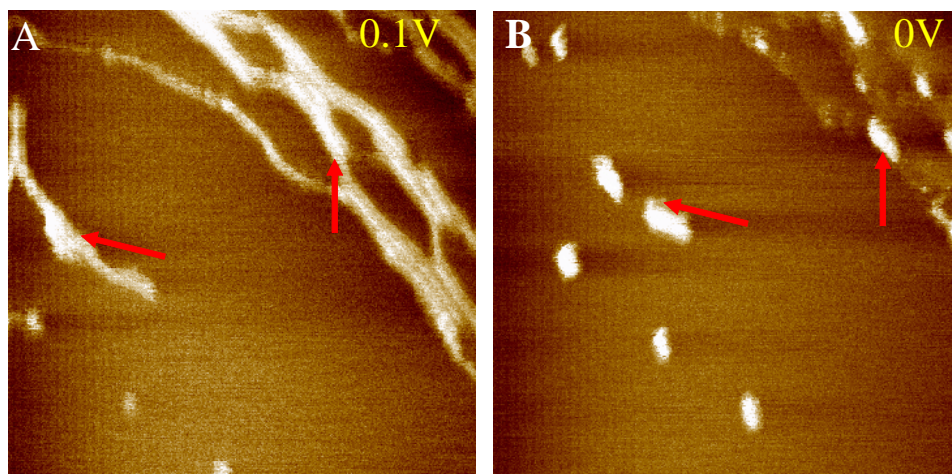


Figure 7-11 AFM images of electrodeposited islands on Au(111) under $1 \mu\text{M}$ AgClO_4 10 mM SDS. Image size: $200 \times 200 \text{ nm}^2$. A: isolated stripes, as indicated by arrows, are observed at 0.1 V . B: the stripes collapse to form more circular islands at 0 V .

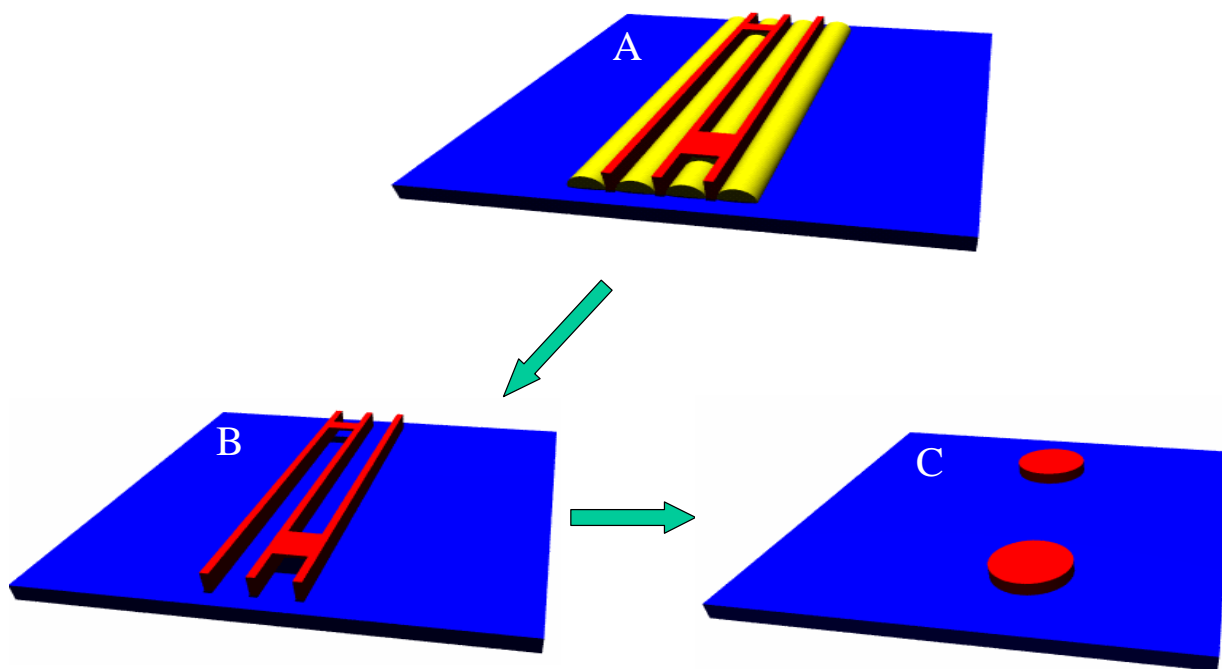


Figure 7-12 Proposed mechanism for the formation of circular islands at 0 V. Without the support of surface micelles, the silver nanostructures collapse into islands.

Two other points remain unclear. The first one is the inability to resolve surface micelles in majority of the area at 0.1 V_{SCE} (Figure 7-11A). Only isolated surface micelle-Ag adducts were observed. In a pure SDS solution, the onset of SDS desorption is about -0.25 V_{SCE} ($10 \mu C/cm^2$). SDS molecules should still form full coverage surface micelles around 0 V_{SCE} . The second question is why the surface micelle-Ag adducts collapse at 0 V. We can not completely exclude the possibility that surface micelles are still present but they can not be imaged due to change of force gradient in the presence of silver. However, a more reasonable explanation is partial charge transfer from the Ag

nanostructures to the Au substrate. Atomic clusters of silver are known to be good electron donors [41]. Once deposited on Au, which has higher work function, the silver may undergo partial electron transfer. Hence, the Au substrate becomes more negatively charged and less favorable to the presence of surface micelles. By contrast, the Ag structures that undergo charge transfer are less negatively charged or even positively charged, which may interact more strongly with the sulfate headgroups in SDS. This strong interaction between charged silver and SDS may explain the observation of isolated Ag-surface micelle adducts. At a more negative potential, such a mutual stabilization effect is weakened. Consequently, the micelles are desorbed and silver wire-like structures collapse.

7.3.2.3. *STM results of Ag deposition on SDS.*

Although AFM is very sensitive to the local structure of surface micelles, the resolution of AFM is limited. In addition, it is difficult to distinguish between silver nanostructures and surface micelles with AFM. The difference in contrast mechanisms makes STM a good compliment to AFM. Ag nanowires deposited on the surface, in principle, can be unambiguously identified by STM because they should be significantly more conductive than the surface micelles that mainly consist of insulating alkyl chains.

The STM image of SDS on Au(111) shows alternate bright and dark stripes with a periodicity of 4.5 nm (Figure 7-13), in good agreement with AFM measurements. The height difference between the bright and dark areas is only 0.2 Å. The resolution is, however, insufficient to clearly resolve individual alkyl chains. According to Lipkowski

et al., the lower regions correspond to the spacing between headgroups and the higher regions correspond to alkyl chains [31]. In addition to the periodic structure, some small islands appear. These islands are 1 nm wide and 1.5 Å high, suggesting the presence of small metal islands. The immediate question is the origin of the metal. We found that the Ag reference electrode used releases trace amount of silver (see Appendix D). Therefore, we assume that the trace amount of Ag was deposited onto the surface to form these islands. Upon close inspection, these islands appear exclusively in the lower regions. Some of the islands appear slightly elongated along the direction of the stripes. The width of these islands is about 1 nm, close to the 0.8 nm distance between the sulfate groups in adjacent unit cells. This provides evidence that, at least in the initial stage, the silver ions prefer to deposit onto the trenches.

Imaging SDS in the presence of higher metal ion concentration, 1 μM of Ag⁺, was unsuccessful with W tips. The images appear very noisy and the height kept increasing, suggesting electrodeposition on W tips. Electrode deposition can also occur on the tip if the tip potential is held about the electrodeposition potential [42]. To minimize leakage current, it is necessary to keep the tip potential between -0.1 to 0.2 V_{SCE}. However, in this potential range, silver becomes deposited onto the tip. Pt-Ir tips, which can operate at a potential where silver deposition does not occur, should in principle resolve this problem.

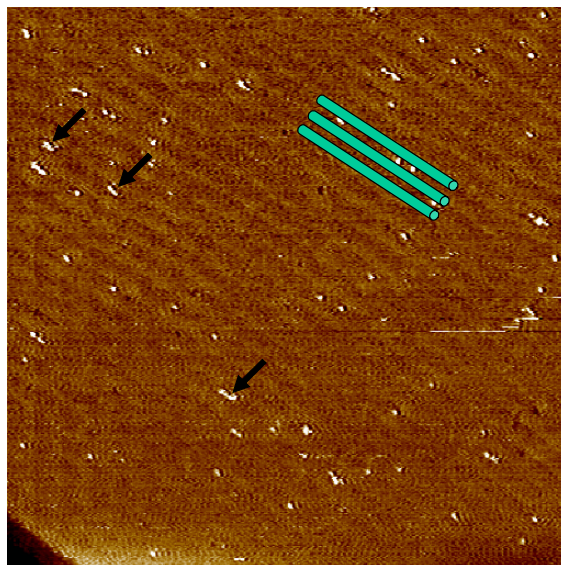


Figure 7-13 STM image of surface micelles on Au(111) under 10 mM SDS. Image size: $125 \times 125 \text{ nm}^2$. Electrode potential 0.2 V. Sample bias: 0.3 V. Tunneling current: 0.5nA. Some bright islands are resolved. The black arrows indicate elongated islands. Three cylinders overlaid with the surface micelles suggest that the islands grow in the trench sites.

7.3.2.4. *STM study of Ag deposition on hexadecane self-assembled templates.*

In addition to SDS templates, we also studied the deposition of silver on hexadecane adlayers.

Hexadecane molecules self-assemble into ordered rows 2.2nm wide on Au(111). The long axes of molecules are titled by 60 degree with respect to the direction of the molecular rows (Figure 7-14) (See Chapter 4 for more details on structures of adsorbed hexadecane.).

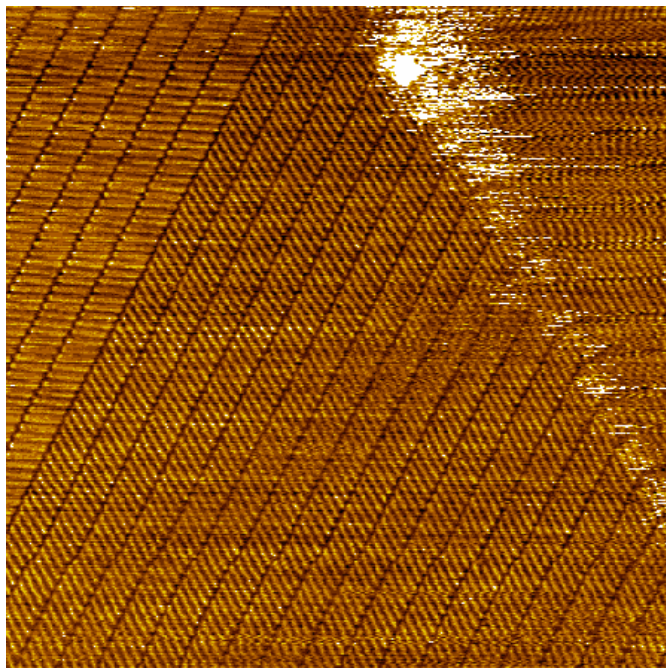


Figure 7-14 STM image of hexadecane adlayer on Au(111) in 0.1 M HClO₄ solution at 0.25 V_{SCE}. Image size: 34.5 × 34.5 nm².

Again silver is introduced by the slight dissolution of the silver wire reference electrode instead of intentionally added silver ions. Figure 7-15A suggests the formation of 0.7 ± 0.2 nm wide 1.5 \AA high parallel wires. In addition to wires, some islands about 2 \AA high are present, suggesting that these islands are monolayer metal islands. Similar to STM images in Appendix D, atomic lattice consistent with silver can be observed on the islands and such islands structures are only observed with a bare silver quasi reference electrode. Therefore we attribute the nanowires and islands to reduction of silver ions that are released from the silver reference electrode. The precise concentration of Ag⁺ is unknown. We found that due to electrodeposition, the tungsten tips we use are unstable in the presence of 1 \mu M Ag⁺. By contrast, the STM images acquired in this experiments are stable. Therefore we suggest that the concentration of silver should be lower than 1 \mu M .

The distance between the neighboring wires is 4.8 nm, which corresponds to the length of two hexadecane molecules 4.4nm. However, some of the wires are only 2.4 nm apart, which is similar to the length of one hexadecane molecule 2.2nm. A higher resolution image, Figure 7-15A resolves both the nanowires and the features of individual hexadecane molecules, which are 2nm long 0.5nm wide rods. This provides direct evidence that metal atoms are preferentially deposited in the surface sites between the termini of hexadecane molecules Figure 7-16.

Interestingly, the long axes molecules in the molecular rows are now perpendicular to the direction of molecular rows. By contrast, without the electrodeposited silver, the molecules are always tilted by 60° from the direction of the molecular rows. Therefore, the interaction is mutual. The molecular templates induces site specific deposition of silver. On the other hand the electrodeposited silver induces reorganization of molecular scale templates.

It should be noted that most of the wires are not yet uniform enough. Most of them are separated into 10 -20 nm long segments due to the presence of defects. More optimizations such as varying the concentration of metal ions and the electrode potential, are necessary to improve the structural perfection of these nanowires.

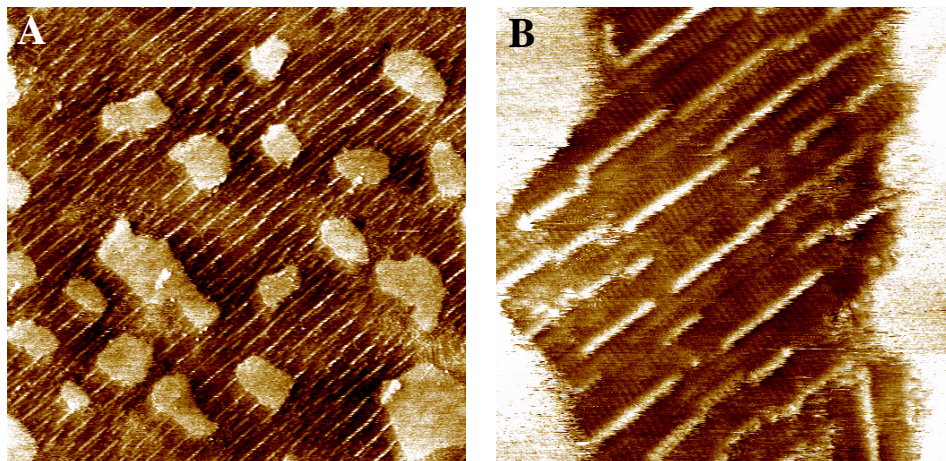


Figure 7-15 Silver deposited onto a surface covered with a hexadecane adlayer at 0.1V under 0.1 M H₂SO₄. 1.5 Å parallel lines connect 2 Å high islands. A: image size 150×150nm². A majority of these lines are 4.8±0.2 nm apart. B: image size: 30×30 nm².

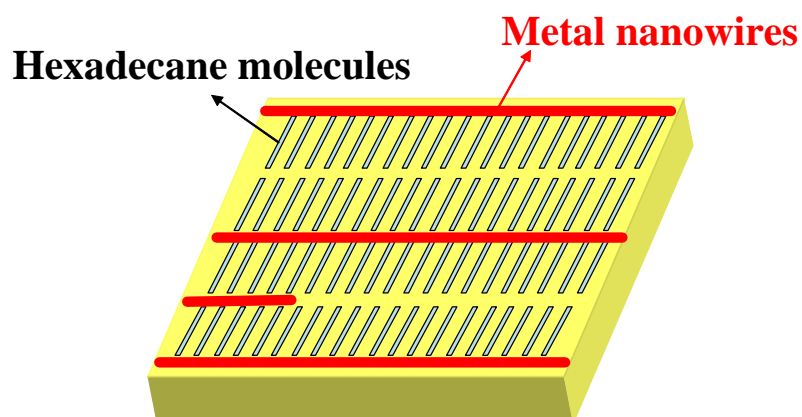


Figure 7-16 A model for preferential electrodeposition on a self-assembled hexadecane template. Silver nanowires are selectively deposited in the space between molecular rows.

7.4. Discussion and conclusions.

7.4.1. Discussion.

The major findings of this study are

- The electrode potential affects the stability of the molecular scale templates as well as the electrodeposited nanostructures.
- The trench sites in the surface micelles and the space between the termini of hexadecane molecules can be the preferred sites for electrodeposition. The observed preferential electrodeposition on two very different systems suggest that this may be a general effect on 2D self-assembled molecular structures.
- The resulting metal nanowires may have a thickness less than 1nm and controlled spacing. However, the wires still have numerous defects. Further experiments are necessary to improve the uniformity of the nanowires.

Surface micelles and hexadecane monolayers are physisorbed templates. One would question whether such physisorbed templates can have any effect on the nanometer scale structures of metal deposition at all as previous studies only showed that surface micelles may suppress the electrodeposition [33-35].

Our results suggest that at appropriate conditions, surface micelles can have a dramatic effect the nanoscale structure of electrodeposited silver, in contrast to previous studies [33, 35]. Our STM results suggest that at Ag^+ concentration $\ll \mu\text{M}$, silver is selectively deposited in the trenches between the hemicylindrical surface micelles. The trenches are the preferred sites because

1. Au substrate is exposed in these sites. The silver atoms deposited in the sites interact with the Au substrate and the sulfate groups.
2. Electron transfer should more facile at the trench sites than on top of the insulating alkyl chains.

However, at Ag^+ concentration of 1 μM , AFM results suggest that the silver atoms are not confined to the trenches. The deposited silver appears to cover part of the top of the surface micelles as well. Clearly the concentration can affect the electrodeposition dramatically.

We first consider how the concentration of metal ions affects the deposition rate. At such low concentrations, the electrodeposition of Ag is often diffusion limited. Consider the reduction process, $\text{Ag}^+ + e \rightarrow \text{Ag}$. Before the electrochemical reduction, the concentration of silver ions in solution is uniform. When the potential is stepped to a value where reduction should occur, the silver ions are reduced to metallic silver on the electrode surface. The rate of reduction depends on the electron transfer process at the electrode surface and the diffusion of silver ions from the bulk solution [8]. At a very low concentration, the reduction process rapidly depletes silver ions near the surface. Hence, the reduction is limited by how rapidly the silver ions diffuse from the bulk to the surface.

According to the Cottrell equation, the current of the diffusion limited electrode reaction, I , as a function of time, t , is described by [8],

$$i(t) = \frac{nFAD_0^{1/2}C_0^*}{\pi^{1/2}t^{1/2}} \quad \text{Equation 7-2}$$

where n is the number of electrons involved in the reduction (1 for Ag^+), F is the Faraday constant, C_0 is the bulk concentration of the ion, and D_0 ($10^{-5} \text{ cm}^2/\text{s}$ for Ag^+ [8]) is the diffusion constant of Ag^+ .

Therefore, the integrated charge density is

$$\sigma(t) = \frac{2nFD_0^{1/2}C_0^*\sqrt{t}}{\pi^{1/2}} \quad \text{Equation 7-3}$$

Assuming $220 \mu\text{C}/\text{cm}^2$ is required to reduce 1 ML Ag [7], the surface coverage of electrodeposited silver under diffusion limited condition can be plotted as a function of time (Figure 7-17).

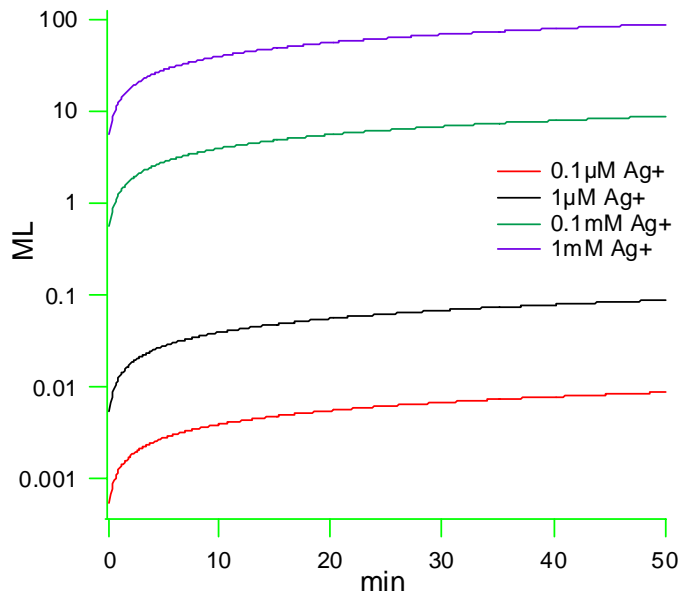


Figure 7-17 Time dependant surface coverage of diffusion limited electrodeposition of Ag at different concentration of Ag^+ .

This approach provides an upper limit of deposited silver since the Cottrell equation assumes an infinite reservoir of electrolyte. Our electrochemical cell has solution of

finite thickness (<1 cm), therefore the actual amount is less. Figure 7-17 suggests that the surface coverage may rapidly exceed 1 ML at 1 mM, a typical concentration used for electrodeposition study. Assuming the trench between the hemicylinders, where Ag can be deposited preferentially, to be 0.8 nm wide, and the periodicity of the surface micelles to be 4.4 nm, the coverage of the trench sites is 0.18 ML. If the coverage of deposited silver is higher than 0.18 ML, all the trench sites are saturated and Ag must be deposited elsewhere. In addition, even if the coverage is below saturation, at a high deposition rate, the deposited Ag will not be able to discriminate different sites.

Our results also suggest that the electrodeposition potential dramatically affects the structure of the surface micelles. A prerequisite to observe the templating effect is that the surface micelles must be stable at the electrodeposition potential. If the potential is too positive, SDS only forms a condensed layer instead of hemicylindrical surface micelles. If the potential is too negative, the surface micelles collapse and the silver nanowires also collapse into circular islands.

7.4.2. Future work.

Our study showed interesting behaviors of electrodeposited metal in the presence of surface micelle templates. Further high resolution STM studies should provide more details of how metal structures grow in the templates and more insights into the interactions between the organic molecules and metal nanostructures. To grow uniform and evenly spaced atomic wires in the molecular templates, the optimum conditions such as sub μM concentration of metal ion and electrode potential need to be explored. In

addition, many other parameters can be explored, for example, the headgroups, which affect the affinity of metal in the trench sites, can be systematically varied. Since our results suggest that anisotropic electrodeposition exist on two quite different molecular self-assembled systems, this suggests that the templating effect of 2D self-assembled structures may be general and One can envision that other 2D self-assembled structures with more sophisticated hierarchical structures [11] may serve as templates to grow more complexed metal nanostructures. In addition, silver nanowires may reduce other noble metal ions. Thus nanostructures of other noble metals can be formed.

BIBLIOGRAPHY

1. Tarlov, M.J., *Silver Metalization of Octadecanethiol Monolayers Self-Assembled on Gold*. Langmuir, 1992. **8**(1): p. 80-89.
2. Dulcey, C.S., J.H. Georger Jr., V. Krauthamer, D. Stenger, T.L. Fare, and J.M. Calvert, *Deep UV photochemistry of chemisorbed monolayers: patterned coplanar molecular assemblies*. Science, 1991. **252**: p. 551-554.
3. Batina, N., D.M. Kolb, and R.J. Nichols, *In situ scanning tunneling microscopy study of the initial-stages of bulk copper deposition on Au(100) - the rim effect*. Langmuir, 1992. **8**(10): p. 2572-2576.
4. Sieradzki, K., S.R. Brankovic, and N. Dimitrov, *Electrochemical defect-mediated thin-film growth*. Science, 1999. **284**(5411): p. 138-141.
5. Blum, L., H.D. Abruna, J. White, J.G. Gordon, II, G.L. Borges, M.G. Samant, and O.R. Melroy, *Study of underpotentially deposited copper on gold by fluorescence detected surface EXAFS*. Journal of Chemical Physics, 1986. **85**(11): p. 6732-8.
6. Manne, S., P.K. Hansma, J. Massie, V.B. Elings, and A.A. Gewirth, *Atomic-resolution electrochemistry with the atomic force microscope: copper deposition on gold*. Science, 1991. **251**(4990): p. 183-6.
7. Herrero, E., L.J. Buller, and H.D. Abruna, *Underpotential deposition at single crystal surfaces of Au, Pt, Ag and other materials*. Chemical Reviews, 2001. **101**(7): p. 1897-1930.
8. Bard, A.J. and L.R. Faulkner, *Electrochemical methods: Fundamentals and applications*. 1980. 718 pp.
9. Xia, Y.N., X.M. Zhao, and G.M. Whitesides, *Pattern transfer: Self-assembled monolayers as ultrathin resists*. Microelectronic Engineering, 1996. **32**(1-4): p. 255-268.
10. Xia, Y.N., J.A. Rogers, K.E. Paul, and G.M. Whitesides, *Unconventional methods for fabricating and patterning nanostructures*. Chemical Reviews, 1999. **99**(7): p. 1823-1848.
11. Giancarlo, L.C. and G.W. Flynn, *Scanning tunneling and atomic force microscopy probes of self-assembled, physisorbed monolayers: Peeking at the peaks*. Annual Review of Physical Chemistry, 1998. **49**: p. 297-+.
12. Hips, K.W., L. Scudiero, D.E. Barlow, and M.P. Cooke, *A self-organized 2-dimensional bifunctional structure formed by supramolecular design*. Journal of the American Chemical Society, 2002. **124**(10): p. 2126-2127.
13. Barth, J.V., J. Weckesser, C.Z. Cai, P. Gunter, L. Burgi, O. Jeandupeux, and K. Kern, *Building supramolecular nanostructures at surfaces by hydrogen bonding*. Angewandte Chemie-International Edition, 2000. **39**(7): p. 1230-+.
14. Yokoyama, T., S. Yokoyama, T. Kamikado, Y. Okuno, and S. Mashiko, *Selective assembly on a surface of supramolecular aggregates with controlled size and shape*. Nature, 2001. **413**: p. 619-621.
15. Thurn-Albrecht, T., J. Schotter, C.A. Kastle, N. Emley, T. Shibauchi, L. Krusin-Elbaum, K. Guarini, C.T. Black, M.T. Tuominen, and T.P. Russell, *Ultra-high-density nanowire arrays grown in self-assembled diblock copolymer templates*. Science, 2000. **290**(5499): p. 2126-2129.

16. Hatzor, A. and P.S. Weiss, *Molecular rulers for scaling down nanostructures*. Science, 2001. **291**(5506): p. 1019-1020.
17. Hong, B.H., S.C. Bae, C.W. Lee, S. Jeong, and K.S. Kim, *Ultrathin single-crystalline silver nanowire arrays formed in an ambient solution phase*. Science, 2001. **294**(5541): p. 348-351.
18. Switzer, J.A., H.M. Kothari, P. Poizot, S. Nakanishi, and E.W. Bohannon, *Enantiospecific electrodeposition of a chiral catalyst*. Nature, 2003. **425**(6957): p. 490-493.
19. Lee, J.O., G. Lientschnig, F. Wiertz, M. Struijk, R.A.J. Janssen, R. Egberink, D.N. Reinhoudt, P. Hadley, and C. Dekker, *Absence of strong gate effects in electrical measurements on phenylene-based conjugated molecules*. Nano Letters, 2003. **3**(2): p. 113-117.
20. Fisher, G.L., A.V. Walker, A.E. Hooper, T.B. Tighe, K.B. Bahnck, H.T. Skriba, M.D. Reinard, B.C. Haynie, R.L. Opila, N. Winograd, and D.L. Allara, *Bond insertion, complexation, and penetration pathways of vapor-deposited aluminum atoms with HO- and CH₃O-terminated organic monolayers*. Journal of the American Chemical Society, 2002. **124**(19): p. 5528-5541.
21. Walker, A.V., T.B. Tighe, M.D. Reinard, B.C. Haynie, D.L. Allara, and N. Winograd, *Solvation of zero-valent metals in organic thin films*. Chemical Physics Letters, 2003. **369**(5-6): p. 615-620.
22. Metzger, R.M., *Unimolecular electrical rectifiers*. Chemical Reviews, 2003. **103**(9): p. 3803-3834.
23. Schneeweiss, M.A., H. Hagenstrom, M.J. Esplandiu, and D.M. Kolb, *Electrolytic metal deposition onto chemically modified electrodes*. Applied Physics - Materials Science & Processing, 1999. **69**(5): p. 537-551.
24. Manne, S. and H.E. Gaub, *Molecular organization of surfactants at solid-liquid Interfaces*. Science, 1995. **270**(5241): p. 1480-1482.
25. Rosen, M.J., *Surfactants and interfacial phenomena*. 1989, New York: John Wiley & Sons. 464 pp.
26. Pashley, R.M. and J.N. Israelachvili, *A comparison of surface forces and interfacial properties of mica in purified surfactant solutions*. Colloids and Surfaces, 1981. **2**(2): p. 169-87.
27. Manne, S., J.P. Cleveland, H.E. Gaub, G.D. Stucky, and P.K. Hansma, *Direct visualization of surfactant hemimicelles by force microscopy of the electrical double-layer*. Langmuir, 1994. **10**(12): p. 4409-4413.
28. Jaschke, M., H.J. Butt, H.E. Gaub, and S. Manne, *Surfactant aggregates at a metal surface*. Langmuir, 1997. **13**(6): p. 1381-1384.
29. Papadopoulos, N., S. Sotiropoulos, and P. Nikitas, *3-dimensional phase-sensitive AC voltammetry for the study of adsorption processes - an application to the adsorption of sodium dodecyl-sulfate at the mercury electrolytic solution interface*. Journal of Electroanalytical Chemistry, 1992. **324**(1-2): p. 375-385.
30. Wandlowski, T., M. Hromadova, and R. deLevie, *On the kinetics of adsorption of dodecyl sulfate at the mercury-water interface*. Langmuir, 1997. **13**(10): p. 2766-2772.
31. Burgess, I., C.A. Jeffrey, X. Cai, G. Szymanski, Z. Galus, and J. Lipkowski, *Direct visualization of the potential-controlled transformation of hemimicellar*

- aggregates of dodecyl sulfate into a condensed monolayer at the Au(111) electrode surface.* Langmuir, 1999. **15**(8): p. 2607-2616.
32. Tang, Z.Y. and E.K. Wang, *Potential-induced transformation for surfactant aggregates on a metal surface.* Journal of Electroanalytical Chemistry, 2001. **496**(1-2): p. 82-87.
 33. Aragon, A., M.G. Figueroa, R.E. Gana, and J.H. Zagal, *Effect of a Polyethoxylate Surfactant on the Electrodeposition of Tin.* Journal of Applied Electrochemistry, 1992. **22**(6): p. 558-562.
 34. Eliadis, E.D. and R.C. Alkire, *In situ studies of Cu deposition in the presence of quaternary ammonium salts.* Journal of the Electrochemical Society, 1998. **145**(4): p. 1218-1226.
 35. Petri, M. and D.M. Kolb, *Nanostructuring of a sodium dodecyl sulfate-covered Au(111) electrode.* Physical Chemistry Chemical Physics, 2002. **4**(7): p. 1211-1216.
 36. Bethell, D., R.E. Fessey, E. Namwindwa, and D.W. Roberts, *The hydrolysis of C-12 primary alkyl sulfates in concentrated aqueous solutions. Part 1. General features, kinetic form and mode of catalysis in sodium dodecyl sulfate hydrolysis.* Journal of the Chemical Society-Perkin Transactions 2, 2001(9): p. 1489-1495.
 37. Senden, T.J. and C.J. Drummond, *Surface chemistry and tip-sample Interactions in atomic force microscopy.* Colloids and Surfaces a-Physicochemical and Engineering Aspects, 1995. **94**(1): p. 29-51.
 38. Wanless, E.J. and W.A. Ducker, *Organization of sodium dodecyl sulfate at the graphite-solution interface.* Journal of Physical Chemistry, 1996. **100**(8): p. 3207-3214.
 39. He, Y., T. Ye, and E. Borguet, *The role of hydrophobic chains in self-assembly at electrified interfaces: Observation of potential-induced transformations of two-dimensional crystals of hexadecane by in-situ scanning tunneling microscopy.* Journal of Physical Chemistry B, 2002. **106**(43): p. 11264-11271.
 40. Poirier, G.E., *Characterization of organosulfur molecular monolayers on Au(111) using scanning tunneling microscopy.* Chemical Reviews, 1997. **97**(4): p. 1117-1127.
 41. Kobayashi, Y. and K. Itoh, *Surface-enhanced resonance Raman scattering spectra of meso-substituted porphines in layered structures having calcium fluoride/porphine/silver and calcium fluoride/silver/porphine configurations.* Journal of Physical Chemistry, 1985. **89**(24): p. 5174-8.
 42. Kolb, D.M., R. Ullmann, and T. Will, *Nanofabrication of small copper clusters on gold(111) electrodes by a scanning tunneling microscope.* Science, 1997. **275**(5303): p. 1097-1099.

Appendix A: Frictional cross-talk in atomic force microscopy.

Two common operational modes of AFM are contact mode and tapping mode. When the AFM probe scans the surface in contact mode, the feedback loop attempts to maintain constant deflection of the cantilever. In tapping mode, the tip gently taps the surface at a set frequency.

The forces exerted on the cantilever in contact mode result in two types of deflection, vertical deflection caused by the attractive or repulsive force normal to the surface and twist induced by friction which is parallel to the scanning direction [1].

The piezoelectric attempts to maintain the same deflection of the cantilever. Thus the same sample-probe distance is maintained if there is no interference of the friction. Thus the position of piezoelectric reflects the true information of topography. If the friction properties of different areas are not uniform and the tip is tilted, the recorded topography during the left scan and right scan may differ dramatically [1]. An example that protrusion is measured in left scan and depression is measured in the left at the same area is shown in Figure A-1. In Figure A-2, the friction on the substrate and island to be zero. In this case, the topographies collected in both scan directions agree and reflect the true topography correctly. In Figure A-3 and A-4, the island has high friction and the substrate still has zero friction. Probe tilt can result from the friction when the probe is scanning the island. In Figure A-2, the probe tilt from friction adds to the original tilt. The piezoelectric must lower the probe to maintain the same probe-sample distance on

the island. If the effect is large enough, the island can appear as depression in contact mode AFM image as suggested by Figure A-1. In Figure A-3, the probe tilt cancels the original tilt. The piezoelectric has to lift the probe to maintain the same probe-sample distance. Therefore the measured island height is larger than the actual height.

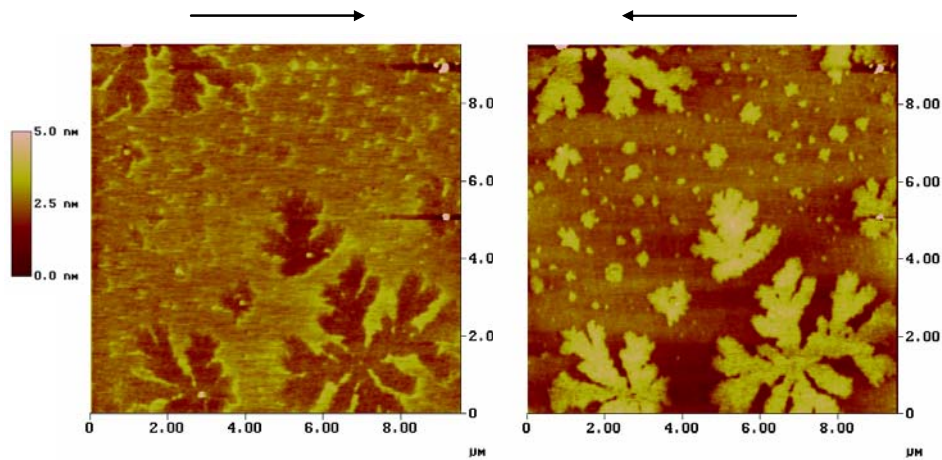


Figure A-1 AFM images of ODS monolayer at identical region acquired during a: Left to right scan and b: Right to left scan. Height scale 5nm.

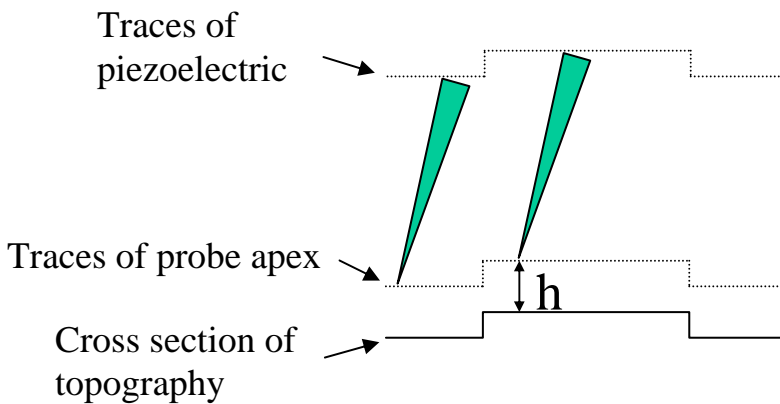


Figure A-2 Left to right and right to left scans when the friction is zero across the surface.

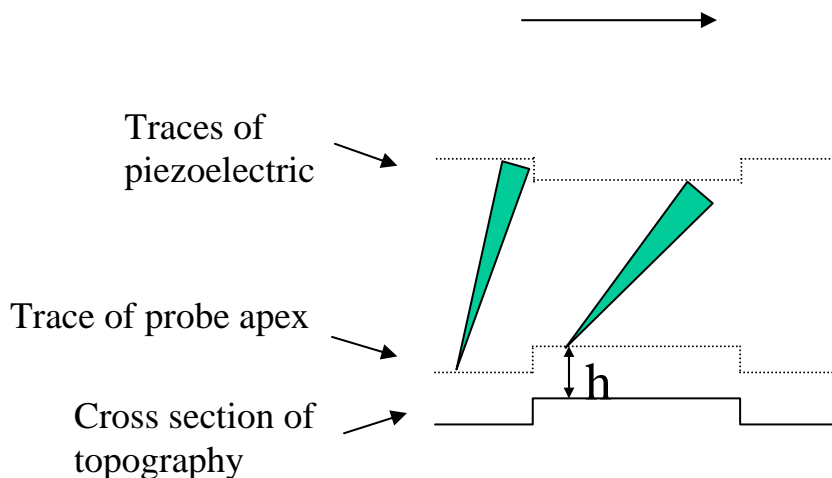


Figure A-3 Left to right scan when the island has higher friction.

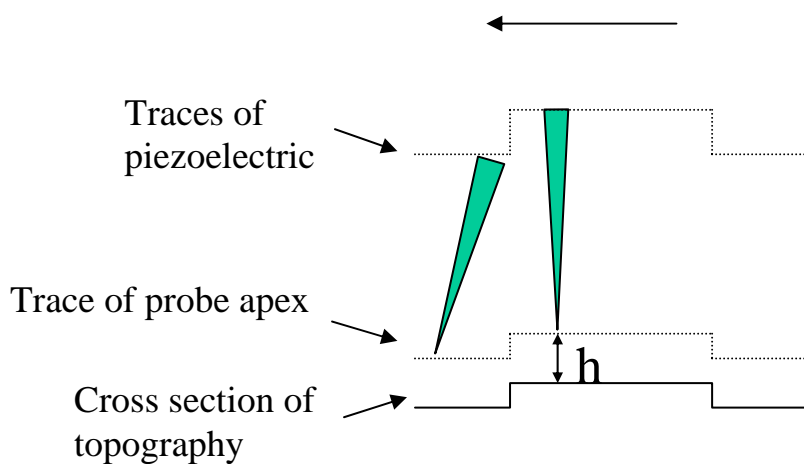


Figure A-4 Right to left scan when island has higher friction.

Our experiment is especially sensitive to the frictional cross-talk because the frictional contrast between the monolayer and bare substrate is large and the monolayer height is very low (less than 2nm). To reduce the cross-talk effect, we choose tapping mode instead of contact mode in imaging highly heterogeneous surfaces. In tapping mode, the influence from the later friction is minimal. Indeed, we found that the islands in UV

irradiated ODS SAMs now appear nearly identical in both left and right scans in tapping mode Figure A-5.

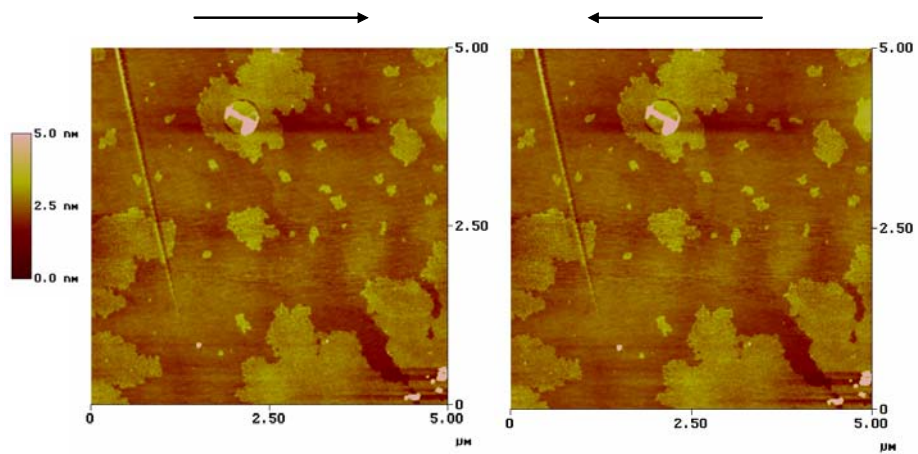
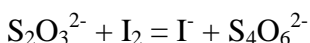
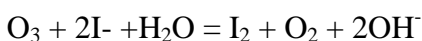


Figure A-5 Tapping mode AFM images. Left to right and right to left scans now display nearly identical topography.

Appendix B: Measuring ozone concentration.

To understand the chemistry inside a UV chamber, the steady concentration of ozone must be determined. A common method is iodometry [2]. Ozone oxidizes iodide into iodine in stoichiometric ratio. The amount of iodine can be determined by titration with $S_2O_3^{2-}$ or by light absorption at 352 nm [2].



However, the sampling of O_3 is challenging under our condition. Liters of gas would be required bubbling through iodide solution to detect O_3 whereas the volume of our UV chamber is only about 800ml. We opted for a photometric method because the sensitivity is higher and the required amount of gas sample is dramatically reduced [2]. In addition, photometry does not require calibration as long as the absorption cross section of ozone is known [2]. The absorbance (A) at the maximum adsorption wavelength 255 nm is measured and Beer-Lambert's law is used to calculate the concentration ozone c. σ is the absorption cross section of ozone at the corresponding wavelength, L is the path length of the optical cell.

$$2.303A = \sigma cL$$

Equation 1

A 1 cm path length quartz cuvette was placed in the UV chamber and UV light was turned on for 30min to allow a steady-state concentration of ozone in the chamber. Before the cuvette was transferred to a UV-vis spectrometer, a Teflon stopper was placed to seal the opening of the cuvette. If the UV chamber has to be opened during capture of

ozone, there is a concern that the ozone concentration will change. As shown in Figure A-6, the stopper is attached to a stainless steel needle. Therefore the stopper can be manipulated without opening the UV chamber. The absorption spectra of the captured ozone as a function of time after transfer from the UV chamber are shown in Figure A-7. The change in absorbance is negligible for the first 15 min, suggesting that the reaction and leakage of ozone is minimal on the time scale of transferring the sample to the spectrometer and taking an initial spectrum (~2 min). Therefore the calculated concentration in the cuvette is an accurate representation of the ozone level in the UV chamber. The absorbance at 255 nm is determined to be 0.012 ± 0.001 . Using the path length 1cm and cross section value of $1150 \times 10^{-20} \text{ cm}^2$ [3], the concentration of ozone is calculated to be $4 \times 10^{-6} \text{ M}$, corresponding to a volume fraction of $100 \text{ ppm} \pm 10 \text{ ppm}$ in the UV chamber used in these studies.

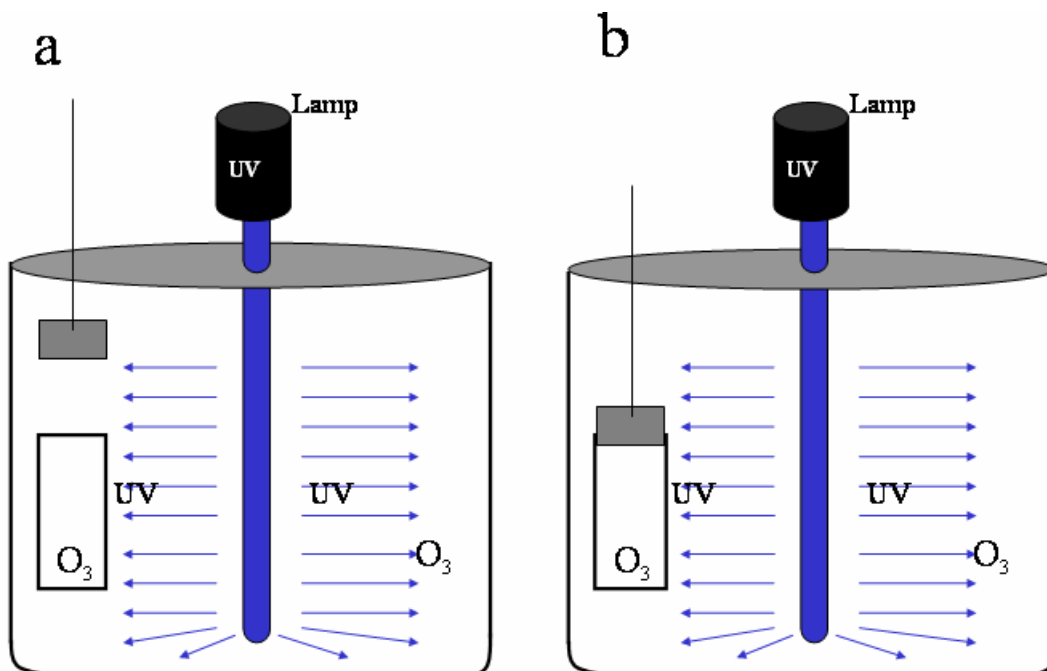


Figure A-6 Sampling ozone in the UV chamber.

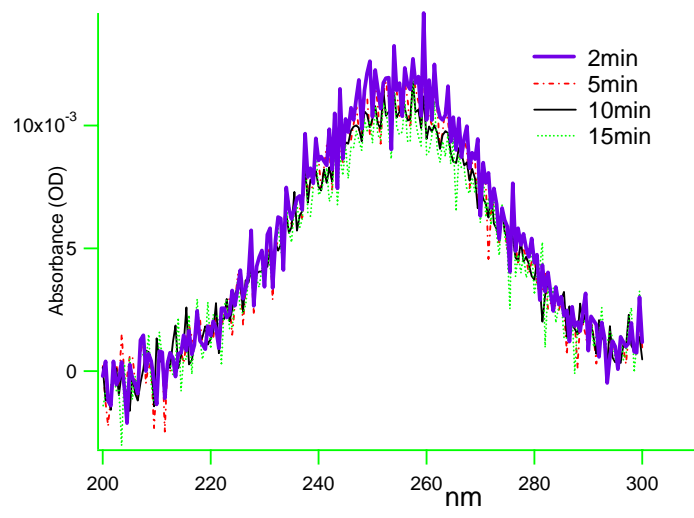


Figure A-7 Absorption spectra of ozone trapped in a quartz cell as a function of time after sampling.

Appendix C: EC-STM tip preparation.

Etching tungsten tips.

Tungsten tips are made by etching in 3 M potassium hydroxide. The tip etching setup is shown in Figure A-8. A 0.25 mm tungsten wire is threaded through a platinum-iridium wire loop 8mm in diameter. The loop is filled with a thin lamella of KOH solution (3 M) and a small AC Voltage (1-5 V) is applied between the loop and the wire. The potassium hydroxide etches the tungsten wire and a small “neck” forms in the wire. This etching continues until the neck is so thin that the weight of the lower-neck wire causes the lower portion of the tip to fall, when the voltage is turned off. Both the lower and upper portions are collected and rinsed with water and methanol.

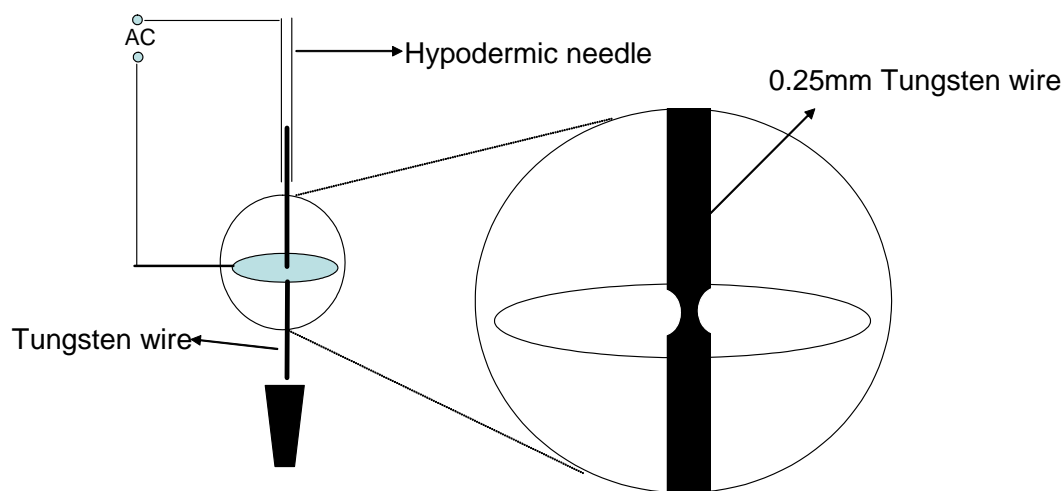


Figure A–8 Tungsten Tip etching: a simple illustration of wire etching. The blue fluid represents a lamella of 3 M KOH. The small cone below is used to receive the fallen tip. Closer examination shows neck is formed as the wire is etched.

Coating tips with wax.

To image under electrolyte, the STM tip must be coated with an insulating material save the atomically sharp end, which is must be uncoated in order to read tunneling current. Two types of coatings are applied. Typically tips are coated with paraffin wax (Aldrich, melting point $\sim 60^{\circ}\text{C}$). The procedure for wax coating is as follows. The wax is melted in a beaker sitting in a water bath at about 75°C . The tip is briefly dipped into the hot wax and withdrawn. To ensure uniform coating, the dipping may be repeated once or twice more. The temperature of the wax is essential. If the temperature is too high, there is little adhesion of the wax to the tip. If the temperature is too low, the tip is overcoated. We found that if the temperature is well controlled, the coating procedure can be very reproducible. Over 80% of the tips have leakage current less than 0.01nA in acidic mediums such as HClO_4 at optimum tip potentials.

Coating tips with polymer.

Paraffin wax coating is simple and can be applied with very high success rate. Paraffin wax introduces minimal amount of contamination because its composition, long chain normal alkanes, has virtually no solubility in most electrolytes. However, we found that the wax coating is unstable in sodium dodecyl sulfate (SDS) solutions with concentration above critical micelle concentration (cmc.). Once the tip is immersed into SDS solution, the leakage current steadily increases (e.g. from 0.01nA to 1nA within a few minutes), suggesting that the wax coating is rapidly dissolved by SDS.

In such cases a polyethylene coating was applied to the tip. This requires the extra equipment shown in Figure A-9. A small copper plate is attached to the end of a soldering iron. The temperature is monitored by a thermal couple and controlled by a thermostat. We use a temperature of roughly 168 °C. After the temperature has stabilized, a polyethylene tablet (Aldrich, low density) is melted in the slit in the hot plate. The tungsten tip is inserted into a tip holder whose position is controlled by a micromanipulator. The tip is pushed through the melted polyethylene in the middle of the plate from below (Figure A-10). It is then taken away from the hotplate, through the U-shaped slit. When the tips it cools a hard polyethylene coating forms. The speed one moves the tip through the polyethylene and the temperature of the hotplate both affect how well the tip is coated. Too cool or fast may leave the tip undercoated, whereas too hot or slow may leave it overcoated. Typically, for both wax and polyethylene coatings a well-coated tip will read a current of 0.01 nA or less under an optimal electrode potential.

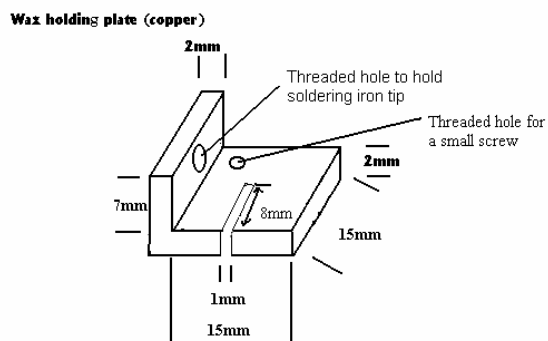


Figure A-9 Schematic of copper hot plate for polymer coating.

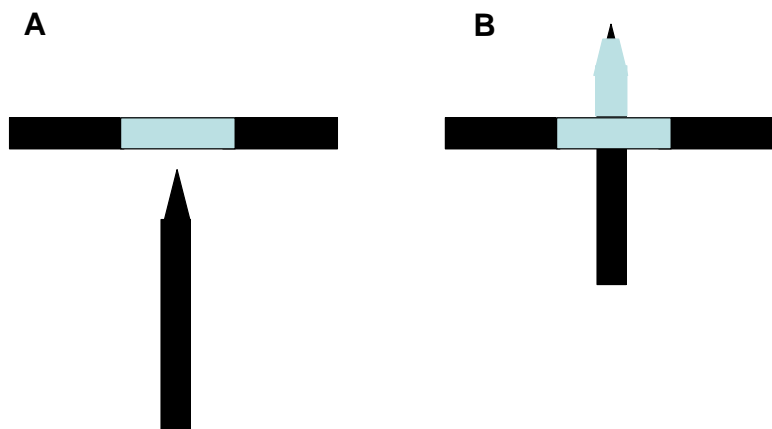


Figure A-10 Schematic of coating STM tips with melted polyethylene.

Appendix D: Reference electrode for EC-STM.

Just as UHV surface science, the cleanliness of the electrode surfaces is of paramount importance for successful STM imaging. In addition to the purity of chemicals and proper cleaning of the cell components, we found that precautions need to be taken on the reference electrode because it may be an important source of contamination.

The reference electrodes used for EC-STM should fulfill two basic requirements.

1. The potential of the reference electrode must be stable.
2. The reference electrode should not introduce impurities to the electrochemical cell.

Ag-AgCl (KCl) reference electrode [4].

The Ag-AgCl (KCl) reference electrode is an excellent reference electrode commonly used in many electrochemical measurements, but Cl^- is a contaminant that adsorbs on many metal substrates. The mobility of Au substrate changes significantly in the presence of trace amount of Cl^- . The frit on the Ag-AgCl(KCl) reference serves as a barrier to slow down the diffusion of the ions in the AgCl/KCl solution. But it is insufficient in EC-STM. Alternatively, a two compartment cell can be used. The Ag/AgCl electrode is not in direct contact with the electrolyte. Instead, it is separated from the cell by a separate compartment containing the supporting electrolyte as the major compartment does. However, this requires major modification of the EC cells commonly used for EC-STM measurements.

Ag wire as a quasi reference electrode.

A common quasi reference electrode used in EC-STM is the Ag wire quasi reference electrode. The potential of the Ag wire quasi reference electrode is stable in many electrolytes, but we often found Ag deposition on the working electrode when we used the Ag wire as a quasi reference electrode. Figure A-11 B shows Ag islands formed on Au substrate when a silver wire is used as the reference electrode. This suggests that a small amount of Ag^+ is dissolved in the electrolyte. The Ag is deposited on working electrode at a sufficiently low electrode potential.

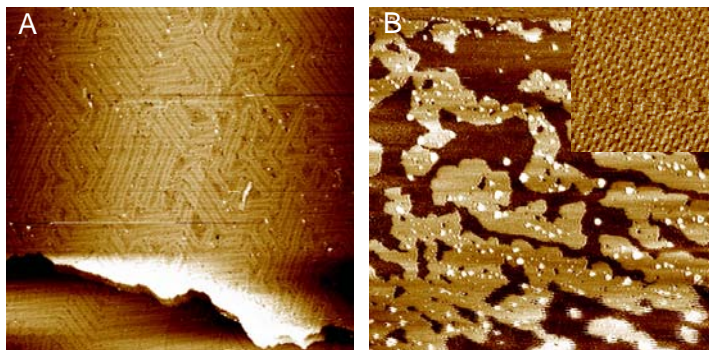


Figure A-11 STM images of Au(111) under 0.1 M HClO_4 , 0.1 V_{SCE} with different reference electrodes. A: Acquired with a Pt reference electrode. Herringbone Au reconstruction is observed, suggesting that the surface is free of metal impurities. Image size: 150 nm \times 150 nm. B: Acquired with a silver wire reference electrode. Image size: 150 nm \times 150 nm. Many islands appear on the surface. Suggesting that metal impurity from the solution is deposited. Inset: An atomic resolution image (6 nm \times 6 nm). The lattice constant, 3 Å and corrugation 0.4 Å is consistent with Ag(111) surface [5].

The reproducibility of potential for Pt wire quasi reference electrode is reasonably good, 20mV. Due to the ease of handling (it can be cleaned by piranha solution) and excellent chemical stability, it becomes our choice in most STM experiments under acidic electrolytes. However, we found that the potential is unstable after potential excursion to hydrogen evolution region. At a sufficiently low electrode potential, H^+ is reduced into

H₂. We suppose that H₂ produced from the working electrode will diffuse and adsorb onto Pt electrode, forming a redox pair H⁺/H₂, and hence dramatically alter the potential. Pt wire quasi reference electrode is not stable under neutral or basic electrolyte such as sodium dodecylsulfate solution.

Sealed Ag quasi reference electrode.

We have designed a new Ag quasi reference electrode. This design provides a stable reference potential. We found the reproducibility of this electrode can be better than 5 mV and the contamination introduced by this electrode is minimal.

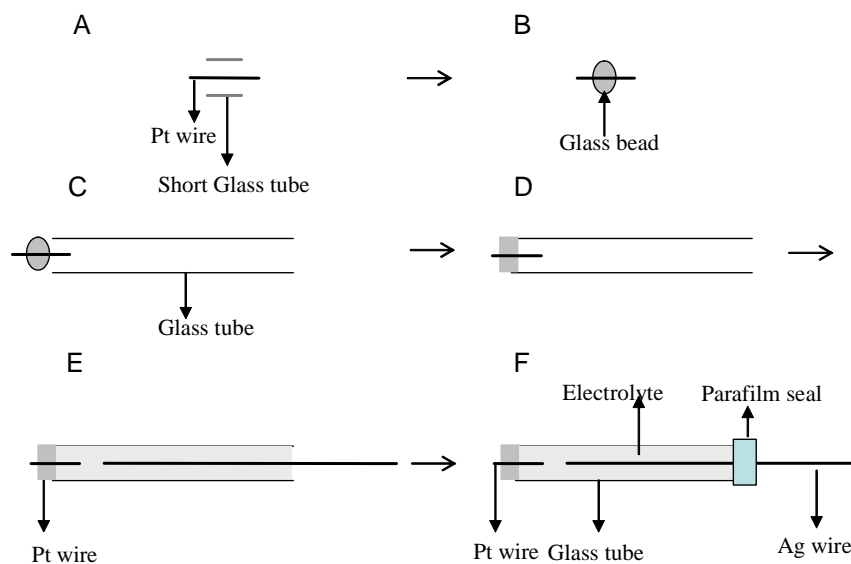


Figure A-12 Schematic of the preparation of a sealed Ag quasi reference electrode. A and B: A short glass tube is melt to form a glass bead on a short Pt wire. C,D: The glass bead is welded to one end of a glass tube. E: The glass tube is filled with supporting electrolyte. And a silver wire is inserted. F: The other end of the glass tube is sealed with parafilm.

The preparation procedure of the sealed electrode is illustrated in Figure A-12. First, we seal a glass tube place Ag wire and the supporting electrolyte such as 0.1 M HClO₄ solution in a small glass tube. One end of the tube is sealed by a Pt wire in melted glass.

Due to the difference between the thermal expansion coefficients of Pt and glass, a small gap between glass and Pt wire is produced, which ensures that the reference is conductive, while the Ag^+ diffusion from the tube to electrochemical cell can be greatly diminished.

It should be noted that:

1. This electrode is a quasi-reference electrode, it should be calibrated with a standard reference electrode such as Ag/AgCl (KCl solution) reference electrode or SCE reference electrode in every experiment. This can be performed by reading the open circuit potential by connecting the reference electrode such as Ag/AgCl to reference electrode terminal and the quasi-reference electrode to the working electrode terminal of a potentiostat.
2. In order to avoid the liquid contact potential difference, the same supporting electrolyte in the tube as in the STM cell must be used.

BIBLIOGRAPHY

1. Colton, R., A. Engle, J. Frommer, H. Gaub, A. Gewirth, R. Guchenberger, J. Rabe, W. Heckel, and B. Parkinson, *Procedures in scanning probe microscopies*. 1998, New York: John Wiley & Sons.
2. Horvath, M., L. Bilitzky, and J. Huntner, *Ozone*. 1985, New York: Elsevier Science Publishing.
3. Jet Propulsion Laboratory, C., *Chemical kinetics and photochemical data for use in stratospheric modeling*. 1997.
4. Selley, N.J., *Experimental approach to electrochemistry*. 1977, New York: Wiley.
5. Obretenov, W., U. Schmidt, W.J. Lorenz, G. Staikov, E. Budevski, D. Carnal, U. Muller, H. Siegenthaler, and E. Schmidt, *Underpotential deposition and electrocrystallization of metals: an atomic view by Scanning Tunneling Microscopy*. Journal of the Electrochemical Society, 1993. **140**(3): p. 692-703.

Appendix E: List of publications.

1. Ye, T., D. Wynn, R. Dudek, and E. Borguet, *Photoreactivity of alkylsiloxane self-assembled monolayers on silicon oxide surfaces*. Langmuir, 2001. **17**(15): p. 4497-4500. (Part of Chapter 2)
2. Fomenko, V., C. Hurth, T. Ye, and E. Borguet, *Second harmonic generation investigations of charge transfer at chemically-modified semiconductor interfaces*. Journal of Applied Physics, 2002. **91**(7): p. 4394-4398.
3. He, Y., T. Ye, and E. Borguet, *The role of hydrophobic chains in self-assembly at electrified interfaces: Observation of potential-induced transformations of two-dimensional crystals of hexadecane by in-situ scanning tunneling microscopy*. Journal of Physical Chemistry B, 2002. **106**(43): p. 11264-11271. (Chapter 4)
4. He, Y., T. Ye, and E. Borguet, *Porphyrin self-assembly at electrochemical interfaces: Role of potential modulated surface mobility*. Journal of the American Chemical Society, 2002. **124**(40): p. 11964-11970. (Chapter 5)
5. McArthur, E., T. Ye, and E. Borguet, *Fluorescence detection of surface bound intermediates produced from UV photoreactivity of alkylsiloxane SAMs*. Journal of the American Chemical Society, In press. (Part of Chapter 2)
6. Ye, T., E. McArthur, and E. Borguet, *Mechanism of ambient UV degradation of alkylsiloxane self-assembled monolayers*. In preparation. (Part of Chapter 2)
7. Ye, T., Y. He, and E. Borguet, *In-situ STM study of electrode reactions and potential induced adsorption-desorption of porphyrin adsorbates*. In preparation. (Chapter 6)
8. Ye, T., Y. He and E. Borguet, *Surface micelles as molecular scale templates for anisotropic electrodeposition*. In preparation. (Chapter 7)

Acknowledgements.

I am deeply indebted to my Ph.D. advisor, Professor Eric Borguet, whose vision, encouragement and trust has been so essential to my growth in science. Dr. Yufan He has played a vital part in the work on electrochemical STM. Without his expertise and insight in electrochemical surface science, I would have been left in the dark for much longer. I acknowledge the important contributions from hardworking and talented undergraduate students, including Bill Lokar and Jasmine Ma in the STM project and Russell Dudek, Darren Wynn, and Eric McArthur in the SAMs project.

It had been a privilege to work with Dora Bodlaki and Vasiliy Fomemko, the senior graduate students in our research group. Their willingness to go out of their way to assist colleagues has helped to build a friendly atmosphere in our lab. I have been encouraged by their bravery in taking over completely new and challenging projects, and their success in these projects. I would also like to thank other graduate students, including Xue Feng and Kramer Camper for sharing inspirations, excitements, as well as frustrations in research.

I have benefited tremendously from the technical and intellectual resources around the chemistry department. Much of my work would not have been possible without the excellent support from the staff members in the machine shop and electronics shop. Acknowledgements go to Professor John Yates and his group. I have been fortunate enough to learn a great deal of surface science by interactions with such a leading surface science group. I would also like to thank Professors Toby Chapman,

Stéphane Petoud, David Waldeck and Gilbert Walker, and their research groups for their valuable technical assistance and suggestions.

Finally, my special thanks to my parents. Through their words and deeds, they always tell me how important it is to see opportunities in trying times and stay true to my aspirations. I cannot imagine how I could come this far without their unconditional love and support.